



universität
wien

DISSERTATION

Titel der Dissertation

Structural Analysis and Geochronology of the Khlong Marui Fault,
Southern Thailand

Verfasser

M.Sc. Pitsanupong Kanjanapayont

angestrebter akademischer Grad

Doktor der Naturwissenschaften (Dr.rer.nat.)

Wien, im September 2009

Matrikelnummer: 0648134

Studienkennzahl lt. Studienblatt: A 091 431

Dissertationsgebiet lt. Studienblatt: Geologie

Betreuer: Univ. Prof. Mag. Dr. Bernhard Grasemann

Contents

	Page
Acknowledgement.....	i-ii
Abstract.....	iii-iv
Zusammenfassung.....	v-vi

Chapter 1

Introduction.....	1-13
1.1 Location.....	3
1.2 Purpose and Scope of Study.....	5
1.3 Physiography.....	6
1.4 Regional Geology.....	8
1.5 Tectonics Setting.....	12

Chapter 2

Remote Sensing Interpretation.....	14-33
2.1 Introduction.....	14
2.2 Lineament Analysis.....	15
2.2.1 Aerial-photographs.....	15
2.2.2 Satellite Image.....	18
2.2.3 SRTM Digital Elevation Model (DEM).....	22
2.2.4 Composite Lineaments.....	25
2.3 Surface Ruggedness Pattern.....	26
2.4 Morphotectonics.....	29
2.5 Structural Interpretation.....	33

Chapter 3

Khlong Marui Shear Zone.....	34-54
3.1 Introduction.....	34
3.2 Geology.....	35
3.3 Structural Geology.....	44
3.3.1 Ductile Deformation.....	44
3.3.2 Kinematic Indicators.....	46
3.3.3 Brittle Deformation.....	50
3.4 Structural Model.....	54

Chapter 4

Microstructures.....	55-86
4.1 Introduction.....	55
4.2 Petrography and Microstructures.....	56

Contents (conct.)

	Page
4.3 Quartz Textures.....	79
4.4 Microstructures Deformation.....	86
 Chapter 5	
Geochronology.....	87-110
5.1 Introduction.....	87
5.2 Sample Preparation and Methodology.....	89
5.2.1 Whole Rock: Rb-Sr and Sm-Nd Isotope Analysis.....	89
5.2.2 Mica: Rb-Sr Isotope Analysis.....	89
5.2.3 Garnet: Sm-Nd Isotope Analysis.....	89
5.2.4 Zircon: U-Pb Isotope Analysis.....	90
5.3 Rb-Sr Analytical Results.....	92
5.4 Sm-Nd Analytical Results.....	94
5.5 U-Pb Analytical Results.....	96
5.6 Geochronology Interpretation.....	108
 Chapter 6	
Discussions.....	111-115
6.1 Deformation Phases.....	111
6.2 Paleostress Field Reconstruction.....	112
6.3 Tectonics Implication.....	113
 Chapter 7	
Conclusions.....	116-118
References.....	119-126
Appendix.....	127-135
A: Abbreviations.....	128
B: Sample Location.....	129
C: Data for LA-ICP-MS U-Pb Analysis of Zircon.....	130
Curriculum Vitae.....	136-137

List of Figures

Figure	Page
1.1 Regional tectonics framework in Thailand showing major strike-slip zones and related structures modified from Morley (2002), Polachan and Sattayarak (1989), Searle et al. (2007), and Watkinson et al. (2008). Box refers to Fig.1.2.	2
1.2 Shuttle Radar Topography Mission (SRTM) digital elevation model of the Khlong Marui Fault zone and Khao Phanom area. Box refers to Fig.1.3.	4
1.3 Topography of the study area is showed by Shuttle Radar Topography Mission (SRTM) digital elevation model combined with the digital map of the main rivers. The river named “Khlong Marui” drains the area flowing towards SSW.	7
1.4 Geology of the study area dominated by Permo-Carboniferous sedimentary rock and igneous intrusions (modified after Department of Mineral Resources, 1982).	9
2.1 Mosaic of aerial-photographs with lineament interpretations.	16
2.2 Lineament map from aerial-photographs and rose diagram showing a major maxima at 030° NNE-SSW, and two minor local maxima of 065° ENE-WSW and 130° NW-SE respectively.	17
2.3 LANSAT image bands 7, 5, and 4 with false-color composites RGB with lineament interpretation.	20
2.4 Lineament map with rose diagram based on LANSAT image lineament analysis shows the major trend at NNE-SSW with minor trending at NEE-SWW and NW-SE.	21
2.5 Hillshade map generated from SRTM digital elevation model (sun azimuth 315°, altitude 045°) with lineament interpretations.	23
2.6 Lineament map extracted from hillshade map presents with three main directions of 030° NNE, 060° ENE and 130° NW in rose diagram.	24
2.7 Rose diagrams from the lineaments extraction of air-photographs (a), satellite image (b), SRTM digital elevation model (c), and composite lineaments (d) show the major NNE-SSE with minor ENE-WSE and NW-SE trends.	25
2.8 Aspect map of the Khlong Marui Fault zone dominated the northwest and southeast domains.	27
2.9 Slope map presents the potential area of the last tectonics event at the slope break between 12.07-16.57° and 16.57-20.83°.	28
2.10 Fault scarp, fault valley and drainage network interpretation presented in mosaic of aerial-photographs.	30
2.11 3D model of the Khlong Marui Fault looking from the south. The model combines the geological map (Fig. 1.4) and the SRTM digital elevation model, which has 5 times exaggeration.	31
2.12 Triangular facets along the fault scarps can be observed throughout the study area; (a) along the Khlong Marui Fault; (b) west of Khao Phanom; (c) northeast of Khao Phanom; (d) southeast of Khao Phanom.	32

List of Figures (conct.)

Figure	Page
2.13 Rose diagram of all lineaments (a) and the NNE-SSW lineament interprets to the major fault zone with ENE-WSW synthetic and NW-SE antithetic secondary faults (b).	33
3.1 Geology of the Klong Marui shear zone consisting of mylonitic meta-sedimentary rocks associated with orthogneisses, mylonitic granites, and pegmatitic rocks (modified after Department of Mineral Resources, 1982).	36
3.2 Geologic cross-section showing steep dipping of the rocks in the Khlong Marui shear zone (see Fig. 3.1 for correlation).	37
3.3 Typical Permo-Carboniferous Kaeng Krachan group consisting of sandstone (a) and pebbly mudstone (b) at the west boundary of the study area.	37
3.4 Gneissic banding of the orthogneiss is represented by tourmaline-biotite rich layers and quartz-feldspar augen structures (a, b) in Mae Yai waterfall.	37
3.5 Granite at the western part of the area shows pinkish grey of K-feldspar in between the black biotite mylonitic layers (a) and quartz veins concordant parallel to the mylonitic foliation (b) at western Khao Phanom.	38
3.6 Variation of metapelite lithology from the west to the east of the shear zone; (a) reddish brown in western area; (b) dark brown in southwestern area; (c) greenish brown at the middle of Khao Phanom; (d) yellowish brown in eastern area; (e) reddish and yellowish brown in southwestern area; (f) reddish and greenish brown at southern Khao Phanom. It is caused by the different compositions.	39
3.7 Pebbly metapelite to metacglomerate outcrop shows thick layers lying to the NNE-SSW at the Ton Ha Chan waterfall (a). Variation of the pebbles sizes; (b) small pebbles at the same outcrop; (c) big pebbles in Ton Chan waterfall; and (d) stretching small pebbles at local waterfall in eastern area.	40
3.8 The impurity of quartzite showed the color variation from the west to the east of the shear zone; (a) yellowish and reddish brown in western area; (b) milky to yellowish brown at the western Khao Phanom; (c, d) yellowish brown in middle area; (e) milky to yellowish brown in eastern area; and (f) greenish brown in northeastern Khao Panom.	41
3.9 Pegmatitic veins concordant with the mylonitic metasedimentary rock with a different width at the eastern area of Khao Phanom (a, b). Tourmalines forming either as black layers at the pegmatite rims (a) or as veins into the mylonite at the same outcrop (b).	42
3.10 Proto-cataclasites to cataclasites are associated with a fault plane in the eastern (a) and western margins of the shear zone (b).	43

List of Figures (conct.)

Figure	Page
3.11 Outcrops along the Khlong Marui Fault showing major structure of foliations and stretching lineation in the orthogneiss at the Mae Yai waterfall (a), mylonitic granite of western area (b), metapelite in northern area (c), metapelite with pebbles at the Bang Tao Mae waterfall (d), quartzite in western area (e), and quartz vein in middle area (f).	45
3.12 Stereographic plots of the ductile deformation. Contour poles of the foliations (S_1) showing steeply dipping either WNW or ESE, and the lineations (L_1) trend to NNE-SSW. Contours are 1%, 2%, 3%, 4%, and 5% per 1% area by gauss counting method (Robin and Jowett, 1986).	46
3.13 The mylonitic structures of the pebbles in the metapelite show dextral shear of quartz grains σ -shape; (a, b) at the Ton Chan waterfall; (c) at the Ton Ha Chan waterfall; (d) in middle area; (e) in northern Khao Phanom; (f) at the Bang Tao Mae waterfall.	47
3.14 Fragmented quartz lenses showing shear band type (a) and domino-type (b) in the mylonites at middle Khao Phanom.	48
3.15 Shear band illustrated by S-C fabrics in metapelite with quartz pebble at the Bang Tao Mae waterfall (a). S-C' fabrics in mylonitic granite in western area (b) and metapelite in middle Khao Phanom (c, d).	48
3.16 Quartz layer deformed into boudinage at the Bang Tao Mae waterfall (a) and local waterfall in the northern area (b). Asymmetric folds via dextral sense of shear in orthogneiss at the Mae Yai waterfall (c) and at middle area (d).	49
3.17 Pegmatite lineations of tourmaline are NNE trending, parallel to the lineation in the host mylonitic metasedimentary rocks in eastern Khao Phanom (a, b).	49
3.18 Major joints in metapelite of western area (a) and quartzite at the Bang Tao Mae waterfall (b) striking WNW-ESE perpendicular to the main foliation.	50
3.19 Normal faults along the eastern margins of the Khao Phanom ductile core (a, b). Slickenside and striations record a normal fault component in general view (c) and zoom view (d).	51
3.20 Minor faults in the mylonite; (a) dextral kinematics ENE-WSW striking cuts through sinistral faults which are NW-SE strike in the metapelites at middle area; (b) ENE-WSW dextral in metapelite at the same outcrop; (c) ENE-WSW dextral in metaconglomerate at local waterfall in eastern area; (d) sinistral Riedel shear orientated NW-SE in metapelite at northeastern Khao Phanom; (e) ENE-WSW dextral Riedel shear in metaconglomerate at the Ton Ha Chan waterfall; (f) sinistral Riedel shear in metaconglomerate at the same outcrop.	52

List of Figures (conct.)

Figure	Page
3.21 The representation of brittle deformation is illustrated by rose diagram of WNW-ENE striking major joints (a). Stereographic plots of the fault planes (f) and their striations (s) indicate the NNE-SSW normal fault component with the ENE-WSW and NW-SE minor faults (b).	53
3.22 Schematic positive flower structure of Khlong Marui shear zone in between Permo-Carboniferous and Mesozoic sedimentary units. The dextral shear sense refers to the ductile deformation.	54
4.1 Photomicrograph of medium grained sandstone (a, b), fined grained sandstone (c, d), and mudstone interlayered with very fine grained sands at the west boundary of the study area (e, f). (a, c, e, PPL; b, d, f, CPL)	57
4.2 Orthogneiss at the Mae Yai waterfall shows the composition of quartz, feldspar, biotite, and tourmaline (a, b). Grain boundary migration (GBM) in quartz (c). Feldspars show oscillatory zoning (d), typical for magmatic crystallization, undulose extinction (e), and fracture with right lateral offset (f). (a, PPL; b-f, CPL)	58
4.3 Mineral composition and mylonitic structure of granite in western area (a, b), subgrain rotation (SGR) (c), grain boundary migration (GBM) (d), “V”-pull-apart structure (e), and asymmetric myrmekite (f). (a, PPL; b-f, CPL)	60
4.4 Low-grade mylonite showing fine grained quartz and mica at southeast area (a, b), pebble clasts in fined grained mica matrix at southern area (c, d), elongate quartz rods with S-C’ fabric at the same outcrop (e, f). (a, c, e, PPL; b, d, f, CPL)	61
4.5 Different grain sizes of quartz and biotite in the mylonites. (a, b) Fine grained at western area; (c, d) medium grained at middle Khao Phanom; (e, f) course grained at eastern area. (a, c, e, PPL; b, d, f, CPL)	62
4.6 Variation of the metapelite composition. (a, b) Biotite rich in eastern area; (c, d) quartz rich in middle area; (e, f) isolated quartz lens cut through the metapelite at the Bang Tao Mae waterfall. (a, c, e, PPL; b, d, f, CPL)	63
4.7 Metaconglomerates in the study area show a mylonitic structure and different sorting. (a, b) Poorly sorted metaconglomerate with fine matrix in southern area; (c, d) well sorted medium grained metaconglomerate in southwestern area; (e, f) very poorly sorted elongated grain metaconglomerate at the same outcrop. (a, c, e, PPL; b, d, f, CPL)	64
4.8 Pebbles in metapelite comprise different rock types. (a, b) Quartz and K-feldspar at the local waterfall in eastern area; (c, d) granitic rock comprises quartz, feldspar and amphibole at northeastern Khao Phanom; (e, f) tourmaline rich granitic rock in western area. (a, c, e, PPL; b, d, f, CPL)	65
4.9 Porphyroclast in metapelite at the middle area of Khao Phanom showing dextral shear. (a, b) Rhomboidal fish; (c, d) quartz sigmoid; (e, f) σ -type K-feldspar porphyroclast. (a, c, e, PPL; b, d, f, CPL)	67

List of Figures (conct.)

Figure	Page
4.10 σ -type K-feldspar porphyroclast with stair-stepping in mylonitic metasedimentary rocks. (a, b) Small K-feldspar clast in middle area; (c, d) synthetic fracture forming in K-feldspar clast at northern area; (e, f) antithetic fracture forming in K-feldspar clast at middle area. (a, c, e, PPL; b, d, f, CPL)	68
4.11 Different types of dextral mica fish. (a) Lenticular mica fish at the Bang Tao Mae waterfall; (b) half-lenticular fish at the same outcrop; (c) fish with high aspect ratio at the same outcrop; (d) fish with small aspect ratio at the same outcrop; (e) aggregate of mica fish in lenticular shape at middle area; and (f) aggregate of mica fish forming in high aspect ratio at the same outcrop. CPL	69
4.12 Sinistral shear bands in different minerals. Domino type-fragmented quartz (a) and K-feldspar in northern Khao Phanom (b). Shear band in fibrolitic sillimanite at the Bang Tao Mae waterfall (c). (a, c, e, PPL; b, d, f, CPL)	70
4.13 Small-scale fault cuts through the matrix at southern area (a, b). Domino boudins in mepelite (c, d) and quartz lenses in western area (e, f). (a, c, e, PPL; b, d, f, CPL)	71
4.14 Quarter structures in mylonitic metasedimentary rock. Quarter mats at middle area (a, b) and asymmetric myrmekite at northern area (c, d). (a, c, CPL)	72
4.15 Quartzite with a varying grain size, from fine grained at western area (a, b), medium grained in northern area (c, d), to coarse grained at western area (e, f). (a, c, e, CPL; b, d, f, Gypsum plate inserted)	73
4.16 Variation of quartz grain size and composition. (a, b) Intercalated coarse and fine grained layers at western area; (c, d) quartz lens cuts through quartzite in eastern area; (e, f) accessory minerals of mica and K-feldspar in quartzite composition at the same outcrop. (a, c, e, CPL; b, d, f, Gypsum plate inserted)	74
4.17 Dynamic recrystallisation in the rocks of the Khlong Marui shear zone. (a) Highly elongated grain in southern area; (b) undulose extinction of monocrystalline quartz pebbles with basal gliding at southwestern area; (c) bulging (BLG) at western area; (d) undulose extinction and bulging (BLG) at the same outcrop; (e) subgrain rotation (SGR) in southwestern area; and (f) grain boundary migration (GBM) in western area. (a, PPL; b-f, CPL)	75
4.18 Pegmatitic rocks at eastern area show equigranular grains of quartz, feldspar, white mica, and tourmaline (a). Minerals forming lineations are present in garnet pegmatites (b). (a, c, PPL; b, d, CPL)	76
4.19 Fine grained tourmalines at eastern area are formed as a layer at the pegmatite rims (a, b). Contact zone between pegmatitic rock and the metapelite country rock at eastern Khao Phanom (c, d). (a, c, PPL; b, d, CPL)	77
4.20 Cataclasites of quartzite (a), metapelite (b), metaconglomerate (c, d). Fine-grained cataclasites at the contact zone between the fault rock and the intact country wall rock (e, f). CPL	78

List of Figures (conct.)

Figure	Page
4.21 Sketch showing the relative orientation of eigen vector (a_1 and a_2), instantaneous flow elements (ISA_1 and ISA_2), and their angular relationship in (a) transpression physical space and (b) transtension physical space. (c) The angle, δ , between the oblique grain shape fabric and the main foliation. (d) The angle, β , between the perpendicular to the central girdle segment of quartz c -axis fabric and the main foliation.	80
4.22 Angle between the oblique grain shape fabric and the main foliation under crossed polarized light of the sample 3A1 (a), 22C3 (b), 1E2 (c), 88A2 (d), 1D1 (e), and 14C1 (f).	81
4.23 Angle between the oblique grain shape fabric and the main foliation under cross polarized light for samples 14B1 (a) and 26D1 (b).	82
4.24 (previous page) Sterographic plots of $\langle 001 \rangle$, $\langle 100 \rangle$ and $\langle 110 \rangle$ from the west to the east of the Khlong Marui shear zone with the angle between the perpendicular to the central girdle segment of quartz axis fabric and main foliation.	83
4.25 Diagram plots of the angle between the normal to the central girdle and the foliation (β) and the mean vorticity number (W_m) showing the ellipticity of the finite strain ellipsoid (R_f).	85
5.1 Geological map of the Khlong Marui Fault and adjacent area, modified after Department of Mineral Resources (1982), showing the locations of the $^{40}\text{Ar}/^{39}\text{Ar}$ dated samples (Charusiri, 1989) and this study dated samples. The ages were presented in Ma. (Bt=biotite; Grt=garnet; Hb=hornblende; Ms=moscovite; Wm=white mica; Zr=zircon)	88
5.2 Rb-Sr isochron plots for (a) Bt-wr of mylonite (PK9A1); (b) Bt-wr of orthogneiss (PK29A1); (c) Bt-wr of mylonitic granite (PK2A1); (d) Wm-wr of pegmatite (PK30Z); (e) Wm-wr of pegmatite (PK25C). All errors are smaller than the size of the symbols.	93
5.3 Backscattered electron images and corresponding garnet element distribution profiles of pegmatite (PK30Z) (a, c). Element distribution profile of garnet from pegmatite (PK30Z) (b, d). Backscattered electron images showing phosphate micro-inclusions in garnet (e).	94
5.4 Sm-Nd isochron plot for wr and 3 different Grt fractions of pegmatite sample PK30Z.	95
5.5 Cathodoluminescence (CL) images of zircon used for LA-ICP-MS U-Pb analysis of sample PK29A1 (a, c, e). U-Pb concordia diagrams of the sample PK29A1 (part1) (b, d, f).	97
5.6 Cathodoluminescence (CL) images of zircon used for LA-ICP-MS U-Pb analysis of sample PK29A1(a, c, e). U-Pb concordia diagrams of the sample PK29A1 (part2) (b, d, f).	98

List of Figures (conct.)

Figure	Page
5.7 Cathodoluminescence (CL) images of zircon used for LA-ICP-MS U-Pb analysis of sample PK29A1(a, c, e). U-Pb concordia diagrams of the sample PK29A1 (part3) (b, d, f).	99
5.8 Cathodoluminescence (CL) images of zircon used for LA-ICP-MS U-Pb analysis of sample PK2A1(a, c, e). U-Pb concordia diagrams of the sample PK2A1 (part1) (b, d, f).	100
5.9 Cathodoluminescence (CL) images of zircon used for LA-ICP-MS U-Pb analysis of sample PK2A1(a, c, e). U-Pb concordia diagrams of the sample PK2A1 (part2) (b, d, f).	101
5.10 Cathodoluminescence (CL) images of zircon used for LA-ICP-MS U-Pb analysis of sample PK2A1(a, c). U-Pb concordia diagrams of the sample PK2A1 (part3) (b, d).	102
5.1 Cathodoluminescence (CL) images of zircon used for LA-ICP-MS U-Pb analysis of sample PK30Z(a, c, e). U-Pb concordia diagrams of the sample PK30Z (part1) (b, d, f).	103
5.12 Cathodoluminescence (CL) images of zircon used for LA-ICP-MS U-Pb analysis of sample PK30Z(a, c, e). U-Pb concordia diagrams of the sample PK30Z (part2) (b, d, f).	104
5.13 Cathodoluminescence (CL) images of zircon used for LA-ICP-MS U-Pb analysis of sample PK26 (a, c, e). U-Pb concordia diagrams of the sample PK26 (b, d, f).	105
5.14 Sketch of zircon structure from the granitic materials in the Khlong Marui shear zone illustrates the intergrowth zoning. They share the same systematic of ages from the Pre-Cambrian core to the Eocene rim.	107
5.15 Ages model plot from overall geochronology data presents the major exhumation time of the fault core is in Eocene.	108
5.16 White mica composition of (a) sample PK30Z and (b) sample PK25C from electron-microprobe measurement.	109
5.17 Different sizes of white mica grain from 2 pegmatites; (a) small white mica of sample PK30Z; and (b) big white mica of sample PK25C.	109
6.1 Integrated kinematic analyses indicated the E-W maximum principal stress axis (σ_1) with N-S tensional stress (σ_3) of D_{n-2} and D_{n-1} (a) before changing stress pattern to N-S maximum principal stress axis (σ_1) of D_n (b).	112
6.2 Tectonics reconstruction in Eocene based on Charusiri et al. (1993), Hall (2002), Mitchell (1993), Mitchell et al. (2007), Morley (2002), and Sarle et al. (2007). The collision between India and Asia had influenced the exhumation of the Khlong Marui ductile core.	115

List of Tables

Table		Page
2.1	Landsat thematic mapper (TM) spectral bands (after Sabins, 1996).	18
2.2	Evaluation of TM color combinations (after Sabins, 1996).	19
4.1	Summarized data from quartzite samples in the Khlong Marui shear zone.	84
5.1	Rb-Sr analytical results of samples from the Khlong Marui shear zone.	92
5.2	Sm-Nd analytical results of garnet fractions and the whole rock of pegmatite sample PK30Z.	95

Acknowledgement

My doctoral dissertation under the financial support of the Austrian Exchange Service (ÖAD) through Technologiestipendien Südostasien Doktorat allowed me to share my time and experiences at the Department of Geodynamics and Sedimentology, University of Vienna. There are many people to warmly thank for their generous contribution to complete my doctoral dissertation during last three years.

First of all, I would like to express my deeply grateful acknowledgement to my supervisors Prof. Dr. Bernhard Grasemann of Structural Processes Group, Department of Geodynamics and Sedimentology, University of Vienna, who gave me a hand from the beginning to the end of my doctoral research. He also provided a financial support for the second field work transportation to Thailand, gave many fruitful discussions on structural geology, microstructures, and tectonics, assisted during the second field work, and corrected and revised this dissertation manuscript.

A great sincere acknowledgement is also given to Dr. Michael Edwards for valuable suggestions, early field assistant, and improve the manuscripts the dissertation. Many thanks to you, Mike, for making my life easier and comfortable in all along the period of my research in Vienna.

The thanks are furthermore due to Prof. Dr. Urs Klötzli, Department of Lithospheric Research, University of Vienna for his scientific advices, U-Pb isotope analysis, and discussions on geochronology at all time. He made the thing easy in case of solving any kind of problems. Dr. Eva Klözli from Department of Lithospheric Research, University of Vienna and Dr. Helga Prievalder from Geological Survey of Austria are gratefully thanked for cathodoluminescence (CL) images.

This is a great opportunity to express my respect to Prof. Dr. Martin Thöni, Department of Lithospheric Research, University of Vienna. I am also indebted to him for the plentiful discussions on Sm-Nd and Rb-Sr isotope analyses. I am pleased to thank Prof. Dr. Harald Fritz, Institute of Earth Sciences, University of Graz for quartz texture measurement. Prof. Dr. Theodoros Ntaflos, Department of Lithospheric Research, University of Vienna, is thanked for microprobe management.

I am also grateful to Department of Geology, Faculty of Science, Chulalongkorn University to allow me a full time leave during this doctoral study. Assoc. Prof. Dr. Punya Charusiri and Dr. Montri Choowong are gratefully thanked for supporting the transportation during the field work in Thailand and for the sample shipping.

Many thanks to Mag. Andras Zamolyi for help me a lot to understand the world of ArcGIS. Dr. Gerlinde Habler is gratefully thanked for assistance on the petrography and microstructure

analysis. Thanks are extended to Dr. Kurt Decker for the software TectonicsFP version 1.5., Dr. Ulrike Exner for GPS device, Dr. Hugh Rice for improvement the manuscript on the publication, Dr. Erich Draganits for manuscript improvement, Mag. Andreas Beidinger and Dr. Marcel Frehner for Zusammenfassung improvement. Thanks are due to my university colleagues who are Mag. Christoph Iglseder, M.Sc. Basanta Raj Adhikari, Mag. Darko Spahic, Mag. Zekeriya Günes, Monika Müller, Linda Lerchbaumer, Vicky Haider, Christine Hörfarer for encouragements, discussions, and for sharing many recreation times during last three years in Vienna.

I am indebted to many people who gave their technical assistances all along the period of my doctoral study including Norbert Irnberger for graphic stuffs, Werner Füzi, Leopold Slawek, Sigrid Hrabe, and Claudia Beybel for making this-sections, Franz Biedermann for mineral separation, Ing. Monika Horschinegg for Sm-Nd and Rb-Sr isotope analyses, Franz Kiraly for microprobe analysis.

Special recognition and thanks are due to Department of Mineral Resources Thailand through Kavin Kedpiroj for the regional geologic data. Field assistances are thanked to Natsarun Siripaguysak and Patinya Jaitan. I also would like to warmly thank to the extremely friendly people in Phang Nga, southern Thailand. I met them when I was working in the field. I would mention the name of Mr. Mongkon Kongnarong who has provided me with necessary assistance during the field work.

Finally, I am indebted to my parents and my two sisters who provide the accommodation during the field work, and encourage me in everything to the highest education.

Abstract

The Khlong Marui Fault cuts across Thai peninsula trending NNE-SSW stretching approximately 150 km from the Gulf of Thailand to the Andaman Sea. The shear zone affects an area up to 10 km in width from the Khlong Marui Fault eastward to the Bang Kram Fault. This zone, marked by a large valley with the high topographic lozenge shape 40 km by 6 km body named Khao Phanom, was the focus of this study. The area to the west is bounded by a long, north-south trending mountain range of Western Belt Granite and Permo-Carboniferous sedimentary rock. The east boundary is represented by a huge valley of Bang Kram Fault which comprises a geographically long cliff of Permian carbonate and Triassic sedimentary rock. The geology within this wrench zone consists of steep strongly deformed layers of mylonitic meta-sedimentary rocks associated with orthogneisses, mylonitic granites, and pegmatitic veins. The mylonite belonging to the Permo-Carboniferous Kaeng Krachan Group has been deformed and developed a mylonitic structure with varying grades of metamorphism. Brittle cataclastic zones were localized in the eastern and western margin of this ductile core zone.

The Khlong Marui shear zone had been deformed by three deformation phases; D_{n-2} , D_{n-1} , and D_n . The early two phases of strike-slip deformation, which have similar orientation of strike 030° and dips to WNW and ESE, are characterized by dextral ductile deformation but under different metamorphic grades. It is represented by the two stretching lineations recorded in the quartzite and quartz textures in the eastern Khao Phanom. Isolated block of fibrolitic sillimanite mylonites indicate that the rocks have experienced amphibolite metamorphic condition of D_{n-2} before overprinted by the D_{n-1} .

D_{n-1} is dominated the deformation in the Khlong Marui Faults by the major lineament, foliation, and stretching lineation. Mylonitic foliation (C), secondary synthetic foliations (C'), and lineation indicate dextral sense of shear as well as σ -shaped clasts, domino-type boudinage, shear band-type foliation, asymmetric folds, asymmetric myrmekite, and "V"-pull-apart. Synkinematic behavior of the pegmatite intrusion during the ductile stage is established by the parallel nature of tourmaline lineations in pegmatites and stretching lineations in the country rocks. Dynamically recrystallizing quartz records undulose extinction, basal gliding, bulging (BLG), subgrain rotation (SGR), and local grain boundary migration (GBM) under the dextral strike-slip deformation. Microstructures and mineral assemblages suggest that the rocks in the Khlong Marui shear zone have been metamorphosed at low to medium greenschist facies. Mean vorticity number (W_m) of quartz texture indicates simple shear flow with a small finite strain ellipsoid (R_f) in a transpression zone. Strain partitioning within the Khlong Marui shear zone is responsible for local transtension blocks. A major joint set towards 110° , which is orientated perpendicular to the 030° stretching lineation, represents tension fracturing. Mylonitic structures in this area are spectacularly overprinted by the Riedel shear fractures (R and R') and D_n . The synthetic Riedel shear fractures (R) are oriented in ENE-WSW and the associated antithetic Riedel shear

fractures (R') trend to NW-SE. They are generally restricted to in between the major NNE-SSW striking faults.

D_n involves the brittle normal faulting dominantly oriented striking between 000° and 030°. The faults in the area are geomorphically expressed by the fault scarp, triangular facets, and linear valley. The steeply dipping faults are associated with proto-cataclasites to cataclasites along both side of the ductile core. Normal fault component is suggested by the slickenside, striation, and associated shear sense indicators.

The NNE striking dextral shearing and two secondary fractures constrain the orientation of the maximum principal stress axis (σ_1) in the E-W direction of D_{n-2} and D_{n-1}. They suggest that the tensional stress, represented by σ_3 , is oriented in the N-S direction. The two dextral ductile phases of the Khlong Marui Fault and the Western Granite magmatism were significantly influenced by the Western Burma and Shan-Thai collision and/or the subduction along the Sunda Trench in the Late Cretaceous. The same age of inherited core from all zircons in the Khlong Marui shear zone indicates that they have the same material from the Archean period with the different evolution. They share the same systematic ages although the mylonitic granite has the different intergrowth zoning from others. The Upper Triassic to Upper Cretaceous outer core zircon ages of the mylonitic granite is probably related to the granite intrusion period. The similar zoning patterns and ages in zircon, from the pegmatites and the orthogneisses indicate that the pegmatites were derived from the orthogneiss material.

The intense deformation conditions of rock in between un-deformed sedimentary host rock units suggests that the core of the Khlong Marui shear zone had been exhumed at mid-to-upper crustal levels to its present level. The continuation of dextral movement and E-W compression may have caused the exhumation of the fault core forming the positive flower structure. The major exhumation period of the ductile core in the Eocene is indicated by U-Pb, Rb-Sr, and Sm-Nd dating. Palaeogeographic reconstructions in Eocene suggest the dextral shear of the NNE-SSW strike-slip systems. This period was tectonically influenced in the SE Asia region by the early time of India-Asia collision. The exhumed faults related to the positive flower structure are pre-existing anisotropic in the rotated stress field producing NNE-SSW normal faults in the study area after Eocene. The palaeostress field of D_n, which is N-S direction of σ_1 and E-W direction of σ_3 , fits quite well with the E-W extension model. Therefore, the changing stress field in the Khlong Marui Fault, which has affected by switching from dextral strike-slip to the normal faulting, relates to the changing of the stress pattern caused by the India-Asia collision.

Zusammenfassung

Das NNE - SSW streichende Khlong Marui Störungssystem quert die Thailändische Halbinsel vom Golf von Thailand bis zum Andamanischen Meer und erstreckt sich über eine Länge von ca. 150 km. Die ca. 10 km breite Scherzone, ist begrenzt durch die Khlong Marui Störung im Westen, welche die Scherzone gegen die N-S streichende Gebirgskette des "Western Belt Granite" und Permokarbone Sedimentgesteine abgrenzt. Gegen Osten wird die Scherzone durch die Bang Kram Störung abgegrenzt, welche durch ein grosses Tal gekennzeichnet wird und eine geologische Klippe Permischer Karbonate und Triadischer Sedimentgesteine beinhaltet. Hauptaugenmerk der Arbeit ist eine rhomboidale topographische Erhöhung innerhalb der Scherzone, namens Khao Phanom. Die Lithologie innerhalb der Scherzone wird charakterisiert durch steil einfallende, stark deformierte mylonitische Metasedimente der Permokarbonen Kaeng Krachan Gruppe, welche unterschiedliche Metamorphosegrade aufweisen. Die mylonitischen Metasedimente werden begleitet von Orthogneiss-Lagen, mylonitisierten Graniten und pegmatitischen Gängen. An den Rändern der duktilen Kernzone bildeten sich lokal spröde kataklastische Zonen aus.

Die Khlong Marui Scherzone wurde während drei Phasen D_{n-2} , D_{n-1} und D_n deformiert. Die frühen Phasen D_{n-2} , D_{n-1} weisen eine dominante horizontale Scherdeformation auf. Beide zeigen ein ähnliches Streichen (ca. 030°) und Einfallen (WNW und ESE) und sind durch duktile Deformation unter verschiedenen Metamorphosebedingungen charakterisiert. Die zwei Deformationsphasen weisen zwei ähnliche Streckungslineare in den Quarziten und Quarztexturen am östlichen Khao Phanom auf. Isolierte Mylonitblöcke mit fibrösem Silimanit zeigen eine D_{n-2} Deformation unter amphibolitfaziellen Bedingungen, welche anschließend von D_{n-1} überprägt wurde.

Die dominierende Deformation im Khlong Marui Störungssystem rührt von der Deformationsphase D_{n-1} her, die durch dextrale Scherung gekennzeichnet ist. Der dextrale Schersinn kann von im Gelände beobachteten S-C-Gefügen und von Mikrostrukturen aus Dünnschliffanalysen abgeleitet werden. Solche Mikrostrukturen sind zum Beispiel sigmoidal geformte Klasten (σ -Klasten), asymmetrische Boudins, S-C-Gefüge, asymmetrische Falten, asymmetrische Myrmekite und "V-Pull-Apart" Strukturen. Die zur duktilen Deformationsphase synkinematische Pegmatitintrusion ist durch die in den Pegmatiten parallel zur Streckungslineation eingeregelter Turmaline belegt. Dynamisch rekristallisierte Quarze zeigen undulöse Auslöschung, "basal gliding", "bulging" (BLG), "subgrain rotation" (SGR) und lokal "grain boundary migration" (GBM) unter dextraler Scherung. Mikrostrukturen und Mineralzusammensetzungen deuten eine grünschieferfazielle Metamorphose für die Deformation D_{n-1} an. Die "mean vorticity number" (W_m) der Quarztexturen deutet auf eine einfache Scherung mit einer kleinen finiten Verformungselipse (R_f) in einer transpressiven Zone. Lokal auftretende Transtension in der Khlong Marui Scherzone wird durch "strain partitioning" verursacht. Ein auf den Scherzonenrand normal stehendes Kluftsystem repräsentiert spröde Zugbrüche. Die

mylonitischen Strukturen werden durch Riedelbrüche (R und R'), die ebenfalls dextralen Schersinn anzeigen, und die Deformation D_n überprägt. Die ENE-WSW streichenden synthetischen und NW-SE streichenden antithetischen Riedelbrüche sind beschränkt auf den Bereich zwischen den die Scherzone begrenzenden NNE-SSW streichenden Hauptstörungen.

Die Deformationsphase D_n beinhaltet spröde NNE-SSW streichende Abschiebungen, deren geomorphologischer Ausdruck "fault scarps", "triangular facets" und langgestreckte Täler ist. Protokataklasite und Kataklasite, assoziiert mit den steil einfallenden Abschiebungen, sind an beiden Seiten des duktilen Kernes der Scherzone zu finden.

Die NNE streichende dextrale Scherung während D_{n-2} , D_{n-1} gemeinsam mit den syn- und antithetischen Riedelscherbrüchen zeigen eine E-W Orientierung der größten Hauptnormalspannung σ_1 und eine N-S Orientierung der kleinsten Hauptnormalspannung σ_3 . Die Deformationsphasen D_{n-2} , D_{n-1} , sowie der "Western Granite" Magmatismus stehen mit der Kollision von Westburma und Shan-Thai und/oder mit der Subduktion entlang des Sunda Grabens in der Späten Kreide im Zusammenhang. Datierte Zirkonkerne von granitischen Gesteinen innerhalb der Scherzone geben ein Archaisches Alter an, wobei die anschliessende Entwicklung unterschiedlich verläuft. Hierbei unterscheiden sich die mylonitisierten Granite von anderen granitischen Gesteinen durch unterschiedliche Zonierung. Die mylonitisierten Granite weisen Obertriadische bis Oberkretazische Alter für äußere Kerne auf und stehen wahrscheinlich mit den Granitintrusion in der Späten Kreide im Zusammenhang. Ähnliche Zonierungsmuster und Alter aus Zirkonen in den Pegmatiten und Orthogneisen lassen darauf schließen, dass die Pegmatite von Material aus den Orthogneisen abstammen.

Das Auftreten intensiv deformierter Gesteine innerhalb der Scherzone zwischen undeformierten Sedimenten weist auf eine Exhumation des Kernes der Khlong Marui Scherzone aus mittel- bis oberkrustalen Tiefen hin. Die Exhumation könnte durch eine positive Blumenstruktur, geformt durch das gemeinsame Auftreten von dextraler Scherung und E-W Kompression, verursacht worden sein. Das Eozäne Exhumationssalter des duktilen Kernes wird durch U-Pb, Rb-Sr, und Sm-Nd Datierungsmethoden belegt. Die Phase der dextralen Scherung entlang des NNE-SSW streichenden Störungssystems wird durch pläogeographische Rekonstruktionen ebenfalls als Eozän angegeben. Diese Periode war gekennzeichnet durch die frühe Kollision von Indien und Asien. Eine anschließende Rotation des Spannungsfeldes führte zur Reaktivierung der exhumierten NNE-SSW streichenden Störungen als Abschiebungen (D_n). Die N-S Orientierung von σ_1 und die E-W Orientierung von σ_3 während der Deformation (D_n) korreliert mit dem E-W gerichteten Extensionsmodell. Folglich steht die Rotation des Spannungsfeldes, welches den Wechsel von dextraler Bewegung zu abschiebender Bewegung bewirkt, im Zusammenhang mit der Änderung des Spannungsmuster während der Kollision von Indien und Asien.

Chapter 1

Introduction

In southern Thailand, in the famous tin-tungsten mining area, past geological studies have focused on the “Tin Belt”, or the Sn-W-REE bearing “S-type Central and Western Granite Belt” (Charusiri et al., 1993; Garson et al., 1975; Ishihara et al., 1980; Schwartz et al., 1995). The structural geology of the area is dominated by a long linear northeast strike-slip system including Khlong Marui Fault.

The Khlong Marui Fault is well known as one of the four major strike-slip faults in Thailand these are the: (i) Mae Ping (Wang Chao), (ii) Three Pagodas, (iii) Ranong, and (iv) Khlong Marui (Fig. 1.1). The Mae Ping and Three Pagodas faults strike northwest parallel to the Ailao Shan-Red River Fault in China while the Ranong and Khlong Marui faults strike northeast-southwest. The Ailao Shan-Red River, Mae Ping, and Three Pagodas faults were interpreted as strike-slip faults that facilitated the southeast Indochina block extrusion during India-Asia collision in Eocene to Miocene (Tapponnier et al., 1986). The northwest strike-slip systems started with left-lateral movement during the initial collision period and inverted to right-lateral motion in late Miocene (Charusiri et al., 2002; Gilley et al., 2003; Huchon et al., 1994; Lacassin et al., 1997; Leloup et al., 1995, 2001; Searle, 2006; Tapponnier et al., 1982, 1986, 1990).

The Three Pagodas Fault seems to be intersected by the Ranong Fault in the northern Gulf of Thailand. The Ranong and Khlong Marui faults were interpreted to be conjugate faults of the Mae Ping and the Three Pagodas Fault (Lacassin et al., 1997; Tapponnier et al., 1986). Their movement started as ductile dextral motion and changed to brittle sinistral at the same time as the northwest strike-slip systems were inverted in the Miocene (Charusiri et al., 2002; Lacassin et al., 1997; Tapponnier et al., 1986).

This conjugate system contributed to Cenozoic basin development in South China Sea, Andaman Sea and the Gulf of Thailand (Briais et al., 1993; Charusiri et al., 2002; Morley, 2001, 2002; Packham, 1993; Pigott and Sattayarak, 1993; Polachan et al., 1991; Polachan and Sattayarak, 1989; Tapponnier et al., 1986). The idea was applied to offshore geology for high potential hydrocarbon resources namely “Tertiary basins” in Thailand. They were mentioned as strike-slip faults controlling basin formation (Pigott and Sattayarak, 1993; Polachan et al., 1991; Polachan and Sattayarak, 1989). Other concepts of extensional models have been developed by Huchon et al. (1994), Morley (2001, 2002), Morley and Westaway (2006).

Despite the regional importance of this major structure, the intra-plate Khlong Marui strike-slip zone has received few modern structural geology studies (Garson and Mitchell, 1970; Garson et al., 1975; Watkinson et al., 2008).

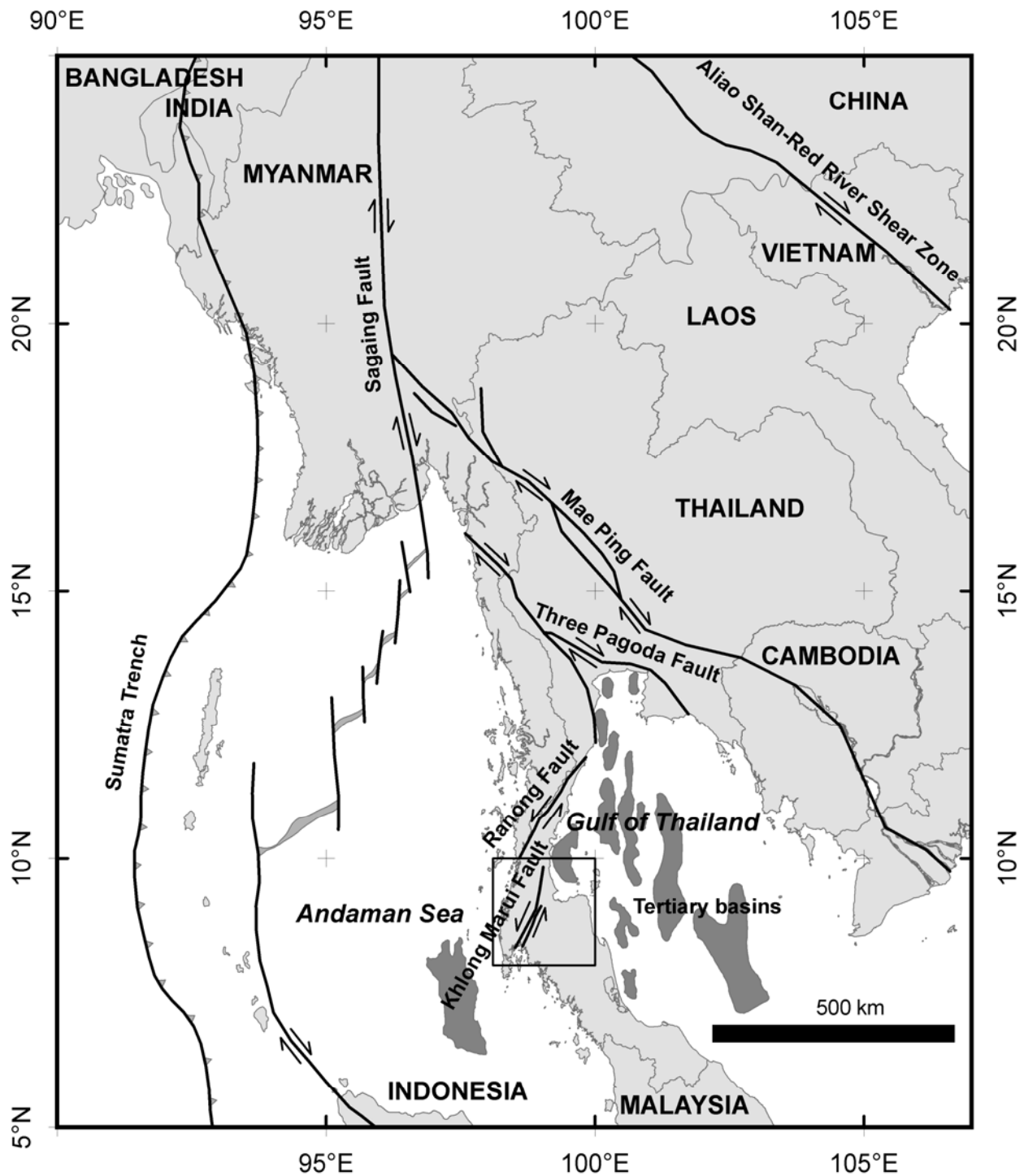


Figure 1.1 Regional tectonics framework in Thailand showing major strike-slip zones and related structures modified from Morley (2002), Polachan and Sattayarak (1989), Searle et al. (2007), and Watkinson et al. (2008). Box refers to Fig.1.2.

1.1 Location

The Khlong Marui Fault is located in Surat Thani, Phang Nga, and Krabi province, southern Thailand between Latitudes 8°20'00" N to 9°40'00" N, and Longitudes 98°30'00" E to 99°10'00" E (Fig. 1.2). The wrench zone of the Khlong Marui Fault including the Bang Kram Fault is roughly 150 km by 10 km trending NNE-SSW from the Gulf of Thailand to the Andaman Sea. In many cases, the fault trace extends to Phuket island in Andaman Sea (Garson et al., 1975, Watkinson et al., 2008). The area is dominated by a clear topographic mountain range named Khao Phanom which is bounded to the west through the Khlong Marui Fault by Western Granite Belt and Permo-Carboniferous sedimentary rocks, and to the east by Permian to Triassic sedimentary rocks through the Bang Kram Fault. Khao Phanom is approximately 40 km. long and 6 km. wide and is mainly composed of high deformed rocks; so this area was interpreted to the fault core.

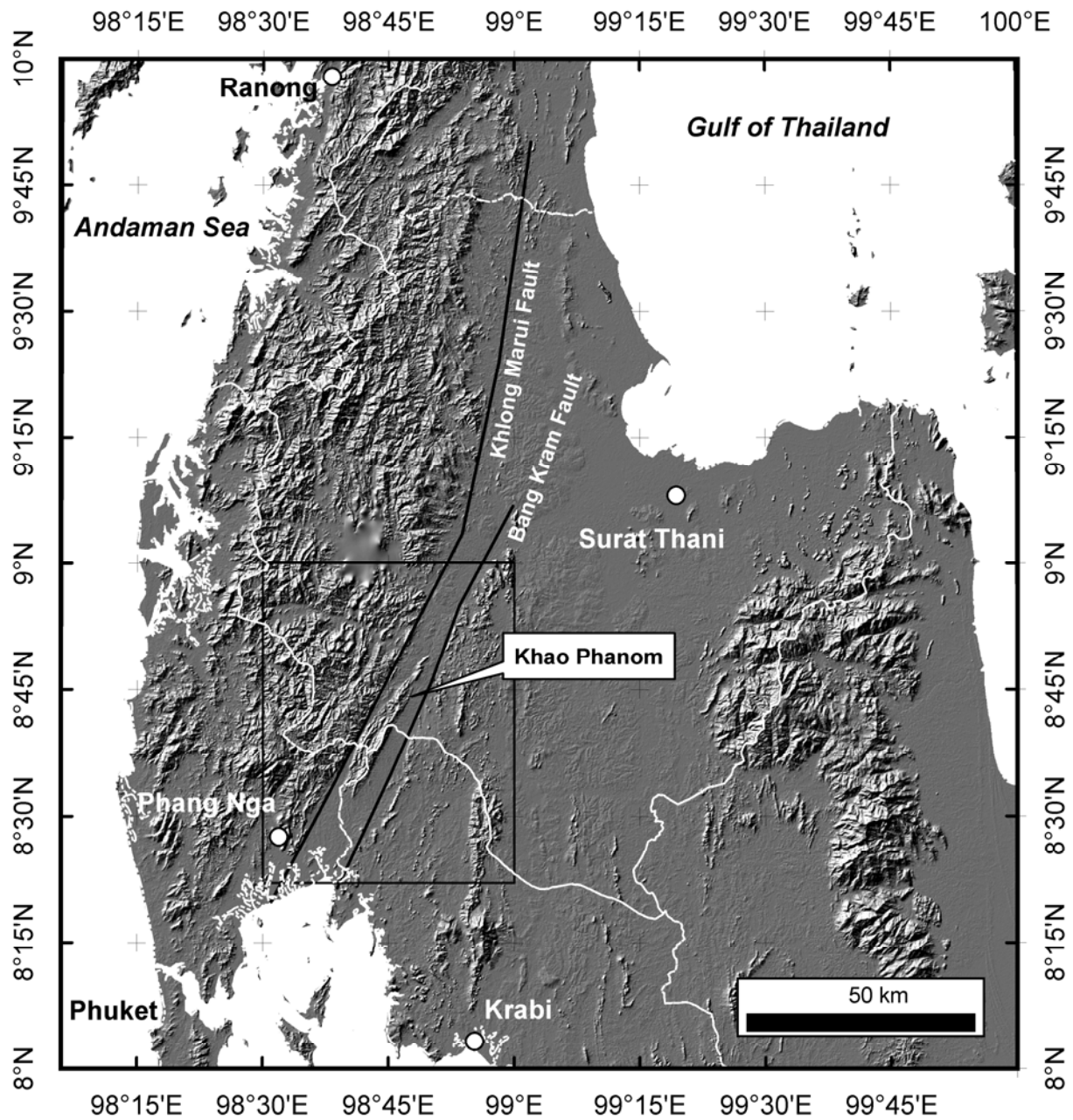


Figure 1.2 Shuttle Radar Topography Mission (SRTM) digital elevation model of the Khlong Marui Fault zone and Khao Phanom area. Box refers to Fig.1.3.

1.2 Purpose and Scope of Study

This study deals with the structural geology of the Khlong Marui Fault and its evolution and focuses on the Khao Phanom area, which records a progressed structural deformation history. Macroscopic, mesoscopic, and microscopic scales are studied by means of structural geology and geochronology.

The early steps of this study involved the literature reviews and study planning. The general geologic data such as the geological map and previous works have been collected, reviewed and compiled. Macroscopic structures have been studied via three different remote sensing datasets including aerial-photographs, Landsat TM satellite image, and SRTM digital elevation model (DEM). Each data source has been integrated in an ArcGIS geodatabase for quantitative spatial lineament interpretation. Spatial lineament orientations have been quantified, plotted, and statistically analyzed in rose diagrams. The field investigations include detailed structural mapping of the Khlong Marui Fault zone focusing on mesoscopic studies in the Khao Phanom area. Spatial data have been measured, quantified and plotted in equal-area stereographic projections and rose diagrams for statistical analysis. Thin sections and rock chips microstructures have been studied from oriented samples. Additionally, minerals have been separated from selected samples in order to perform U/Pb zircon, Sm/Nd garnet, and Rb/Sm mica geochronology.

1.3 Physiography

The Khlong Marui Fault cuts across Thai peninsula trending NNE-SSW stretching approximately 150 km from the Gulf of Thailand to the Andaman Sea (Fig. 1.3). The shear zone affects an area up to 10 km in width from the Khlong Marui Fault eastward to the Bang Kram Fault. This zone, marked by a large valley with the high topographic core named Khao Phanom, was the focus of this study. The mountain range of Khao Phanom forms a lozenge shape 40 km long and 6 km wide body lying parallel between the Khlong Marui and Bang Kram faults. The area to the west is bounded by a long, north-south trending mountain range of Western Belt Granite and Permo-Carboniferous sedimentary rock. The west valley houses the river “Khlong Marui” flowing southwest from the middle area to the Phang Nga bay, and the river “Khlong Phanom” flowing northeast to the river “Khlong Phum Duang”. The east boundary is represented by a huge valley of Bang Kram Fault which comprises a geographically long cliff of Permian carbonate and Triassic sedimentary rock. In this valley is situated the river “Khlong Cha Un”, running to the northeast.

The climate of peninsular Thailand, which covers the study area, is influenced by the monsoon. The monsoon, which is represented by hot and humid condition, typically produces rain periods and a dry season. The rainy season is normally longer than the dry season with small temperature differences between the two. Southwest monsoon season starts from May until October. Another rainy period (the northeast monsoon) brings heavy rain to the eastern coastal areas from November to January. Geologically, this is relevant in the extreme rates of erosion but also soil profile development and vegetation cover. This influences remote sensing in terms of bedrocks to soil spectral signals in datasets.

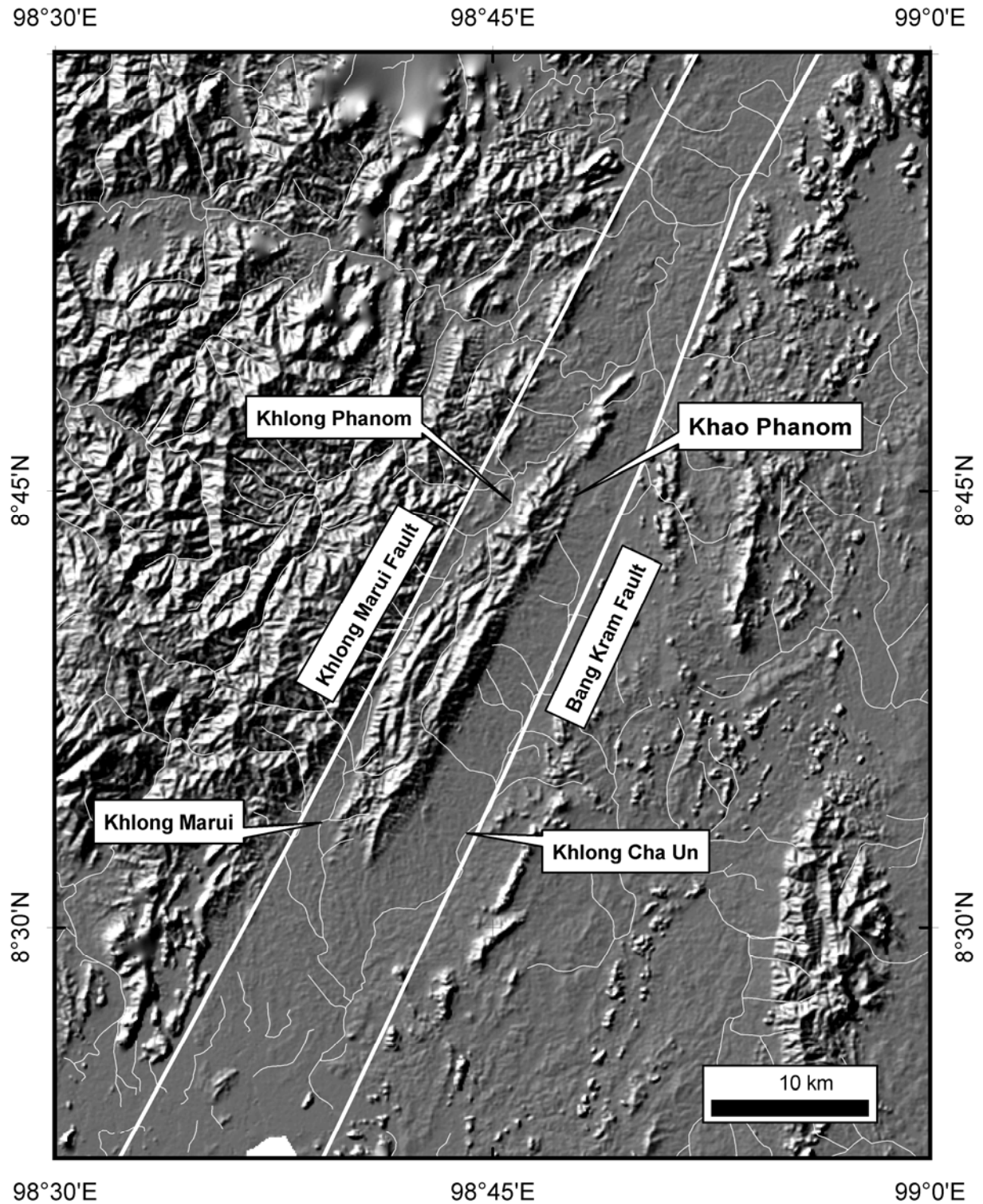


Figure 1.3 Topography of the study area is showed by Shuttle Radar Topography Mission (SRTM) digital elevation model combined with the digital map of the main rivers. The river named “Khlong Marui” drains the area flowing towards SSW.

1.4 Regional Geology

The Khao Phanom and adjacent area of the Khlong Marui Fault zone encompasses rock ages from Permo-Carboniferous to Quaternary. The geology is illustrated by geological map sheet Changwat Phangnga NC47-14 scale 1:250,000 of Department of Mineral Resources in 1982 (Fig. 1.4). Although the 1999 version of geologic map was published, the geologic map of scaling 1:1,000,000 is insufficient for detailed study.

Geology on the west boundary of the study area is mainly the Permo-Carboniferous Kaeng Krachan Group and Permian Ratburi Group. Both rocks are cross cut by the Cretaceous age Western Belt Granite. The Permian carbonate rocks are generally associated with Triassic Chaiburi Formation on the east boundary. Quaternary sediments deposits are widespread along the valley and flat areas. The descriptive geology in the study area by rock units is listed below in ascending order;

Permo-Carboniferous Kaeng Krachan Group

The Kaeng Krachan Group, the main rocks of the study area, was firstly described by Piyasin (1975) and revised by Raksaskulwong and Wongwanich (1993). Originally, three formations were proposed for the Kaeng Krachan Group (Piyasin, 1975): (i) The Huai Phu Noi, (ii) Khao Phra, and (iii) Khao Chao formations. The group is subdivided into four formations: (i) Khao Wang Kradat, (ii) Spillway, (iii) Ko He, and (iv) Khao Phra (Ko Yao Noi) respectively. The Khao Wang Kradat Formation is composed of the intercalation of greywacke, arkose, siltstone and shale. A Bouma sequence is revealed in their internal structure indicating turbidity deposits. The Spillway Formation comprises laminated mudstone interbedded with shale, siltstone, greywacke and arkose. Burrows, bioturbation, soft sediment deformation, slumping, dewatering cracks are typical sedimentary structures. Exotic clasts or lonestone (a descriptive term) of quartzite, granite, limestone, vein quartz, sandstone and schist varying in size from pebble to boulder, are easily observed. Some lonestones show faucet features and drop structures (Tantiwanit et al., 1983). Conglomeratic sandstone lenses which represent channel filled deposits are occasionally found. The sharp base and wavy surfaces with sporadically intervene hummocky cross bedding in the succession are present in the quartzitic sandstone. The Spillway Formation is interpreted as a continental shelf deposit under the influence of ice-rafting and storm surge. The Ko He Formation is distinguished by both stratified and non-stratified pebbly rocks or diamictites accumulated by debris flows and re-sedimentation. The Khao Phra Formation consists of arkose, quartzitic sandstone, mudstone, siltstone, shale, and occasional chert beds. Systematic description of bryozoas, brachiopods, crinoids, and other fossil assemblages indicates an Early Permian age (Sakagami, 1970; Waterhouse et al., 1981; Yanagida, 1970). This formation is interpreted to indicate a subtidal to intertidal depositional environment.

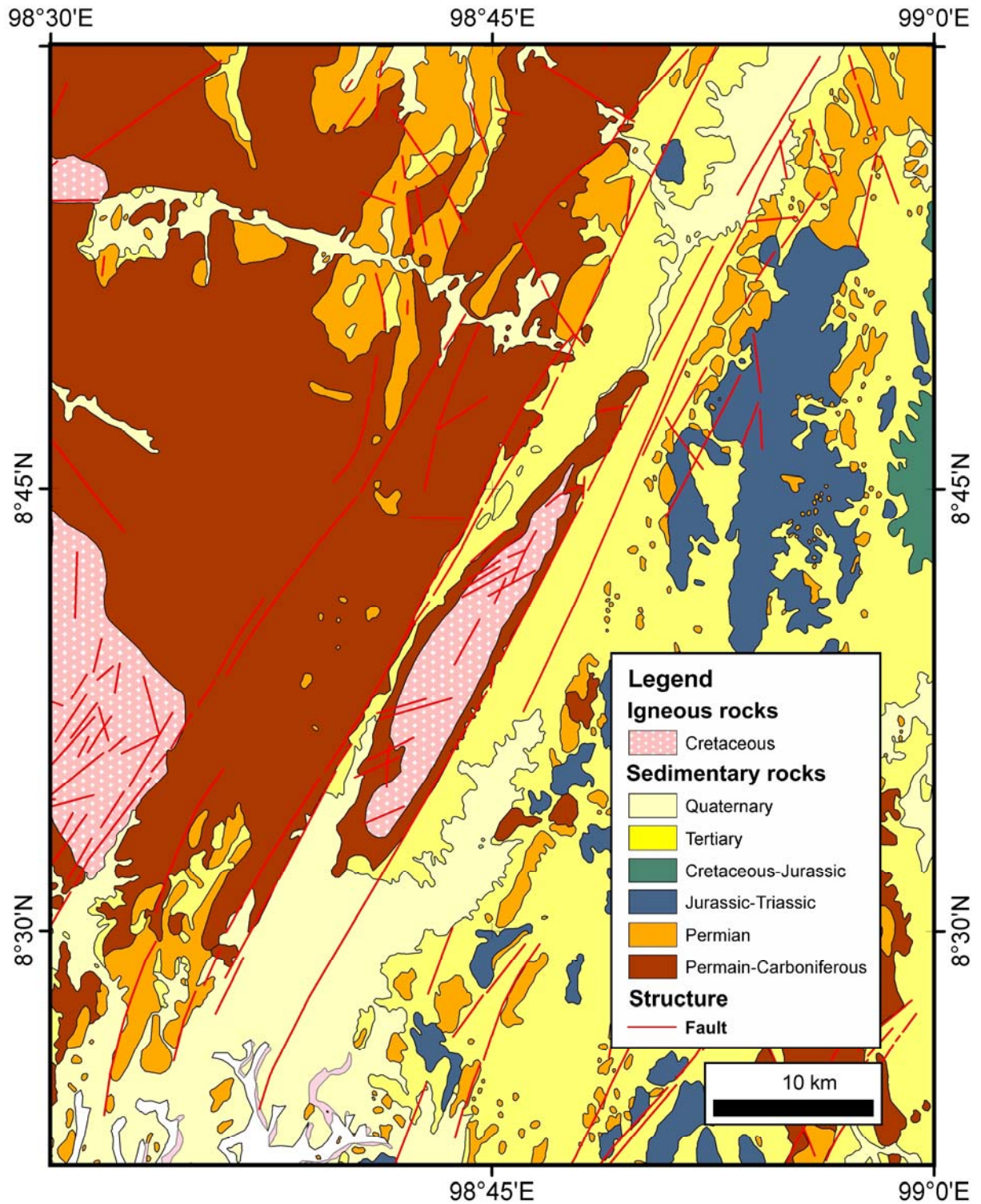


Figure 1.4 Geology of the study area dominated by Permo-Carboniferous sedimentary rock and igneous intrusions (modified after Department of Mineral Resources, 1982).

Permian Ratburi Group

Permian rocks which are known as Ratburi Limestone (Brown et al., 1951) or Ratburi Group (Javanaphet, 1969) commonly form the typical karst topography widespread in Thai Peninsula. This carbonate rock conformably overlies the Permo-Carboniferous Kaeng Krachan Group. Its lithology dominantly consists of thin-bedded and massive limestones with a thickness of approximately 800 m, intercalated with clastic rocks. In the lower and middle part of the sequence chert nodules are present commonly. Bryozoan, fusulinids, brachiopods, algae and foraminifera fossil assemblages in the limestone indicate Middle to Late Permian (Grant, 1976; Sakagami, 1970; Waterhouse et al., 1981; Yanagida, 1970).

The Ratburi Group is exposed in the vicinity of Suratthani province nearby the study area and is divided into four formations, namely the Thung Nang Ling, the Phab Pha, the Pra Nom Wang and the Um Luk formations respectively (Harrison et al., 1997). The roughly 80 m thick Thung Nang Ling Formation, which lies conformably on the clastic rocks of the Kaeng Krachan Group, is composed of dark, pale grey, medium to thick bedded fossiliferous limestones. The Phab Pha Formation which is ca. 200 m in thickness consists of the intercalation of dark grey thin-medium bedded limestones, mudstones and shales. The Phanom Wang Formation contains mainly coarse-grained medium to thick-bedded limestone, dolomitic limestone and dolomite. The Um Luk Formation is over 200 m thick and consists dominantly of pale grey thick massive bedded limestones.

The Ratburi Limestone records six different characteristics: (i) It contains poor fauna which are represented by many individuals to few species and show low diversity. Floras are commonly poor in green algae. (ii) Corals are restricted to few localities. (iii) Ages range from Middle to Late Permian. (iv) Large parts of the Lower Permian are composed of clastic sediments. (v) Analysis of the boron content of the pebbly mudstone close to the boundary between the Carboniferous and the Permian do not strongly support a glacial event. (vi) The Ratburi limestone was deposited on a shelf relatively far from the coast and contains rare, small, mainly planktonic fossils (Fontaine and Sutheethorn, 1988).

Triassic Chaiburi Formation

Triassic rocks around the eastern part of Bang Kram Fault are mainly composed of limestones having similar lithologies to those recorded in the Permian Ratburi Group. Because of the biostratigraphic correlation, the rock sequence has been correlated with the Chaiburi Formation, which is unconformably underlain by the Permian rock. The Chaiburi Formation has been described in the Phatthalung area as marine Triassic rocks (Ampronmaha, 1995). The formation consists of 3 members: (i) the Phukhaothong Dolomite, (ii) the Chiak Limestone and (iii) the Phanomwang Limestone members, respectively. The 500 m formation thickness comprises pale grey to violet grey, well-bedded, thin- to thick-bedded limestones, dolomitic limestones and dolomites. The lower part of the formation consists of dolomites which contain the new

ichthyopterygian (Reptilia) of Early Triassic age (Mazin et al., 1991). On the basis of the microfacies analysis, the middle part comprises limestones intercalated with nodular and thin-bedded cherts and the upper portion is composed of thick to massive limestones. Age determination of the rocks is based mainly on conodonts, indicating that the formation ranges from Lower to Upper Triassic.

Quaternary unit

Quaternary deposits along the Khlong Marui Fault area are represented by terrace and fluvial sediments which progressively work through the topographic relief-decreasing processes. Terrace deposits mainly comprise gravel, sand, and laterite of rejuvenated river and fluvial deposit composed of gravel, sand, and clay.

Igneous rock

The Khao Phanom igneous rock belongs to the north-south Western Belt Granite (Charusiri et al., 1993). The Khlong Marui Fault is probably the boundary between the Thailand Western and Central Granitoid Belt. The lithology is characterized by fine-to-medium grained granitoids with mineral assemblages consisting of brown biotite, muscovite, and tourmaline associated with Sn-W-REE deposits. Hornblende is not common. About 98% of the granitoid rocks are geochemically S-type and ilmenite-series. I-type or magnetite-series granitoids are represented locally in small area. Age determination using the $^{40}\text{Ar}/^{39}\text{Ar}$ method on the granitoids of the western belt gave Late Cretaceous to Early Tertiary ages (50-88 Ma) which can be subdivided into 2 periods as 65-88 Ma and 50-60 Ma respectively (Charusiri et al., 1993). The country rocks within this granite belt are mainly Permo-Carboniferous Kaeng Krachan Group.

1.5 Tectonics Setting

The Thai peninsula is structurally dominated by the northeast trending Khlong Marui Fault and is a part of the Palaeozoic supercontinent Gondwana named Shan-Thai (Bunopas, 1981) or Sibumasu (Metcalf, 1991). The Shan-Thai terrain completely amalgamated with the Indochina microcontinent in the Late Triassic and collided with Western Burma in the late Cretaceous to Early Tertiary (Bunopas, 1981; Charusiri, 1989; Charusiri et al., 2002; Hutchison, 1996; Mitchell, 1981). Magmatism developed during these prolonged subduction phases forming three N-S elongate batholiths named the Eastern, Central, and Western Granite belts, respectively. I-type characterizes the Eastern Granitoid Belt with Cu-Fe-Au-Sb mineralization; S-type dominates the Central Belt with Sn-W-REE deposits that are separated by major NW and NE strike-slip faults related in the subduction of Shan-Thai and Indochina. The Sn-W-REE rich S- and I-type Western Granite Belt lies along the western boundary of the Khlong Marui Fault, which formed as a result of the Shan-Thai and Western Burma microcontinental plate collision (Charusiri et al., 1993; Charusiri et al., 2002; Hutchison, 1996).

The strike-slip models of the NE-SW striking faults in southern Thailand have been related to the India-Asia collision leading to the southeast extrusion of Indochina block. These faults are interpreted to form a conjugate system with the Ailao Shan-Red River Fault, Mae Ping Fault, and Three Pagodas Fault respectively (Lacassin et al., 1997; Tapponnier et al., 1986). The extrusion tectonics describe that the Indian-Asian collision has resulted in a rotation about 25° and extrusion of Indochina of about 800 km to the southeast in the Eocene to Miocene. After that, further N-normal movement resulted in clockwise rotation of about 40° Indochina and strike-slip shear sense was reversed in the late Miocene (Tapponnier et al., 1986).

The motion of strike-slip faults induced by extrusion tectonics, and in particular the great Ailao Shan-Red River Fault has provoked lively discussion on its deformation extent and timing (Briais et al., 1993; England and Houseman, 1986; Gilley et al., 2003; Leloup et al. 1995, 2001; Rangin et al. 1995a, b; Searle 2006; Wang E. et al. 1998; Wang P. et al., 2000; Wang Y. et al., 2006). The northwest Mae Ping and Three Pagodas fault indicate that its sinistral motion terminated around 30.5 Ma based on $^{40}\text{Ar}/^{39}\text{Ar}$ dating (Lacassin et al., 1997). The Ranong fault was dextrally displaced about 200 km (Tapponnier et al., 1986) and about 20 km sinistrally (Garson and Mitchell, 1970). Displacement estimates of Khlong Marui fault have ranged between 100 km dextral (Kornsawan and Morley, 2002) to at least 200 km sinistral (Garson and Mitchell, 1970). The timing of the shear sense inversion is implied to be the same as the inversion along the conjugate northwest trending fault (Lacassin et al., 1997). The kinematic history of the northeast Ranong and Khlong Marui faults developed in two phases of ductile dextral shear starting before Late Cretaceous and ending in the Paleocene to Eocene (Watkinson et al., 2008). These early two ductile phases of movement on the faults had preceded the start of the India-Asia collision (Watkinson et al., 2008). The brittle sinistral phase overprints and exhumes the ductile fault rocks as a progressive response to the extrusion tectonics.

The NW and NE conjugate system contributed to Cenozoic basin development in the South China Sea, Andaman Sea and Gulf of Thailand (Briais et al., 1993; Charusiri et al., 2002; Morley, 2001, 2002; Packham, 1993; Pigott and Sattayarak, 1993; Polachan et al., 1991; Polachan and Sattayarak, 1989; Tapponnier et al., 1986). The conjugate set comprises a right lateral NW and left lateral NE strike-slip fault. The Indian-Asian collision since 40-50 Ma or Eocene caused clockwise rotation of Southeast Asia and movements on the strike-slip faults forming Tertiary pull-apart basin development in the Late Oligocene (Pigott and Sattayarak, 1993; Polachan et al., 1991; Polachan and Sattayarak, 1989). Later extension controlled models were more influenced by changing stress patterns at nearly 180° around the eastern Himalayan syntaxes from east-west to north-south (Huchon et al., 1994). Other models involved subduction rollback-back arc extension model combined with strike-slip motion that inverted about 30 Ma (Morley, 2001, 2002), as well as lower crustal flow model (Morley and Westaway, 2006).

Chapter 2

Remote Sensing Interpretation

2.1 Introduction

Analysis of remote sensing data is an important approach for regional scale studies including mapping of rock types and their extent and characteristic soil and vegetation products, topographic pattern, and structural and tectonic features. The surface expression of geological structures such as fractures and foliations are strikingly expressed as lineaments on airborne and orbital remote sensing data. Remote sensing techniques are necessary for understanding the geology in southern Thailand because of the tropical climate the outcrop exposures are poor and a dense vegetation cover developed.

This chapter deals with the surface processes interpreted/interpolated from remote sensing techniques including lineament analysis, surface ruggedness pattern, and morphotectonics. The remote sensing data used in this study are aerial-photographs, Landsat TM satellite images, and SRTM digital elevation model (DEM). Each three different data sources are integrated in an ArcGIS geodatabase and used as basic data set for quantitative spatial lineament interpretation. The spatial lineament orientations are quantified, plotted, and statistically analyzed in rose diagrams. Lineaments derived from trends for all different data sources are compared and compiled in a single diagram to represent the major lineament trend of the area.

The surface ruggedness pattern is presented by the aspect and slope map. ArcGIS software is used for processing a SRTM digital elevation model to generate the aspect and slope map. The surface ruggedness was processed by the function of raster surface in 3D analyst tools of ArcToolbox menu.

Morphotectonics methods are used for the structural interpretation of the remote sensing data. This reveals tectonics-indicated features through the morphology. The morphotectonics study was performed by using remote sensing interpretation technique combining with the topographic evidence from the field work.

2.2 Lineament Analysis

Lineaments are defined as straight linear elements, visible at the earth's surface, which are the expressions of geological and/or geomorphological phenomena (Clark and Wilson, 1994). In remote sensing study, the lineaments are normally associated with a change in terrain elevation such as slope-breaks and valley lines. The major brittle structures of the study area have been mapped using lineament analysis.

Lineaments are extracted from three different remote sensing data sources: (i) aerial-photographs, (ii) satellite images, and (iii) the SRTM Digital Elevation Model. Aerial-photographs are used to study the Earth's surface in 3D by using a stereoscope. Satellite images were processed by selected 3 band mixing of thematic mapper with false-color composites. The SRTM 90 m DEM, which recently widespread used for multipurpose by data processing, was processed to generate the hillshade map for the lineament analysis.

2.2.1 Aerial-photographs

Aerial-photographs under the stereoscope illustrate three-dimensional information. The black-and-white vertical stereo-paired aerial-photographs of an approximate scale 1:50,000 are used for this study. The lineament features are transferred to a map scale of 1:250,000 (Fig. 2.1).

The rose diagram of 73 lineaments is statistically analyzed. The major trend shows maxima in NNE-SSW with minor ENE-WSW and NW-SE directions. The major trend is in NNE-SSW with a strike of 030°. The others two lineaments are striking 065° ENE-WSW and 130° NW-SE (Fig. 2.2).

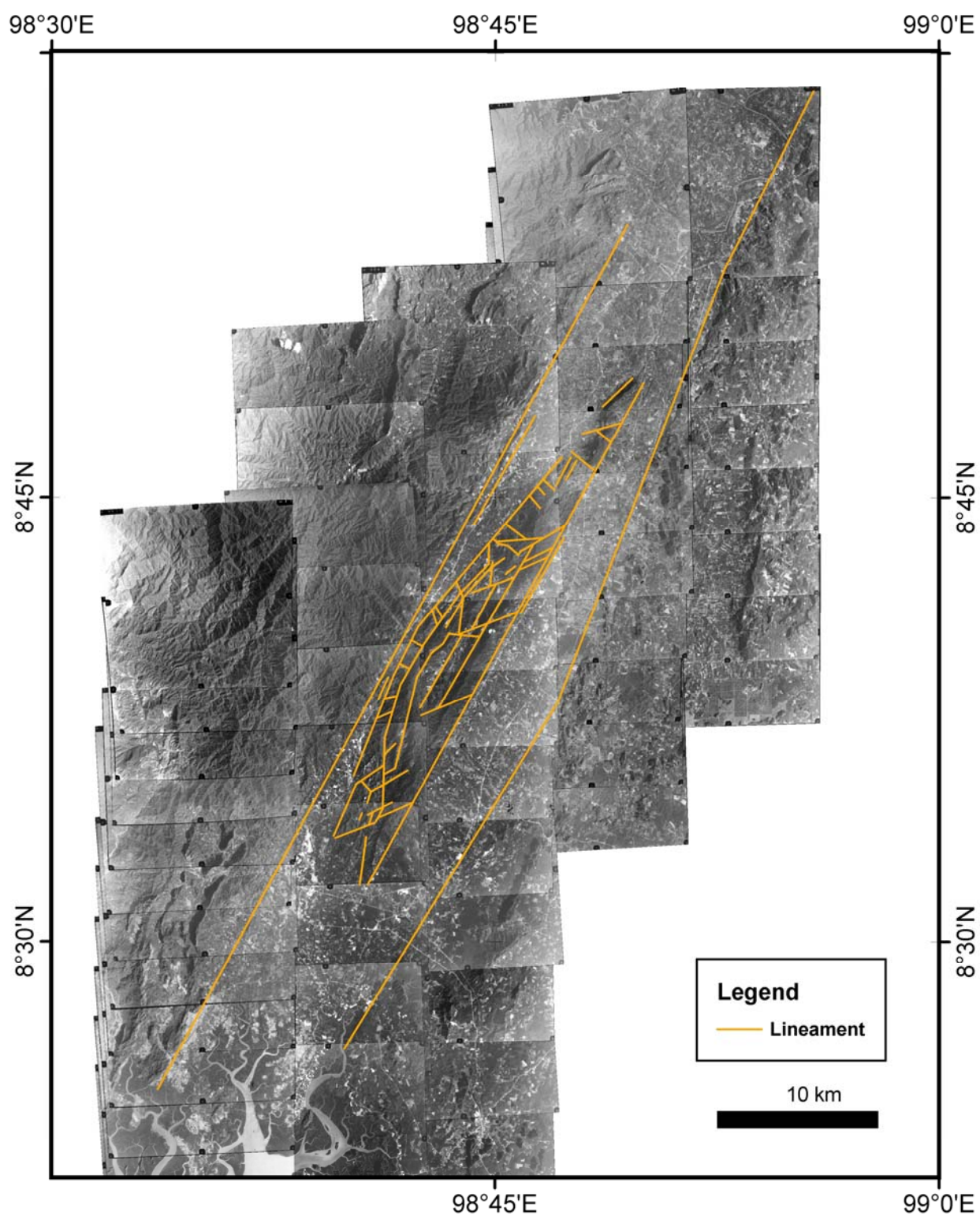


Figure 2.1 Mosaic of aerial-photographs with lineament interpretations.

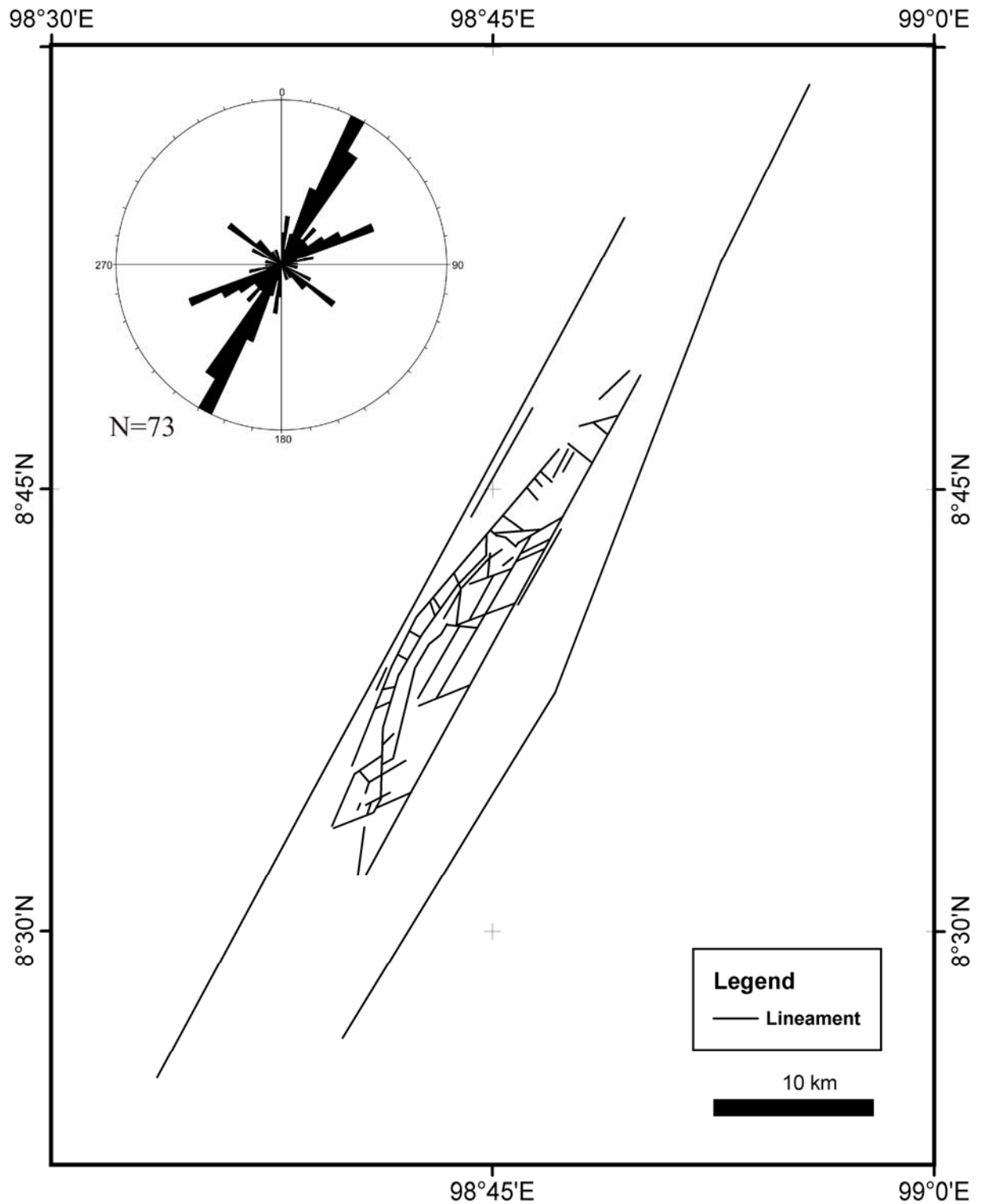


Figure 2.2 Lineament map from aerial-photographs and rose diagram showing a major maxima at 030° NNE-SSW, and two minor local maxima of 065° ENE-WSW and 130° NW-SE respectively.

2.2.2 Satellite Image

This study uses LANDSAT TM data (path 129 row 54 on 22 October 2001 of the scale 1:2,500,000). The thematic mapper bands are classified by wavelengths which have different characteristics at the Earth's surface in Table 2.1. The thematic mapper of bands 7, 5, and 4 with the false-color composites red, green, blue (RGB) were the most appropriate channels for lineament and geologic interpretation for this area in Table 2.2. The satellite image was processed by choosing the thematic mapper bands directly in ArcMap software. The identification of lineaments from the 7-5-4 Landsat image is mainly based on geomorphological features such as slope-break and valley-strike. Straight drainage channel segments and linear scarp faces are considered to mark major lineaments. The lineaments were visually identified and interactively digitized in the Landsat TM images (Fig. 2.3).

Table 2.1 Landsat thematic mapper (TM) spectral bands (after Sabins, 1996).

Band	Wavelength, μm	Characteristics
1	0.45 to 0.52	Blue-green. Maximum penetration of water, which is useful for bathymetric mapping in shallow water. Useful for distinguishing soil from vegetation and deciduous from coniferous plants.
2	0.52 to 0.60	Green. Matches green reflectance peak of vegetation, which is useful for assessing plant vigor.
3	0.63 to 0.69	Red. Matches a chlorophyll absorption band that is important for discriminating vegetation types.
4	0.76 to 0.90	Reflected IR. Useful for determining biomass content and for mapping shorelines.
5	1.55 to 1.75	Reflected IR. Indicates moisture content of soil and vegetation. Penetrates thin clouds. Provides good contrast between vegetation types.
6	10.40 to 12.50	Thermal IR. Nighttime images are useful for thermal mapping and for estimating soil moisture.
7	2.08 to 2.35	Reflected IR. Coincides with an absorption band caused by hydroxyl ions in minerals. Ratios of bands 5 and 7 are used to map hydrothermally altered rocks associated with mineral deposits.

Table 2.2 Evaluation of TM color combinations (after Sabins, 1996).

Display colors*	Advantages	Disadvantages
1-2-3	Normal color image. Optimum for mapping shallow bathymetric features.	Lower spatial resolution due to band 1. Limited spectral diversity because no reflected IR bands are used.
2-3-4	IR color image. Moderate spatial resolution.	Limited spectral diversity.
4-5-7	Optimum for humid regions. Maximum spatial resolution.	Limited spectral diversity because no visible bands are used.
2-4-7	Optimum for temperate to arid regions. Maximum spectral diversity.	Unfamiliar color display, but interpreters quickly adapt.

*TM bands are listed in the sequence of projection colors: blue-green-red.

The result of Landsat interpretation is presented by 55 lineaments plotted in a rose diagram showing a major trend at 030° NNE-SSW, 060° ENE-WNW, and 130° NW-SE respectively (Fig. 2.4).

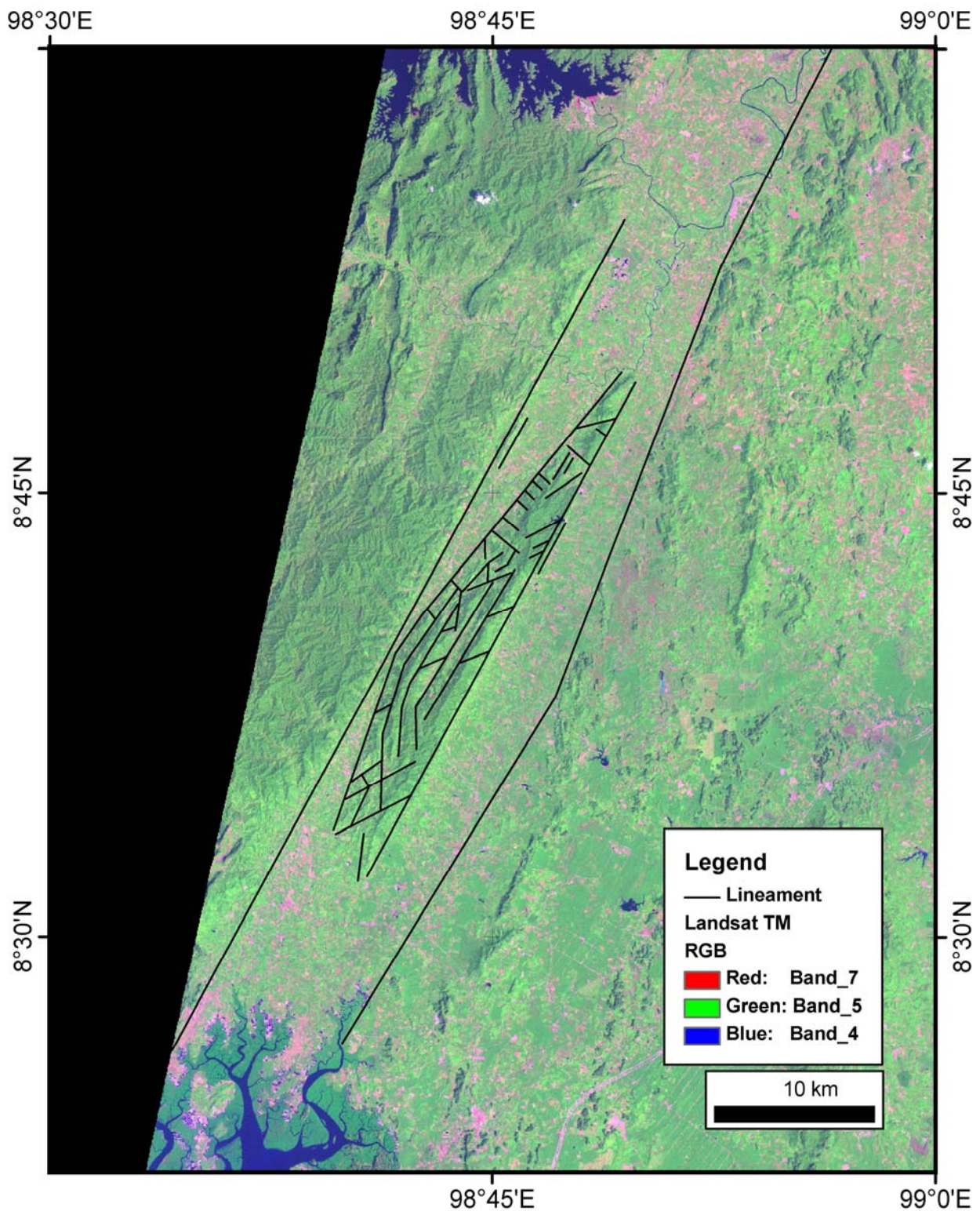


Figure 2.3 LANSAT image bands 7, 5, and 4 with false-color composites RGB with lineament interpretation.

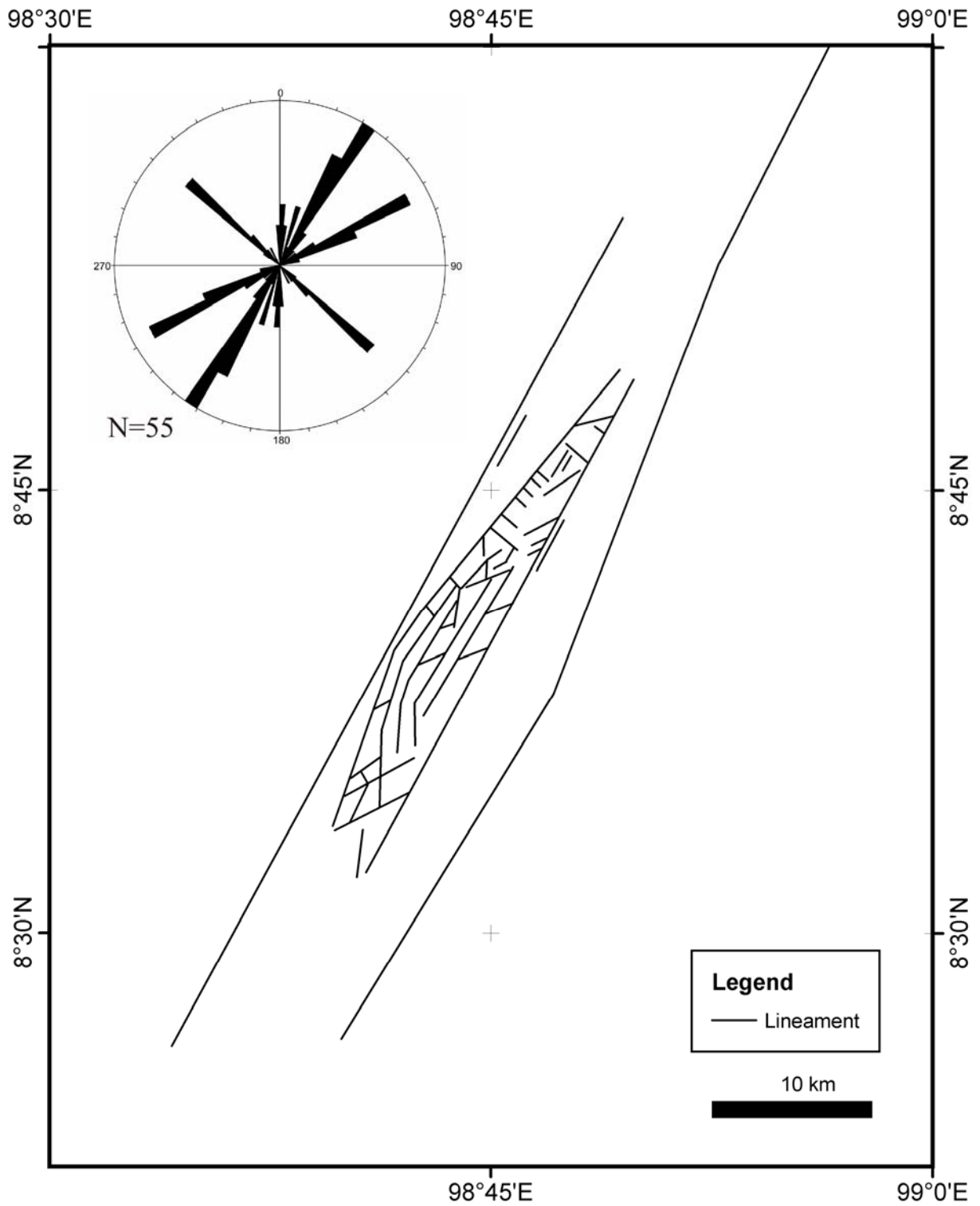


Figure 2.4 Lineament map with rose diagram based on LANSAT image lineament analysis shows the major trend at NNE-SSW with minor trending at NEE-SWW and NW-SE.

2.2.3 SRTM Digital Elevation Model (DEM)

The SRTM 90m DEM is used for qualification of the topographic signal. The SRTM digital elevation model is processed by ArcGIS software to produce hillshade maps which illustrate the ruggedness of the topography. The hillshade command was located in ArcToolbox menu; 3D analyst tools; raster surface. Hillshade values were computed for a raster surface by considering the illumination angle and shadows. The advantage of the hillshade function is to highlight the structure in every directions of light. The morphology controlled by fracture from hillshade map is interpreted to lineaments (Fig. 2.5).

The 60 lineaments which were plotted in rose diagram show three main directions: NNE-SSW, ENE-WNW, and NW-SE (Fig. 2.6). The major NNE-SSW strikes 030°, ENE-WNE 060° and NW-SE 130°.

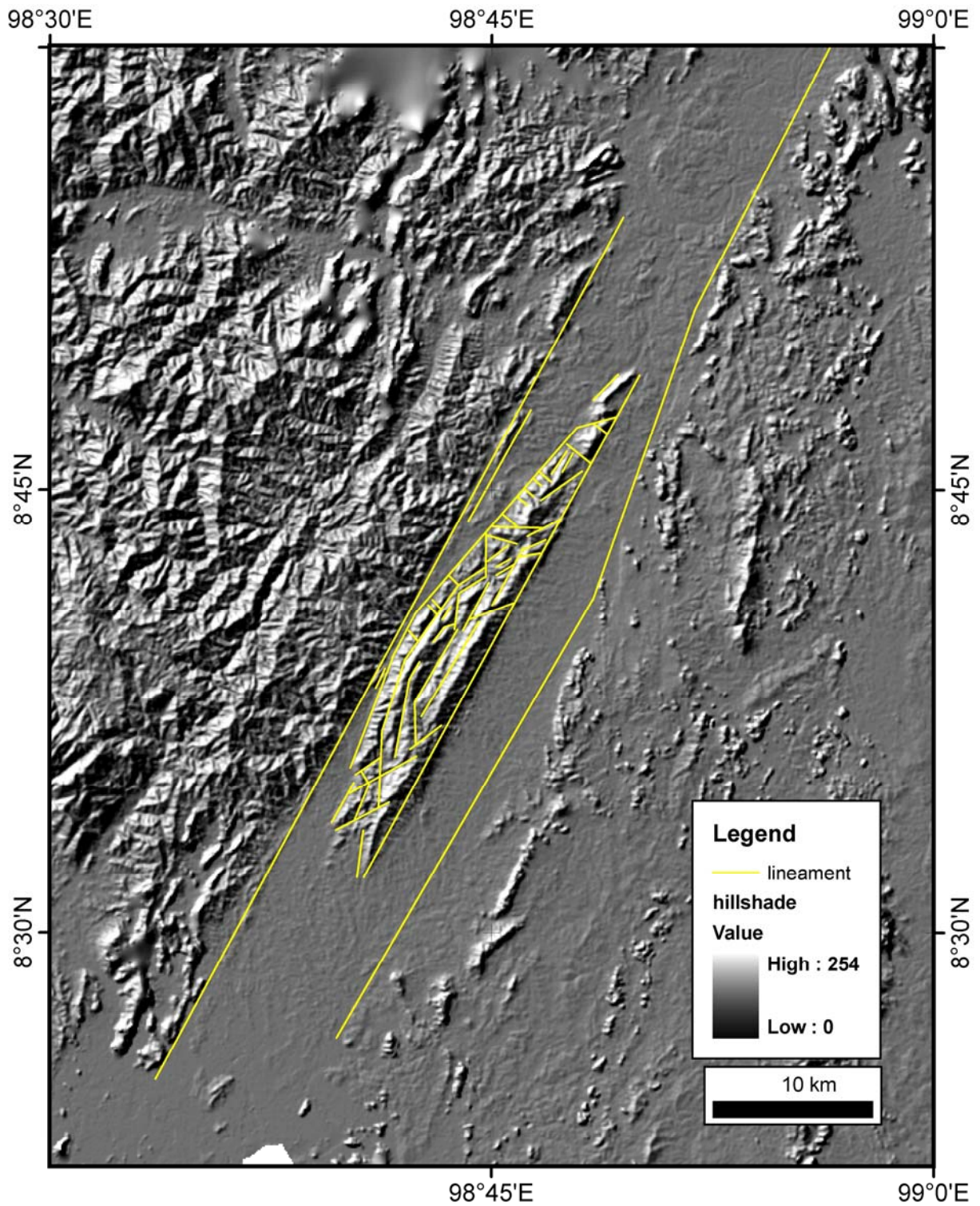


Figure 2.5 Hillshade map generated from SRTM digital elevation model (sun azimuth 315°, altitude 045°) with lineament interpretations.

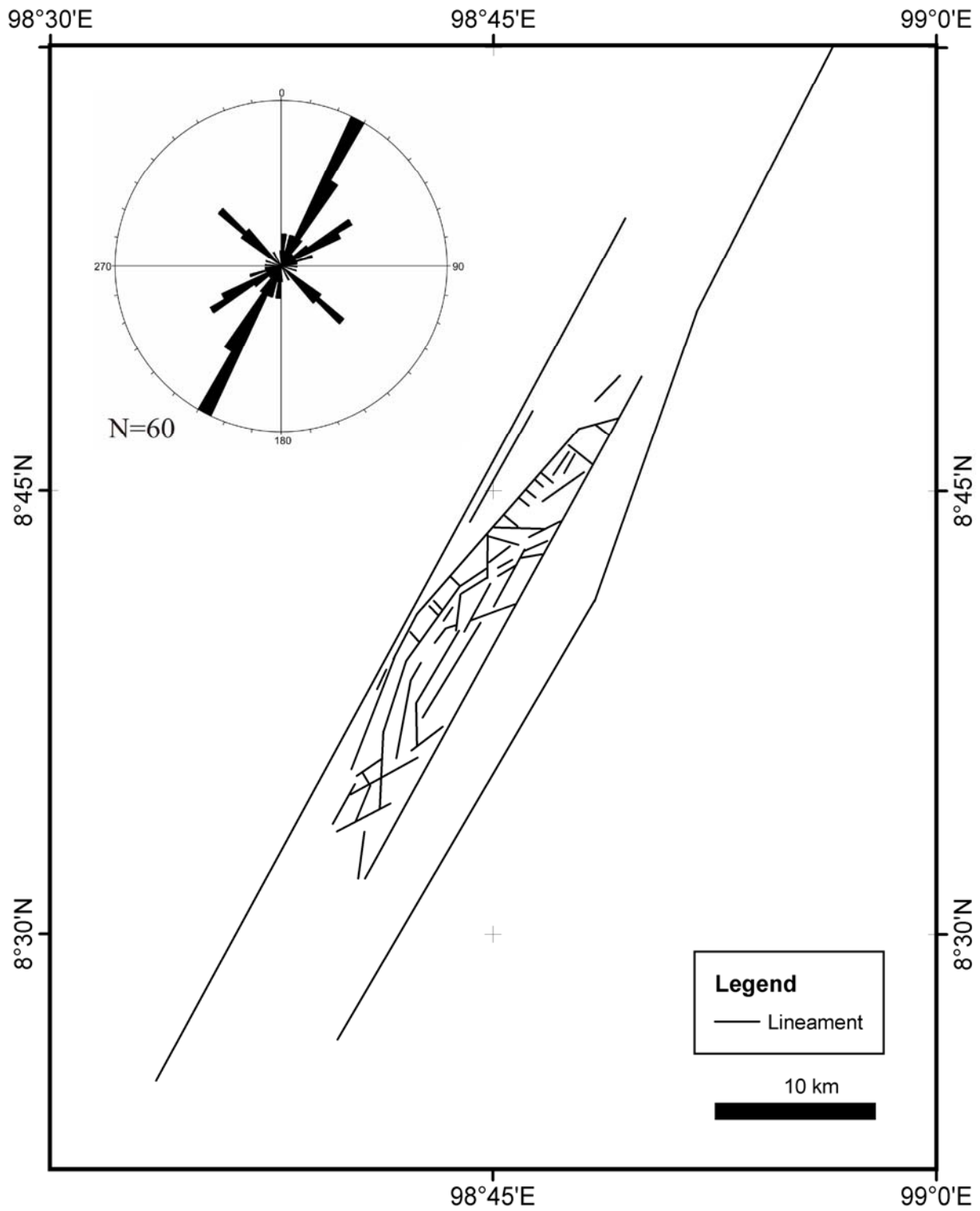


Figure 2.6 Lineament map extracted from hillshade map presents with three main directions of 030° NNE, 060° ENE and 130° NW in rose diagram.

2.2.4 Composite Lineaments

The results from each remote sensing data source show that the major lineament trends are oriented in the roughly same directions with differences in quantitative values (Fig. 2.7A, 2.7B, 2.7C). For this reason, the lineaments from three data sources were compiled in a single rose diagram for statistical quantification of the major lineament trends (Fig. 2.7D). The 188 lineaments of all remote sensing data sources indicate that most lineament structures trend NNE-SSW with minor local maxima at NEE-SWW and NW-SE. The NNE-SSW major trend striking 030° is more dominant than the 060° ENE-WSW, and 130° NW-SE directions.

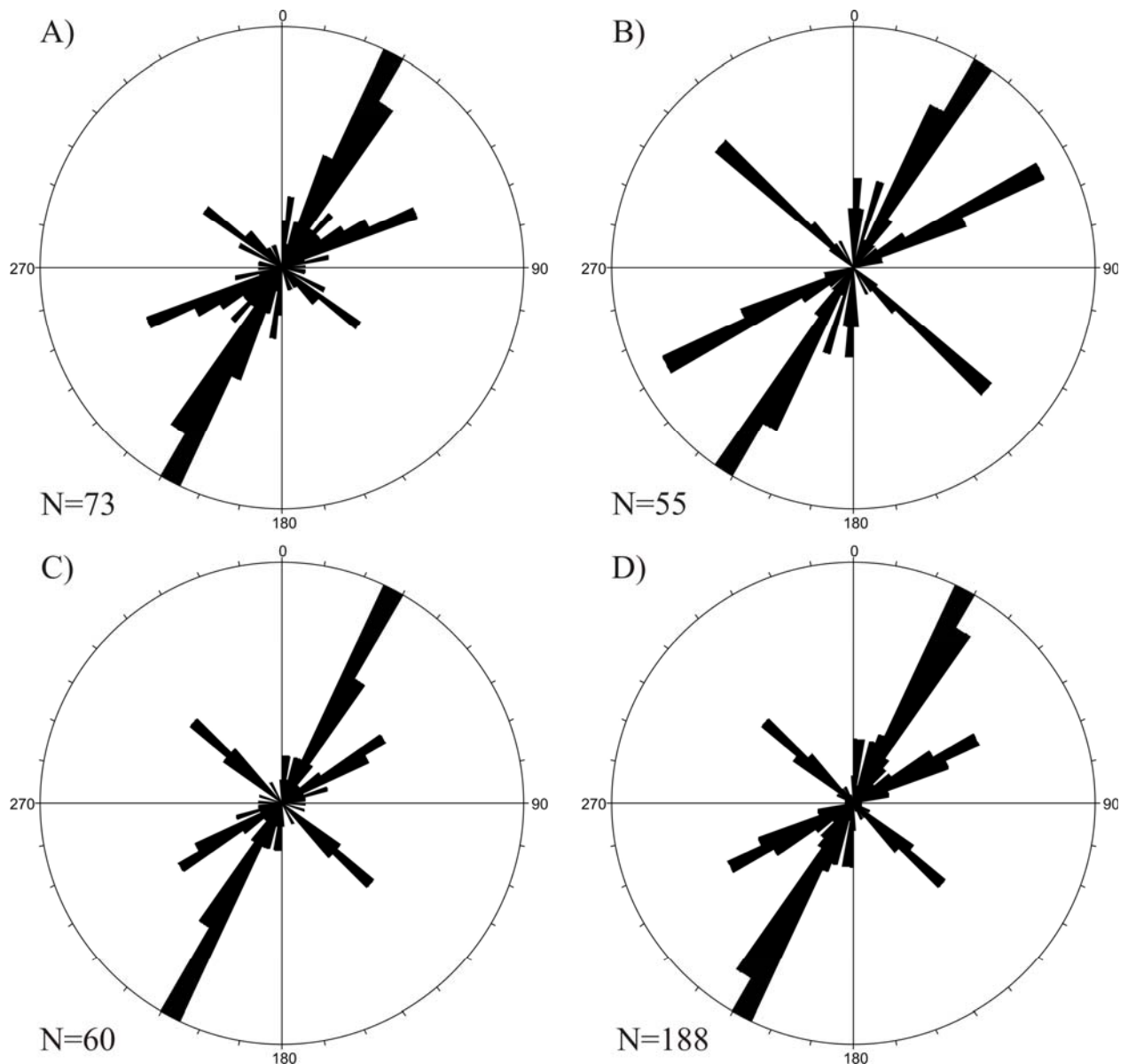


Figure 2.7 Rose diagrams from the lineaments extraction of air-photographs (a), satellite image (b), SRTM digital elevation model (c), and composite lineaments (d) show the major NNE-SSE with minor ENE-WSE and NW-SE trends.

2.3 Surface Ruggedness Pattern

The surface ruggedness pattern relates to the slope angle distribution. The more rugged the surface is, the larger the slope angles vary. This surface ruggedness pattern is analyzed using aspect and slope maps generated by ArcGIS software. The aspect was derived from a raster surface to generate the map. The slope was identified by the rate of maximum change in the elevation from each DEM cell. Both functions were located in ArcToolbox menu; 3D analyst tools; raster surface.

The aspect map classified as the slope direction against the north of SRTM digital elevation model pixels as flat (-1°), north ($0-22.5^\circ$), northeast ($22.5-67.5^\circ$), east ($67.5-112.5^\circ$), southeast ($112.5-157.5^\circ$), south ($157.5-202.5^\circ$), southwest ($202.5-247.5^\circ$), west ($247.5-292.5^\circ$), northwest ($292.5-337.5^\circ$), and north ($337.5-360^\circ$) (Fig. 2.8). From the aspect map, the direction of northwest and southeast domains by dominated in the Khlong Marui Fault zone.

The slope map was generated to distinguish the sharp changing of the slopes. It has been classified by natural breaks into 9 classes as $<3.08^\circ$, $3.08-7.34^\circ$, $7.34-12.07^\circ$, $12.07-16.57^\circ$, $16.57-20.83^\circ$, $20.83-25.10^\circ$, $25.10-30.07^\circ$, $30.07-37.88^\circ$, $>37.88^\circ$ (Fig. 2.9). The high angle slopes correspond to the ridges. Slope break between $12.07-16.57^\circ$ and $16.57-20.83^\circ$ are concentrated in between the Khlong Marui Fault and Bang Kram Fault which has been marked as a potential area of the last tectonics event.

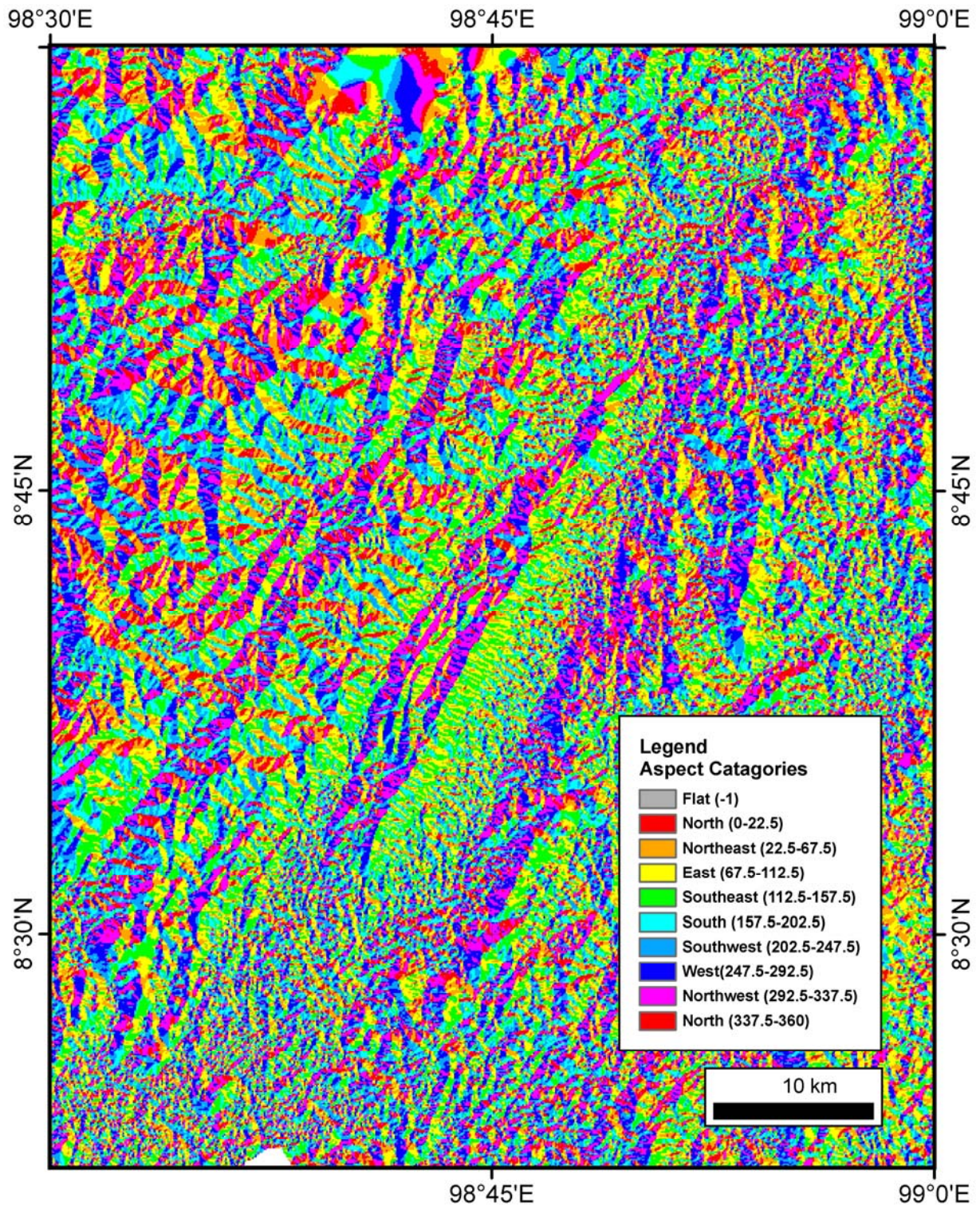


Figure 2.8 Aspect map of the Khlong Marui Fault zone dominated the northwest and southeast domains.

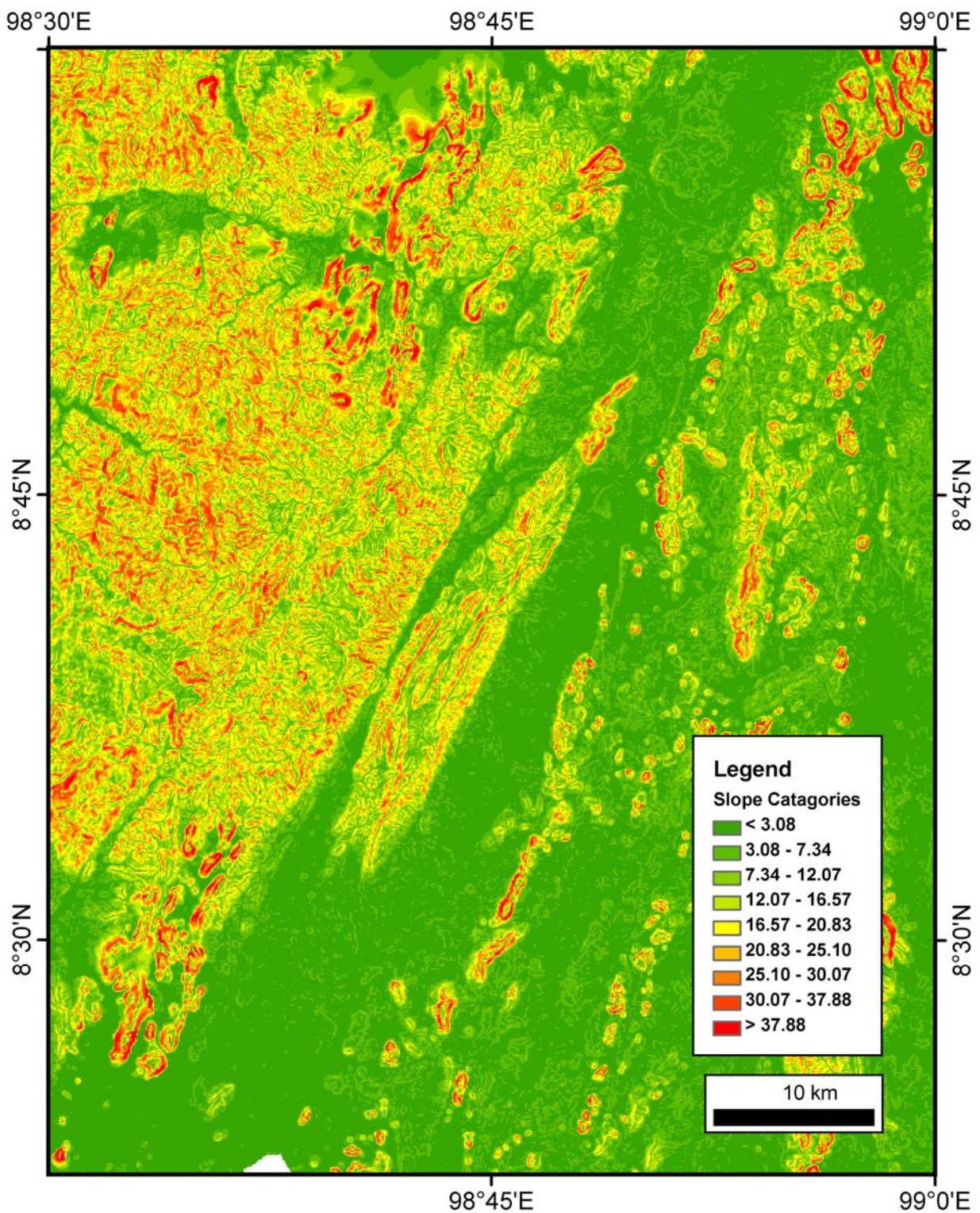


Figure 2.9 Slope map presents the potential area of the last tectonics event at the slope break between 12.07-16.57° and 16.57-20.83°.

2.4 Morphotectonics

Geomorphic features in the study area were investigated from remote sensing interpretation together with field work. Remote sensing data quantified specific landforms that might record tectonic history. Fractures represent exposed zones of rock weakness leading to intense erosion and hence the geomorphic features such as fault scarps form along fault lines. For this study area, the morphotectonics features are distinguished by fault scarps and triangular facets, linear valleys, and drainage networks which are described below.

Fault scarps and triangular facets

The most distinguished geomorphic features found in the study area are triangular facets running through the long fault scarps in NNE-SSW direction (Fig. 2.10). The morphology is best visualized in 3D DEM models combined with the geological map by ArcScene software (Fig. 2.11). The major NNE-SSW lineaments are also represented by this major fault zone including the Khlong Marui Fault, the western and the eastern sides of the Khao Phanom and Bang Kram faults. The scarps run with straight lines except on the western side of Khao Phanom showing more curved segments. These features are clearly present not only in remote sensing but also in the field area (Fig. 2.12).

Linear valley

The linear valley is characterized by the long NNE-SSW lineaments up to 20 km through Khao Phanom (Fig. 2.10). The long parallel valleys are identically present in all remote sensing data, especially in aerial-photographs. They typically run parallel to the fault scarps on the western and the eastern sides of Khao Phanom, which might suggest that the fault scarps and linear valley are probably generated by the same tectonics origin.

Drainage network

The network of drainage along the Khlong Marui Fault zone is composed of the main stream course, which runs roughly in NNE-SSW direction with the NW-SE trending tributaries (Fig. 2.10). Along the NNE-SSW fault scarp, the NW-SE drainage pattern is obviously straight without offset in any of the fault locations. This feature indicates that no strike-slip tectonics influences the last deformation of this fault area.

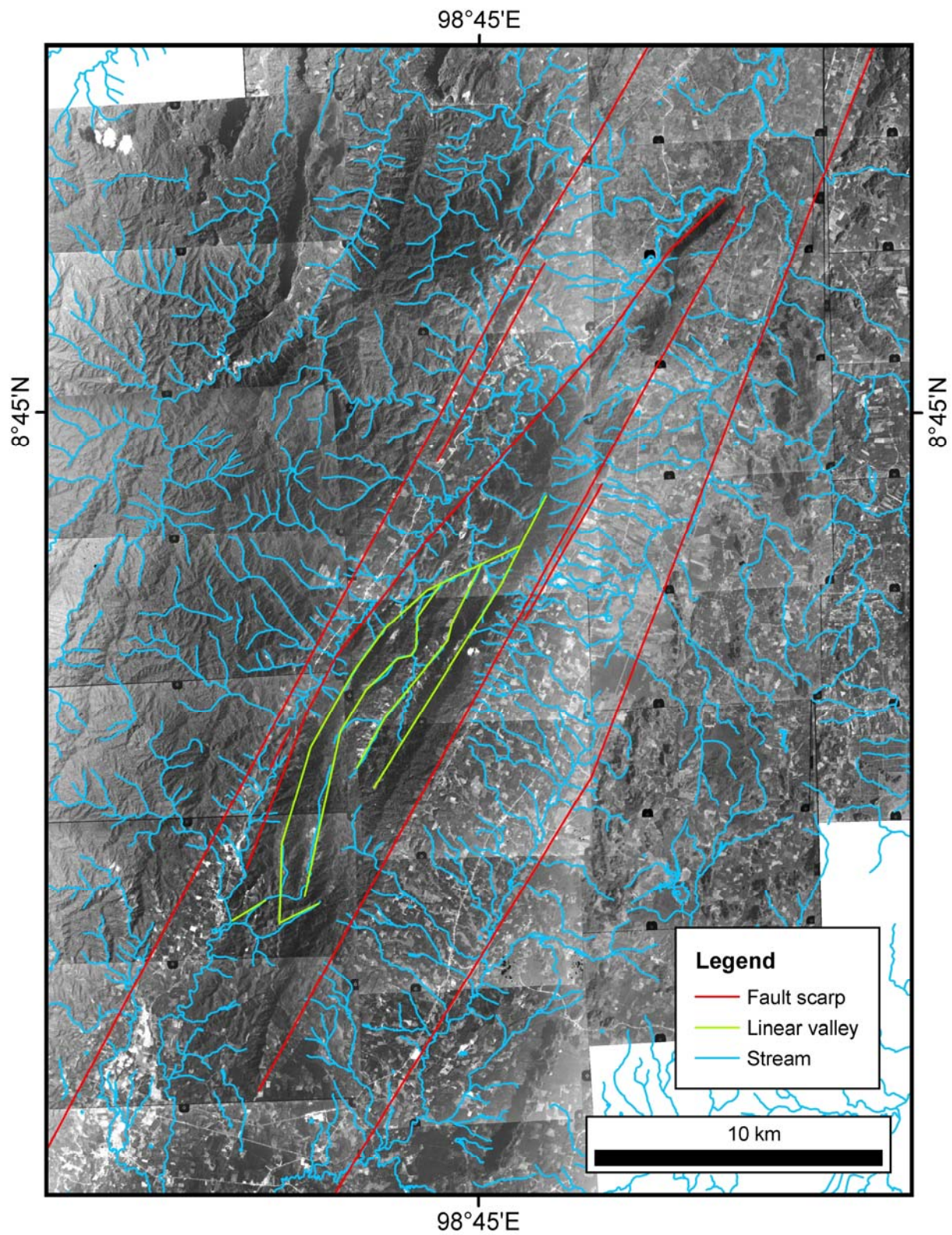


Figure 2.10 Fault scarp, fault valley and drainage network interpretation presented in mosaic of aerial-photographs.

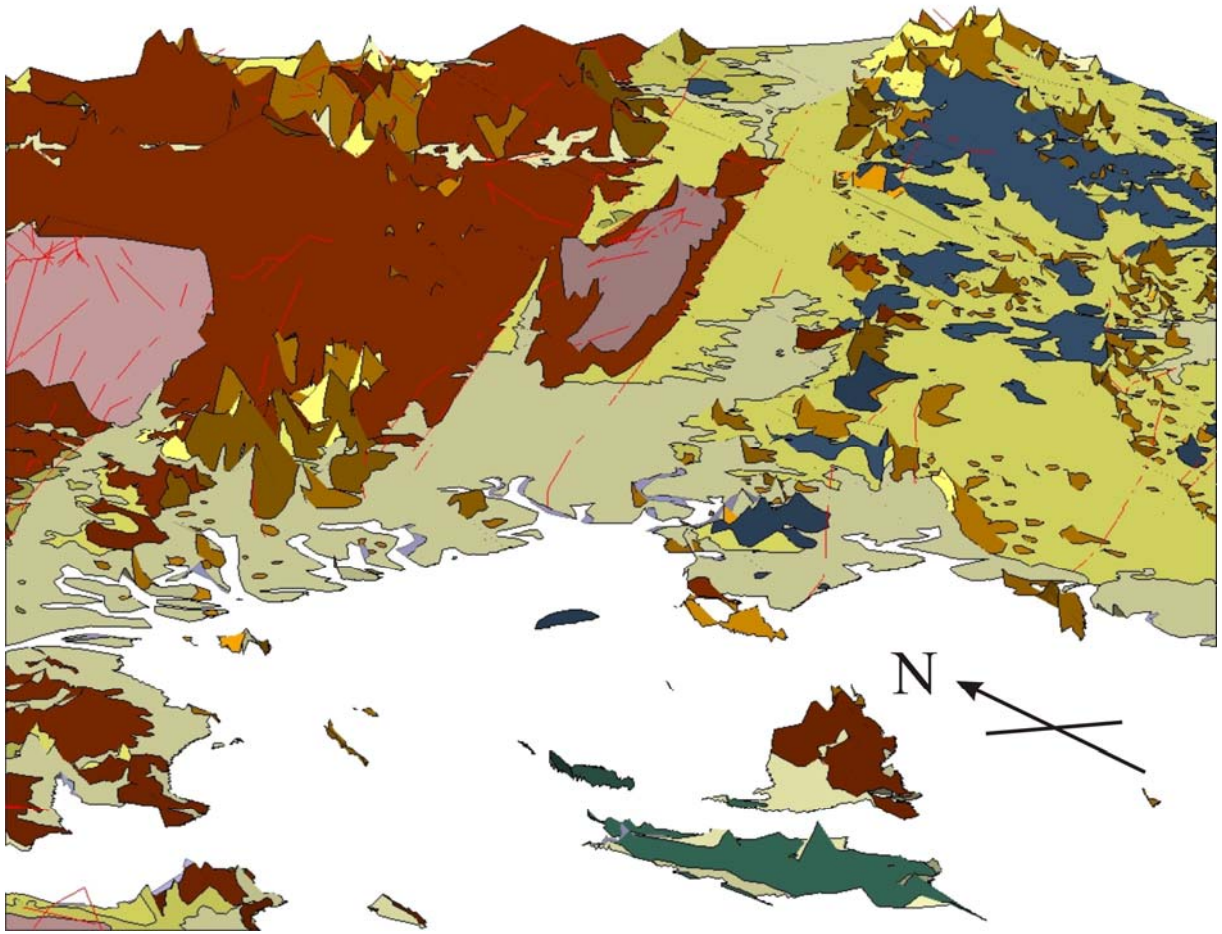


Figure 2.11 3D model of the Khlong Marui Fault looking from the south. The model combines the geological map (Fig. 1.4) and the SRTM digital elevation model, which has 5 times exaggeration.

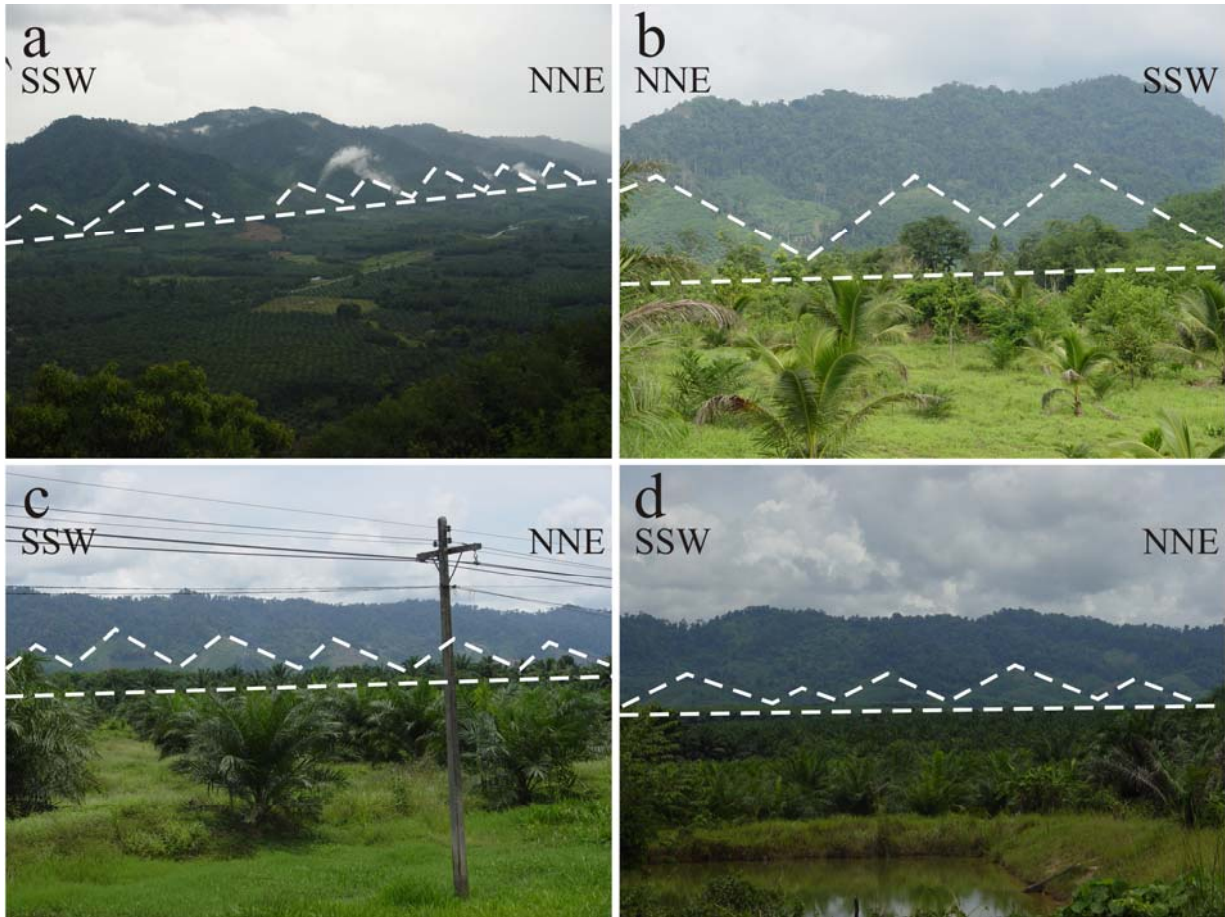


Figure 2.12 Triangular facets along the fault scarps can be observed throughout the study area; (a) along the Khlong Marui Fault; (b) west of Khao Phanom; (c) northeast of Khao Phanom; (d) southeast of Khao Phanom.

2.5 Structural Interpretation

Lineament relationship and characterization

The relationship of the three lineament sets; NNE-SSW, ENE-WSW and NW-SE were identified from the cross-cutting relationship and the length (Fig. 2.2, 2.4, 2.6). The NNE-SSW set is the most dominant with a length from 5 km up to >10 km and cuts across the ENE-WSW and NW-SE trends. This major lineament set normally lies along the fault scarp, linear valley, and parallel to the main stream. In contrast, the ENE-WSW and NW-SE trending sets are classified as minor lineaments in terms of geometry; their length compares to the major NNE-SSW direction. Both two minor lineament sets are restricted to in between the major lineament. The ENE-WSW trend with an average of 3 km length is more widespread than the NW-SE which is about 1 km long. They morphologically form small valleys and short streams.

Strike-slip tectonics

According to the tectonic setting of the area, the lineaments are considered and interpreted in the strike-slip tectonics framework. Lineament trends in the rose diagram are transposed to the sketch diagram (Fig. 2.13a). The major NNE-SSW lineament, which lies along the fault scarp, linear valley, and parallel to the main stream, is interpreted as the main fault (Fig. 2.13b). The minor ENE-WSW and NW-SE lineament sets belong to the conjugate shear secondary faults which are generally situated in between the major NNE-SSW direction. The ENE-WSW trending set represents the synthetic secondary fault (R) and the NW-SE direction is interpreted as the associated antithetic fault (R').

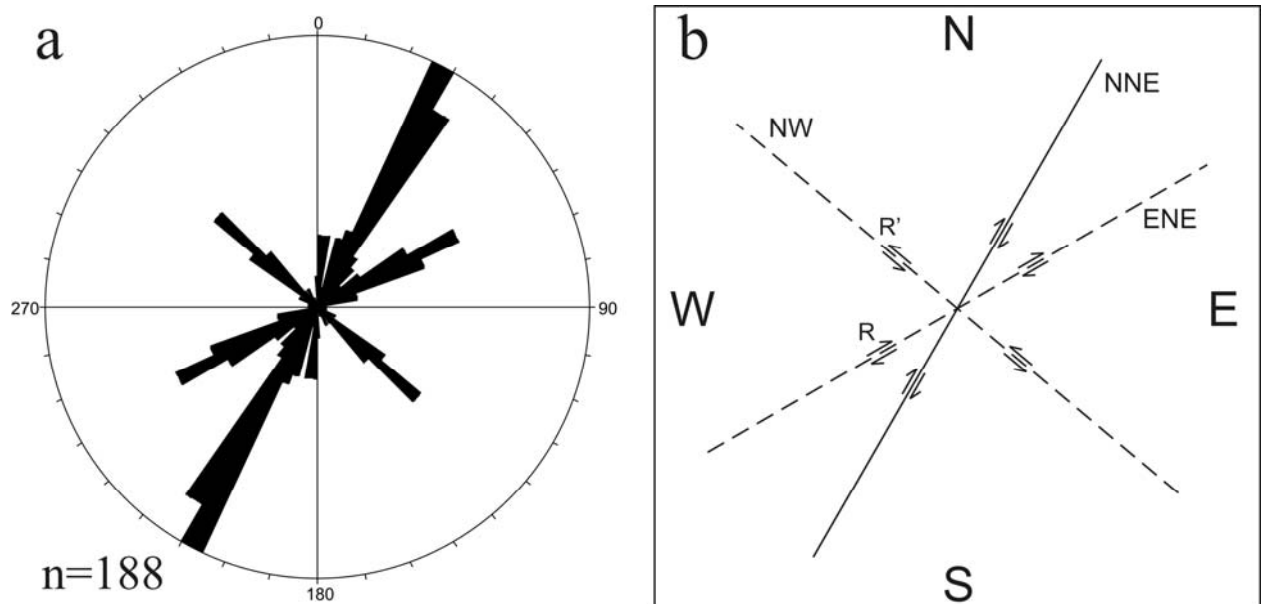


Figure 2.13 Rose diagram of all lineaments (a) and the NNE-SSW lineament interprets to the major fault zone with ENE-WSW synthetic and NW-SE antithetic secondary faults (b).

Chapter 3

Khlong Marui Shear Zone

3.1 Introduction

This chapter presents the geological and structural field study of the Khlong Marui Fault. The Khlong Marui Fault is recognized as a wrench zone from its fault line eastward to the Bang Kram Fault (Fig. 1.2). The core of the Khlong Marui shear zone is represented by a topographic range approximately 40 km long and 6 km broad termed Khao Phanom. The field investigation here focused along the Khao Phanom area where deformed rocks and related structures are best exposed.

The field work comprised geological mapping, measuring of structural data, and collecting of oriented samples. Used for mapping are a topographic map (scale 1:50,000) and remote sensing images. Regional geology is based on geological map after Department of Mineral Resources in 1982 sheet Changwat Phangnga NC47-14 scale 1:250,000 (Fig. 1.4). The rocks types and their boundaries are illustrated in the geological map, in geologic cross-section and in the description of outcrop.

Structural geology involved the analysis of kinematics and the measurement of spatial data, which are via stereographic projections and rose diagrams. Kinematic structures such as shear bands, boudinage, and asymmetric folds are described and used for inferring sense of shear. The mylonitic foliations, lineations, fault orientations, and slickensides are quantified and plotted in stereographic projections while the fracture orientations were plotted in rose diagrams with no dip information. All the plots are analyzed using the software TectonicsFP version 1.5. The statistical maxima of the structural elements represent the major structures of the Khlong Marui shear zone.

The architecture of the Khlong Marui Fault, which is illustrated by a 3D structural model, is derived from the geological and structural data. The geologic map was draped over a SRTM 90m digital elevation before integrating the structural cross-section into the model. The kinematic data is added into the 3D model in order to illustrate the history of the Khlong Marui shear zone.

3.2 Geology

The geology of the Khlong Marui Fault suggests that the Khao Phanom area mainly consists of mylonitic meta-sedimentary rocks associated with orthogneisses, mylonitic granites, and pegmatitic veins. These results contradict the mapping of Cretaceous granite surrounded by Permo-Carboniferous sedimentary rock that is published by the Department of Mineral Resources geological map in 1982 (Fig 3.1). The mylonite belongs to the Permo-Carboniferous Kaeng Krachan Group. It has been deformed and developed a mylonitic structure with varying grades of metamorphism. For example, the mylonites in the southern part have been deformed at lower metamorphic grade than the mylonite in the central area. The orthogneiss is located at the center of the shear zone, and the mylonitic granite is situated at the western area (Fig 3.2). Both rocks are orientated with foliation parallel to the steeply dipping mylonitic meta-sedimentary rocks. Pegmatitic veins concordantly cross cut the country rocks and limited only at the eastern part of Khao Phanom. The changing of dip in the western area is interpreted as a minor fold. In the areas which are close to the fault lines, proto-cataclasite to cataclasite zones can be distinguished.

The un-deformed host rocks of the shear zone are Permian to Triassic sedimentary units in the eastern part and Permo-Carboniferous on the west side. The Permo-Carboniferous Kaeng Krachan Group generally crops out as sequences of mudstone, pebbly mudstone, shale, sandstone, and conglomerate which have the same composition as the mylonite in the shear zone (Fig 3.3). Permian carbonate rocks forming karst towers can be found on both sides along the fault area. Quaternary deposits progressively overlie in lower elevations. They are dominantly widespread in the eastern part near the Bang Kram Fault. The description of the detailed geology in the area is listed below.

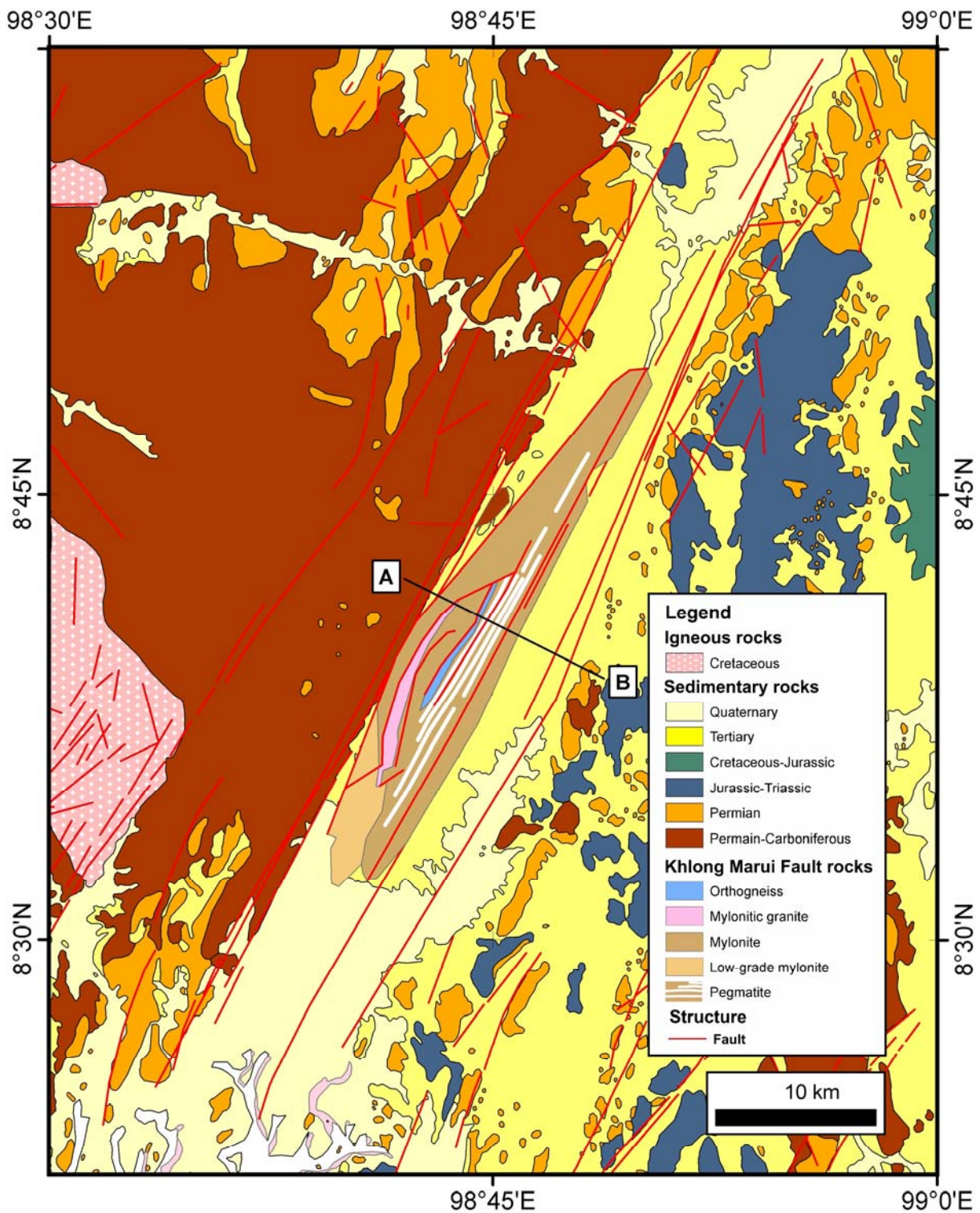


Figure 3.1 Geology of the Khlong Marui shear zone consisting of mylonitic meta-sedimentary rocks associated with orthogneisses, mylonitic granites, and pegmatitic rocks (modified after Department of Mineral Resources, 1982).

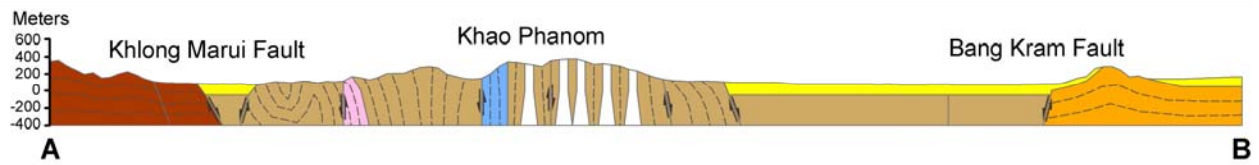


Figure 3.2 Geologic cross-section showing steep dipping of the rocks in the Khlong Marui shear zone (see Fig. 3.1 for correlation).



Figure 3.3 Typical Permo-Carboniferous Kaeng Krachan group consisting of sandstone (a) and pebbly mudstone (b) at the west boundary of the study area.

Orthogneiss

The orthogneiss is located in the middle area of Khao Phanom. The rocks clearly crop out at the Mae Yai waterfall (Fig. 3.4). These high grade metamorphic rocks are mainly composed of quartz, feldspar, tourmaline and biotite. Tourmalines form large crystals up to 3x5 mm long, parallel to the foliation. Augen structures of the quartz-feldspar form part of the gneissic banding.

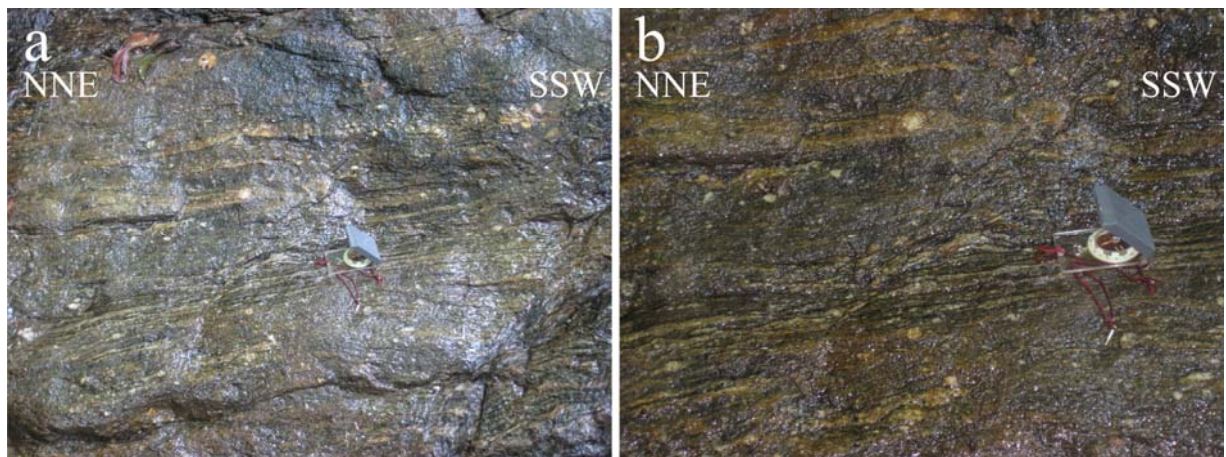


Figure 3.4 Gneissic banding of the orthogneiss is represented by tourmaline-biotite rich layers and quartz-feldspar augen structures (a, b) in Mae Yai waterfall.

Mylonitic granite

Granitic rocks in the western area generally show strong mylonitic microstructures (Fig. 3.5). The major mineral assemblage is medium grained quartz, K-feldspar, plagioclase, and biotite. K-feldspar phenocrysts are characterized by pinkish gray color in between the black biotite mylonitic layers. Quartz veins sized 1-1.5 cm are typically associated with the mylonitic foliation.



Figure 3.5 Granite at the western part of the area shows pinkish grey of K-feldspar in between the black biotite mylonitic layers (a) and quartz veins concordant parallel to the mylonitic foliation (b) at western Khao Phanom.

Mylonite

The mylonite deformed the metasedimentary rocks of Kaeng Krachan Group as seen in the mylonitic structure around Khao Phanom. The sequences of clastic sedimentary rock, mainly mudstone, pebbly mudstone, shale sandstone, and conglomerate, have been deformed into metapelite, quartzite, and metaconglomerate throughout the shear zone. Outcrops exposures are very poor because of the high weathering in the tropical climate. Low-grade mylonite at the southern area does not show a different physical appearance. The rock colors vary from yellowish brown, greenish brown, reddish brown to dark brown with black, red, and brown weathered colors (Fig. 3.6). It is caused by the different compositions. Well developed mylonitic structure is illustrated by the foliated mica and sigma quartz pebbles.

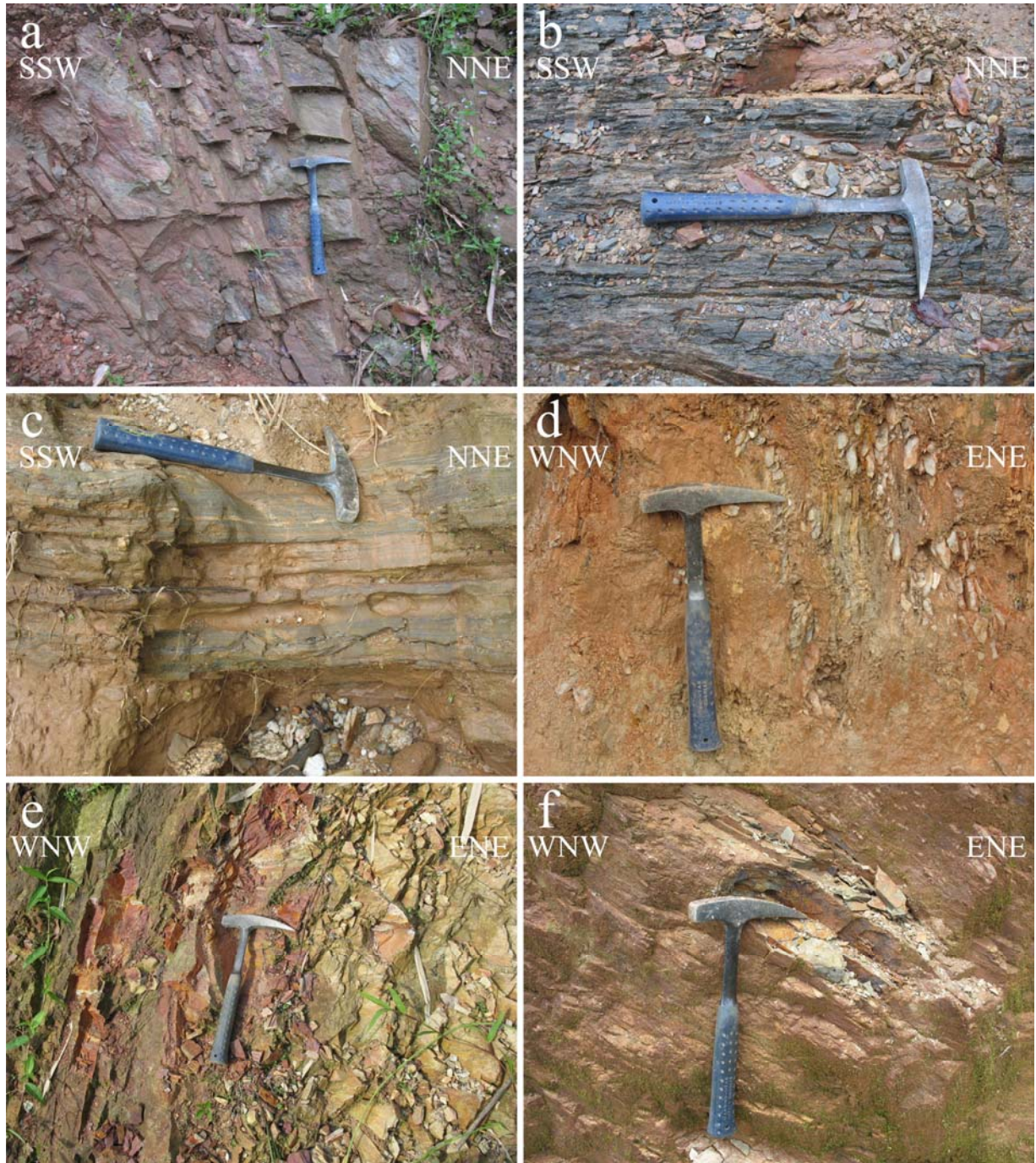


Figure 3.6 Variation of metapelite lithology from the west to the east of the shear zone; (a) reddish brown in western area; (b) dark brown in southwestern area; (c) greenish brown at the middle of Khao Phanom; (d) yellowish brown in eastern area; (e) reddish and yellowish brown in southwestern area; (f) reddish and greenish brown at southern Khao Phanom. It is caused by the different compositions.

The pebbly metapelite to metaconglomerate is characterized by highly competent beds in the massive metapelite (Fig. 3.7a). This rock typically crops out at waterfalls in the Khao Phanom area such as the Ton Chan, Ton Ha Chan, and Bang Tao Mae waterfalls. The rocks are dominantly greenish color composing of quartz, fine grained biotite, chlorite with different shape and size of pebble clasts (Fig 3.7b-d).



Figure 3.7 Pebbly metapelite to metaconglomerate outcrop shows thick layers lying to the NNE-SSW at the Ton Ha Chan waterfall (a). Variation of the pebbles sizes; (b) small pebbles at the same outcrop; (c) big pebbles in Ton Chan waterfall; and (d) stretching small pebbles at local waterfall in eastern area.

Like the metaconglomerate, quartzites are usually interlayered in the metapelite, throughout the area (Fig. 3.8a-b). Mylonitic structure is represented by the foliation of quartzite layers. Fine grained micas usually are present within the quartzite lithology. The impurity of quartzite and the deformation mechanism is indicated by the variation of its colors from milky to yellowish brown with some red.

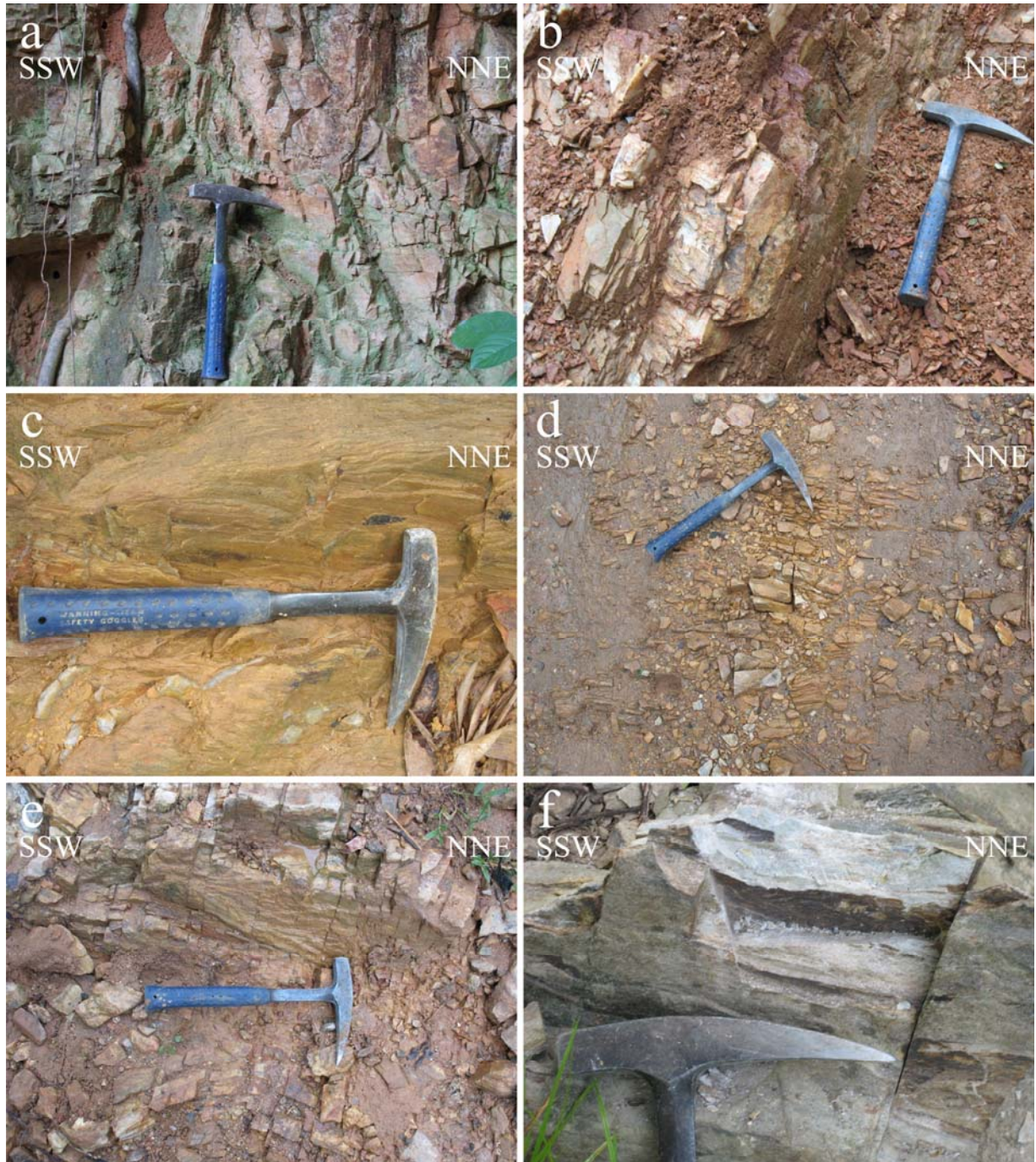


Figure 3.8 The impurity of quartzite showed the color variation from the west to the east of the shear zone; (a) yellowish and reddish brown in western area; (b) milky to yellowish brown at the western Khao Phanom; (c, d) yellowish brown in middle area; (e) milky to yellowish brown in eastern area; and (f) greenish brown in northeastern Khao Panom.

Pegmatitic rocks

The pegmatitic rocks are characterized by concordant veins sized from 1 cm to 3 m associated with the eastern part of the mylonite unit (Fig. 3.9a-b). The rocks are mainly pegmatites with rare granitic and aplitic composition. The lithology comprises coarse grained quartz, feldspar, white mica, and tourmaline. Garnet crystals (1-2 mm) are locally present in the pegmatites. Tourmaline enrichments usually either form black layers at the pegmatite rims or intrude as veins into the mylonite (Fig. 3.9c-d).



Figure 3.9 Pegmatitic veins concordant with the mylonitic metasedimentary rock with a different width at the eastern area of Khao Phanom (a, b). Tourmalines forming either as black layers at the pegmatite rims (a) or as veins into the mylonite at the same outcrop (b).

Cataclasites

Cataclasites can be observed at the eastern and western margin of the shear zone (Fig. 3.10). The brittle rocks range from proto-cataclasite to cataclasite, have the same lithology as the mylonite sequences, and have been produced by multiple fault activities. The fragments of cataclasite form the high angular shape. At the eastern area, non-cohesive cataclasites can be found with cohesive cataclasites.

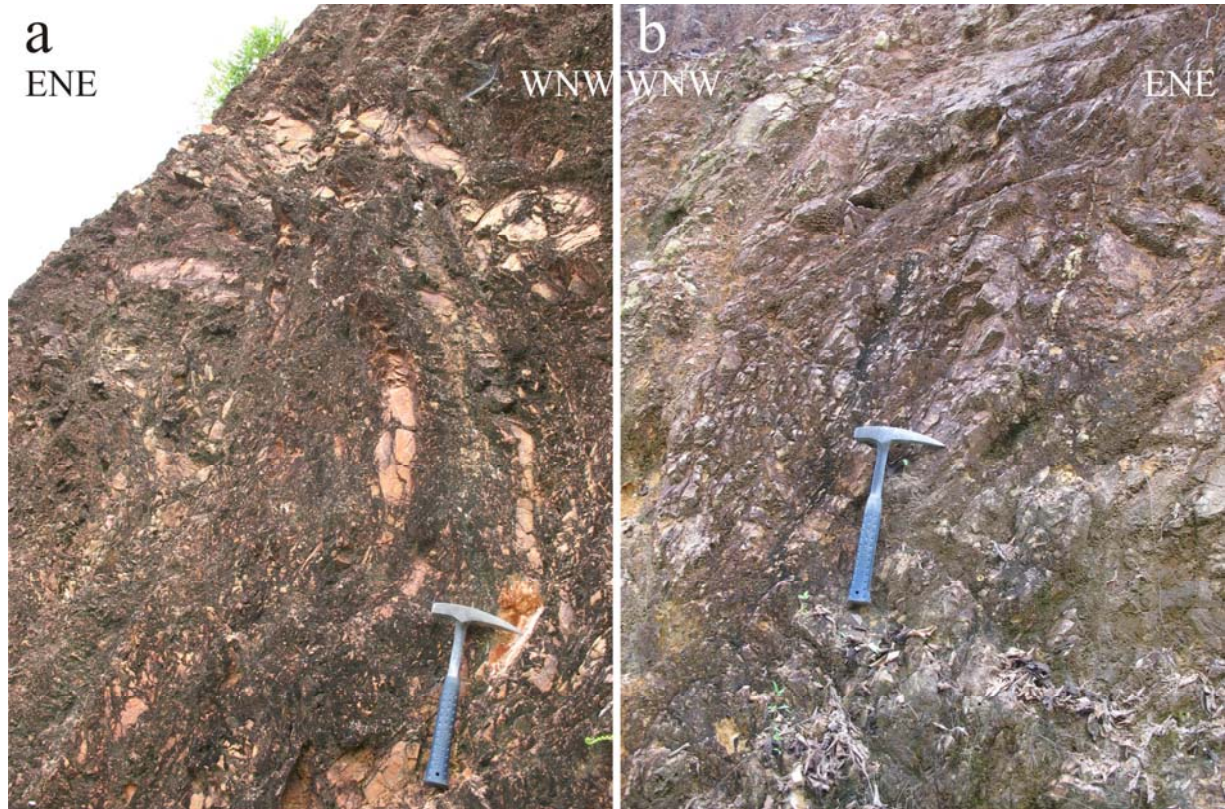


Figure 3.10 Proto-cataclasites to cataclasites are associated with a fault plane in the eastern (a) and western margins of the shear zone (b).

3.3 Structural Geology

The structural geology in the study area is dominated by the Khao Phanom fault core which is bounded by the Khlong Marui Fault and Bang Kram Fault juxtaposed with the gentle bedding of the Permo-Carboniferous to Triassic sedimentary host rocks. According to the macroscopic study described in the chapter 2, the fault lines and topography trend NNE-SSW, geomorphically represented by a set of triangular facets around Khao Phanom (Fig. 2.12). The result from remote sensing interpretation indicated that the major fault zone trends to NNE-SSW composite with the NE-SW synthetic secondary fault (R) and the NW-SE associated antithetic fault (R') (Fig. 2.13). The outcrop scale structures reflect and are associated with the macrostructure.

Mesoscopic structures in the Khao Phanom area record foliations, stretching lineations, joint sets, fault orientation, slickensides and striations, all of which have been observed and measured in the field. All structures were classified and described into the ductile deformation and brittle phase.

3.3.1 Ductile Deformation

The Khlong Marui shear zone is dominantly expressed by the ductile core. The orthogneiss, mylonitic granite, and mylonitic metasedimentary rocks record the foliations, stretching lineations, and mylonitic structures which developed during the ductile phase (Fig. 3.11). Foliations are well developed in the rocks which are mica-rich, such as metapelites. They form steep-vertical dipping foliations dominantly striking NNE parallel with the marked topography.

Stretching lineations are clearly observed in all rock types. In the orthogneiss and mylonitic granite, they are generally defined by elongated quartz grains which are parallel to the orientation of K-feldspar and tourmalines. Like the orthogneiss and mylonitic granite, quartz stretching can be observed in the sequences of metapelite, metaconglomerate and quartzite.

At least two lineation sets are recorded in the quartzite especially at the eastern part of Khao Phanom. Both lineations indicate dextral shear.

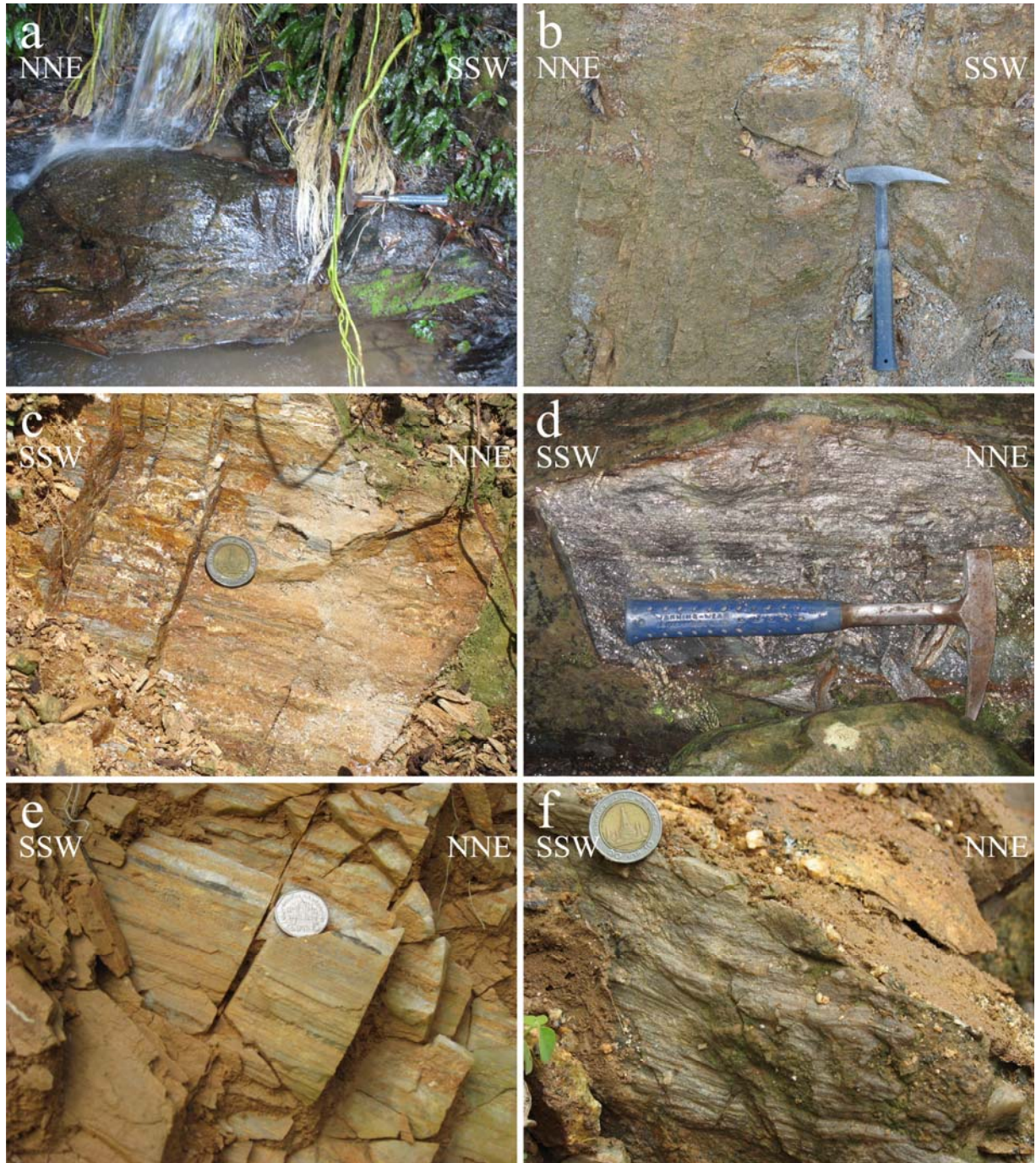


Figure 3.11 Outcrops along the Khlong Marui Fault showing major structure of foliations and stretching lineation in the orthogneiss at the Mae Yai waterfall (a), mylonitic granite of western area (b), metapelite in northern area (c), metapelite with pebbles at the Bang Tao Mae waterfall (d), quartzite in western area (e), and quartz vein in middle area (f).

Poles of the foliations were plotted and calculated for the contours in stereographic net by gauss counting method (Robin and Jowett, 1986). Contours of the plotting are 1%, 2%, 3%, 4%, and 5% per 1% area. The girdle shape of contour shows that the mylonitic foliation strikes NNE steeply dipping either WNW or ENE dipping and the subhorizontal stretching lineation has a clearly defined maximum at NNE-SSW (Fig. 3.12).

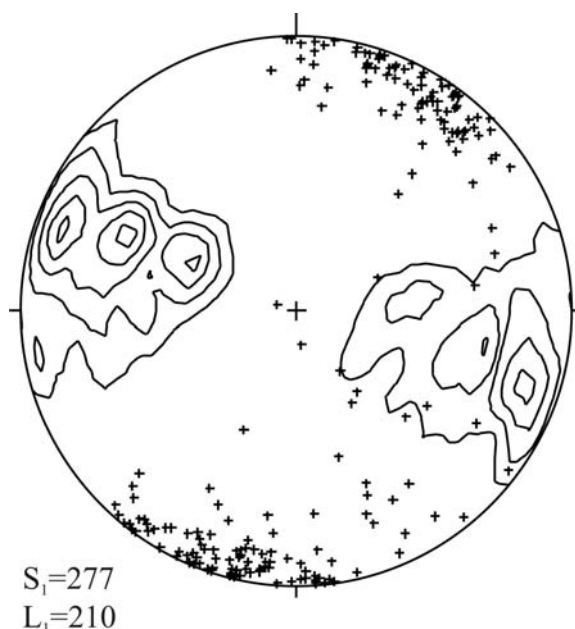


Figure 3.12 Stereographic plots of the ductile deformation. Contour poles of the foliations (S_1) showing steeply dipping either WNW or ESE, and the lineations (L_1) trend to NNE-SSW. Contours are 1%, 2%, 3%, 4%, and 5% per 1% area by gauss counting method (Robin and Jowett, 1986).

3.3.2 Kinematic Indicators

Abundant kinematic indicators can be observed within the Khlong Marui Fault core. Spectacular dextral sheared monoclinic quartz lenses defining σ -shapes are frequently present in the mylonite sequences (Fig. 3.13). Dextral ductile deformation is recorded by domino-type and shear band type fragmented quartz lenses (Fig. 3.14). S-C' fabrics of dextral shear are well developed in the biotite-rich bands of the orthogneiss, mylonitic granite, and metapelites (Fig. 3.15). Boudinage of quartz lenses in the mylonite and asymmetric fold in the orthogneiss and metapelite confirm for dextral movement (Fig. 3.16). All of them indicate that the ductile deformation had a dextral movement.

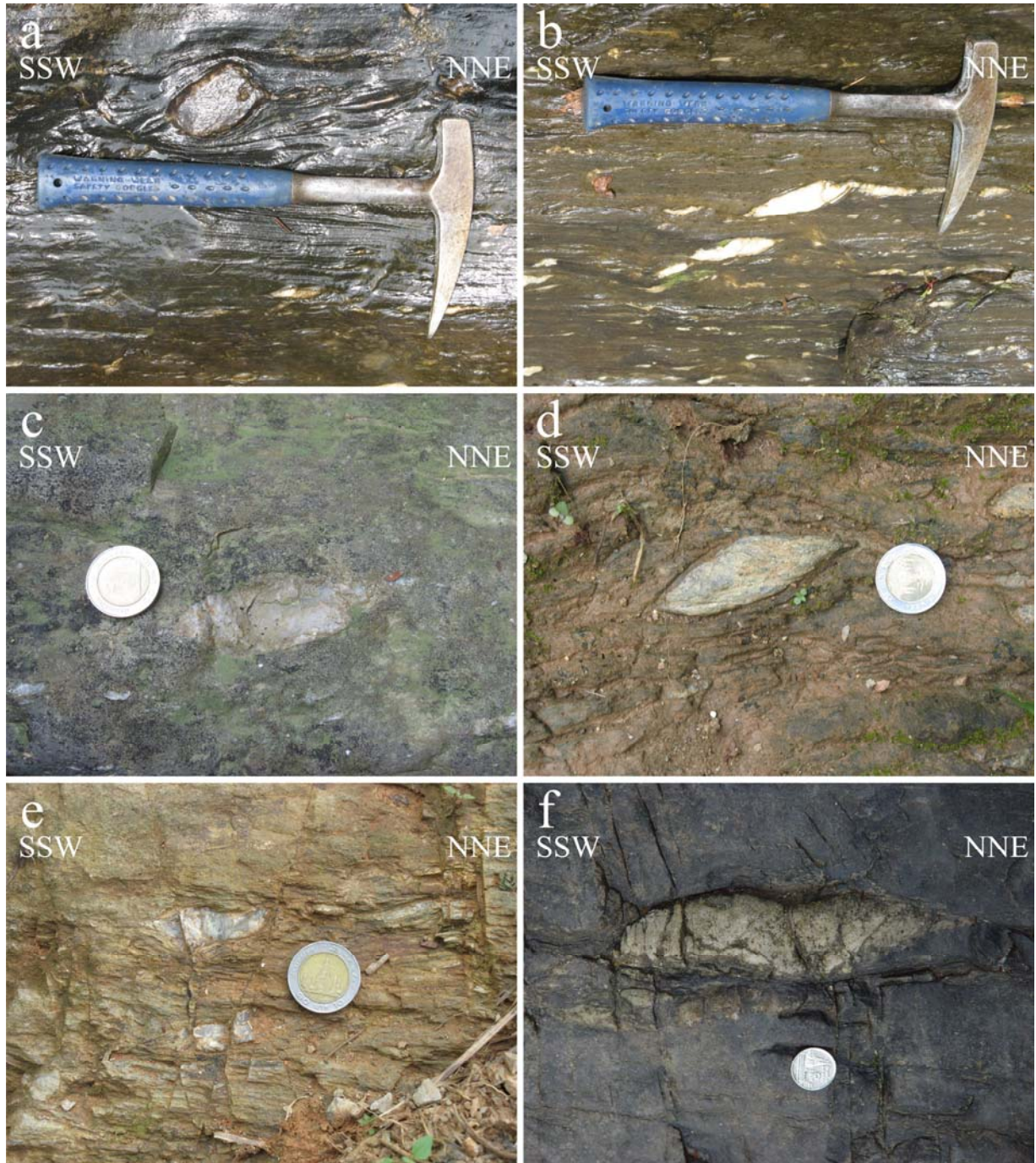


Figure 3.13 The mylonitic structures of the pebbles in the metapelite show dextral shear of quartz grains σ -shape; (a, b) at the Ton Chan waterfall; (c) at the Ton Ha Chan waterfall; (d) in middle area; (e) in northern Khao Phanom; (f) at the Bang Tao Mae waterfall.

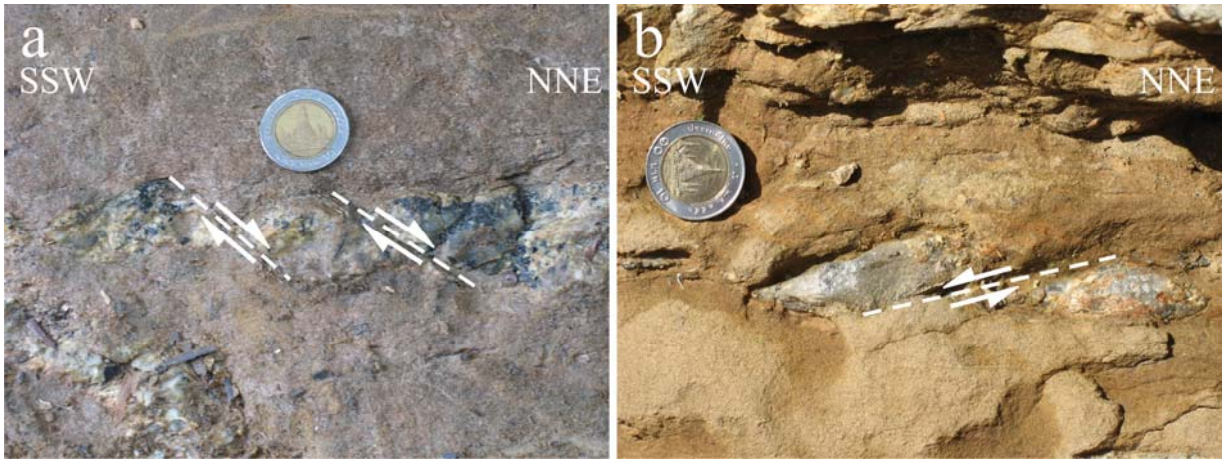


Figure 3.14 Fragmented quartz lenses showing shear band type (a) and domino-type (b) in the mylonites at middle Khao Phanom.



Figure 3.15 Shear band illustrated by S-C fabrics in metapelite with quartz pebble at the Bang Tao Mae waterfall (a). S-C' fabrics in mylonitic granite in western area (b) and metapelite in middle Khao Phanom (c, d).

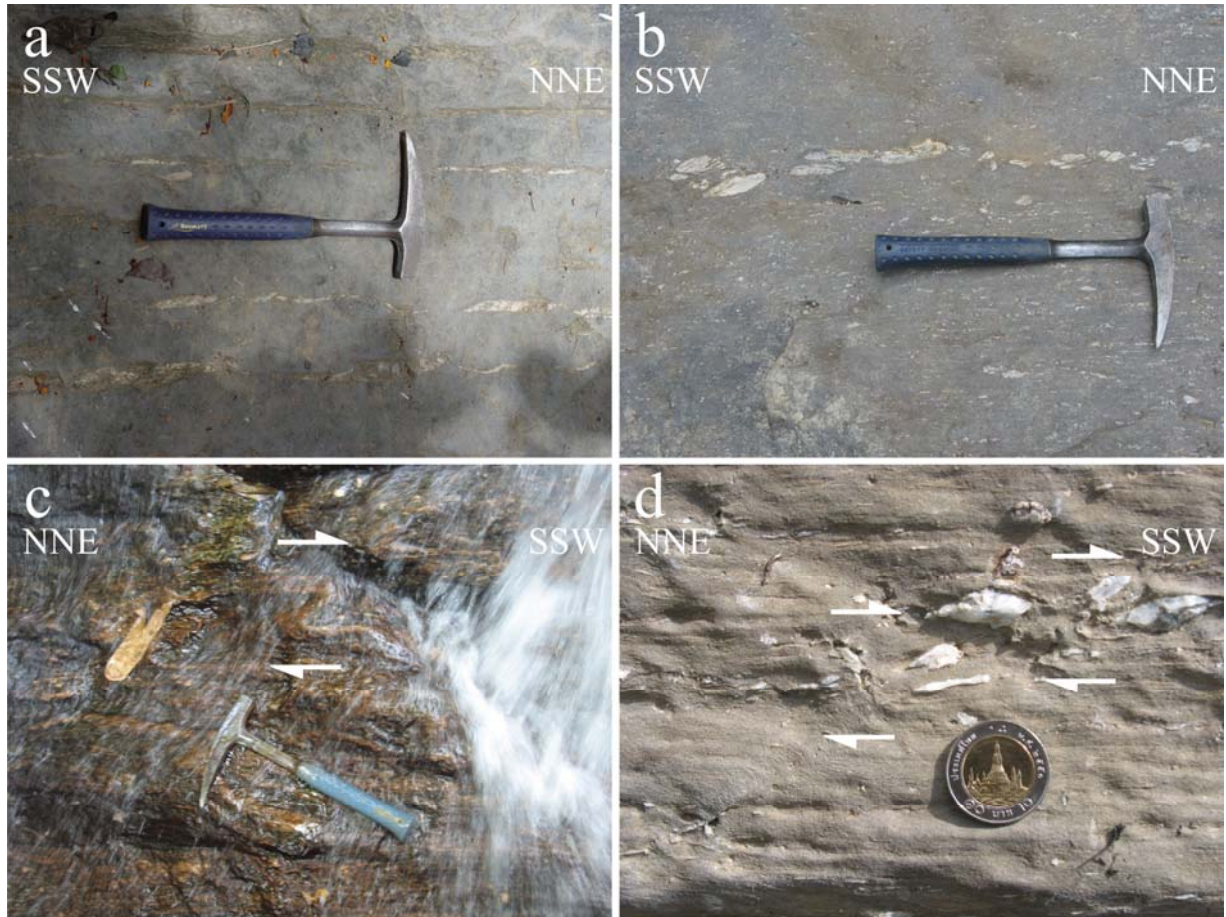


Figure 3.16 Quartz layer deformed into boudinage at the Bang Tao Mae waterfall (a) and local waterfall in the northern area (b). Asymmetric folds via dextral sense of shear in orthogneiss at the Mae Yai waterfall (c) and at middle area (d).

The lineations of tourmalines in the pegmatites are orientated in NNE-SSW (Fig. 3.17). They are parallel to the stretching lineation of the host mylonitic metasedimentary rocks. The foliations can be locally found at the pegmatite rims which are contact with the country rocks.

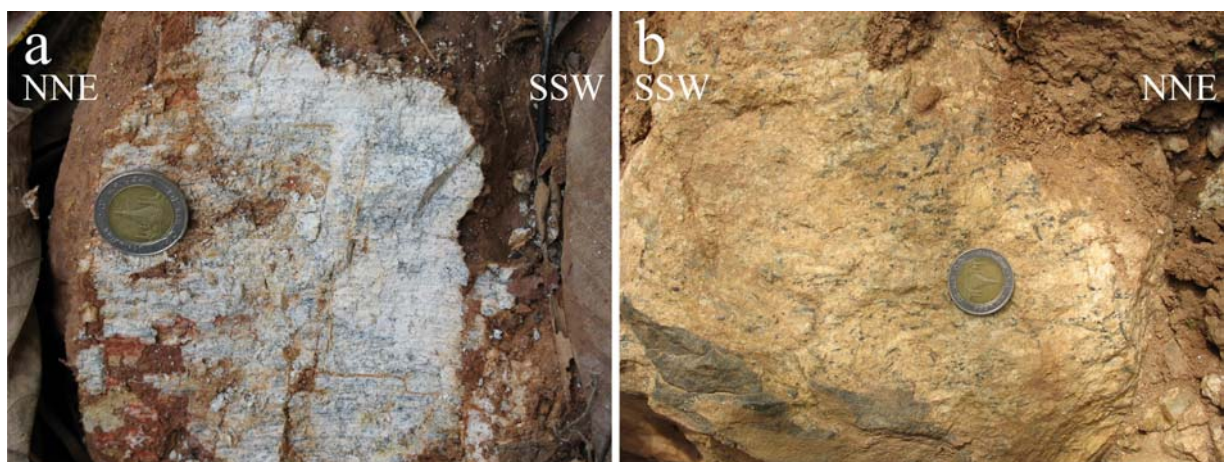


Figure 3.17 Pegmatite lineations of tourmaline are NNE trending, parallel to the lineation in the host mylonitic metasedimentary rocks in eastern Khao Phanom (a, b).

3.3.3 Brittle Deformation

Brittle deformation in the study area is represented by joints, faults, and cataclasite zones. Abundant joint sets transect WNW-ENE, perpendicular to the main foliations and stretching lineations (Fig. 3.18). Joint spaces range from 15 cm to 3 m. Joints are spectacularly lucid in quartzite sequences.



Figure 3.18 Major joints in metapelite of western area (a) and quartzite at the Bang Tao Mae waterfall (b) striking WNW-ESE perpendicular to the main foliation.

Major fault zones striking NNE are associated with proto-cataclasites to cataclasites at the margins of the Khao Phanom ductile core (Fig. 3.19). The faults produce cataclasite zones up to 10 m width. Polished surfaces can be observed along this damage zone. The steeply dipping slickensides and striations show evidence for a normal faulting component of one of the last deformation events. The hanging wall is overlain by the Quaternary sediments and thick soil development. Displacement of the normal faults is estimated via elevation differences to be about 400 m. Minor faults and Riedel shears within the area are oriented in ENE-WSW and NW-SE (Fig. 3.20). The ENE-WSW trend reflects dextral movement and usually cuts across the sinistral NW-SE striking sets.

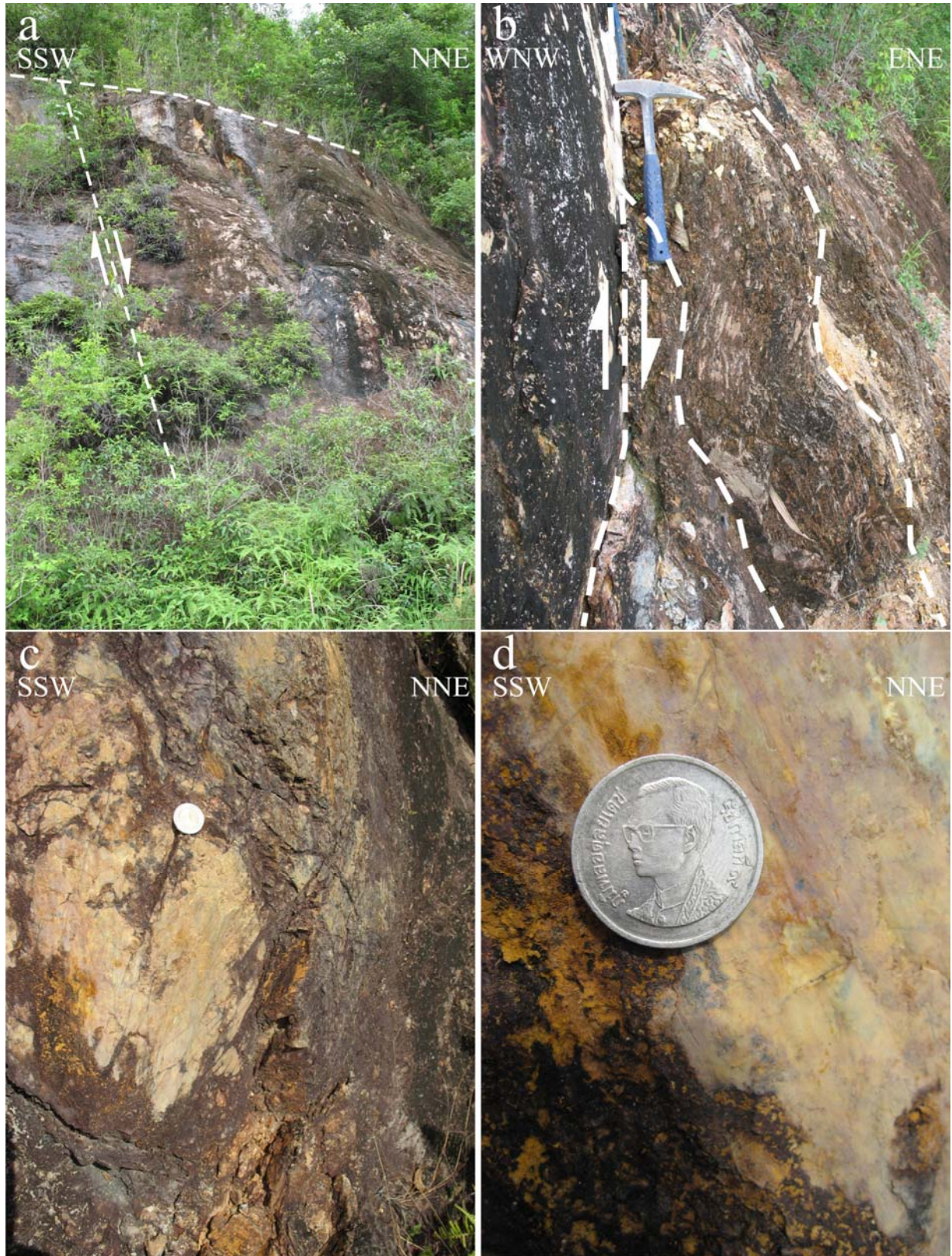


Figure 3.19 Normal faults along the eastern margins of the Khao Phanom ductile core (a, b). Slickenside and striations record a normal fault component in general view (c) and zoom view (d).

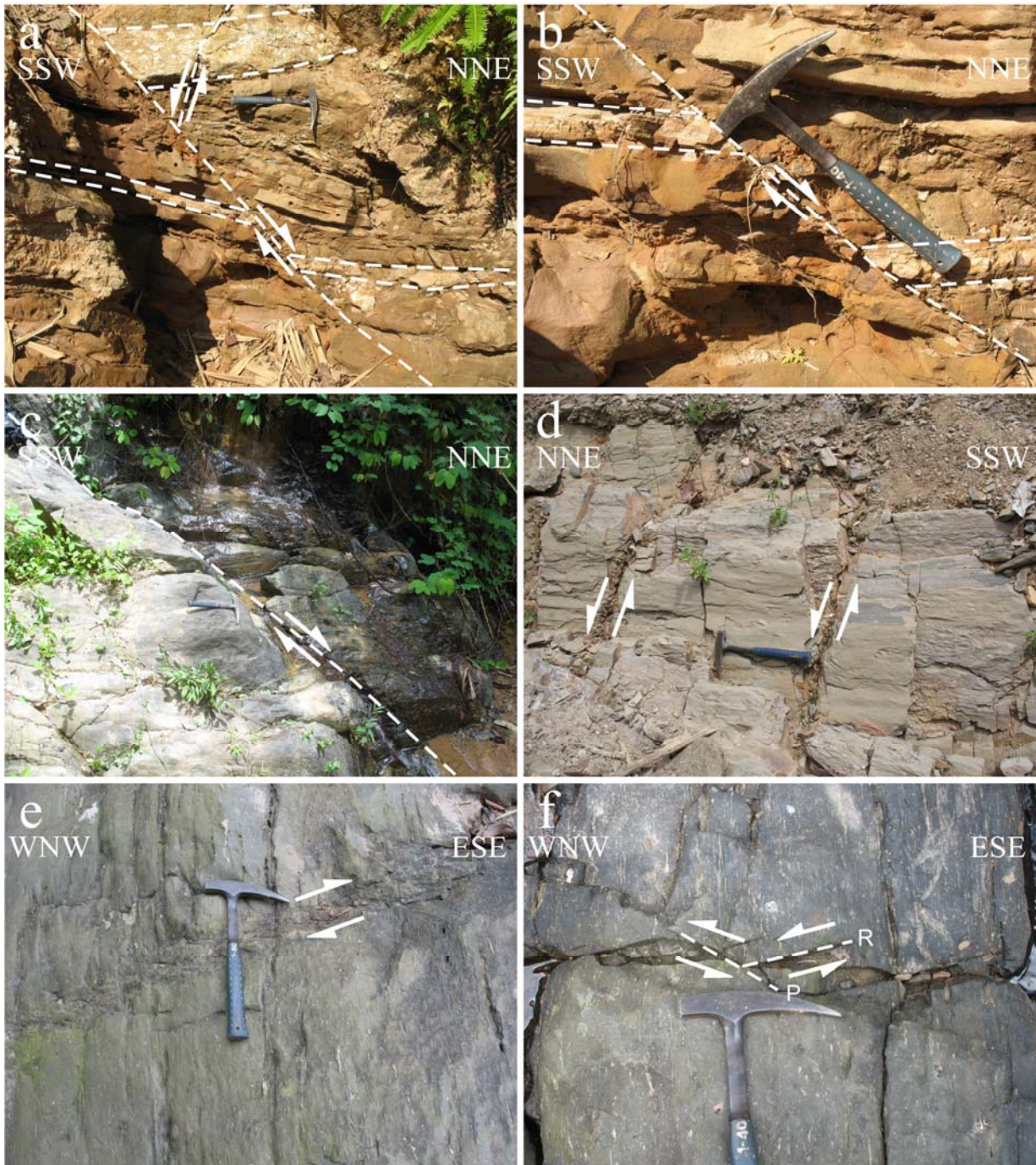


Figure 3.20 Minor faults in the mylonite; (a) dextral kinematics ENE-WSW striking cuts through sinistral faults which are NW-SE strike in the metapelites at middle area; (b) ENE-WSW dextral in metapelite at the same outcrop; (c) ENE-WSW dextral in metaconglomerate at local waterfall in eastern area; (d) sinistral Riedel shear orientated NW-SE in metapelite at northeastern Khao Phanom; (e) ENE-WSW dextral Riedel shear in metaconglomerate at the Ton Ha Chan waterfall; (f) sinistral Riedel shear in metaconglomerate at the same outcrop.

Brittle deformation is recorded in a pervasive joint set striking dominantly 120°SE and 140°SE which vary about 20° each way in rose diagram (Fig. 3.21a). Steeply dipping fault planes and striations of cataclasites show the major NNE-SSW orientation of the normal faults in stereographic plots (Fig. 3.21b). The minor faults orientate in ENE-WSW and NW-SE.

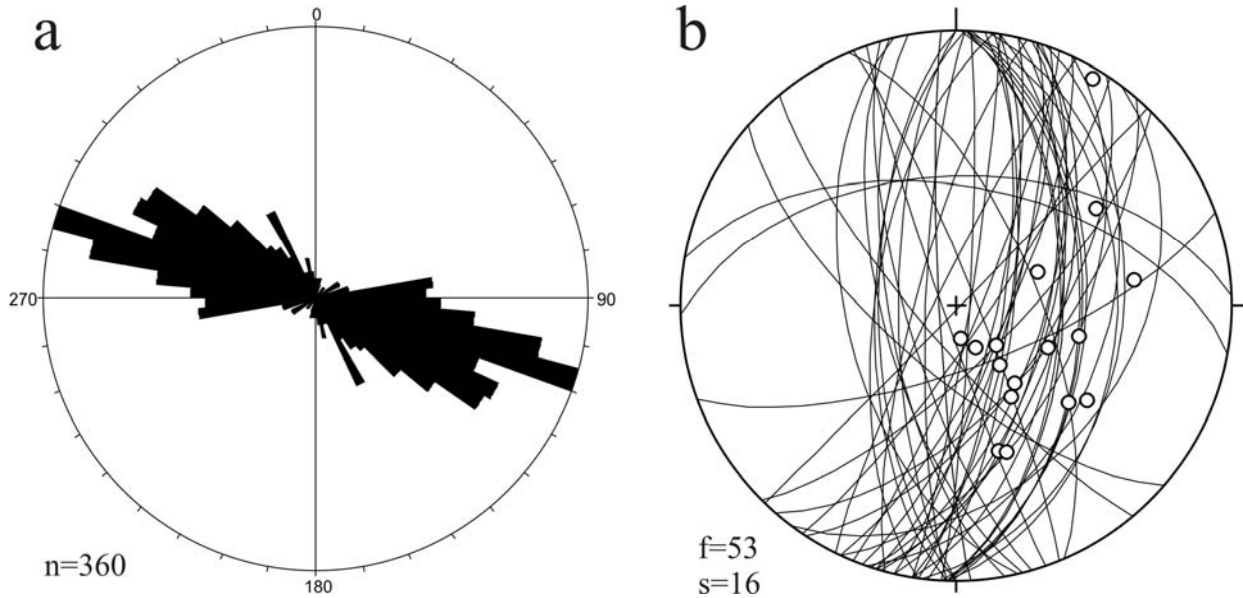


Figure 3.21 The representation of brittle deformation is illustrated by rose diagram of WNW-ENE striking major joints (a). Stereographic plots of the fault planes (f) and their striations (s) indicate the NNE-SSW normal fault component with the ENE-WSW and NW-SE minor faults (b).

3.4 Structural Model

Ductile deformation was recorded in shear bands, foliations and lineations in orthogneiss, mylonitic granite, and mylonite. These indicated that early stage movement was dextral in the NNE-SSW direction. Two lineation sets in quartzite indicate that there are at least two dextral ductile phases. Synkinematic behavior of the pegmatite intrusion during the ductile stage is established by the parallel nature of tourmaline lineations in pegmatites and stretching lineations in the country rocks. Tension fracturing is represented by a major joint set towards 110° which is orientated perpendicular to the 030° stretching lineation.

Mylonitic structures in this area are spectacularly overprinted by brittle fractures. The NNE-SSE normal faults and the Riedel shear fractures (R and R') were activated during the brittle deformation stage. The intense deformation conditions of rock in between un-deformed sedimentary host rock units suggests that the core of the Khlong Marui shear zone had been exhumed up to its present level, forming a positive flower structure (Fig. 3.22). Particularly at the east margin of the shear zone, cataclasites and slickensides suggest a normal displacement component of the last deformation.

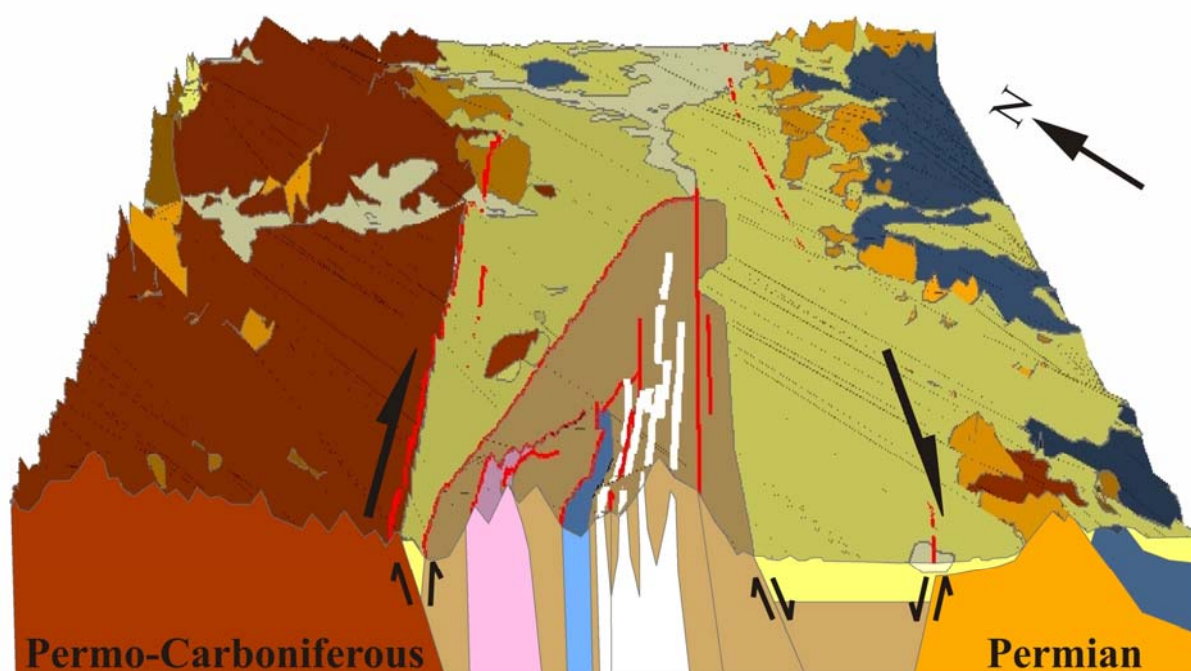


Figure 3.22 Schematic positive flower structure of Khlong Marui shear zone in between Permo-Carboniferous and Mesozoic sedimentary units. The dextral shear sense refers to the ductile deformation.

Chapter 4

Microstructures

4.1 Introduction

To understand the deformation and metamorphism processes of the rocks in microscopic scale, microstructure and rock fabric analysis played a role in this study. The microstructure gives information on the shear sense direction, flow type, and the mechanisms of deformation. This information is a useful tool to constrain temperatures during deformation and also to estimate the strain qualitatively. The microstructure results were used to reconstruct the structural and metamorphic history of the area.

The orientated samples collected from the field were prepared for optical microscopes description. Thin sections of the rocks from Khao Phanom were studied for petrography and microstructure under the polarized-light microscope. The mineral content and the textural relationships within the rocks are described along with their deformation behavior. Kinematic indicators were observed in order to understand the sense of shear. Constraining temperatures during deformation is based on deformation behavior of the minerals. For example, quartz illustrates a range of temperature-sensitive dynamic recrystallisation mechanisms, including basal gliding, bulging (BLG), subgrain rotation (SGR), and grain boundary migration (GBM) (Passchier and Trouw, 1996). Shear sense is established by the kinematic indicators such as geometry or orientation of sigmoids, σ -objects, mineral fish, domino-sets, shear bands, and quarter structures.

The rock samples of quartzite are studied both for petrography and deformation mechanism as well as quartz texture, including grain shape preferred orientation (GSPO) and optic axis lattice preferred orientation (LPO). The angle between the oblique grain shape fabric and the main foliation (δ) and the angle between the perpendicular to the central girdle segment of quartz c -axis fabric and the main foliation (β) were measured for calculating the mean vorticity number (W_m). Deformation settings of transpression or transtension were identified by the summation of δ and β angles using physical spaces. The β angle and the mean vorticity number (W_m) were plotted on the diagram for ellipticity of the finite strain ellipsoid (R_f) (Grasemann et al., 1999; Xypolias, 2009).

Finally, the interpretation from petrography and microstructure is used to characterize the microstructure deformation.

4.2 Petrography and Microstructures

The petrography and microstructure studies of the rocks in the Khlong Marui shear zone use as a framework the geological map in the chapter 3 (Fig. 3.1). Microstructures of the rock from the study area show deformation structures from highly ductile to brittle behavior. Ductile deformation of the Khlong Marui shear zone is represented by mylonitic foliation in orthogneiss, mylonitic granite, and mylonitic metasedimentary rock. Brittle deformation encompasses proto-cataclasites to cataclasites. Thin sections of the samples have been examined for the petrography and microstructures of the study area in the following paragraphs.

Un-deformed sedimentary rocks of Permo-Carboniferous Kaeng Krachan Group are studied and compared to the rocks in the Khlong Marui shear zone in order to understand the deformation process. The medium grained sandstone, fine-grained sandstone, and mudstone are considered in this study. Medium grained sandstone shows the composition of quartz, K-feldspar, plagioclase to be well rounded and well sorted (Fig. 4.1a-b). A higher proportion of rock fragments characterize finer grained grain sandstones (Fig. 4.1c-d). Mudstone comprises abundant clay minerals, and is interlayered with the very fined-grained sands (Fig. 4.1e-f).

Orthogneiss

The major components of the orthogneiss are quartz, K-feldspar, and biotite. Plagioclase, tourmaline, and white mica are characterized as accessory mineral (Fig. 4.2a-b). Zircon crystals can be found throughout the rocks. Most minerals are orientated parallel to the foliation plane.

Quartz crystals have been dynamically recrystallized under high temperature ($>500\text{ }^{\circ}\text{C}$) conditions which represented by grain boundary migration (GBM) (Fig. 4.2 c). Oscillatory zoning in K-feldspar represents original magmatic crystallization (Fig. 4.2 d). Undulose extinction is present in K-feldspar porphyroblasts (Fig. 4.2 e). Dextral shear is clearly preserved in the gneissic texture especially in K-feldspar, which was sheared and developed fractures with right lateral offset (Fig. 4.2 f).

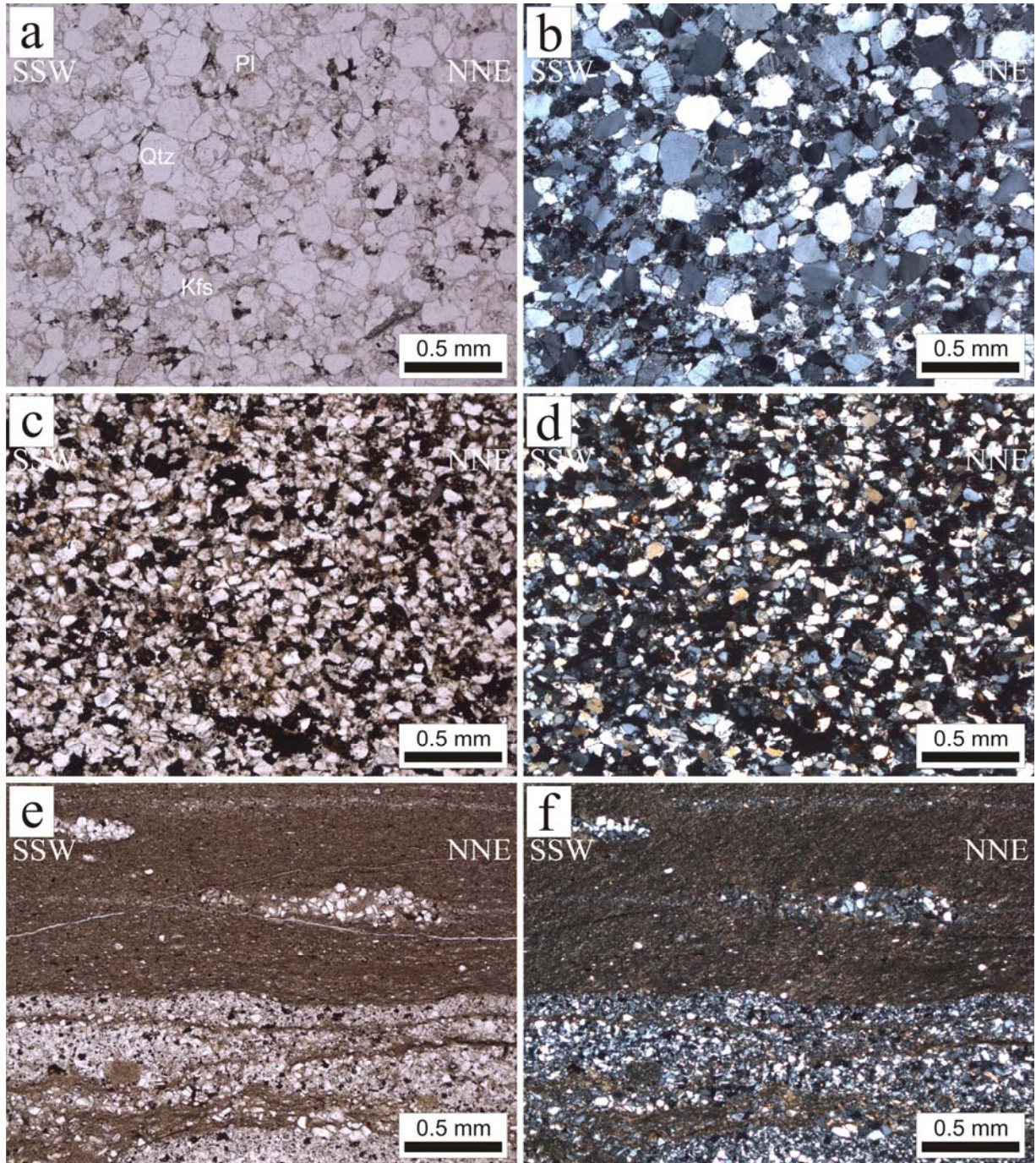


Figure 4.1 Photomicrograph of medium grained sandstone (a, b), fined grained sandstone (c, d), and mudstone interlayered with very fine grained sands at the west boundary of the study area (e, f). (a, c, e, PPL; b, d, f, CPL)

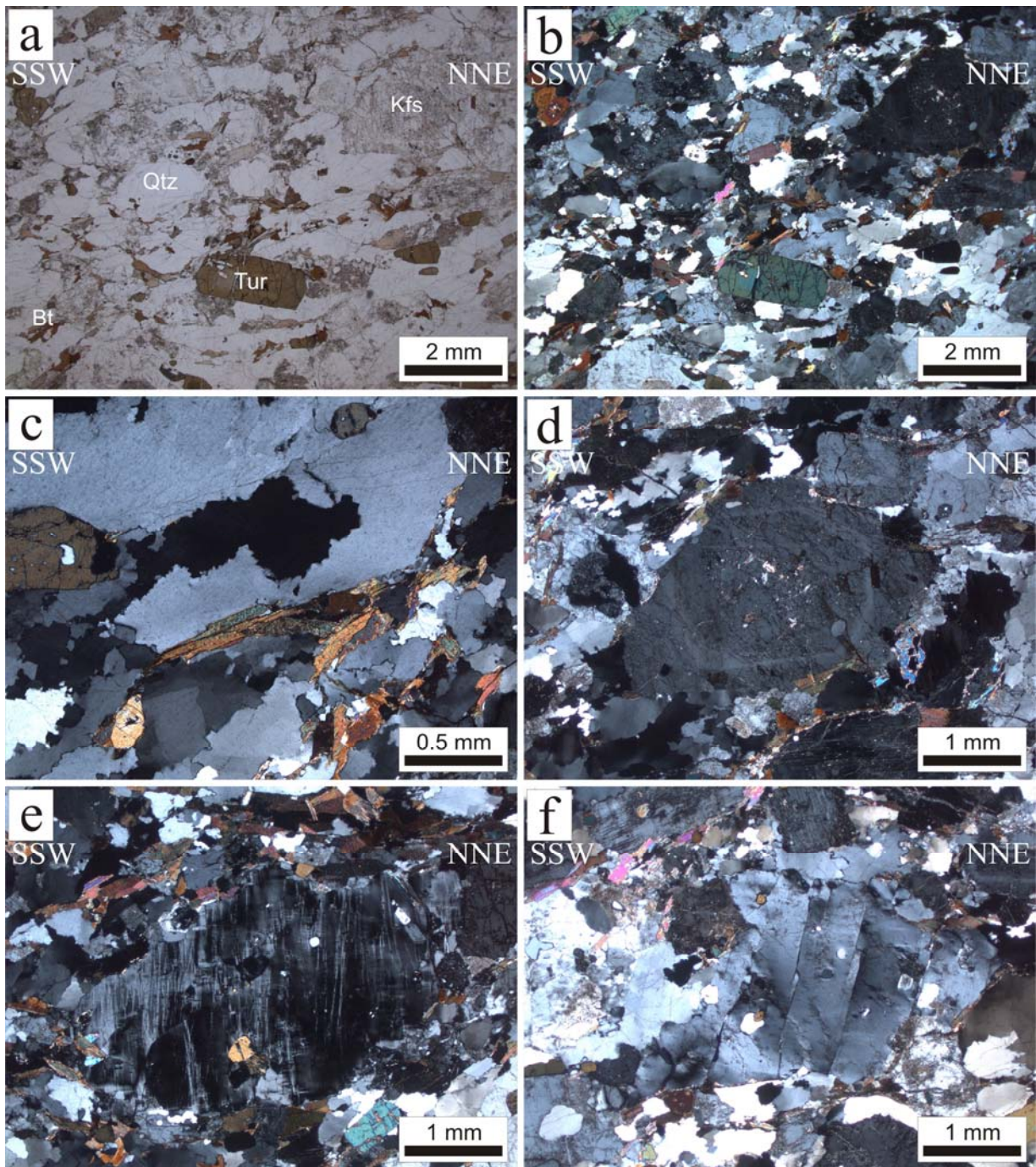


Figure 4.2 Orthogneiss at the Mae Yai waterfall shows the composition of quartz, feldspar, biotite, and tourmaline (a, b). Grain boundary migration (GBM) in quartz (c). Feldspars show oscillatory zoning (d), typical for magmatic crystallization, undulose extinction (e), and fracture with right lateral offset (f). (a, PPL; b-f; CPL)

Mylonitic granite

Medium grained granite in the study area dominantly comprises quartz, K-feldspar, plagioclase, and biotite with accessory minerals of tourmaline, chlorite and opaque minerals (Fig. 4.3a-b).

The mylonitic structure records a dextral shear sense which is consistent with the orthogneiss. Subgrain rotation (SGR) to grain boundary migration (GBM) recrystallisation indicates medium to high temperatures during deformation (Fig. 4.3c-d). “V”-pull-apart structures developed in the K-feldspar indicate dextral shear sense (Hippertt, 1993) (Fig. 4.3e). Further kinematic indicators are asymmetric myrmekite of quartz structures in K-feldspar porphyrocrysts (Fig. 4.3f).

Mylonite

The mylonite and low-grade mylonite are mainly composed of quartz and biotite with variation of grain size and composition throughout the Khlong Marui shear zone. White mica, chlorite, tourmaline, and opaque minerals are the minor components in the mylonite.

Low-grade mylonite is characterized under microscope by a weak mylonitic structure. Quartz and mica generally define the foliation via highly deformed, elongated quartz rods (Fig. 4.4). In mylonite, biotite typically has a subparallel orientation to the schistosity (S) and white mica thereby defining either mylonitic foliations (C) or secondary synthetic foliations (C'). The grain size of quartz and biotite in metapelite range from fine- to coarse-grained (Fig. 4.5). Biotite rich composition, quartz rich composition, and isolated quartz lenses are generally localized throughout the Khlong Marui shear zone (Fig. 4.5). A relict of high grade metamorphic mineral fibrolitic sillimanites is present as a small block at the eastern rim of Khao Phanom.

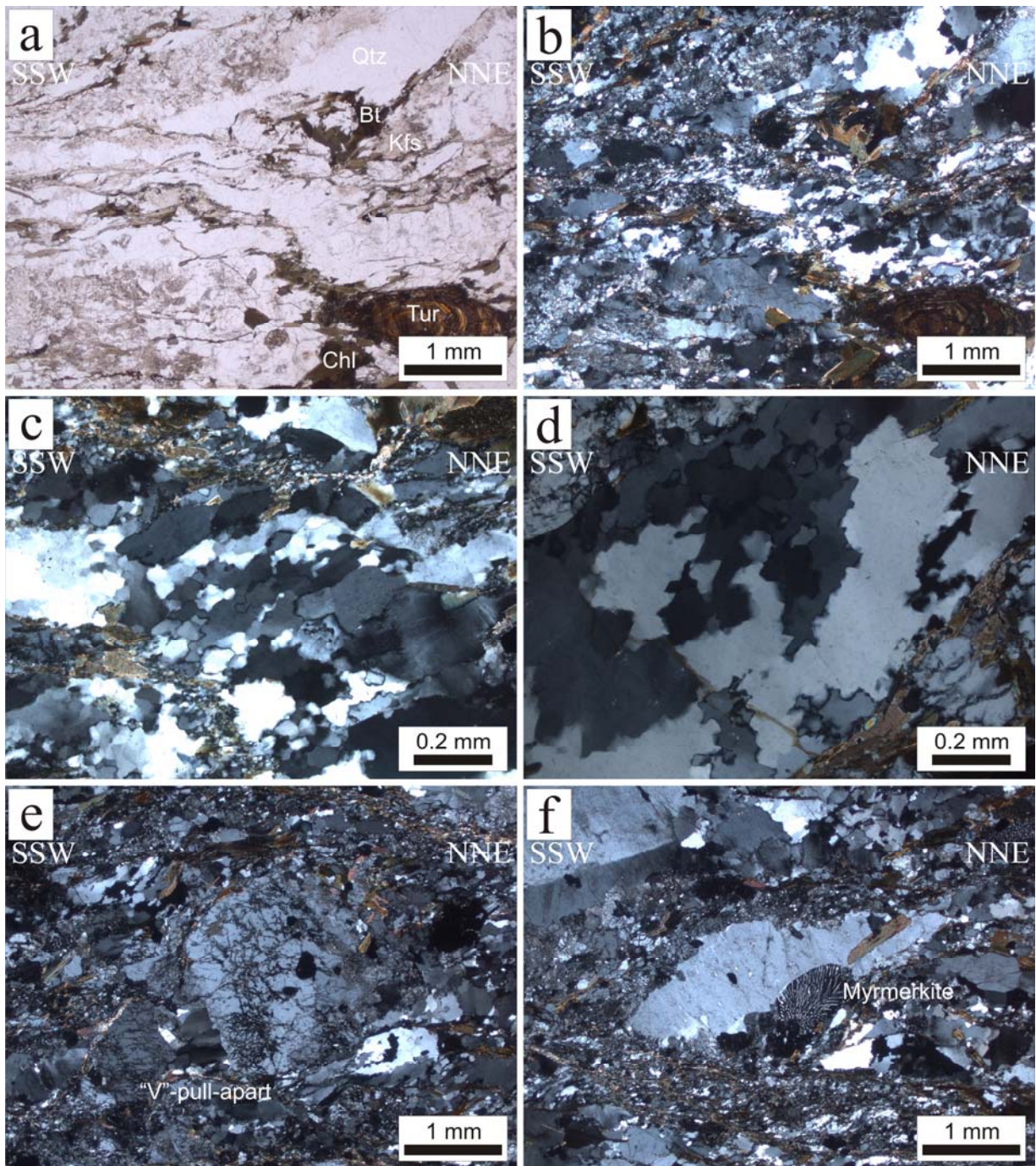


Figure 4.3 Mineral composition and mylonitic structure of granite in western area (a, b), subgrain rotation (SGR) (c), grain boundary migration (GBM) (d), “V”-pull-apart structure (e), and asymmetric myrmekite (f). (a, PPL; b-f; CPL)

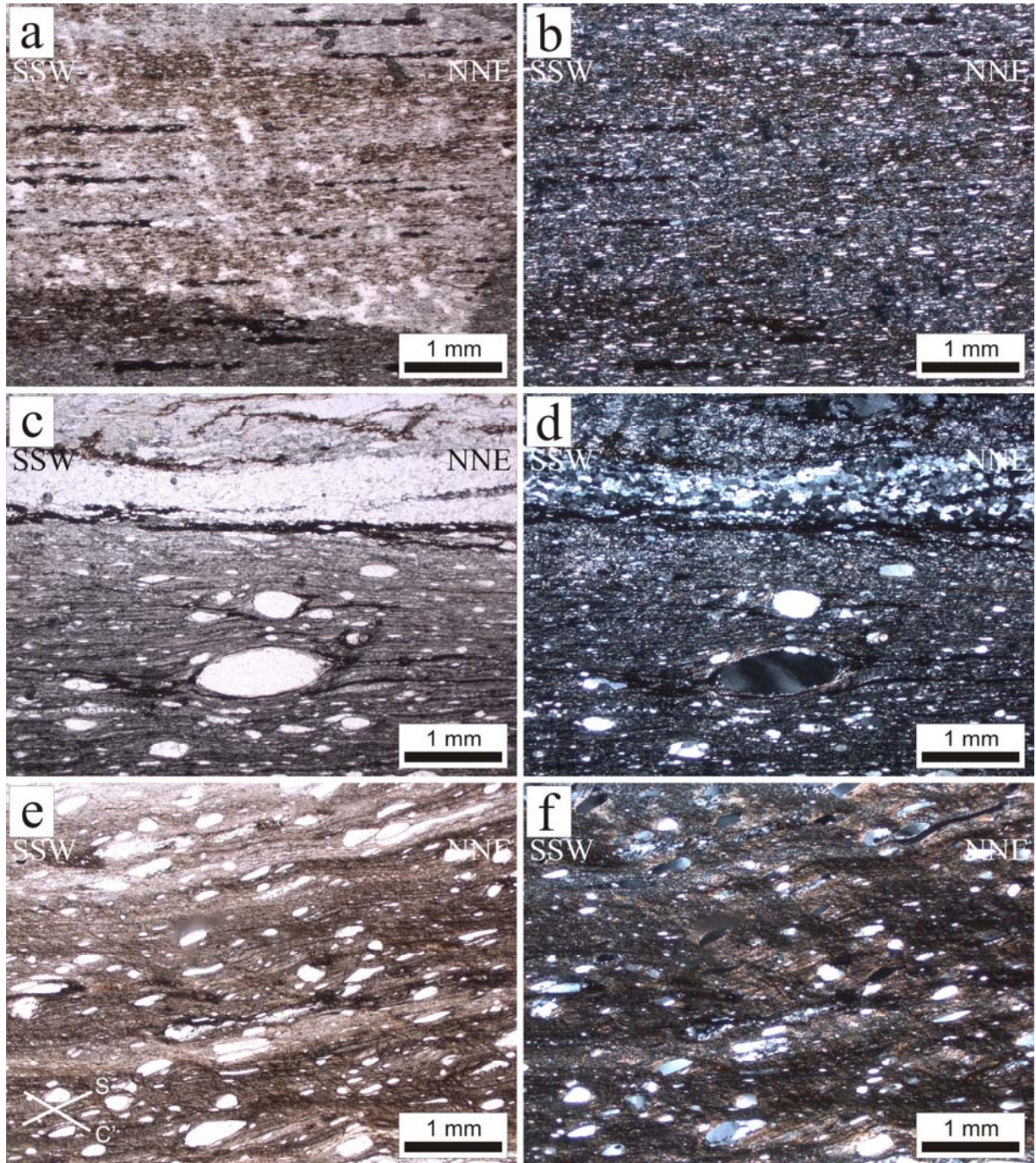


Figure 4.4 Low-grade mylonite showing fine grained quartz and mica at southeast area (a, b), pebble clasts in fined grained mica matrix at southern area (c, d), elongate quartz rods with S-C' fabric at the same outcrop (e, f). (a, c, e, PPL; b, d, f, CPL)

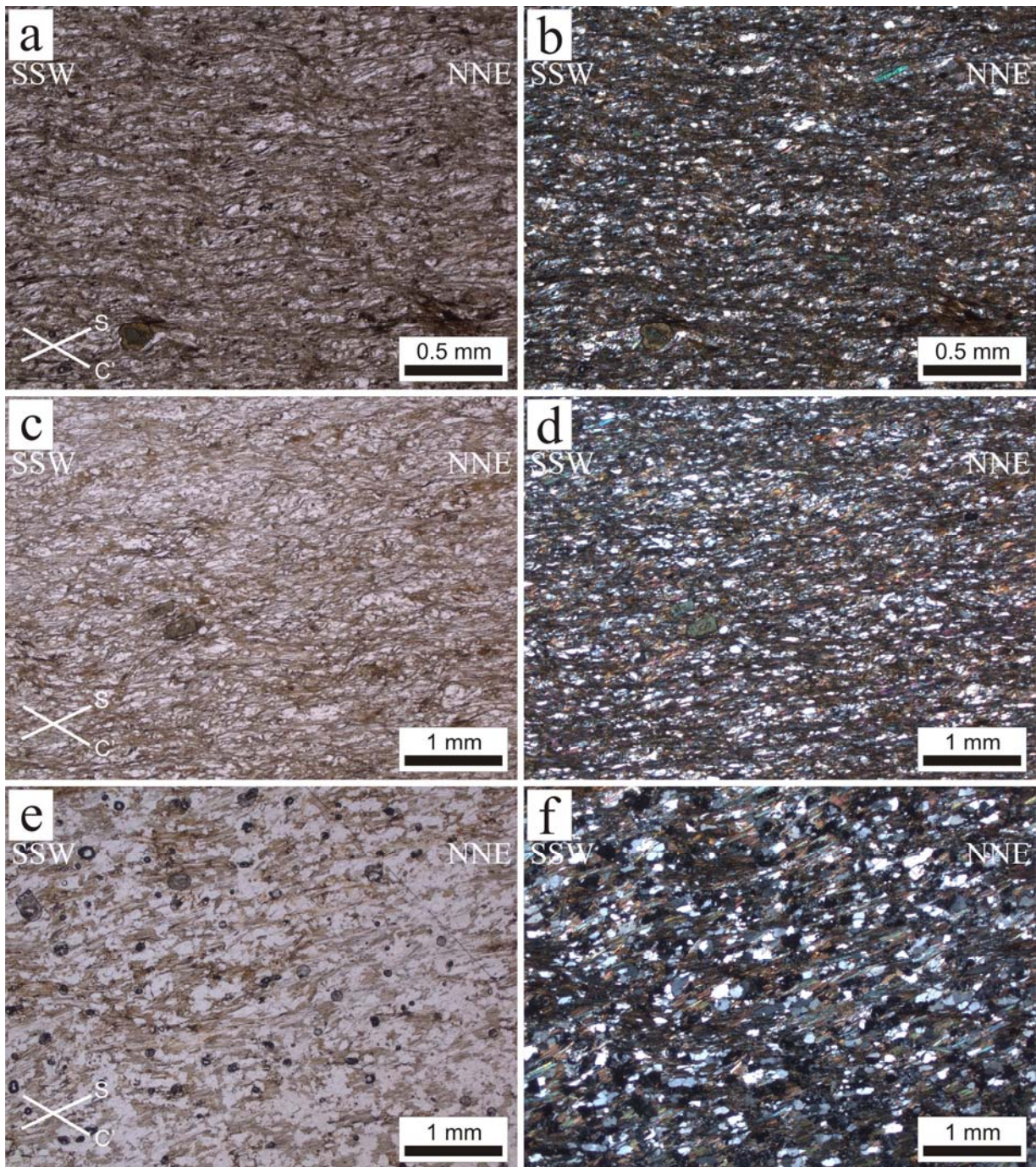


Figure 4.5 Different grain sizes of quartz and biotite in the mylonites. (a, b) Fine grained at western area; (c, d) medium grained at middle Khao Phanom; (e, f) course grained at eastern area. (a, c, e, PPL; b, d, f, CPL)

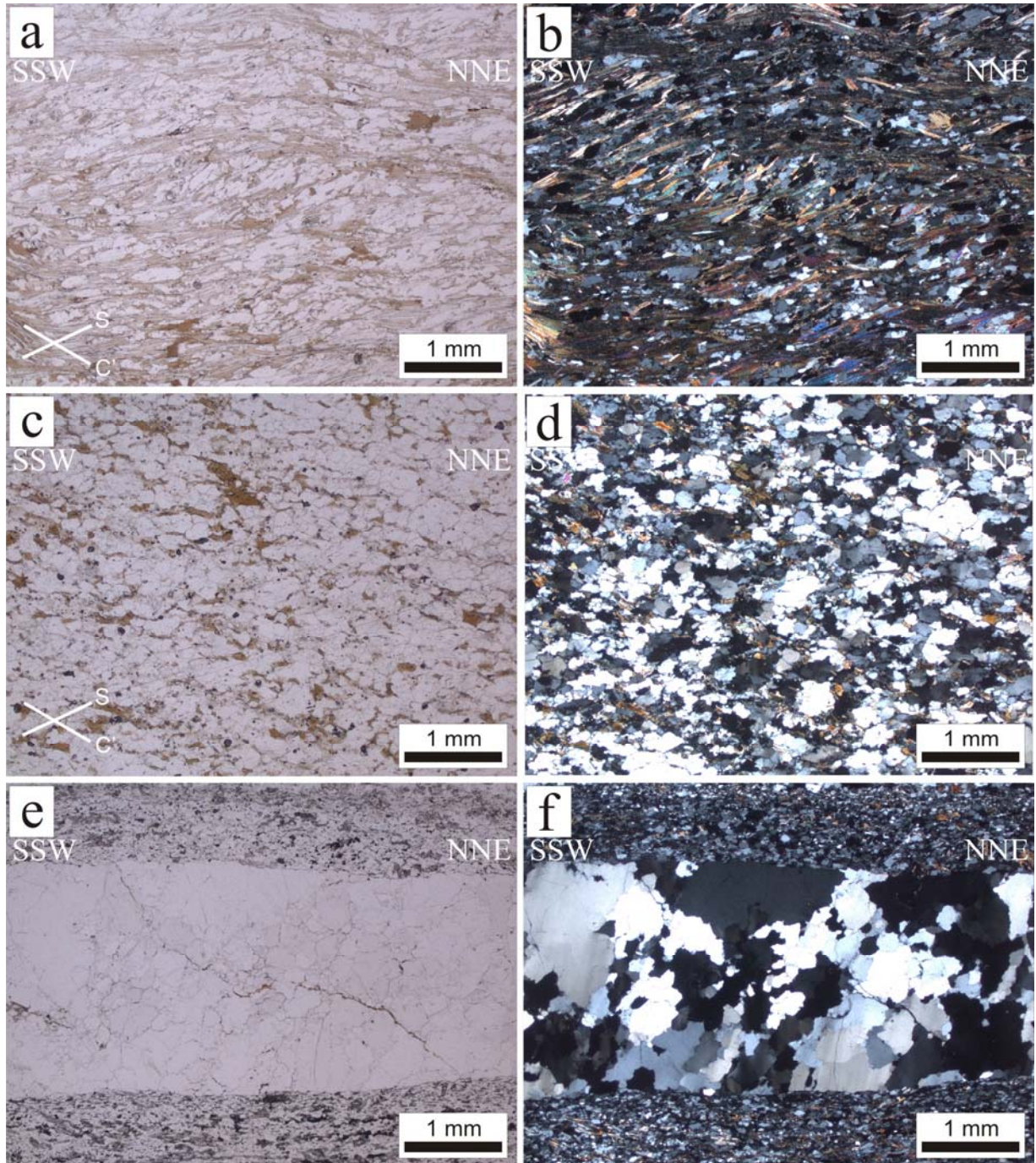


Figure 4.6 Variation of the metapelite composition. (a, b) Biotite rich in eastern area; (c, d) quartz rich in middle area; (e, f) isolated quartz lens cut through the metapelite at the Bang Tao Mae waterfall. (a, c, e, PPL; b, d, f, CPL)

Metaconglomerates comprise quartz pebble clasts with different grain sizes and sorting (Fig. 4.7). Mylonitic structures are clearly distinguished in the metaconglomerates with quartz grain recrystallisation characterized by basal gliding and bulging (BLG). The metapelite clasts comprise different rock types such as pegmatite and granitic rocks with varying composition of quartz, feldspar and amphibole, tourmaline (Fig. 4.8).

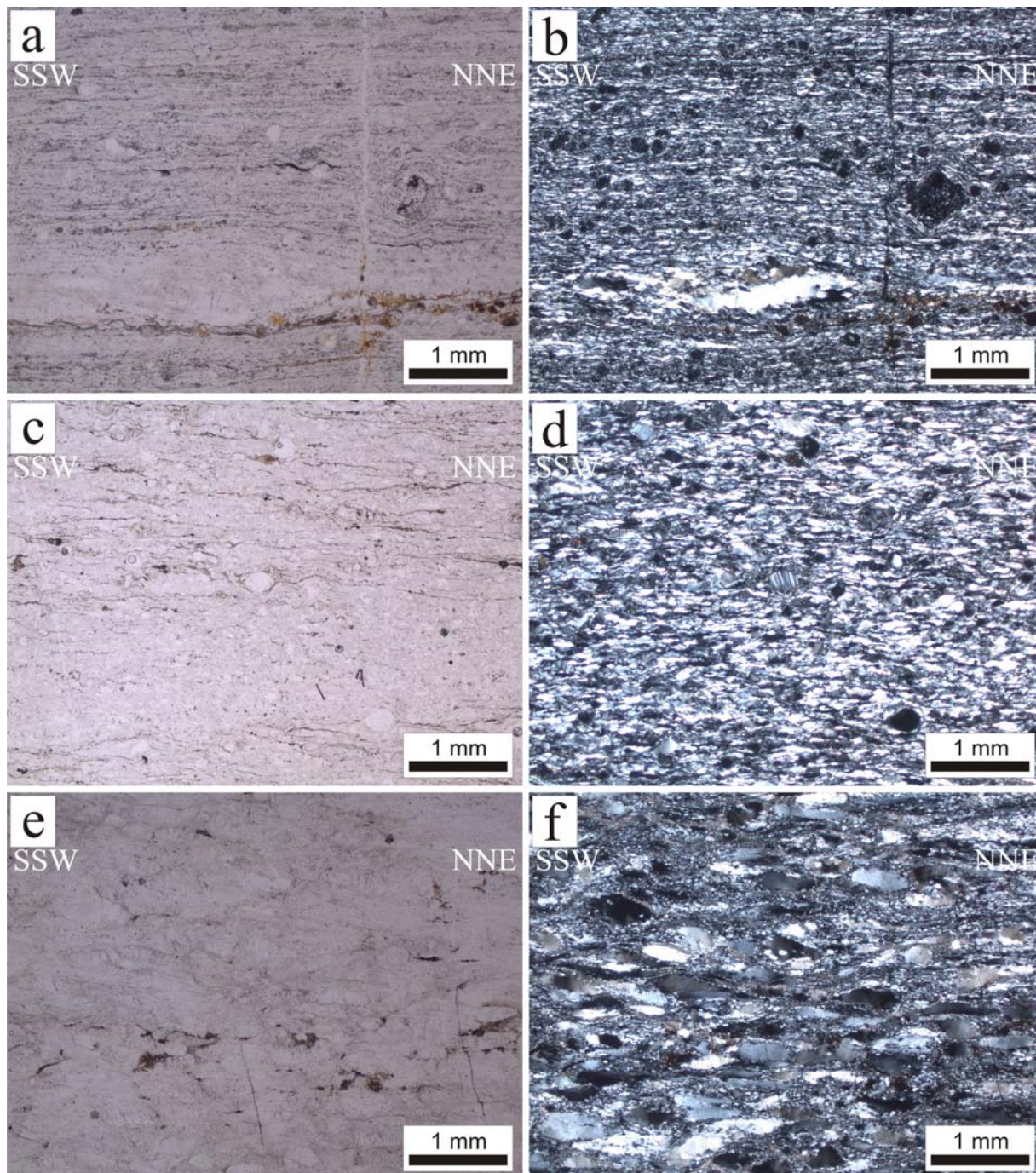


Figure 4.7 Metaconglomerates in the study area show a mylonitic structure and different sorting. (a, b) Poorly sorted metaconglomerate with fine matrix in southern area; (c, d) well sorted medium grained metaconglomerate in southwestern area; (e, f) very poorly sorted elongated grain metaconglomerate at the same outcrop. (a, c, e, PPL; b, d, f, CPL)

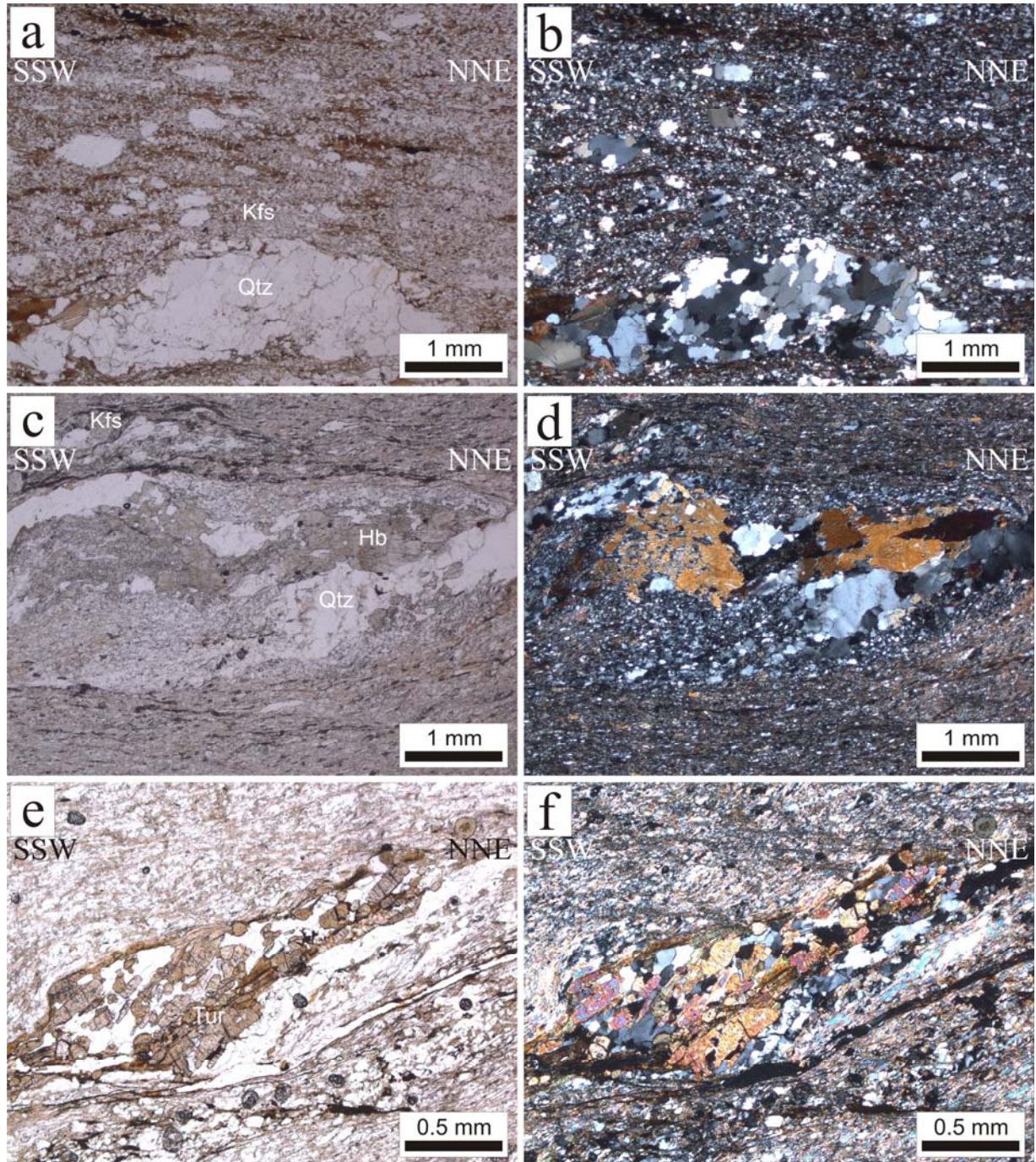


Figure 4.8 Pebbles in metapelite comprise different rock types. (a, b) Quartz and K-feldspar at the local waterfall in eastern area; (c, d) granitic rock comprises quartz, feldspar and amphibole at northeastern Khao Phanom; (e, f) tourmaline rich granitic rock in western area. (a, c, e, PPL; b, d, f, CPL)

Kinematic indicators clearly reflect a ductile dextral sense of shear in the study area. Quartz and feldspar porphyroclasts are usually deformed into fish, sigmoids, and σ -types in mylonitic metasedimentary rocks (Fig. 4.19, 4.10). Dextral mica fish in metapelites is illustrated by lenticular shapes with different aspect ratios and usually form as an aggregate in the metapelite (Fig. 4.11). Sinistral shear bands are present together with domino type-fragments of porphyroclast and shear bands of fibrolitic sillimanite (Fig. 4.12). Small-scale faults cutting through the matrix can be observed in the metapelite (Fig. 4.13a-b). Domino boudins can be found in metapelites and quartz lenses (Fig. 4.13c-f).

Quarter structures in mylonitic metasedimentary rock include quarter mats and asymmetric myrmekite (Fig. 4.14). Quarter mats were formed by preferential removal of quartz by solution transfer at stress concentration sites adjacent to porphyroclasts (Passchier and Trouw, 1996). Asymmetric myrmekite was formed by preferential K-feldspar breakdown via reaction and associated volume loss at sites of high differential stress (Simpson and Wintsch, 1989). The arrangement of quartz lamellae in myrmekite may also show an internal monoclinic symmetry which can serve as an independent, internal shear sense indicator (Simpson and Wintsch, 1989).

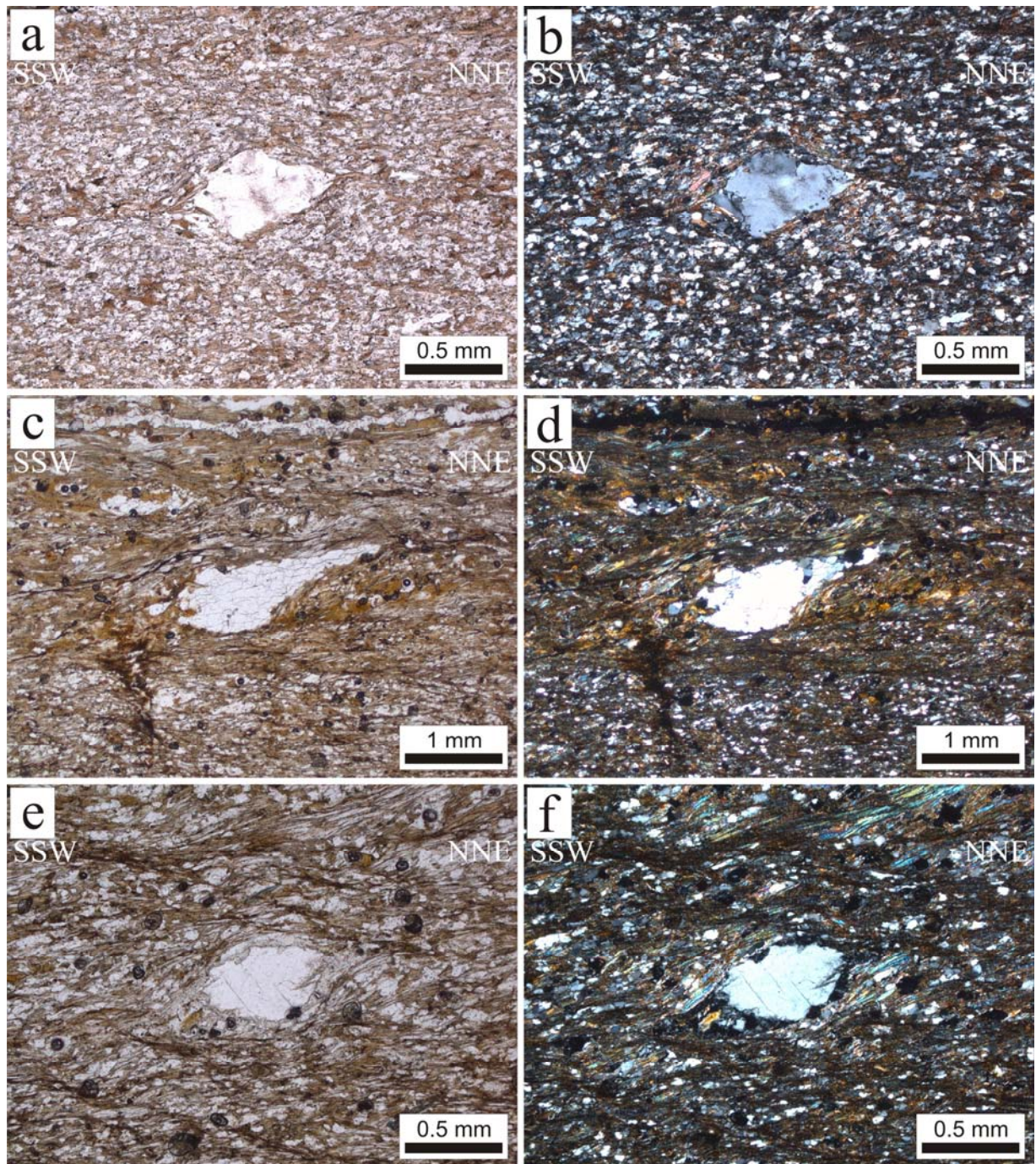


Figure 4.9 Porphyroclast in metapelite at the middle area of Khao Phanom showing dextral shear. (a, b) Rhomboidal fish; (c, d) quartz sigmoid; (e, f) σ -type K-feldspar porphyroclast. (a, c, e, PPL; b, d, f, CPL)

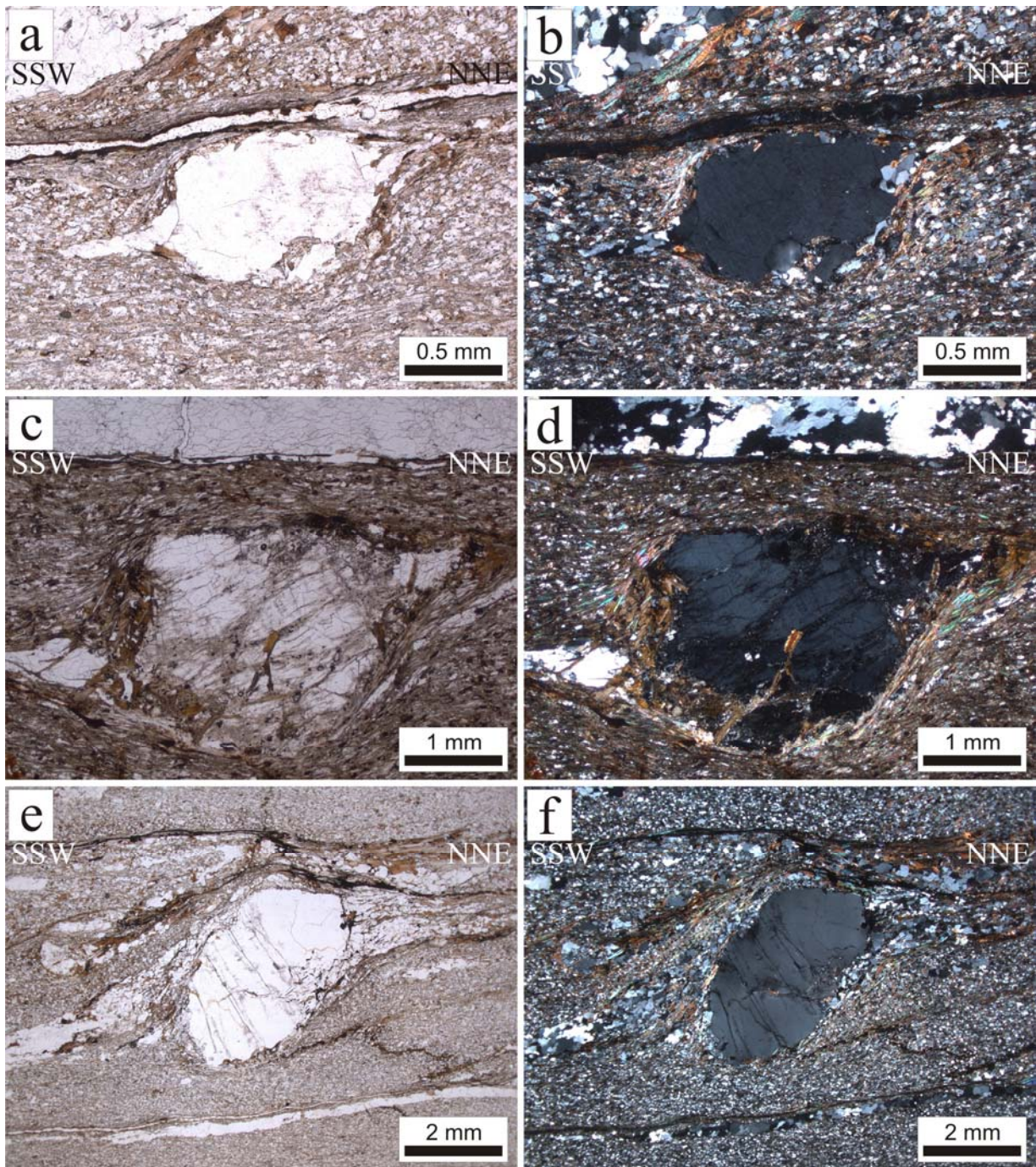


Figure 4.10 σ -type K-feldspar porphyroblast with stair-stepping in mylonitic metasedimentary rocks. (a, b) Small K-feldspar clast in middle area; (c, d) synthetic fracture forming in K-feldspar clast at northern area; (e, f) antithetic fracture forming in K-feldspar clast at middle area. (a, c, e, PPL; b, d, f, CPL)

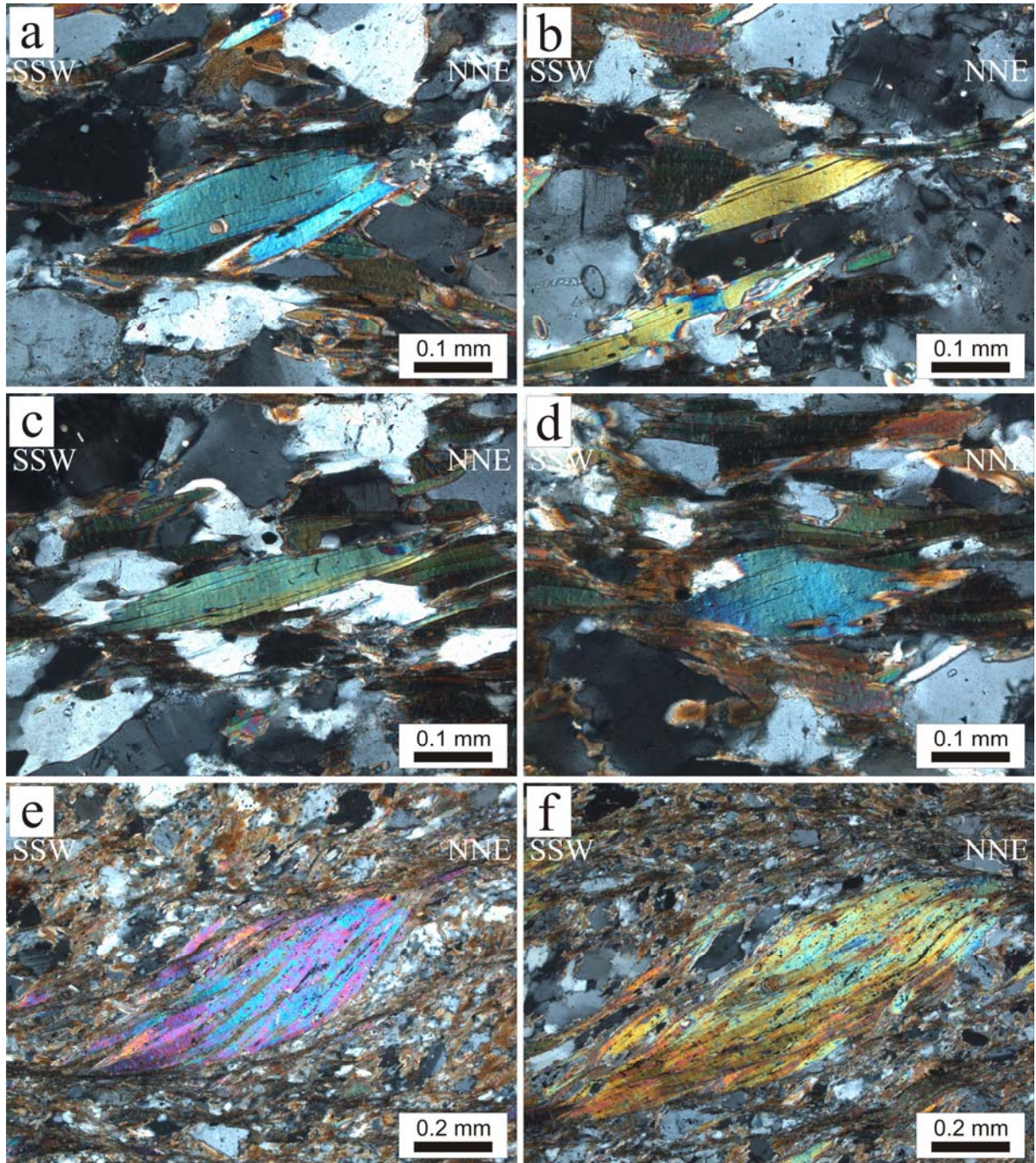


Figure 4.11 Different types of dextral mica fish. (a) Lenticular mica fish at the Bang Tao Mae waterfall; (b) half-lenticular fish at the same outcrop; (c) fish with high aspect ratio at the same outcrop; (d) fish with small aspect ratio at the same outcrop; (e) aggregate of mica fish in lenticular shape at middle area; and (f) aggregate of mica fish forming in high aspect ratio at the same outcrop. CPL

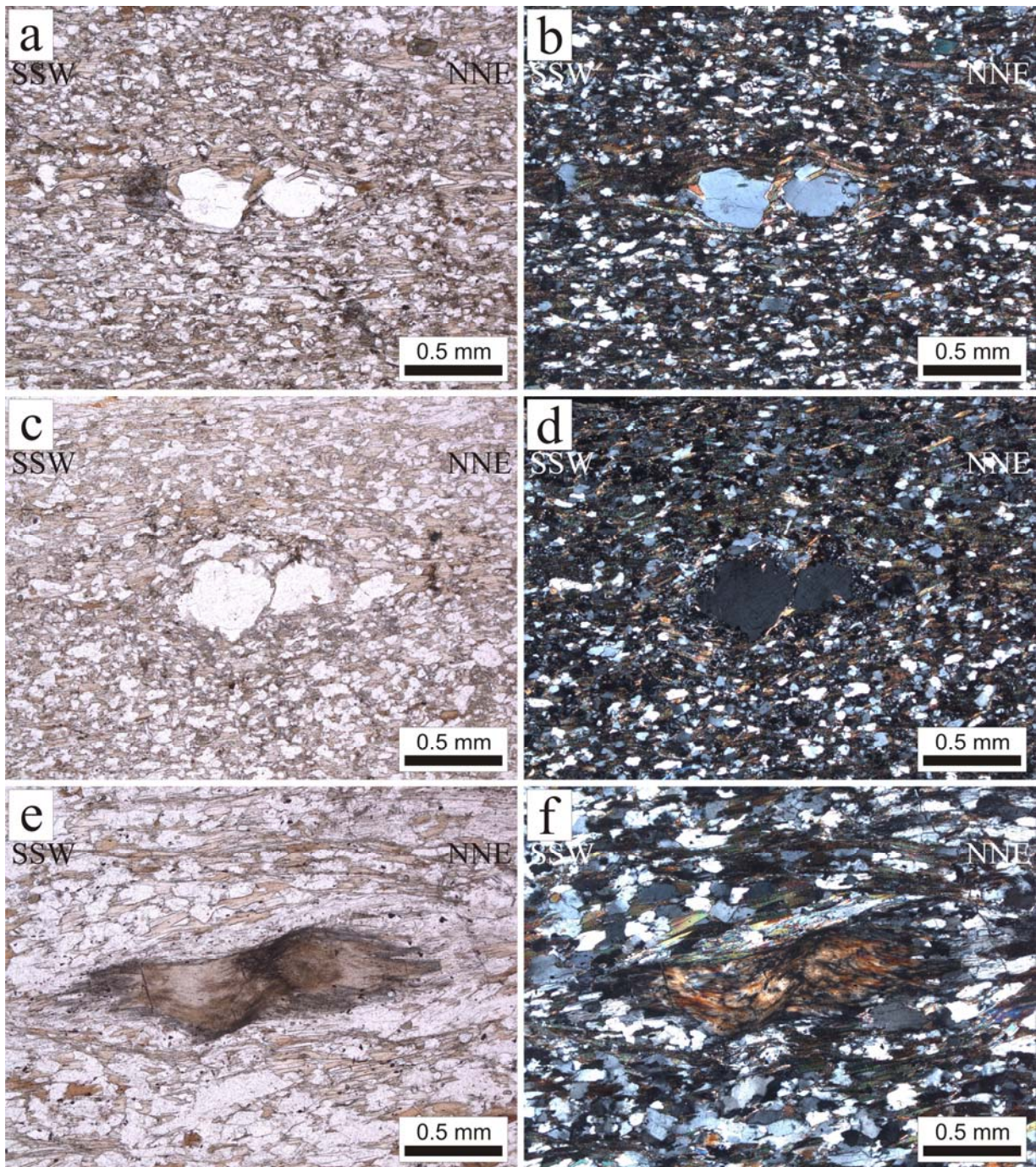


Figure 4.12 Sinistral shear bands in different minerals. Domino type-fragmented quartz (a) and K-feldspar in northern Khao Phanom (b). Shear band in fibrolitic sillimanite at the Bang Tao Mae waterfall (c). (a, c, e, PPL; b, d, f, CPL)

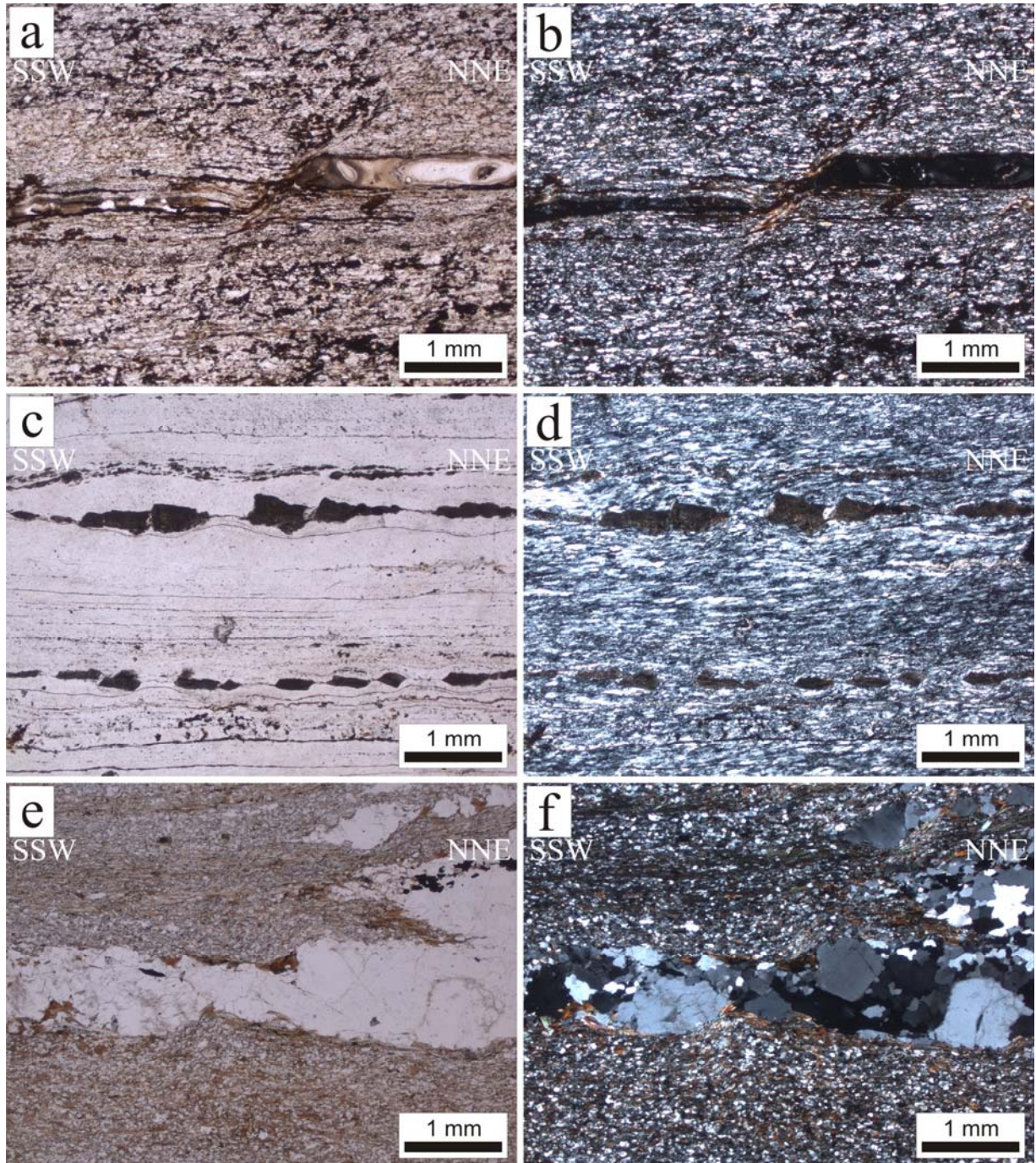


Figure 4.13 Small-scale fault cuts through the matrix at southern area (a, b). Domino boudins in mepelite (c, d) and quartz lenses in western area (e, f). (a, c, e, PPL; b, d, f, CPL)

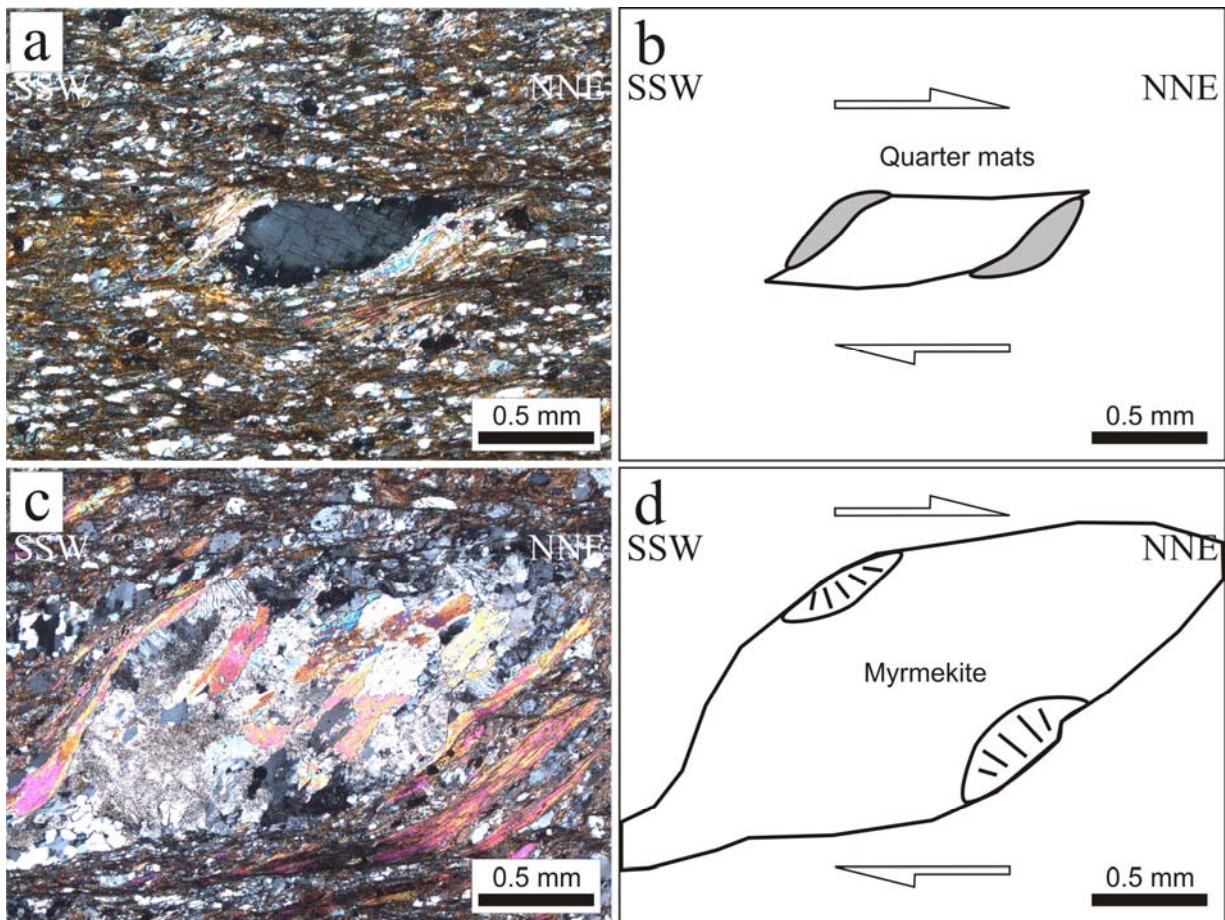


Figure 4.14 Quarter structures in mylonitic metasedimentary rock. Quarter mats at middle area (a, b) and asymmetric myrmekite at northern area (c, d). (a, c, CPL)

Quartzite in the Khlong Marui shear zone has different grain sizes ranging from fine to coarse grained (Fig. 4.15). The intercalation of coarse and fine grained layers is present in some locations (Fig. 4.16a-b). Quartz lenses normally cut through quartzite (Fig. 4.16c-d). Grain shape preferred orientation (GSPO) associated with basal gliding, bulging (BLG), subgrain rotation (SGR) and grain boundary migration (GBM) can be observed in quartzite. Mica and K-feldspar can be found as impurities in quartzite composition (Fig. 4.16e-f).

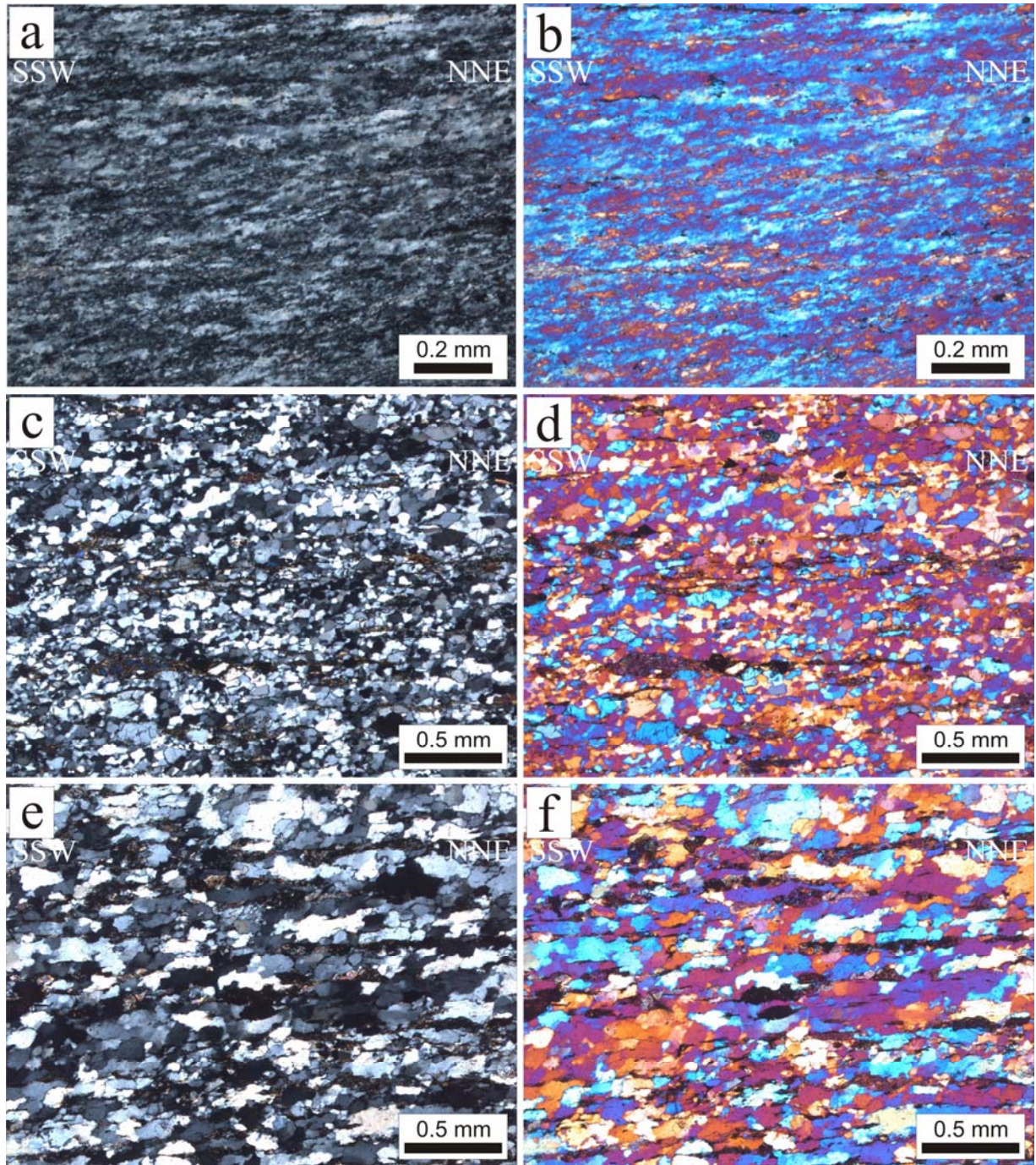


Figure 4.15 Quartzite with a varying grain size, from fine grained at western area (a, b), medium grained in northern area (c, d), to coarse grained at western area (e, f). (a, c, e, CPL; b, d, f, Gypsum plate inserted)

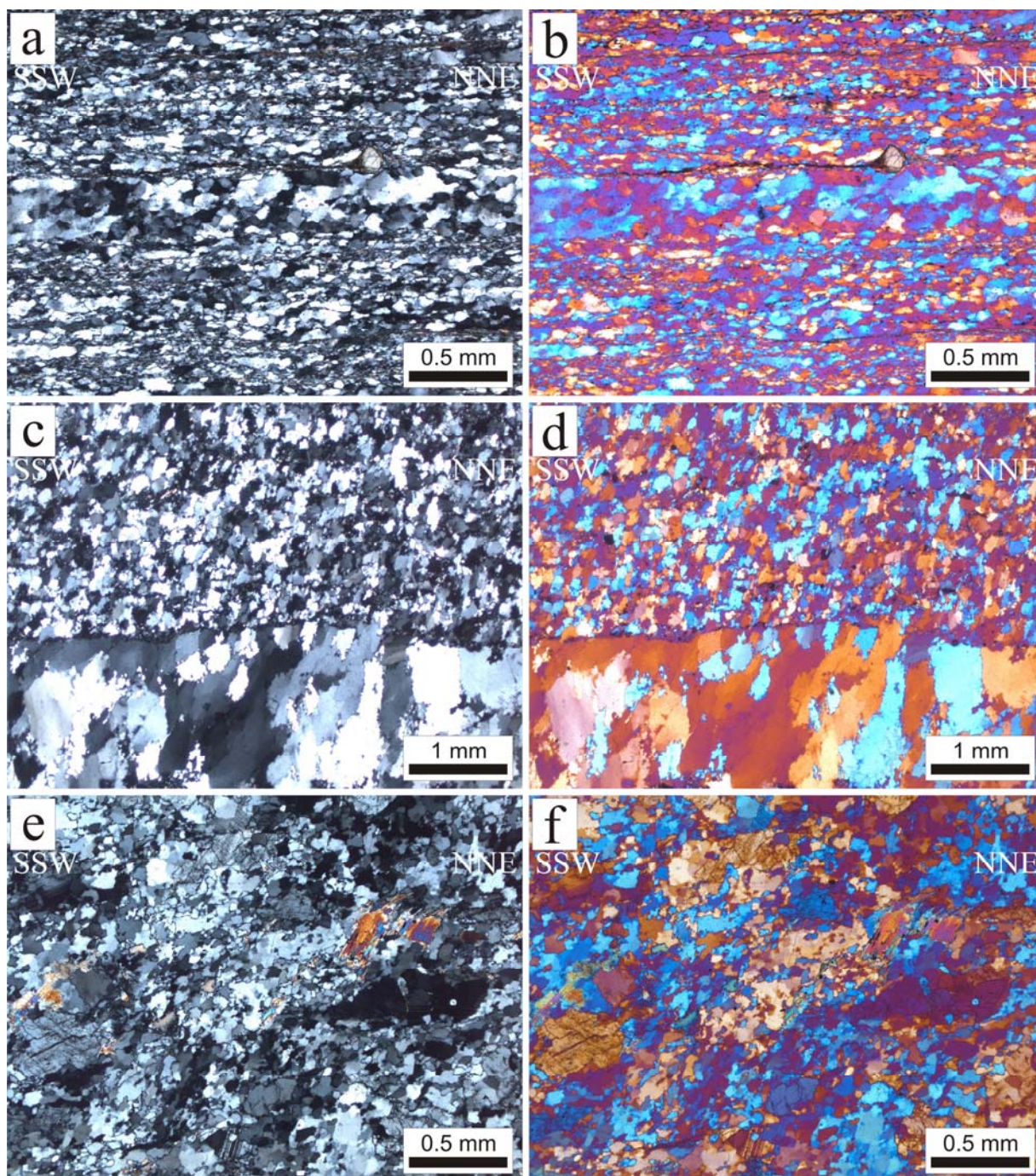


Figure 4.16 Variation of quartz grain size and composition. (a, b) Intercalated coarse and fine grained layers at western area; (c, d) quartz lens cuts through quartzite in eastern area; (e, f) accessory minerals of mica and K-feldspar in quartzite composition at the same outcrop. (a, c, e, CPL; b, d, f, Gypsum plate inserted)

Dynamic recrystallisation that is normally observed in thin-sections from the rocks of the study area ranges from low to medium temperature. Low-grade metamorphism represented by high elongated grains, undulose extinction, basal gliding, and bulging (BLG) (Fig. 4.17a-d). Subgrain rotation (SGR) indicating the medium temperature is clear in quartzite (Fig. 4.17e). The high

temperature grain boundary migration (GBM) can be found in orthogneiss, mylonitic granite, and quartzite (Fig. 4.17f).

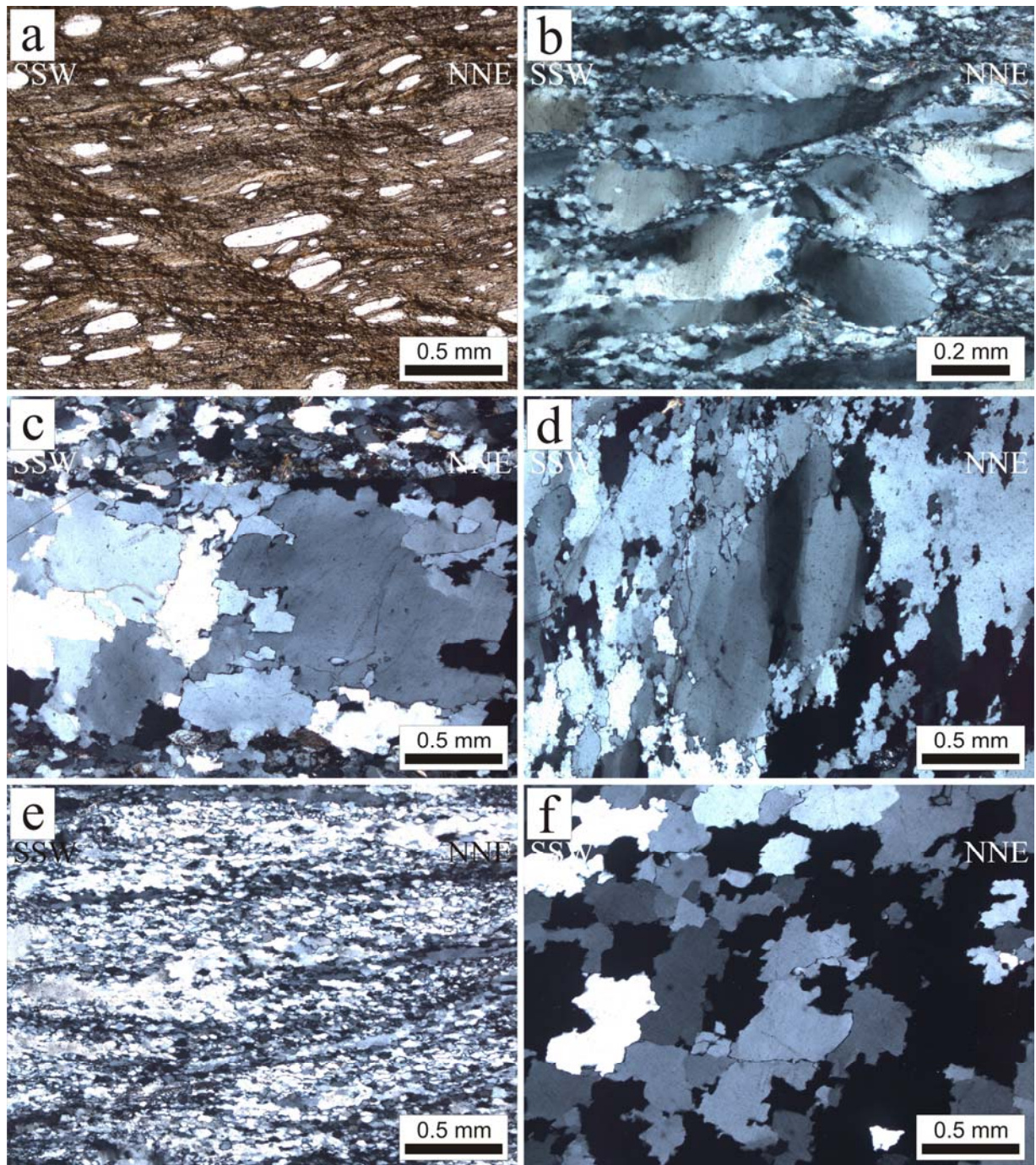


Figure 4.17 Dynamic recrystallisation in the rocks of the Khlong Marui shear zone. (a) Highly elongated grain in southern area; (b) undulose extinction of monocrystalline quartz pebbles with basal gliding at southwestern area; (c) bulging (BLG) at western area; (d) undulose extinction and bulging (BLG) at the same outcrop; (e) subgrain rotation (SGR) in southwestern area; and (f) grain boundary migration (GBM) in western area. (a, PPL; b-f, CPL)

Pegmatitic rocks

Pegmatite mainly comprises coarse grained quartz, K-feldspar, and plagioclase. White mica, tourmaline and garnet and shows foliation and lineation locally (Fig. 4.18). Tourmalines which formed as a black layer in the outcrop are fine grained under microscope (Fig. 4.19a-b). The contact zone between pegmatitic rock and the metapelite country rock is clearly distinguished by the different orientations of mica (Fig. 4.19c-d).

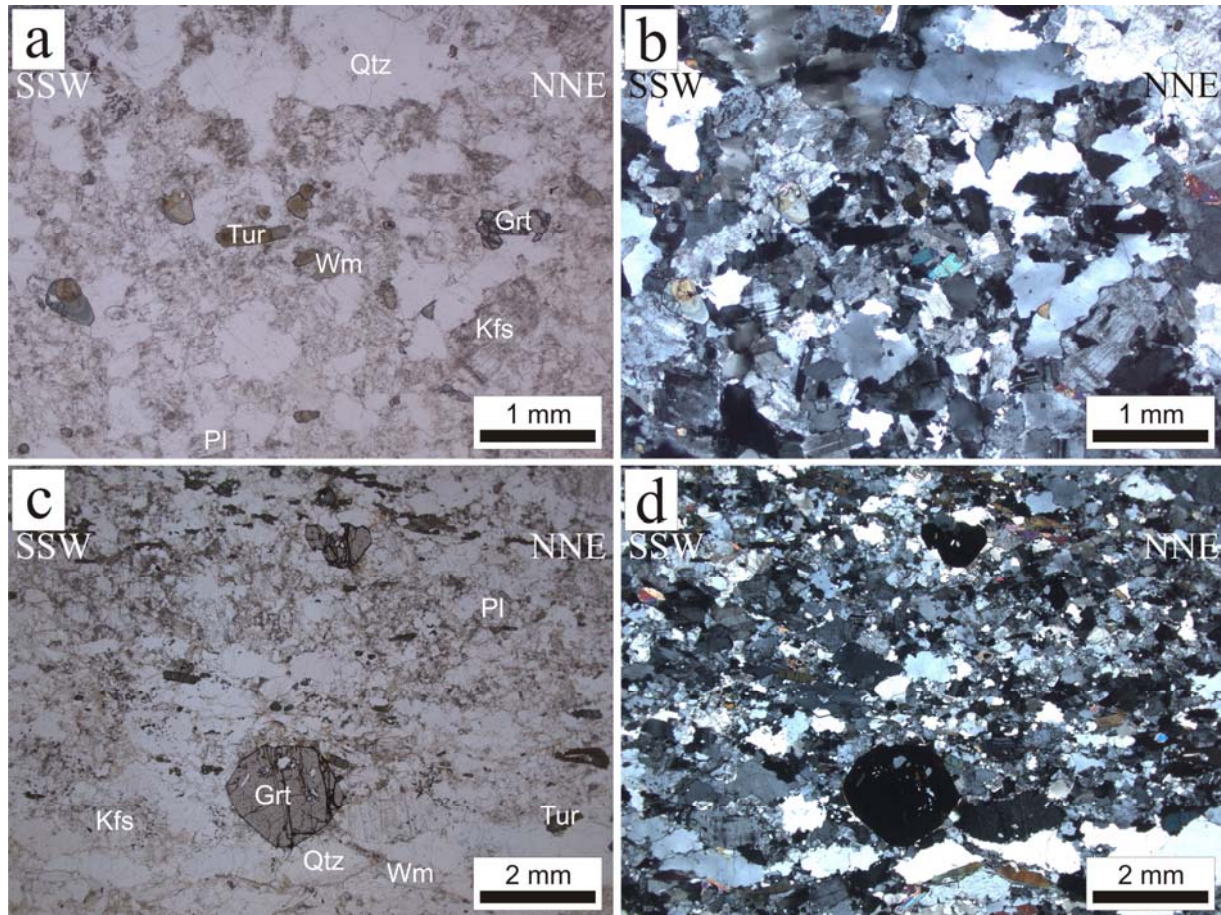


Figure 4.18 Pegmatitic rocks at eastern area show equigranular grains of quartz, feldspar, white mica, and tourmaline (a). Minerals forming lineations are present in garnet pegmatites (b). (a, c, PPL; b, d, CPL)

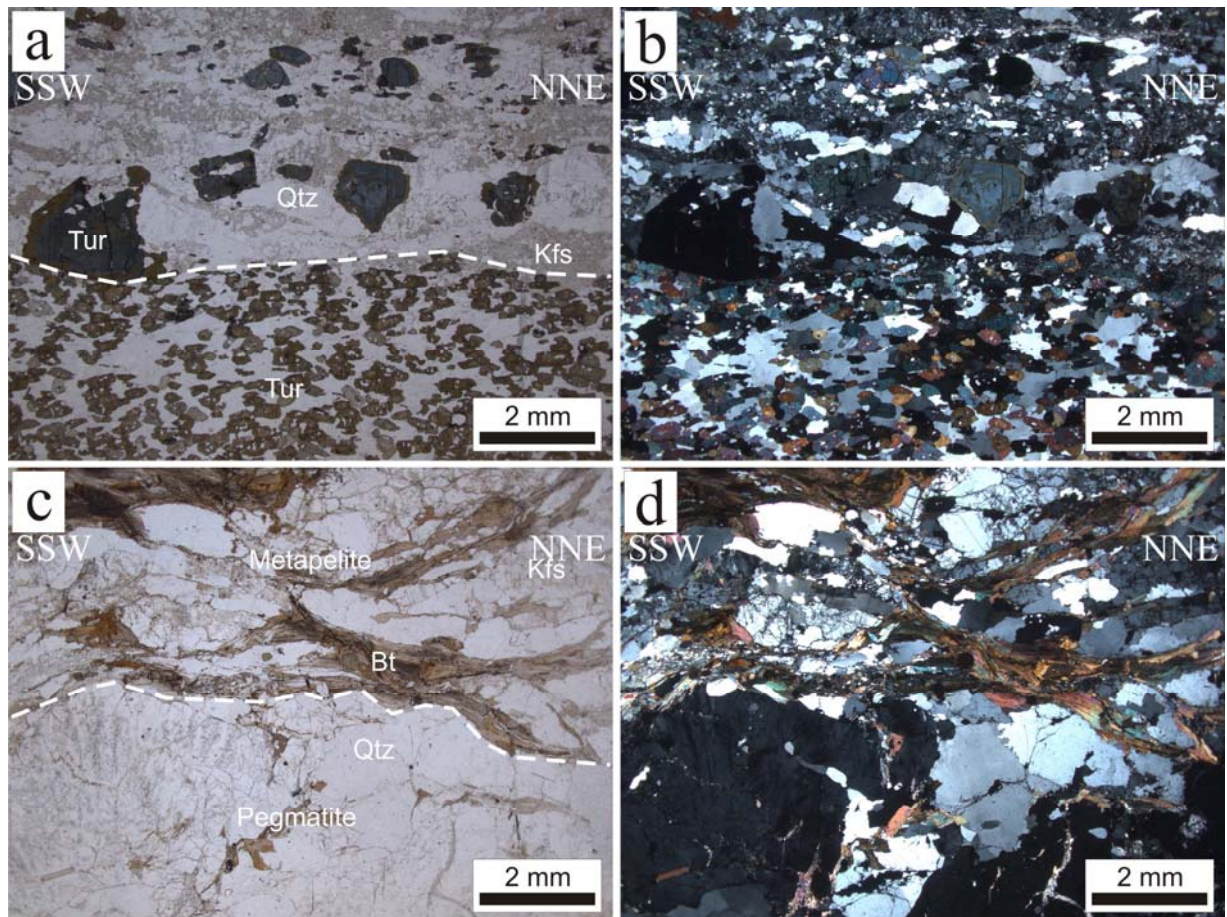


Figure 4.19 Fine grained tourmalines at eastern area are formed as a layer at the pegmatite rims (a, b). Contact zone between pegmatitic rock and the metapelite country rock at eastern Khao Phanom (c, d). (a, c, PPL; b, d, CPL)

Cataclasites

Cataclasites in the study area ranges from proto-cataclasite to cataclasite. Clasts and matrix of metapelite and quartzite have been crushed and broke apart by repeated fault movements thereby producing the fault rocks. Angular fragments with pressure solution are commonly associated with the cataclasites (Fig. 4.20a-d). The contact between the fault rock and the intact country wall rock shows high deformation intensity by way of fine-grained cataclasite development (Fig. 4.20e-f).

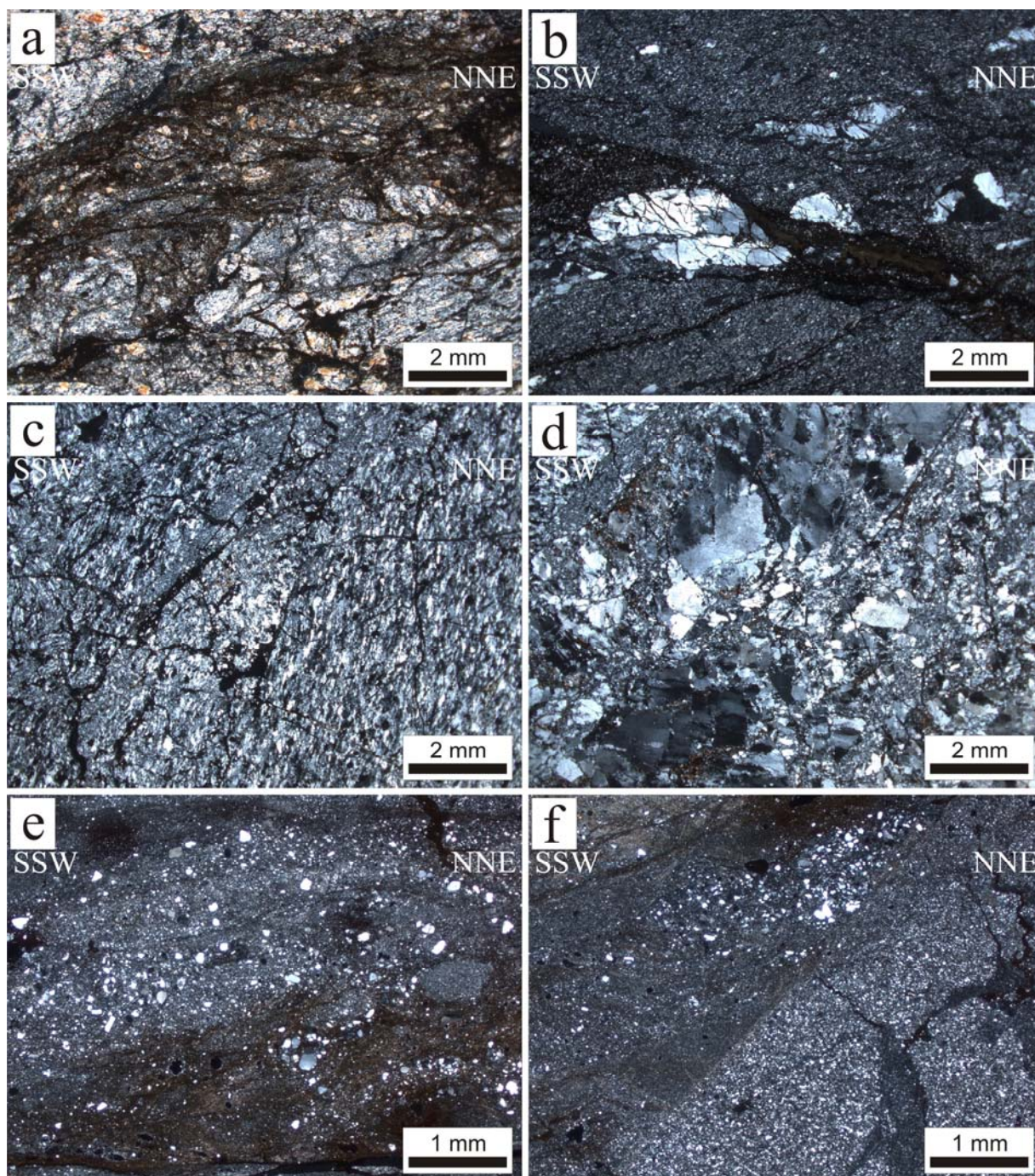


Figure 4.20 Cataclasites of quartzite (a), metapelite (b), metaconglomerate (c, d). Fine-grained cataclasites at the contact zone between the fault rock and the intact country wall rock (e, f). CPL

4.3 Quartz Textures

Kinematics of flow can be determined by well-developed *c*-axis fabrics in naturally deformed quartzites (Fritz et al., 1996; Grasemann et al., 1999; Lister and Hobbs, 1980; Schmid and Casey, 1986; Wallis, 1992, 1995; Xypolias, 2009). Eight samples of quartzite from WNE to ENE from throughout the Khlong Marui shear zone were analyzed for quartz textures in order to understand the flow parameters.

Physical spaces of the transpression and transtension regimes are applied to determine the angle between eigen vector for the mean vorticity number (W_m) calculation (Xypolias, 2009) (Fig. 4.21a, b). They show the relative orientation of eigen vector (a_1 and a_2), instantaneous flow elements (ISA_1 and ISA_2), and their angular relationship. The angle between the instantaneous stretching axis (ISA_1) and the foliation is represented by the summation of δ and β (Xypolias, 2009). The transtension physical space is used in cases where the δ and β summation is more than 45° . The δ and β angles are defined by two assumptions as follow;

(1) δ angle

The long axis of quartz within an oblique grain shape foliation is parallel to the instantaneous stretching axis (ISA_1) (Wallis, 1995). The oblique foliation (S_B) has a fixed orientation with respect to the external kinematic frame (A_1) during progressive non-coaxial shearing (Herwegh and Handy, 1998; Herwegh et al., 1997; Ree, 1991). Therefore, the angle, δ , between the oblique grain shape fabric (S_B) and the main foliation (S_A) is equal to the angle between the ISA_1 and the largest principal axis of the finite strain (Fig. 4.21c).

(2) β angle

The central girdle segment of quartz *c*-axis fabrics develops orthogonal to the flow plane under progressive simple, pure, and general shear (Law et al., 1990; Lister and Hobbs, 1980; Platt and Behrmann, 1986; Vissers, 1989; Wallis, 1992). From this assumption, the angle (β) between the perpendicular to the central girdle segment of quartz *c*-axis fabric (S_A) and the main foliation is equal to the angle between the flow plane (A_1) and the flattening plane of finite strain (Fig. 4.21d).

The cosine of the θ angle between the two eigen vector gives the mean vorticity number (W_m) in two-dimensional flow (Bobyarchick, 1986; Passchier, 1986; Wallis, 1995). If both angles and are known then an estimate of vorticity number (W_m) can be obtained using the equation:

$$\cos \theta = W_m \quad (1)$$

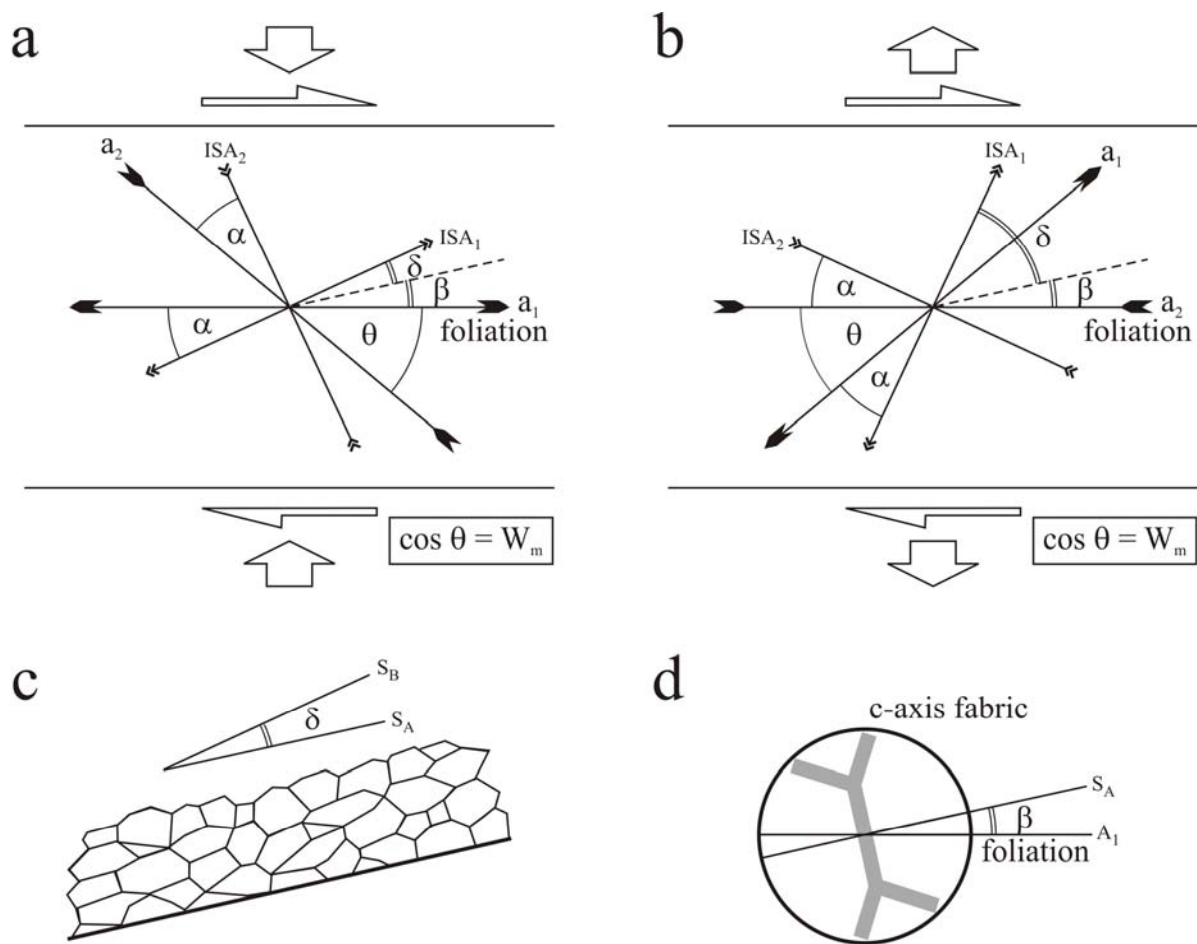


Figure 4.21 Sketch showing the relative orientation of eigen vector (a_1 and a_2), instantaneous flow elements (ISA_1 and ISA_2), and their angular relationship in (a) transpression physical space and (b) transtension physical space. (c) The angle, δ , between the oblique grain shape fabric and the main foliation. (d) The angle, β , between the perpendicular to the central girdle segment of quartz c -axis fabric and the main foliation.

Dynamic recrystallisation of quartz forms well developed grain shape preferred orientation (GSPO) and optic axis lattice preferred orientation (LPO) patterns. The thin-sections of quartzite were measured under microscope for the angle between the oblique grain shape fabric and the main foliation (δ) (Fig. 4.22, 4.23). The δ angles of quartzite in the Khlong Marui shear zone are between 19° and 57°.

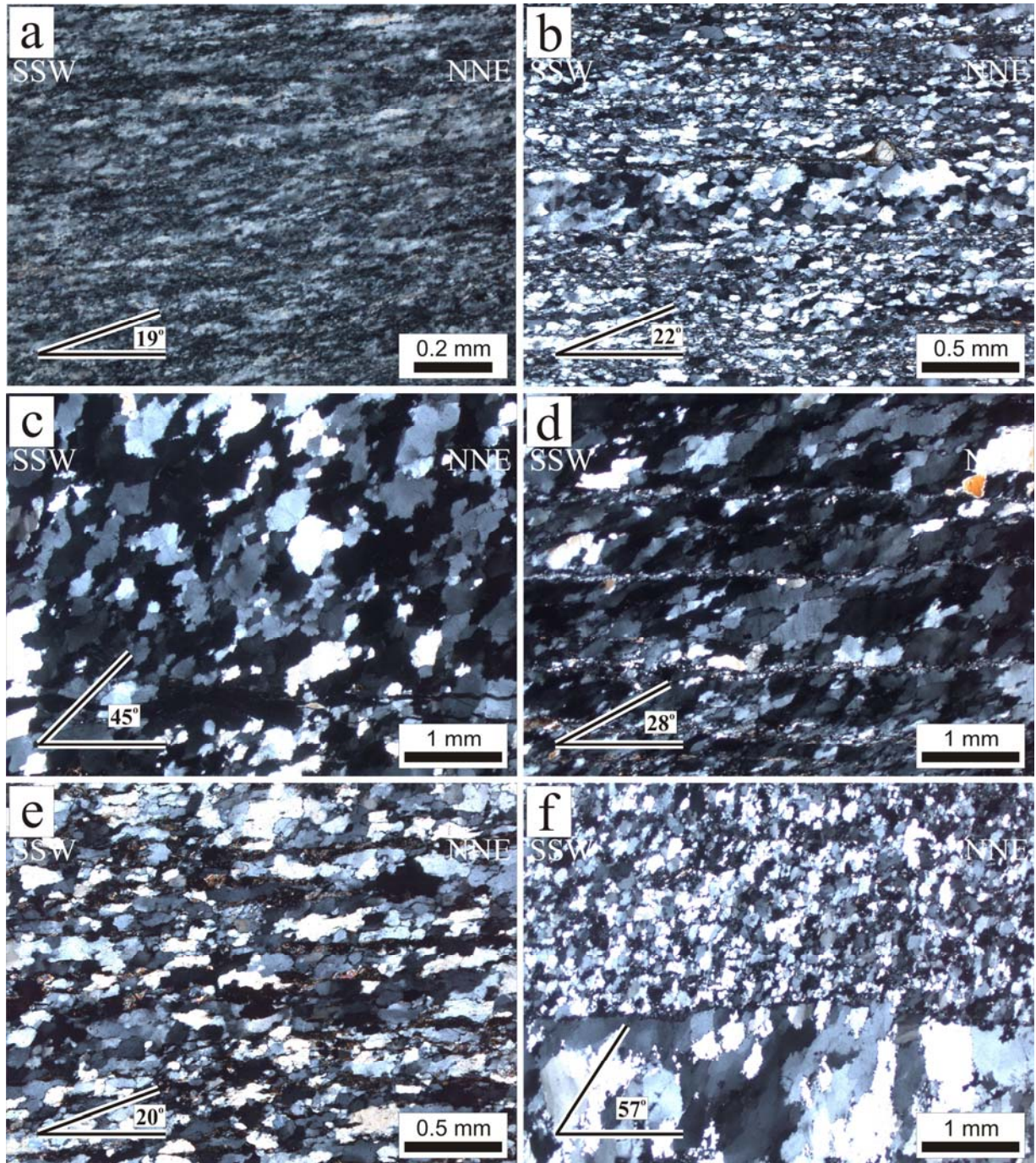


Figure 4.22 Angle between the oblique grain shape fabric and the main foliation under crossed polarized light of the sample 3A1 (a), 22C3 (b), 1E2 (c), 88A2 (d), 1D1 (e), and 14C1 (f).

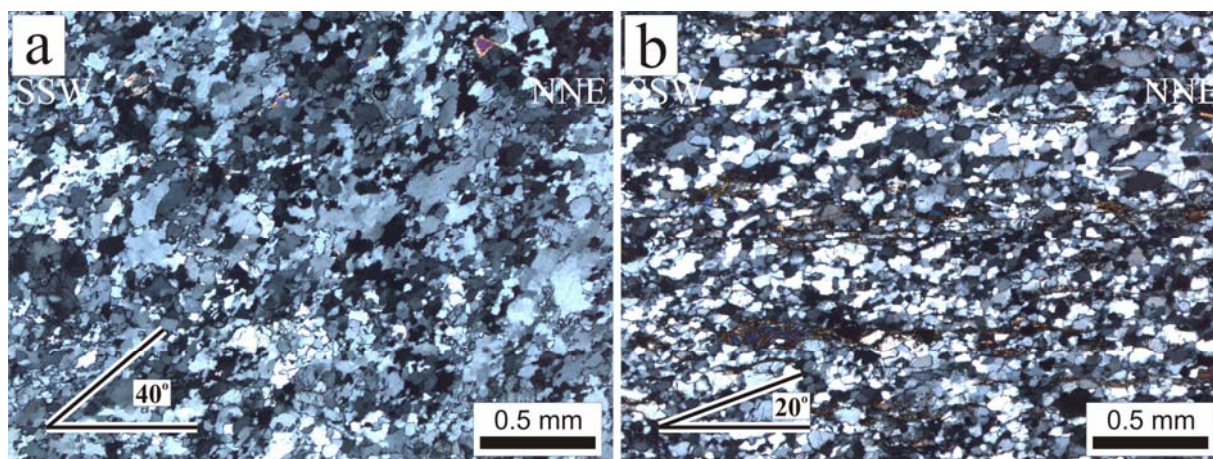


Figure 4.23 Angle between the oblique grain shape fabric and the main foliation under cross polarized light for samples 14B1 (a) and 26D1 (b).

The specimens were cut to a rock chip size of between 10x6x2 mm and 20x10x7 mm and polished for optic axis measurement. They were measured by an x-ray texture goniometer in reflection mode (wavelength $\text{CuK}\alpha=1.5418$, beam current=40 kV and 30 mA). Lattice planes of $\langle 100 \rangle$, $\langle 110 \rangle$, $\langle 102 \rangle$, $\langle 200 \rangle$, $\langle 201 \rangle$, $\langle 112 \rangle$, $\langle 211 \rangle$, $\langle 113 \rangle$ have been measured at angle between 0° (center) and 80° (periphery) at the University of Graz by Prof. Dr. Harald Fritz. Fourier analyses were applied for correction of defocusing effects. Lattice planes $\langle 001 \rangle$, $\langle 100 \rangle$ and $\langle 110 \rangle$ were calculated by the harmonic method of Roe (1965) and Bunge (1969). Detailed description of the technical procedure can be seen in Wenk (1985).

The lattice preferred orientation pattern is displayed in pole figures of $\langle 001 \rangle$, $\langle 100 \rangle$, and $\langle 110 \rangle$ axes (Fig. 4.24). The maximum extension direction X is oriented NNE-SSW parallel to the main foliation, Y is the intermediate, and Z is WNW-ESE in the fabric diagrams. Most samples developed oblique girdle segments with respect to the foliation plane. The optic axis lattice preferred orientation patterns show dextral shear sense across the range of low to high temperature. At distance 1300-1400 m towards fault core from the west of the Khlong Marui shear zone, the maxima at the center of quartz texture sample 1E2 and 88A2 gives the high temperature deformation. Quartz texture of the samples 14C1 and 14B1 at distance 3800-4000 m suggests that the high temperature is overprinted by low temperature deformation. The angle between the perpendicular to the central girdle segment of quartz axis fabric and main foliation (β) is determined for all the quartzite samples.

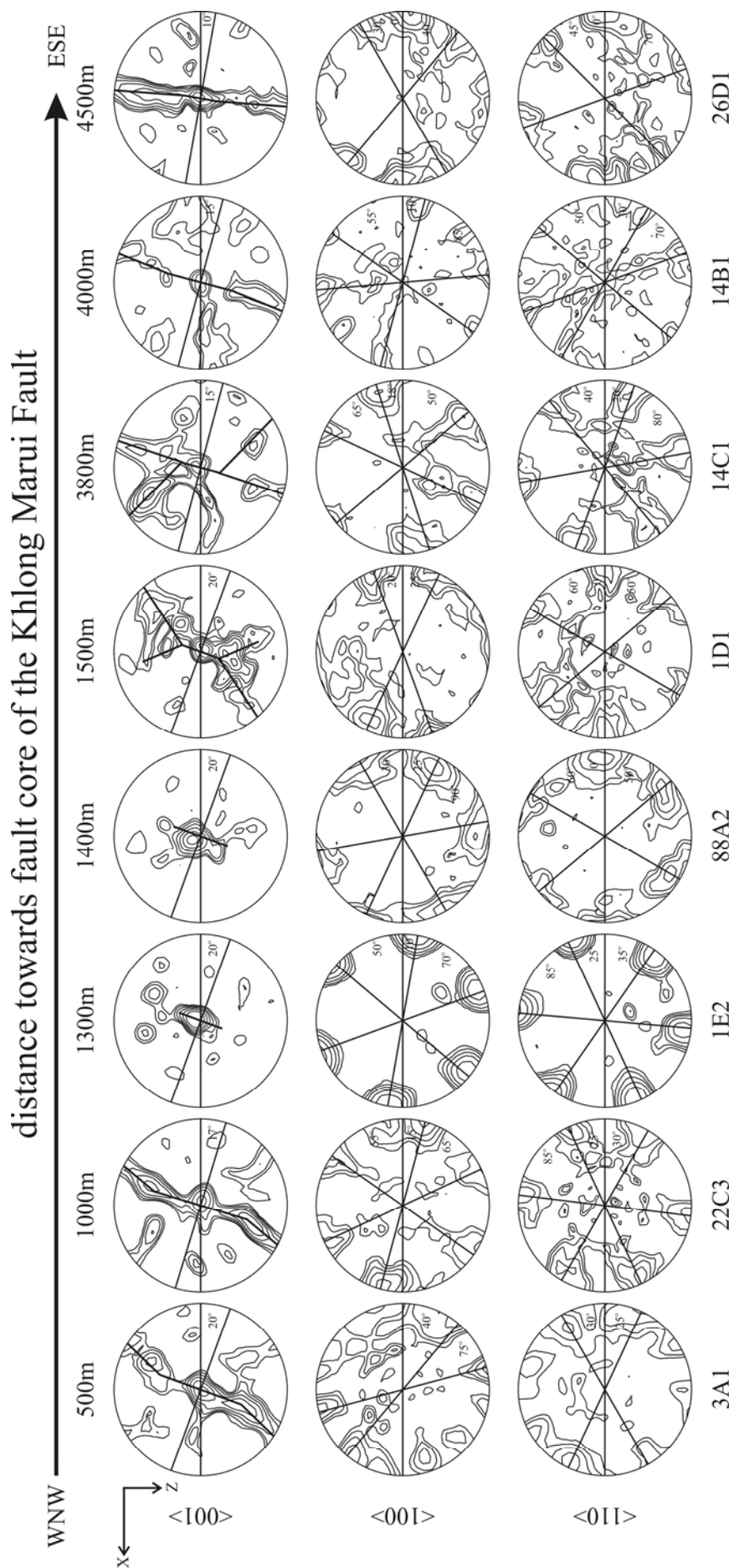


Figure 4.24 (previous page) Sterographic plots of $\langle 001 \rangle$, $\langle 100 \rangle$ and $\langle 110 \rangle$ from the west to the east of the Khlong Marui shear zone with the angle between the perpendicular to the central girdle segment of quartz axis fabric and main foliation.

The angle from the sample measurement and the mean vorticity number (W_m) are summarized in Table 4.1. The summation of δ and β angles indicates that the shear zone mainly deformed in the transpressional environment. The transtensional deformation is represented by the samples 1E2, 88A2, 14C1, and 14B1 which have summation of δ and β of more than 45° .

$W_m=0$ applied to pure shear and simple give $W_m=1$ for the mean degree of non-coaxiality (Bobyarchick, 1986; Passchier, 1986). The mean vorticity number (W_m) indicated that the flow type for the deformation period in the Khlong Marui shear zone is simple shear except the sample 14C1 showing a general shear.

Table 4.1 Summarized data from quartzite samples in the Khlong Marui shear zone.

Sample	δ	β	θ	W_m
3A1	19	20	12	0.98
22C3	22	17	12	0.98
1E2	45	20	40	0.77
88A2	28	20	6	0.98
1D1	20	20	10	0.99
14C1	57	15	54	0.59
14B1	40	15	20	0.94
26D1	20	10	30	0.87

The angle between the normal to the central girdle and the foliation (β) and the mean vorticity number (W_m) are plotted on the diagram (Grasemann et al., 1999). The plot shows two groups of ellipticity of the finite strain ellipsoid (R_f) which have values of about 7 and 1 (Fig. 4.25). The major ellipticity of about 7 represents the strain in the fault core and the ellipticity of about 1 is limited in the area of strain partitioning.

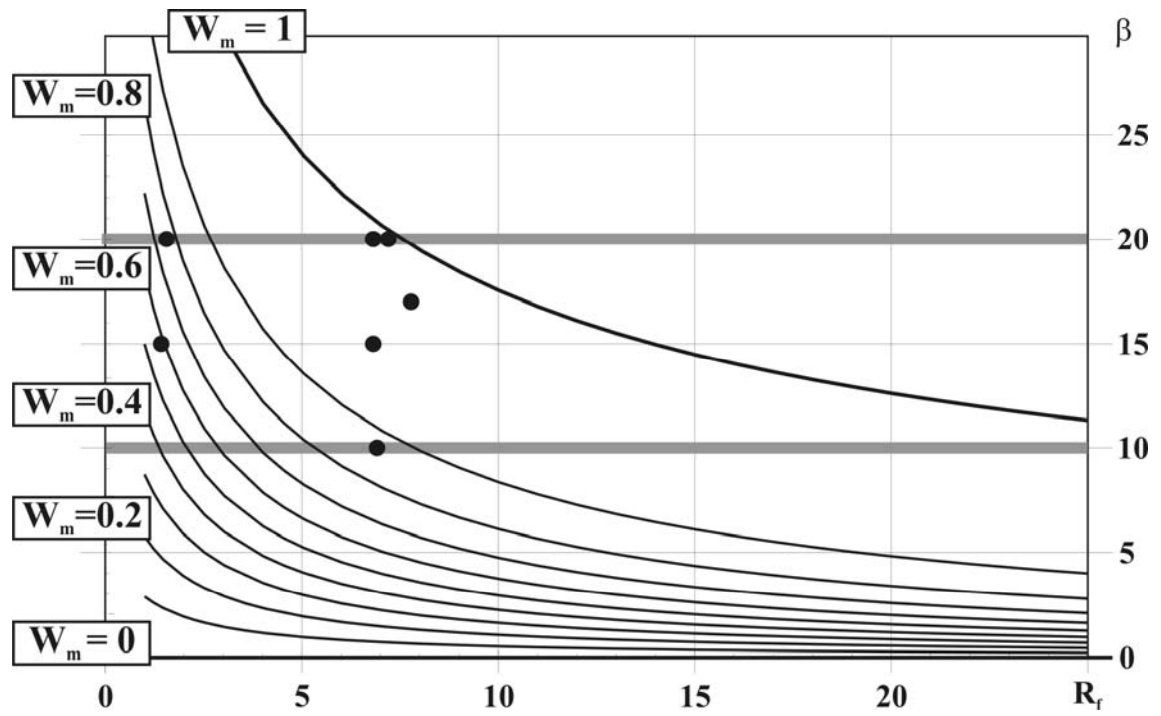


Figure 4.25 Diagram plots of the angle between the normal to the central girdle and the foliation (β) and the mean vorticity number (W_m) showing the ellipticity of the finite strain ellipsoid (R_f).

4.4 Microstructures Deformation

All kinematic indicators show that the area experienced ductile dextral movement in the early stages which confirms the mesoscopic study results in chapter 3. Dynamic recrystallisation in the area composes of undulose extinction, basal gliding, bulging (BLG), subgrain rotation (SGR), and local grain boundary migration (GBM) in quartz. Microstructures and mineral assemblages suggest that the rocks in the Khlong Marui shear zone have been metamorphosed at low to medium greenschist facies. Kinematic indicators such as mineral fish, sigmoids, and σ -types suggest that the sense of shear is dextral as well as asymmetric myrmekite and “V”-pull-apart.

The quartz texture studies indicate simple shear flow with a small finite strain ellipsoid (R_f) in a transpression zone. Transtension is locally associated within the Khlong Marui shear zone as an area of strain partitioning. Quartz textures in the eastern Khao Phanom indicate that higher temperature dextral deformation has been overprinted by lower temperatures with the same sense of shear. The final stage brittle deformation is reflected by proto-cataclasites to cataclasites of the original metapelite and quartzite host rock.

Chapter 5

Geochronology

5.1 Introduction

Geochronological investigations are performed in this study in order to better understand the temporal evolution of the Khlong Marui shear zone. The study involves the age determination of the rocks within a certain degree. The ages are measured by the amount of radioactive decay of a radioactive isotope with a known half-life. Rb-Sr, Sm-Nd, and U-Pb isotope methods are the three major analytical methods of the lithophile isotope geology (Dickin, 2005). All three methods were applied to the samples from the Khlong Marui shear zone by using the Rb, Sm, and U-rich minerals. The Rb-Sr method, which is one of the simplest and most basic dating methods, was performed on biotite and white mica. The Sm-Nd isotope analysis was done by using garnet, and the U-Pb method was analyzed by using zircon.

Geochronology research in southern Thailand has been performed on the granitoid rocks (Beckinsale et al., 1979; Bignell, 1972; Charusiri, 1989; Garson et al., 1975; Ishihara et al., 1980; Nakhapadungrat et al., 1984; Pitakpaivan, 1969; Putthapiban, 1984; Schwartz et al., 1995). The studies were done on the Phuket and Phang Nga region located at the west of the Khlong Marui shear zone. Their interpretation has focused on the age of granitoid magmatism as related to the tectonic evolution of the region. The results show that the major granitoid magmatism is dominantly Late Cretaceous with minor ages of Late Triassic and Paleocene-Eocene based on the cooling ages Rb-Sr, K-Ar, Ar-Ar, and fission track methods. In Khlong Marui shear zone, the previous study has been done on muscovites from muscovite-tourmaline pegmatite by ^{40}Ar - ^{39}Ar method which yields the ages of 41.3 and 42.6 ± 0.5 Ma (Charusiri, 1989) (Fig. 5.1).

The rock samples from the Khlong Marui shear zone were selected and prepared to analyze by geochronology methods. Orthogneiss (PK29A1), mylonitic granite (PK2A1), metapelite (PK9A1), and pegmatites (PK30Z and PK25C) were separated for mica on Rb-Sr isotope analysis. Sm-Nd method was performed on garnet phenocrysts from pegmatite sample PK30Z. The samples for Rb-Sr and Sm-Nd isotope analysis were done for whole rock geochronology aiming to use for two-point isochrones plotting. Zircons from the orthogneiss (PK29A1), mylonitic granite (PK2A1), pegmatite (PK30Z), and aplite (PK26) were measured for U-Pb isotope. By the different cooling temperature of each mineral, the absolute ages from the different isotope system are correlated and interpreted for the Khlong Marui Fault evolution.

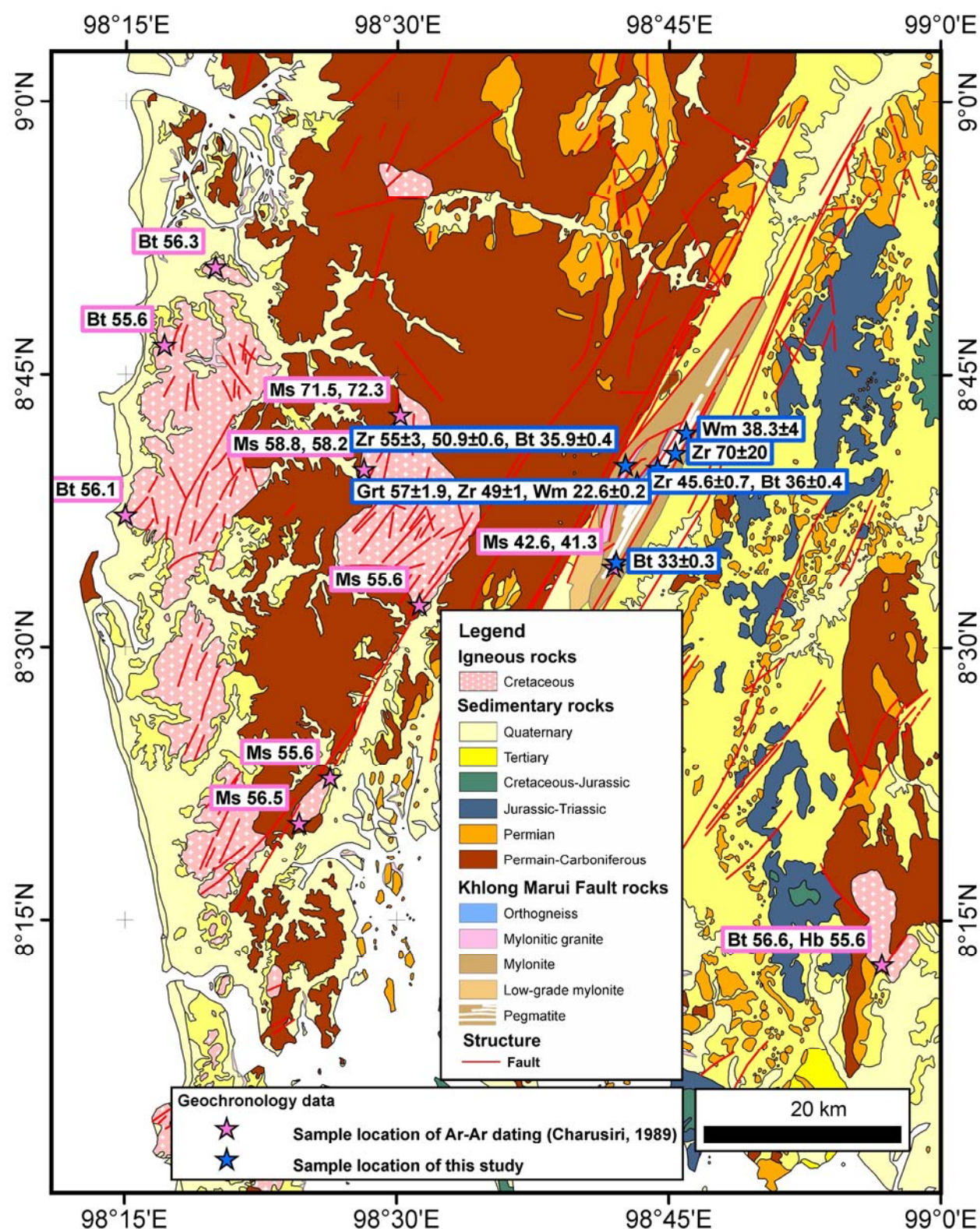


Figure 5.1 Geological map of the Khlong Marui Fault and adjacent area, modified after Department of Mineral Resources (1982), showing the locations of the $^{40}\text{Ar}/^{39}\text{Ar}$ dated samples (Charusiri, 1989) and this study dated samples. The ages were presented in Ma. (Bt=biotite; Grt=garnet; Hb=hornblende; Ms=moscovite; Wm=white mica; Zr=zircon)

5.2 Sample Preparation and Methodology

The mineral separation was done for mica, garnet, and zircon. The selected samples were cleaned by removing the outer weathered portion, dried, and then crushed in a jaw crusher to a size of 5-10 mm chips. After crushing the samples, whole rock splits were taken. The remaining major part of the sample was split by sieving into three different grain size fractions, which are > 1 mm, 0.25-1 mm, and < 0.25 mm. The grain size 0.25-1mm was used for mica separation, while the size < 0.25 mm was used for zircon separation. Garnet was separated from the > 0.45 mm fraction.

5.2.1 Whole Rock: Rb-Sr and Sm-Nd Isotope Analysis

An about 80-100 grams of crushed sample was ground in an agate mill producing a fine powder for whole rock analysis. Whole rock dissolution was performed for 3 weeks in HF/HClO₄ (5:1) at 110 °C, and then the acids were evaporated. The residue was repeatedly treated with 5.8 N HCl. After cooling, c. 10 % of the clear solution was split off and spiked for Sm and Nd concentration determined by isotopic dilution (ID) using a mixed REE tracer (¹⁴⁷Sm-¹⁵⁰Nd spike). For Rb-Sr analysis, a separate sample split was used and spiked directly (i.e., in the solid form), before dissolution, using a ⁸⁷Rb-⁸⁴Sr spike.

5.2.2 Mica: Rb-Sr Isotope Analysis

Highly enriched mica sieve fractions between 0.25-1 mm and > 0.45 mm (only for sample PK25C) were received from the > 0.25 mm grain size fraction, using a magnetic separator. Subsequently, these highly enriched mica fractions were purified by several (2-3) sieving-milling-magnet separation steps to eliminate micro-inclusions and intergrowths from the mica flakes. After careful final separation, using either a dry vibration table and/or a Frantz magnetic separator, the mica concentrates were optically $>> 99$ % pure.

5.2.3 Garnet: Sm-Nd Isotope Analysis

A garnet concentrate of the grain size 0.15-0.45 mm was obtained by repeated crushing and sieving of the > 0.45 mm fraction, consisting of single garnet crystals. In this way, larger inclusions and intergrowths were eliminated in a first step. After washing, using weak HCl and acetone, optically pure garnet crystal fragments were carefully handpicked under a binocular microscope.

Chemical and analytical procedure for Rb-Sr and Sm-Nd isotope analysis

Before decomposition, the handpicked garnet fractions were washed in 2.5 N HCl for 30 minutes at 70°C in order to further remove dust and surface contaminations. Sample weights used for dissolution were between 72 and 108 mg. The leaching experiment (PK30Z Grt3*, see Table 5.2) was performed to eliminate eventually remaining, optically undetected micro-inclusions (primarily phosphates), using concentrated ultrapure H₂SO₄.

(Anczkiewicz and Thirlwall, 2003). Sr and Rb and the REE were extracted from separate aliquots using ultrapure HF/HNO₃ and HF/HClO₄ 5:1 mixture for dissolution, respectively. Rb, Sr, Sm and Nd concentrations were determined from two different sample aliquots by isotope dilution (ID) using ⁸⁷Rb-⁸⁴Sr and ¹⁴⁷Sm-¹⁵⁰Nd spike, respectively. The REE fraction was extracted using AG 50 W-X8 (200-400 mesh, Bio-Rad) resin and 4.0 N HCl. Nd and Sm were separated from the REE fraction using Teflon-coated HDEHP, 0.24 N and 0.8 N HCl, respectively, as elution media. Total procedural blanks were < 100 pg for Sm and Nd, and < 1 ng for Rb and Sr. Rb, Sm and Nd ID samples were measured as metals from a Re (single: Rb; double: Nd and Sm) filament using a Finnigan MAT262 mass spectrometer, while Sr (ID and IC) and Nd IC samples were run on a ThermoFinnigan Triton TI TIMS machine. ⁸⁷Sr/⁸⁶Sr and ¹⁴³Nd/¹⁴⁴Nd ratios for the NBS987 (Sr) and the La Jolla (Nd) international standards during the period of investigation on the Triton instrument were 0.710270±4 (n = 11) and 0.511844±2 (n = 28), respectively. Errors for the ⁸⁷Rb/⁸⁶Sr and ¹⁴⁷Sm/¹⁴⁴Nd ratios are taken as ±1%, or smaller, based on iterative sample analysis and spike recalibration. Age calculation is based on decay constants of 1.42x10⁻¹¹ year⁻¹ for ⁸⁷Rb and 6.45x10⁻¹² year⁻¹ for ¹⁴⁷Sm.

5.2.4 Zircon: U-Pb Isotope Analysis

The sieve fractions of <0.25mm were taken for zircon separation. The separation process was taken by magnetic separator before Wilfley table separator to purify the heavy mineral. After drying, the fractions were obtained in separation of mica using vibration table and Frantz magnetic separator to selected non-magnetic minerals. The heavy minerals were processed by heavy liquid before zircon hand picking under binocular microscope. The zircon grains were mounted in epoxy resin and polished until reaching to the core for LA-ICP-MS analysis. Cathodoluminescence (CL) images were taken for each grain at the Geological Survey of Austria before LA-ICP-MS analysis.

LA-ICP-MS analytical procedure for U-Pb isotope analysis

Zircon ²⁰⁶Pb/²³⁸U and ²⁰⁷Pb/²⁰⁶Pb ages were determined using a 193 nm solid state Nd-YAG laser (New Wave UP193-SS) coupled to a multi-collector ICP-MS (Nu Instruments HR). Ablation in a He atmosphere was done either spot-or raster-wise according to the CL zonation pattern of the zircons. Spot analyses were 20-35 µm in diameter whereas line widths for rastering were 20-35 µm with a raster speed of 5 µm/sec. Energy densities were 5-8 J/cm² with a repetition rate of 10 Hz. The He carrier gas was mixed with the Ar carrier gas flow prior to the plasma torch. Ablation duration was 60 to 120 seconds with a 30 seconds gas and Hg blank count rate measurement preceding ablation. Ablation count rates were corrected accordingly offline. Remaining counts on mass 204 were interpreted as representing 204 Pb.

Static mass spectrometer analysis was as follow ^{238}U in a Faraday detector, ^{207}Pb , ^{206}Pb , and $^{204}(\text{Pb}+\text{Hg})$ were in ion counter detectors. ^{208}Pb was not analyzed. An integration time of 1 second was used for all measurements. The ion counter-Faraday and inter-ion counter grain factors were determined before the analytical session, using standard zircon 915000 (Wiedenbeck et al., 1995) and Plešovice (Sláma et al., 2008). Sensitivity for ^{206}Pb on standard zircon 915000 was ca. 30000 cps per ppm Pb. For ^{238}U the corresponding was ca. 35000 cps. Mass and elemental bias and mass spectrometer drift of both U/Pb and Pb/Pb ratios, respectively, were corrected using a multi-step approach: first-order mass bias is corrected using a dried ^{233}U - ^{205}Tl - ^{203}Tl spike solution which is aspirated continuously in Ar and mixed to the He carrier gas coming from the laser before entering the plasma. This corrects for bias effects stemming from the mass spectrometer. The strongly time-dependent elemental fractionation coming from the ablation process itself is then corrected for using the “intercept method” (Sylvester and Ghaderi, 1997). The calculated $^{206}\text{Pb}/^{238}\text{U}$ and $^{207}\text{Pb}/^{206}\text{Pb}$ intercept values are corrected for mass discrimination from analyses of standards 91500 and Plešovice measured during the analytical session using a standard bracketing method. The correction utilizes regression of standard measurements by a quadratic function. A common Pb correction was applied to the final data using the apparent $^{207}\text{Pb}/^{206}\text{Pb}$ age and the Pb evolution model (Stacy and Kramers, 1975). The ablation area is illustrated by the white outline in the cathodoluminescence (CL) images.

5.3 Rb-Sr Analytical Results

Rb-Sr dating was used for tracing the cooling history of the rocks, using Rb-rich minerals (mica). The biotite from metapelite, orthogneiss, mylonitic granite and white mica from 2 pegmatites were used to determine the Rb-Sr ages. Whole rock analysis was carried out from all these samples for two-point isochrones plotting.

The steep foliations of orthogneiss, mylonitic granite, and metapelite intruded by pegmatite are packed within the Khlong Marui shear zone. Metapelite sample PK9A1 mainly is composed of quartz and biotite and accessory white mica, chlorite, tourmaline, and opaque minerals. The major composition of the orthogneiss sample PK29A1 is quartz, K-feldspar, and biotite. Plagioclase, tourmaline, and white mica represent accessory minerals. Most minerals are orientated parallel to the foliation plane. Mylonitic granite sample PK2A1 is predominantly composed of quartz, K-feldspar, plagioclase, and biotite with accessory minerals of tourmaline, chlorite and opaque minerals. The pegmatite sample PK30Z is interpreted as a synkinematic intrusion, based on the parallel orientation of tourmaline lineation relative to the stretching lineation of the mylonitic host rock. This pegmatite is composed of coarse grained quartz, K-feldspar, plagioclase and accessory white mica, tourmaline and garnet. Another pegmatite sample PK25C has the same lithology as sample PK30Z, except for the greater grain size of white mica (0.45 mm) in sample PK25C. The Rb-Sr analytical results for whole rocks and mineral separates of 5 samples from the Khlong Marui shear zone are given in Table 5.1.

Table 5.1 Rb-Sr analytical results of samples from the Khlong Marui shear zone.

Sample	Rb (ppm)	Sr (ppm)	$^{87}\text{Rb}/^{86}\text{Sr}$	$^{87}\text{Sr}/^{86}\text{Sr}$	$\pm 2\sigma_m$
PK9A1 wr	170.6	150.5	3.295	0.752800	0.000004
PK9A1 Bt	503.8	1.762	867	1.158000	0.001000
PK29A1 wr	429.4	76.23	16.39	0.765207	0.000005
PK29A1 Bt	1955	1.273	5743	3.691455	0.003033
PK2A1 wr	287	221	3.762	0.720300	0.000012
PK2A1 Bt	887.4	8.547	305.4	0.874259	0.000151
PK30Z wr	451	56.69	23.13	0.755349	0.000005
PK30Z Wm	1286	2.325	1693	1.291806	0.000022
PK25C wr	1371	25.95	154.9	0.844678	0.000005
PK25C Wm	4226	1.847	10585	6.522900	0.001600

The Rb-Sr analytical results are individually plotted on isochron diagrams, using the relative whole rock data point and either biotite or white mica fractions (two-point isochrons; Fig. 5.2). Bt-wr isochron regression for metapelite PK9A1 yields an age of 33 ± 0.3 Ma, while orthogneiss sample PK29A1 and mylonitic granite PK2A1 yield 36 ± 0.4 and 35.9 ± 0.4 Ma, respectively. Wm-wr from pegmatites gives an age 22.6 ± 0.2 Ma for sample PK30Z and 38.3 ± 0.4 Ma for sample 252C.

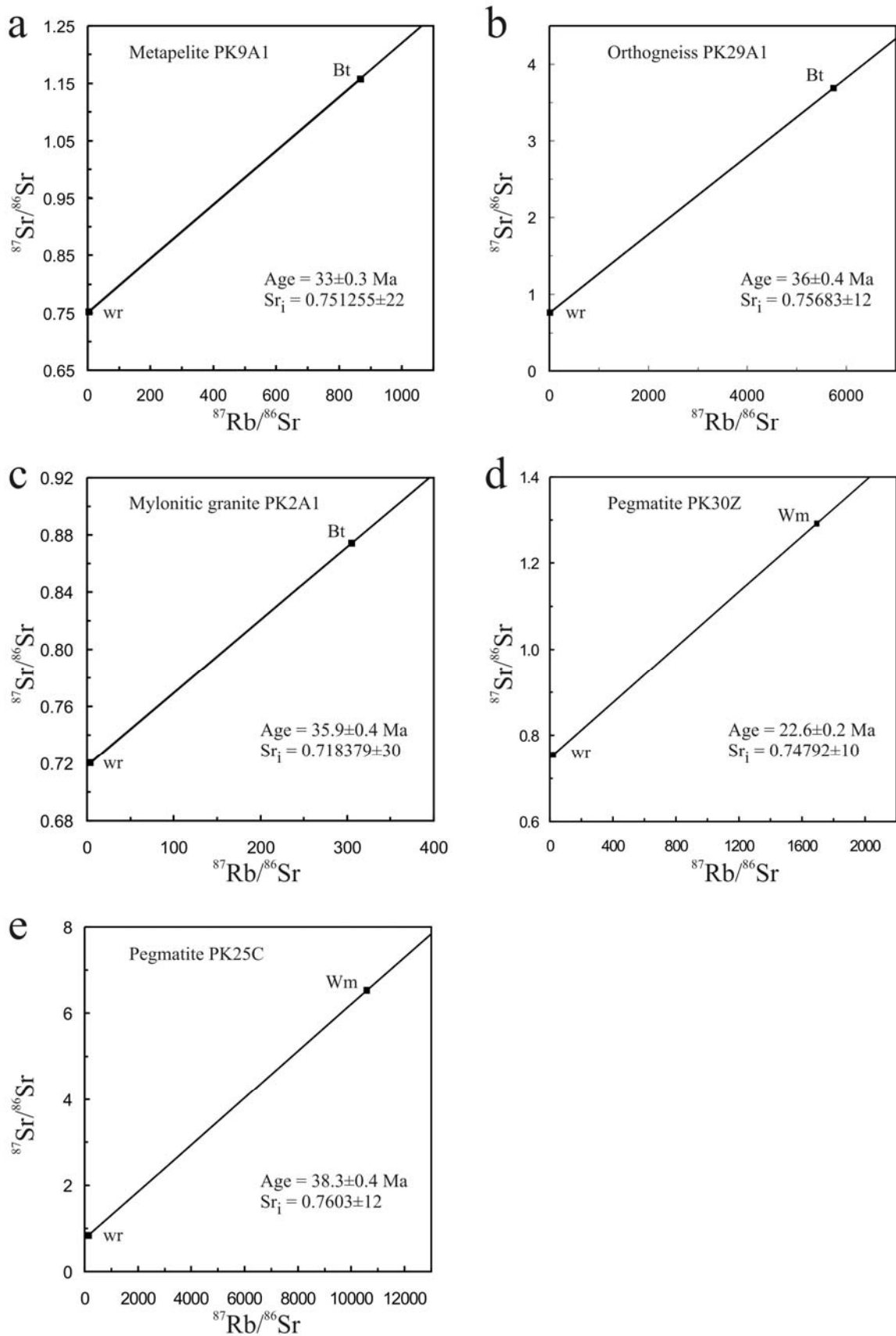


Figure 5.2 Rb-Sr isochron plots for (a) Bt-wr of mylonite (PK9A1); (b) Bt-wr of orthogneiss (PK29A1); (c) Bt-wr of mylonitic granite (PK2A1); (d) Wm-wr of pegmatite (PK30Z); (e) Wm-wr of pegmatite (PK25C). All errors are smaller than the size of the symbols.

5.4 Sm-Nd Analytical Results

Pegmatite sample PK30Z was used not only for Rb-Sr but also for Sm-Nd isotope analysis. The garnet grains are up to 1.5 mm in size with euhedral or partly subhedral shape. Garnets phenocrysts were analyzed for the major element composition and qualitatively also for micro-inclusions by electron-microprobe, prior to Sm-Nd isotope analysis. The results show a simple, continuous growth zoning and an almandine-spessartine-rich composition with increasing FeO and decreasing MnO from core toward the rim, suggesting single phase crystallization (Fig. 5.3 a-d). The detected micro-inclusions are phosphate minerals with less than 1 μm in size (Fig. 5.3 e).

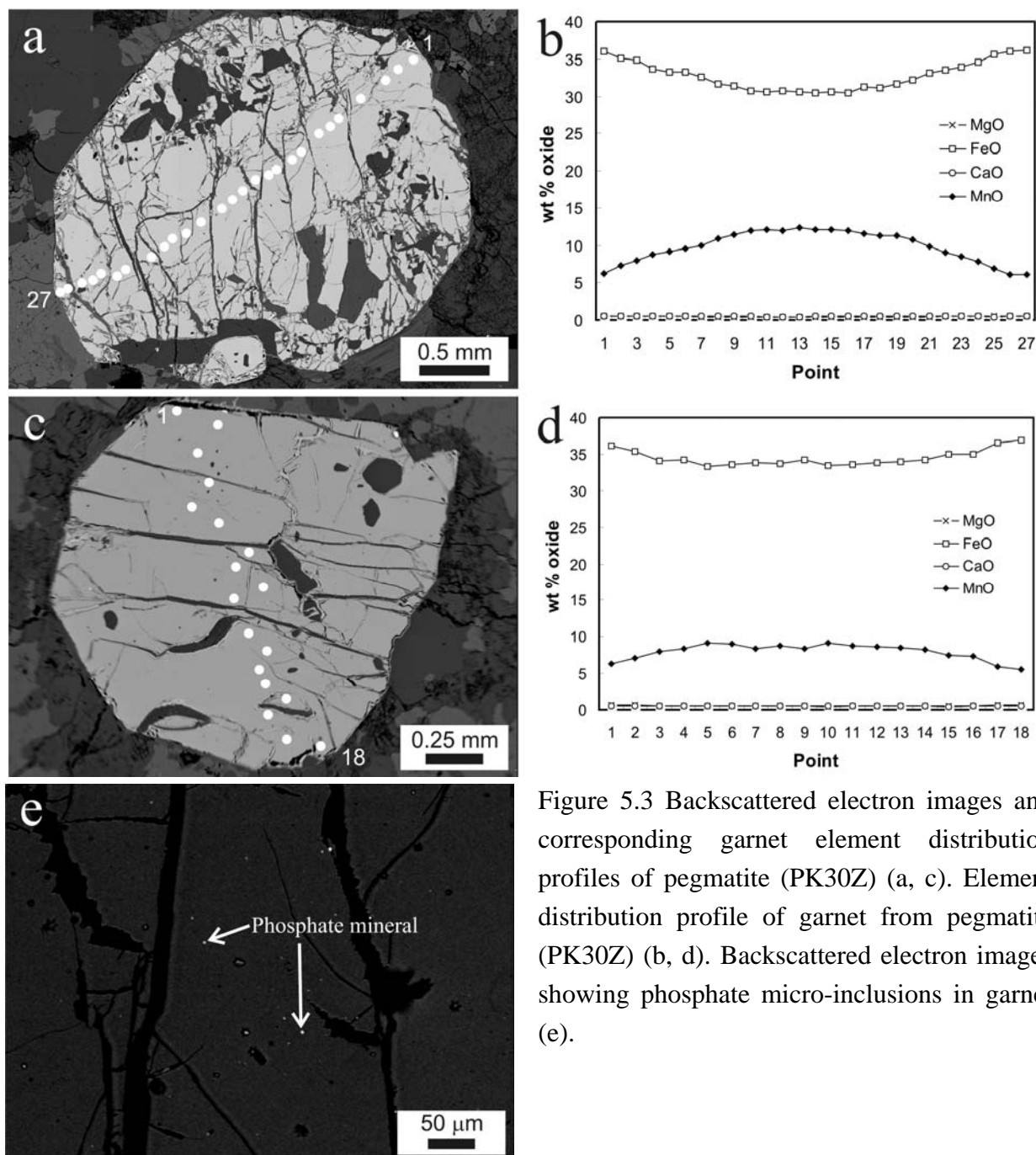


Figure 5.3 Backscattered electron images and corresponding garnet element distribution profiles of pegmatite (PK30Z) (a, c). Element distribution profile of garnet from pegmatite (PK30Z) (b, d). Backscattered electron images showing phosphate micro-inclusions in garnet (e).

Three different garnet fractions were analysed for Sm-Nd isotope systematics: Grt 1 and 2 are handpicked, unleached fractions, while Grt 3 was leached with concentrated H_2SO_4 to eliminate phosphate micro-inclusions which might not have been detected during handpicking. The Sm-Nd analytical results for the whole rock and the 3 garnet fractions of pegmatite sample PK30Z are given in Table 5.2 and plotted in an isochron diagram (Fig. 5.4).

Table 5.2 Sm-Nd analytical results of garnet fractions and the whole rock of pegmatite sample PK30Z.

Sample	Sm (ppm)	Nd (ppm)	$^{147}\text{Sm}/^{144}\text{Nd}$	$^{143}\text{Nd}/^{144}\text{Nd}$	$\pm 2\sigma_m$
PK30Z wr	3.043	12.731	0.144487	0.511701	0.000003
PK30Z Grt 1	0.435	0.409	0.643038	0.511882	0.000015
PK30Z Grt 2	0.388	0.377	0.621615	0.511885	0.000008
PK30Z Grt 3*	0.357	0.168	1.282362	0.512124	0.000020

*residual garnet from H_2SO_4 leaching experiment

Inclusion of all 4 data points (wr and 3 Grt fractions) in one single regression calculation results in a near-best-fit isochron age of 57 ± 1.9 Ma (MSWD = 1.1) and an $\epsilon\text{Nd}(t)$ value of -17.85 (Fig. 5.4). In combination with the “simple” major element zonation, the collinear array of the 4 data points gives confidence that the age of 57 ± 1.9 Ma represents the mean time window for magmatic garnet crystallization in PKZ30, and that the age is not significantly influenced by inherited Nd-rich inclusions. Eventual phosphate micro-inclusions (possibly present in Grt fractions 1 and 2 to a minor extent) are obviously in Nd isotopic equilibrium with the garnet host, i.e., they are cogenetic, as far as the Sm-Nd isotope system is concerned.

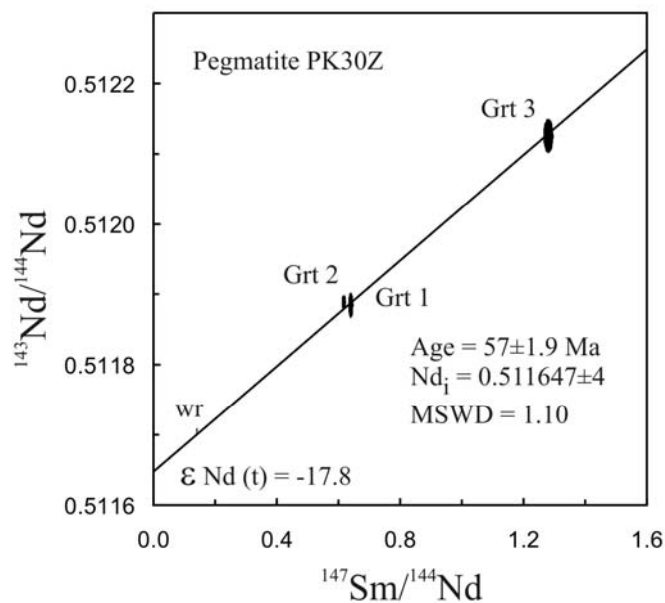


Figure 5.4 Sm-Nd isochron plot for wr and 3 different Grt fractions of pegmatite sample PK30Z.

5.5 U-Pb Analytical Results

U-Pb isotope analysis was done on the granitic materials in the Khlong Marui shear zone. A total of 111 zircons from orthogneiss, mylonitic granite, pegmatite, and aplite were dated in this study. All zircons are clear, long and stubby with sharp edge. The size of zircon is approximately 200 μm . They typically present the broadband oscillatory zoning. The inherited core displays the rounded edge caused by melting because the zircons are derived from the orthogneiss. The recrystallized cores in zircon are frequently found. Data for LA-ICP-MS U-Pb analysis of zircons are presented in Appendix C.

The 45 zircons from orthogneiss sample PK29A1 obtain 9 different ages through the inner, middle, outer core, and the rim (Fig. 5.5-7). The inner core part yields the ages of ~ 3000 and 2350 ± 50 Ma (6 ages). The oldest ~ 3000 Ma can not be calculated for the concordia age but the 2 plots can be determined by the age nearly to 3000 Ma (Fig. 5.5b). The ages of 1150 ± 20 (13 ages), 1000 ± 20 (7 ages), 930 ± 20 (5 ages), 757 ± 9 (7 ages), 534 ± 5 Ma (14 ages), respectively, are presented at the middle core. The oscillatory zoning generally presents the fir-tree structure in the cathodoluminescence (CL) images indicating the magmatic crystallization. The outer core gives an age of 340 ± 60 Ma (5 ages). The rim part of this zircon is recognized by dark signal in cathodoluminescence (CL) images. It yields an age of 45.6 ± 0.7 Ma (9 ages).

The ages of mylonitic granite sample PK2A1 were determined by the analyses of 35 zircons (Fig. 5.8-10). The bright ring in cathodoluminescence (CL) images which separated between the core and the rim is typically presented in this zircon group. The core can be subdivided into 3 parts as inner, middle, and outer core. The 3 different ages are given for the inner core. The oldest age of ~ 2390 is determined from the 2 ages in concordia diagram (Fig. 5.8b). The other ages of the inner core are 900 ± 100 (3 ages) and 440 ± 50 Ma (3 ages). The middle core gives the ages of 220 ± 10 Ma (2 ages) while the outer core gives the ages of 70 ± 2 (5 ages) and 62 ± 1 Ma by (7 ages). The rim which displays broadband zoning yields the ages either 55 ± 3 (4 ages) or 50.9 ± 0.6 Ma (14 ages).

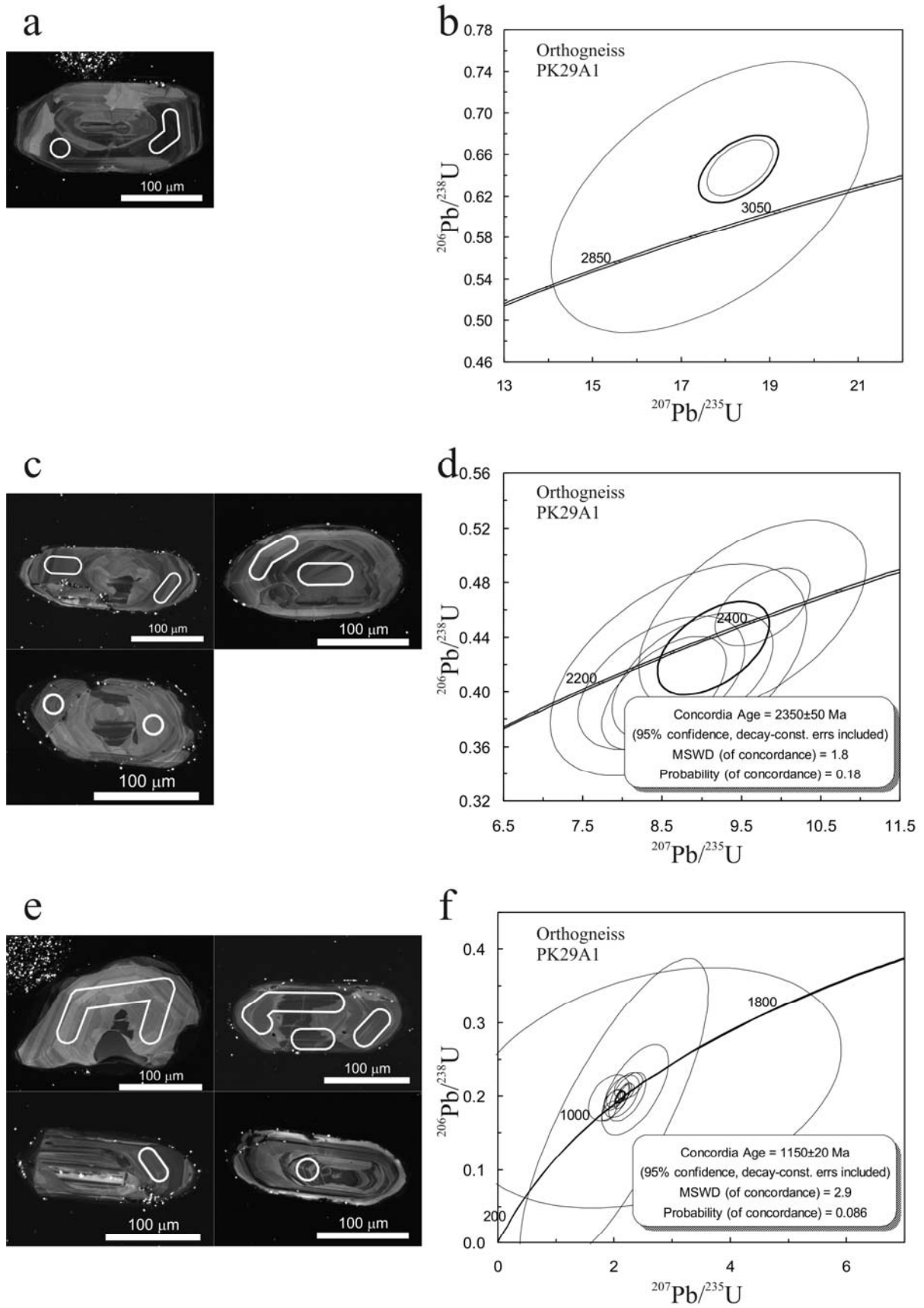


Figure 5.5 Cathodoluminescence (CL) images of zircon used for LA-ICP-MS U-Pb analysis of sample PK29A1 (a, c, e). U-Pb concordia diagrams of the sample PK29A1 (part1) (b, d, f).

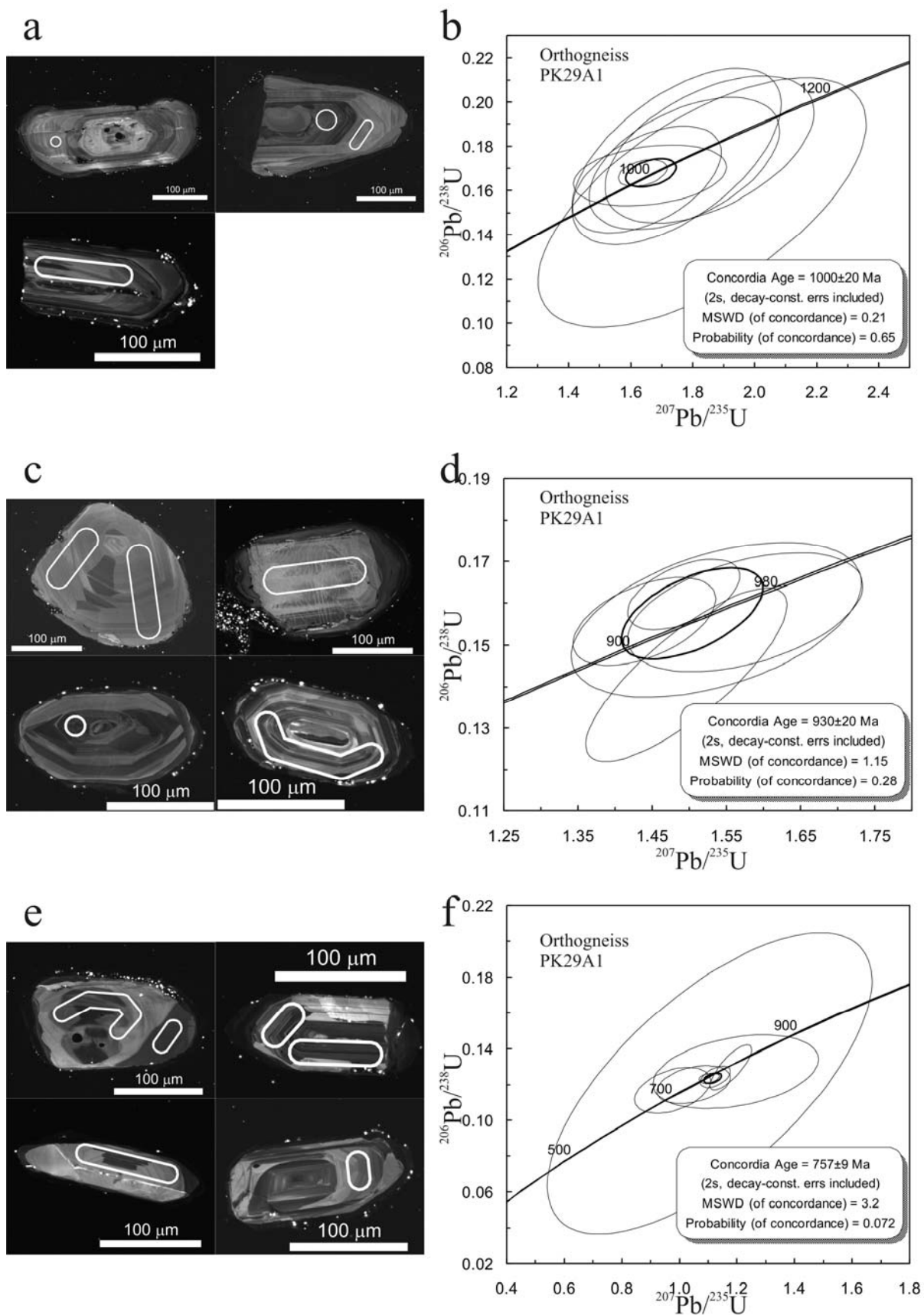


Figure 5.6 Cathodoluminescence (CL) images of zircon used for LA-ICP-MS U-Pb analysis of sample PK29A1(a, c, e). U-Pb concordia diagrams of the sample PK29A1 (part 2) (b, d, f).

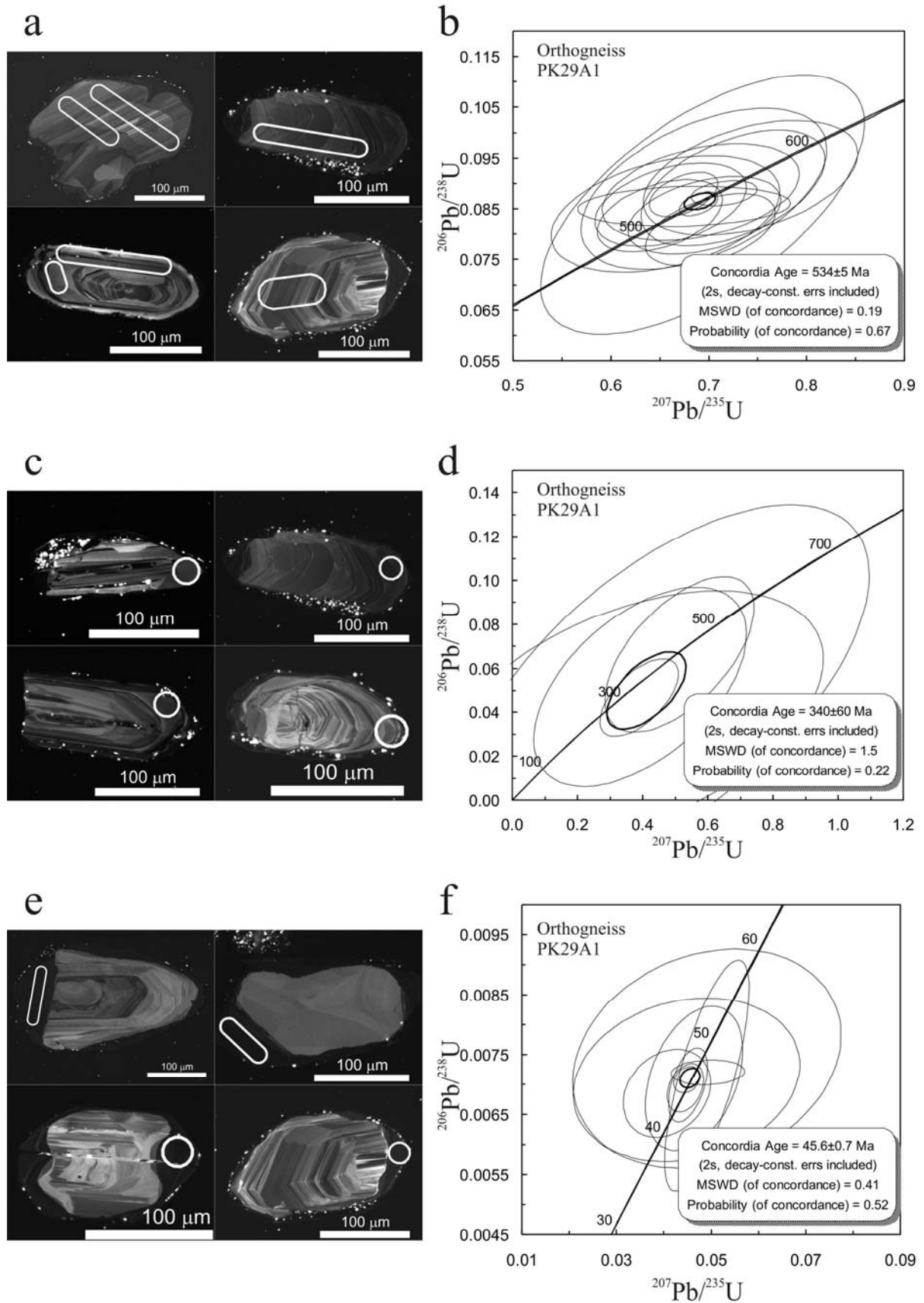


Figure 5.7 Cathodoluminescence (CL) images of zircon used for LA-ICP-MS U-Pb analysis of sample PK29A1(a, c, e). U-Pb concordia diagrams of the sample PK29A1 (part3) (b, d, f).

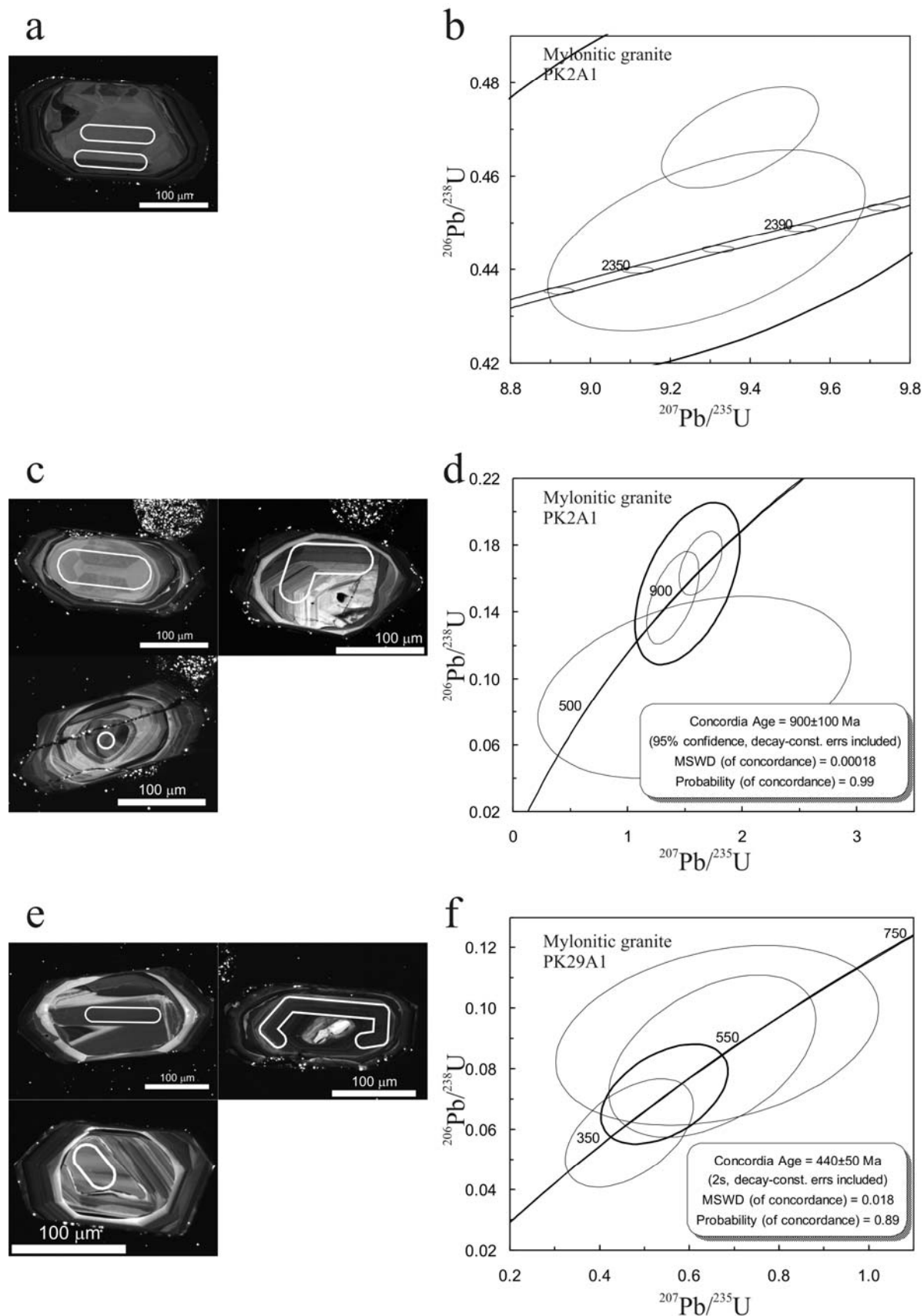


Figure 5.8 Cathodoluminescence (CL) images of zircon used for LA-ICP-MS U-Pb analysis of sample PK2A1(a, c, e). U-Pb concordia diagrams of the sample PK2A1 (part1) (b, d, f).

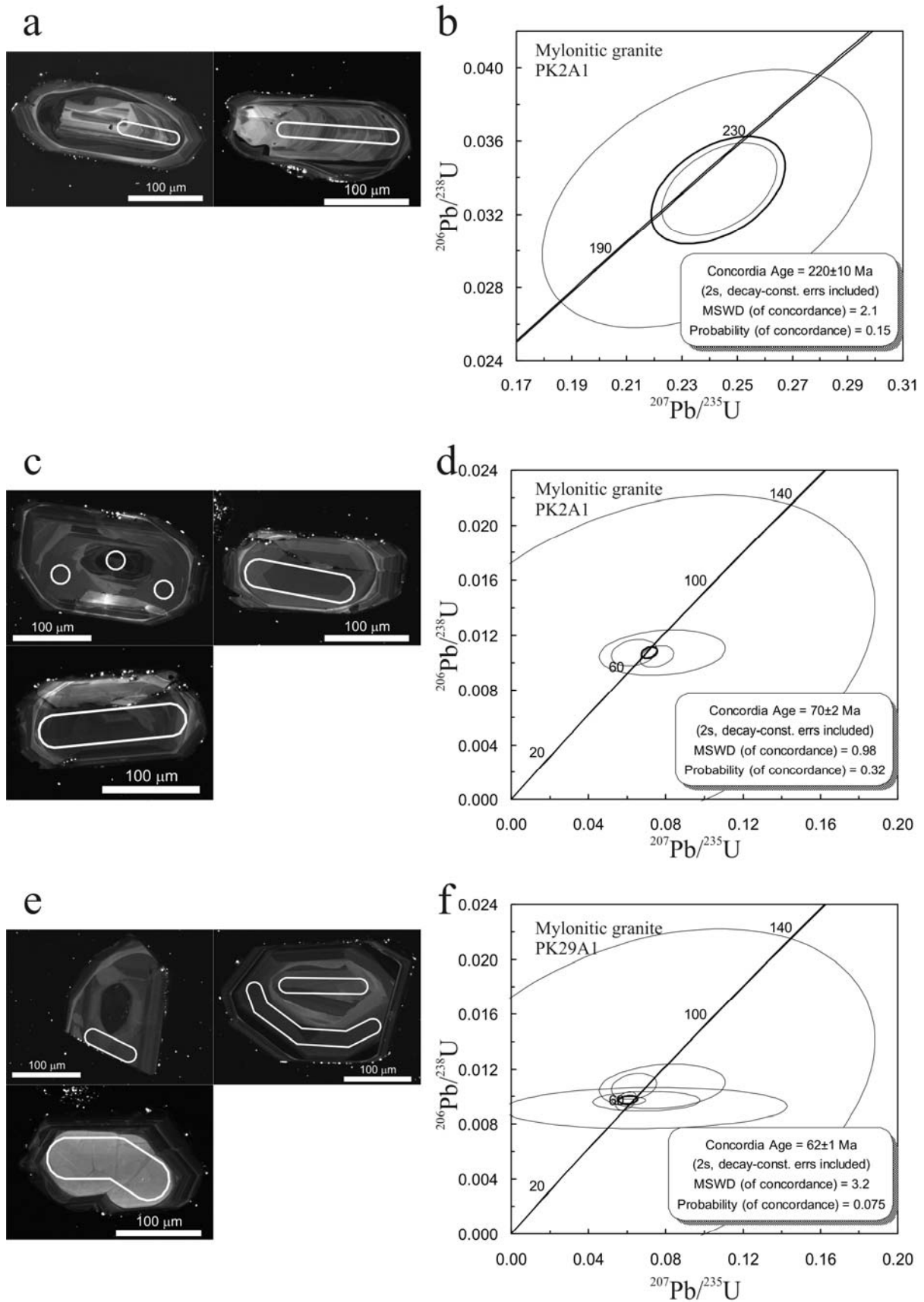


Figure 5.9 Cathodoluminescence (CL) images of zircon used for LA-ICP-MS U-Pb analysis of sample PK2A1(a, c, e). U-Pb concordia diagrams of the sample PK2A1 (part 2) (b, d, f).

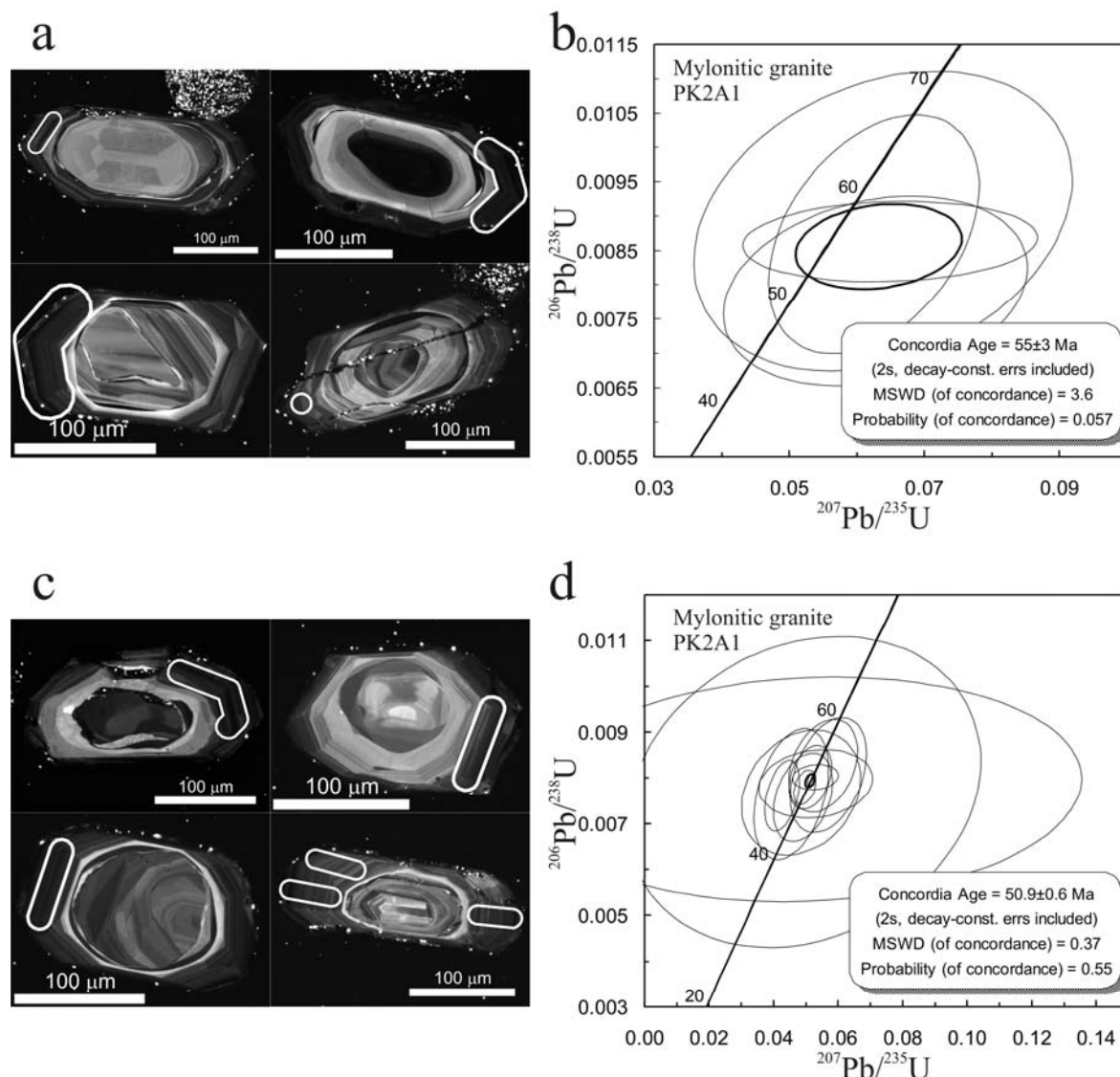


Figure 5.10 Cathodoluminescence (CL) images of zircon used for LA-ICP-MS U-Pb analysis of sample PK2A1(a, c). U-Pb concordia diagrams of the sample PK2A1 (part3) (b, d).

The results of 28 zircons from pegmatite sample PK30Z were presented in concordia diagrams (Fig. 5.11-12). These zircons have the same systematic as the zircons from the orthogneiss except the outer core is missing. The inner core yields the maximum ages of 2930 ± 20 (3 ages) and 2460 ± 40 Ma (4 ages). The outer core, which can be correlated to middle core of the orthogneiss zircon, yields the ages of 1440 ± 50 (5 ages), 900 ± 10 (7 ages), and 525 ± 10 Ma (5 ages) respectively. The rim part which displays dark color in cathodoluminescence (CL) images gives an age of 49 ± 1 Ma (9 ages). The youngest age is partly obtained by the single crystal (Fig. 5.12e).

Three zircons were dated for aplite sample PK26 (Fig. 5.13). The size of this zircon is approximately 100 μm which is smaller than the others. The broadband brighter core gives the core give the ages of 2450 ± 100 (2 ages) and 1670 ± 90 (3 ages). The rim yields an age of 70 ± 20 Ma (2 ages).

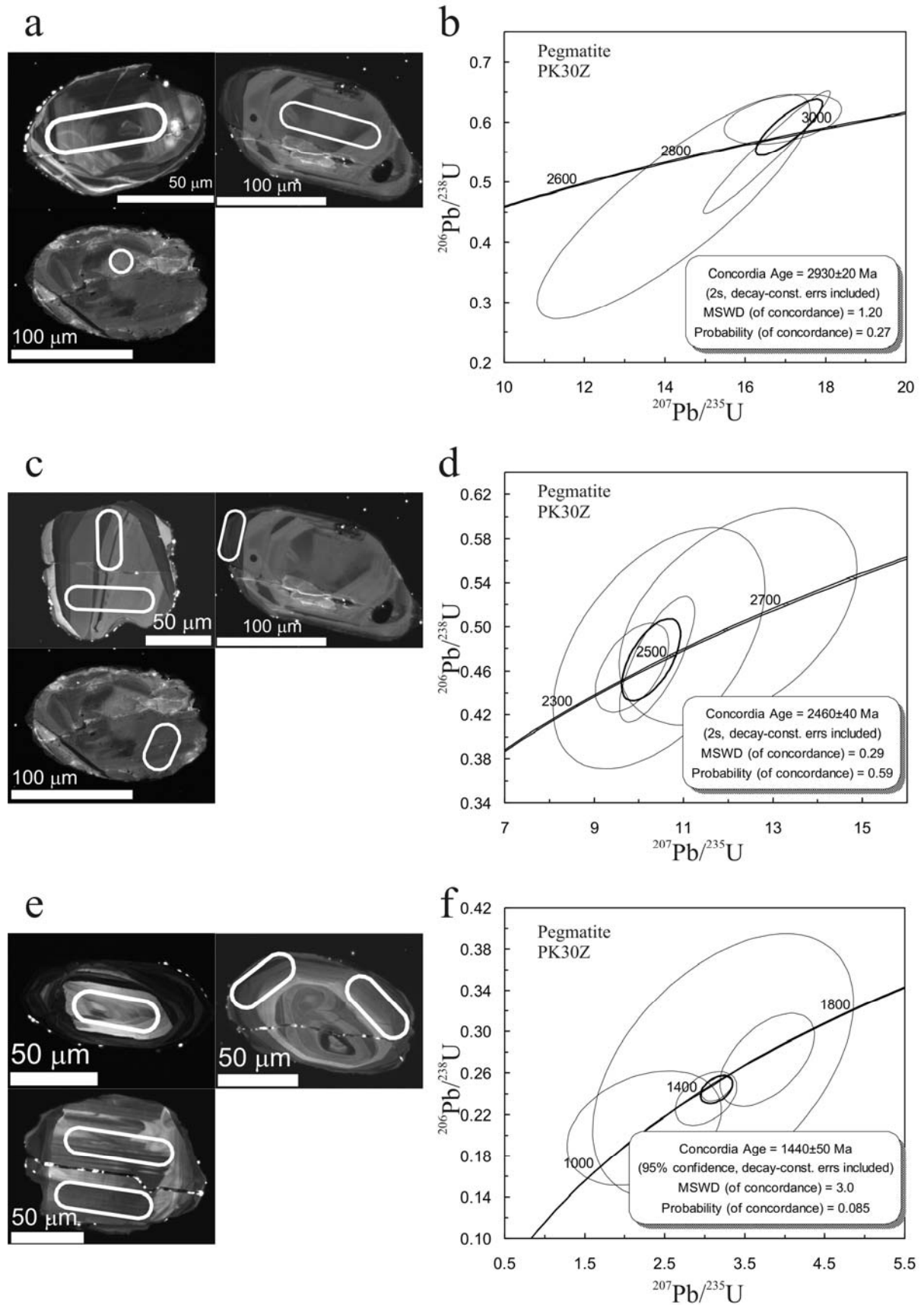


Figure 5.11 Cathodoluminescence (CL) images of zircon used for LA-ICP-MS U-Pb analysis of sample PK30Z(a, c, e). U-Pb concordia diagrams of the sample PK30Z (part1) (b, d, f).

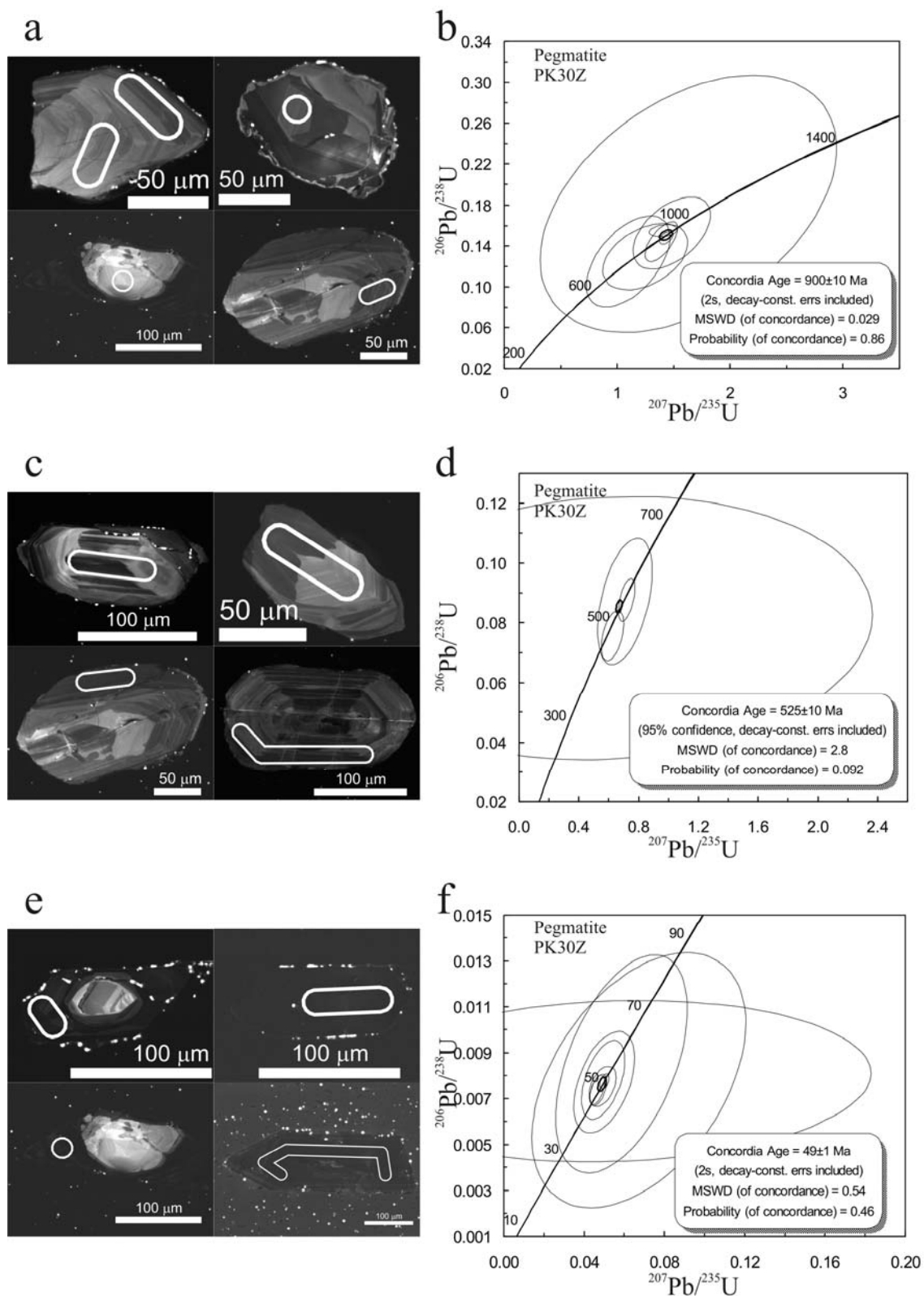


Figure 5.12 Cathodoluminescence (CL) images of zircon used for LA-ICP-MS U-Pb analysis of sample PK30Z(a, c, e). U-Pb concordia diagrams of the sample PK30Z (part2) (b, d, f).

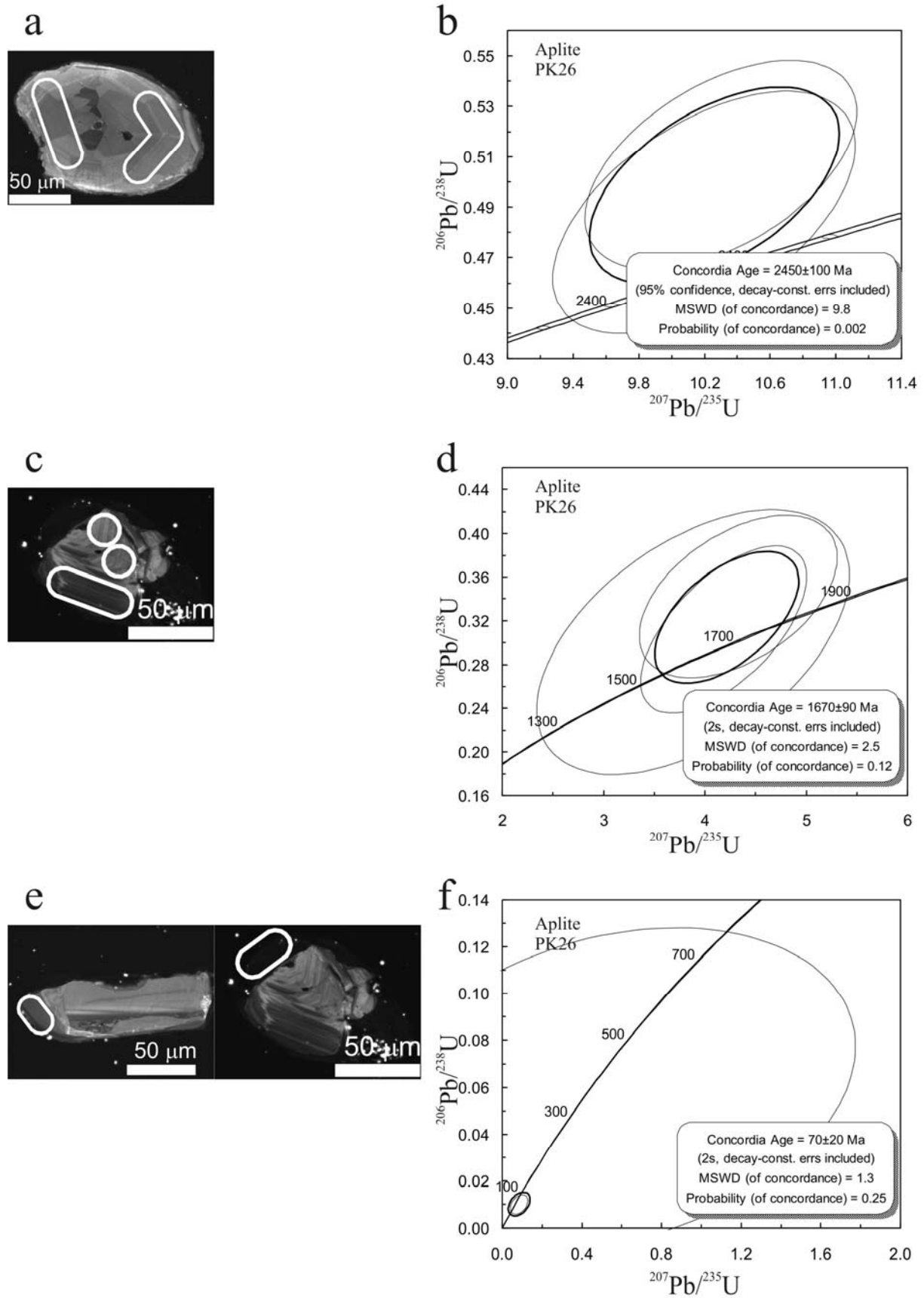


Figure 5.13 Cathodoluminescence (CL) images of zircon used for LA-ICP-MS U-Pb analysis of sample PK26 (a, c, e). U-Pb concordia diagrams of the sample PK26 (b, d, f).

Zircon structures

The overgrowth zoning of zircon in the Khlong Marui shear zone can be illustrated as the rounded edge inherited core and the sharp rim (Fig. 5.14). Zircons of the orthogneiss sample PK29A1, pegmatite sample PK30Z, and aplite sample PK26 have the same systematic overgrowth zoning. They differ from mylonitic granite sample PK2A1 but share the same systematic ages. The core ages are in Pre-Cambrian which usually have overgrowth zone from Archean to Meso-Proterozoic period. The outer core age of Carboniferous can be found in the zircon of the orthogneiss. Mesozoic outer core with the dark and bright ring in cathodoluminescence (CL) images are typically presented in the zircon of mylonitic granite sample PK2A1. This probably indicates the decreasing of the trace elements from the dark to the bright ring. The rim yields the same age of Eocene.

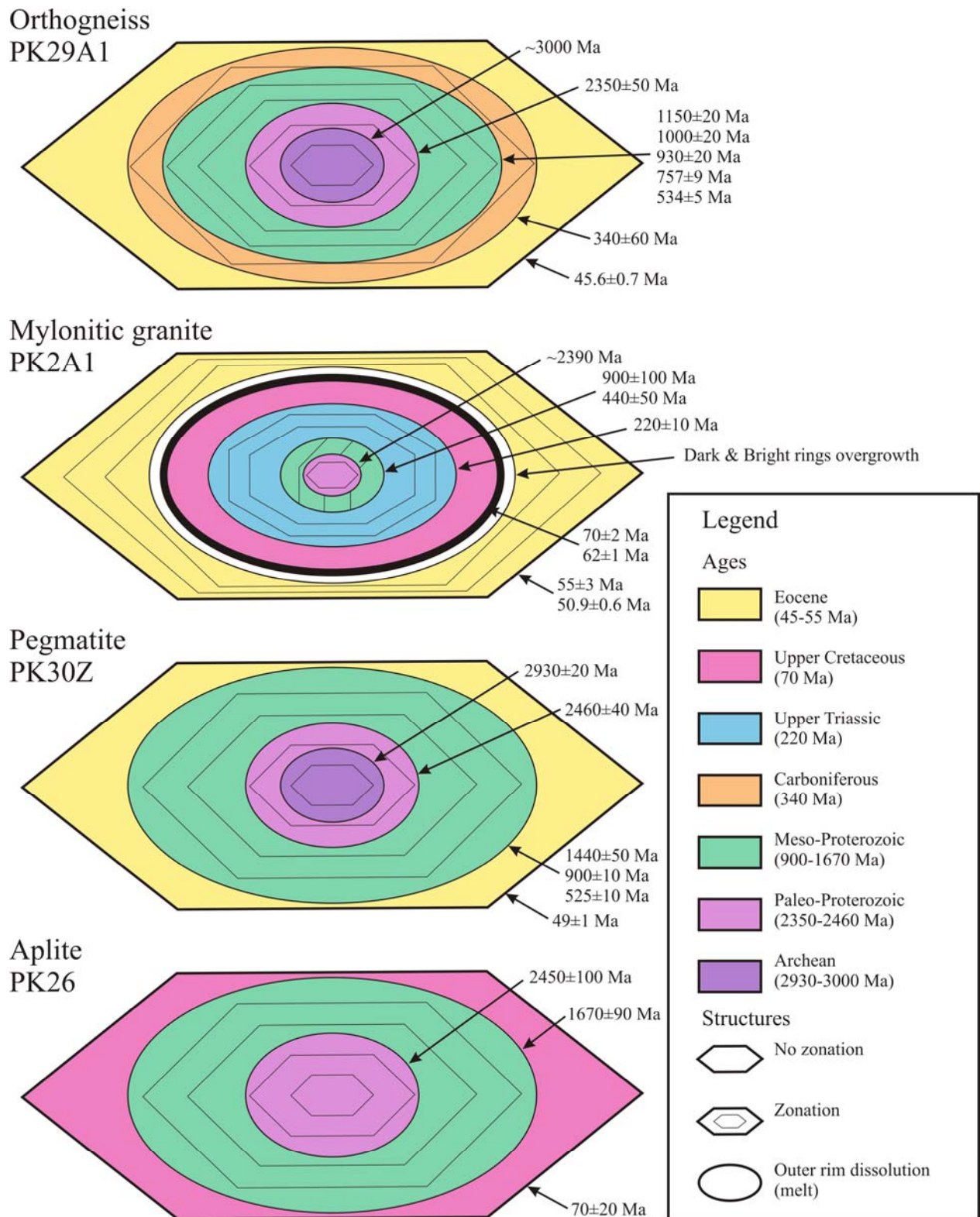


Figure 5.14 Sketch of zircon structure from the granitic materials in the Khlong Marui shear zone illustrates the intergrowth zoning. They share the same systematic of ages from the Pre-Cambrian core to the Eocene rim.

5.6 Geochronology Interpretation

Age model

The age results from U-Pb, Rb-Sr, and Sm-Nd dating were plotted by the geological age in Ma against the closure temperature of each mineral (Fig. 5.15). Error values are added in each age. The roughly 800°C closure temperature of garnet has been estimated from the different Sm-Nd isotope previous works (Cohen et al., 1988; Ganguly et al., 1998; Jung and Hellebrand, 2006; Thöni et al., 2008; Van Orman et al., 2002). Other cooling temperatures giving for this diagram are 750°C for zircon, 500°C for white mica, and 300°C for biotite (Armstrong et al., 1966; Jäger et al., 1967; Tilton et al., 1991). The cooling temperature is plotted in the reverse x-axis which can be implied to the depth. A linear evolution of each sample in different cooling temperature of the different mineral is assumed throughout geological time. The steep linear indicates the major exhumation time of the Khlong Marui shear zone in the Eocene.

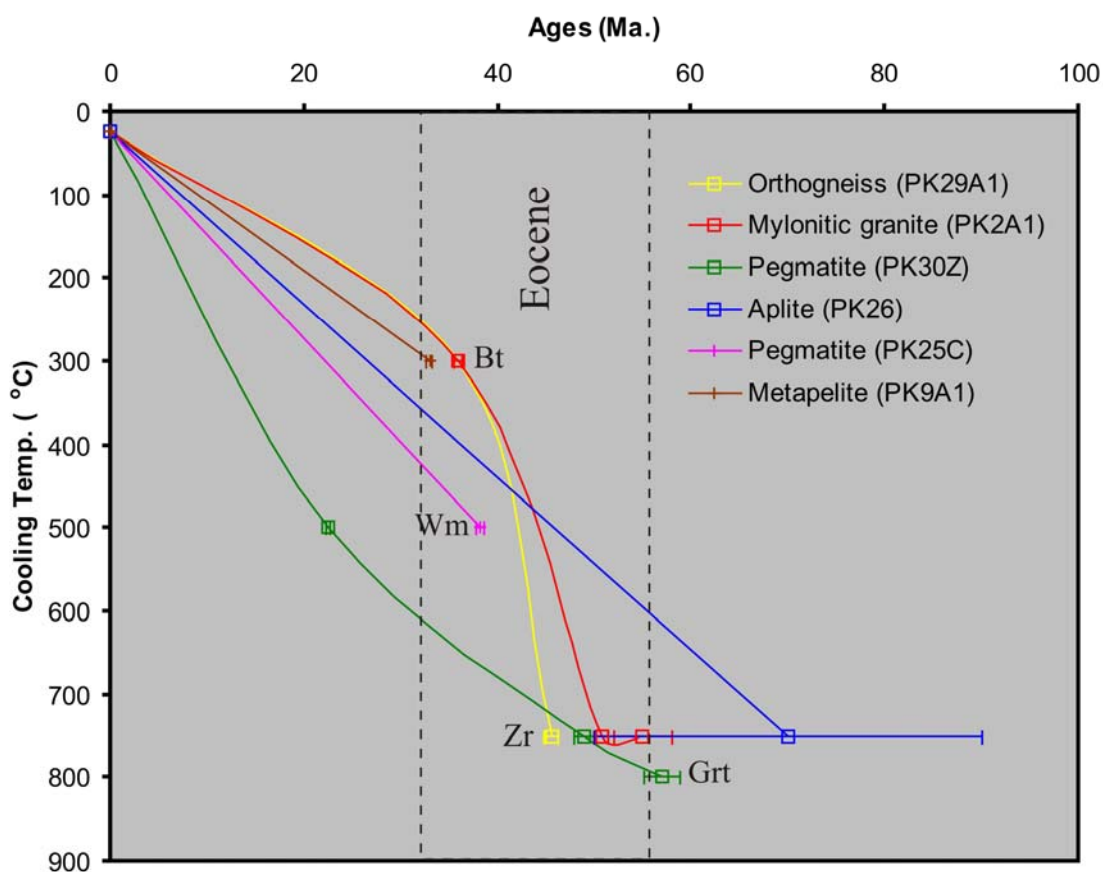


Figure 5.15 Age model plot from overall geochronology data presents the major exhumation time of the fault core is in Eocene.

The age of white mica from pegmatite sample PK30Z is isolated from the others by the effect of the grain size. The chemical compositions of white mica from 2 pegmatites were measured by the electron-microprobe. The results indicate that both pegmatites have the same composition (Fig. 5.16). The bigger grain size of white mica from sample PK252C than sample PK30Z is probably affected the different ages of the pegmatites in the area (Fig. 5.17).

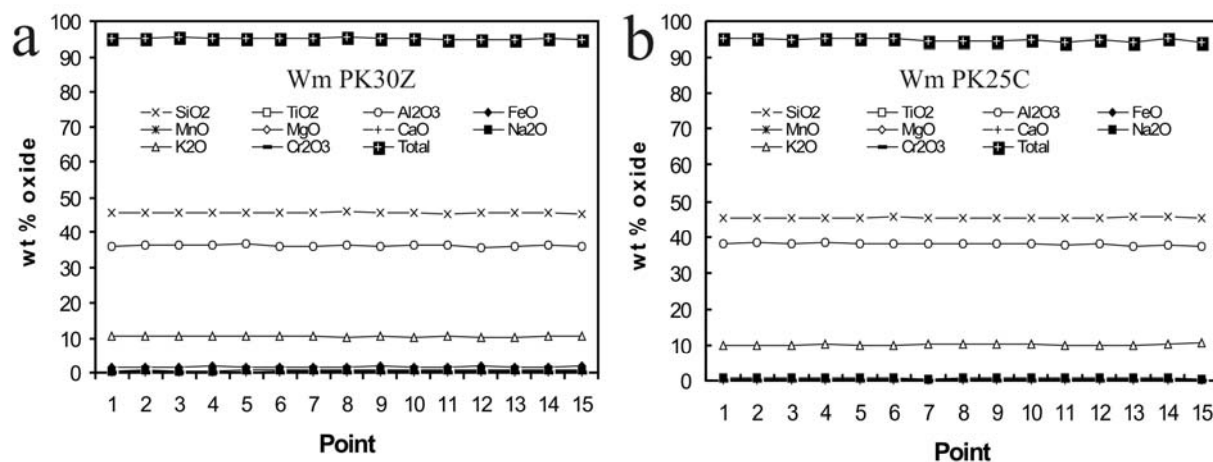


Figure 5.16 White mica composition of (a) sample PK30Z and (b) sample PK252C from electron-microprobe measurement.

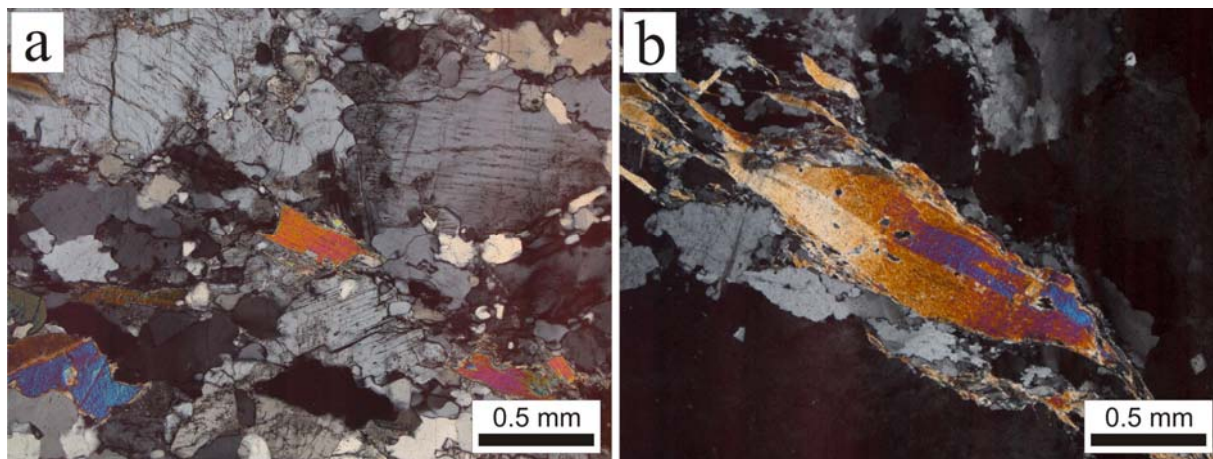


Figure 5.17 Different sizes of white mica grain from 2 pegmatites; (a) small white mica of sample PK30Z; and (b) big white mica of sample PK252C.

Granitic material origin

According to the ages of zircons from the granitic materials, all samples share the same systematic ages although the mylonitic granite sample PK2A1 has the different intergrowth zoning from others (Fig. 5.14). The same age of inherited core indicates that they have the same material from the Archean period with the different evolution. It is supported by the $\epsilon\text{Nd}(t)$ value of -17.85 from Sm-Nd isotope analysis which suggested that gargets crystallize from the old crustal material. The orthogneiss sample PK29A1 was partial melted and intruded as granite which deformed to a mylonitic granite sample PK2A1 in the west of the Klong Marui shear zone. The Upper Triassic to Upper Cretaceous outer core zircon ages is probably related to the granite intrusion period (Fig. 5.14). This interpretation fits with the ages of granitoid rocks around the Khlong Marui shear zone based on the previous geochronology works (Fig. 5.1). The pegmatite sample PK30Z and aplite sample PK26 were melted from the orthogneiss sample PK29A1 and intrude nearby their origin during the shear event.

Chapter 6

Discussions

In the following discussions the results from remote sensing interpretation, structural field work, microstructures, and geochronology are discussed and interpreted in terms of deformation phases, paleostress, and geodynamic evolution.

6.1 Deformation Phases

The Khlong Marui shear zone record a polyphases deformation history both in the ductile core and the brittle fault structures. Three deformation D_{n-2} , D_{n-1} , and D_n are identified.

D_{n-2} and D_{n-1}

The early two phases of strike-slip deformation have similar orientation of strike 030° and dips to WNW and ESE. Both deformation phases are characterized by dextral ductile deformation but under different metamorphic grades. Quartz textures clearly demonstrate that high metamorphic deformation D_{n-2} had been overprinted by D_{n-1} at the lower temperature. The two stretching lineations recorded in the quartzite support a polyphases dextral deformation in the area. D_{n-2} is preserved in isolated block of fibrolitic sillimanite mylonites which indicate that the rocks have experienced amphibolite metamorphic condition before overprinted by D_{n-1} . Grain boundary migration (GBM) and the maxima at the center in stereographic plots of quartz texture represent the first higher temperature deformation phase.

D_{n-1} dominates the deformation in the Khlong Marui Faults and is best preserved in the orthogneisses, mylonitic granites, and mylonites. Microstructures and mineral assemblages suggest that deformation occurred under low to medium greenschist facies. This deformation also forms the major lineament, foliation, and stretching lineation. Mylonitic foliation (C), secondary synthetic foliations (C'), and lineation indicate dextral sense of shear as well as σ -shaped clasts, domino-type boudinage, shear band-type foliation, asymmetric folds, asymmetric myrmekite, and "V"-pull-apart. Dynamically recrystallizing quartz records undulose extinction, basal gliding, bulging (BLG), subgrain rotation (SGR) and local grain boundary migration (GBM), and confirms the dextral strike-slip deformation during low-grade ductile conditions. Mean vorticity number (W_m) of quartz texture suggests simple shear flow type in a transpression zone. Strain partitioning within the Khlong Marui shear zone is responsible for local transtension blocks.

Dextral deformation continues also during cooling and exhumation of the shear zone at mid-to-upper crustal levels forming positive flower structures. Pegmatitic rock bodies intruded into the shear zone during this phase. The similar zoning patterns and ages in zircon, from the pegmatites and the orthogneisses indicate that the pegmatites were derived from the orthogneiss material. Based on the geochronology results, the major period of the cooling and exhumation is in the Eocene. ENE-WSE and NW-SE Riedel shear of D_{n-1} are presented at all scales including macroscopic, mesoscopic, and microscopic scales. Major joints striking 110° but do not form

lineaments visible in remote sensing pictures. These joints are interpreted to represent tension fractures perpendicular to the 030° stretching lineation.

D_n

The last deformation phase involves the brittle normal faulting dominantly oriented striking between 000° and 030°. The fabric of the preceding dextral ductile phases is used as pre-existing anisotropic planes. The steeply dipping faults are associated with proto-cataclasites to cataclasites along both side of the ductile core. Normal fault component is suggested by the slickenside, striation, and associated shear sense indicators. The faults in the area are geomorphically expressed by the fault scarp, triangular facets, and linear valley. There is no clear evidence of sinistral movement of the fault during D_n phase.

6.2 Palaeostress Field Reconstruction

The kinematic of shear and fractures is analyzed in order to understand the stress field dominating the area. The NNE striking dextral shearing, the major fracture, and two secondary fractures constrain the orientation of the maximum principal stress axis (σ_1) in the E-W direction of D_{n-2} and D_{n-1} (Fig. 6.1a). The data suggest that the tensional stress, represented by σ_3 , is oriented in the N-S direction.

On the other hand, the normal fault of D_n indicated that σ_1 is in N-S direction and σ_3 is oriented E-W (Fig. 6.1b).

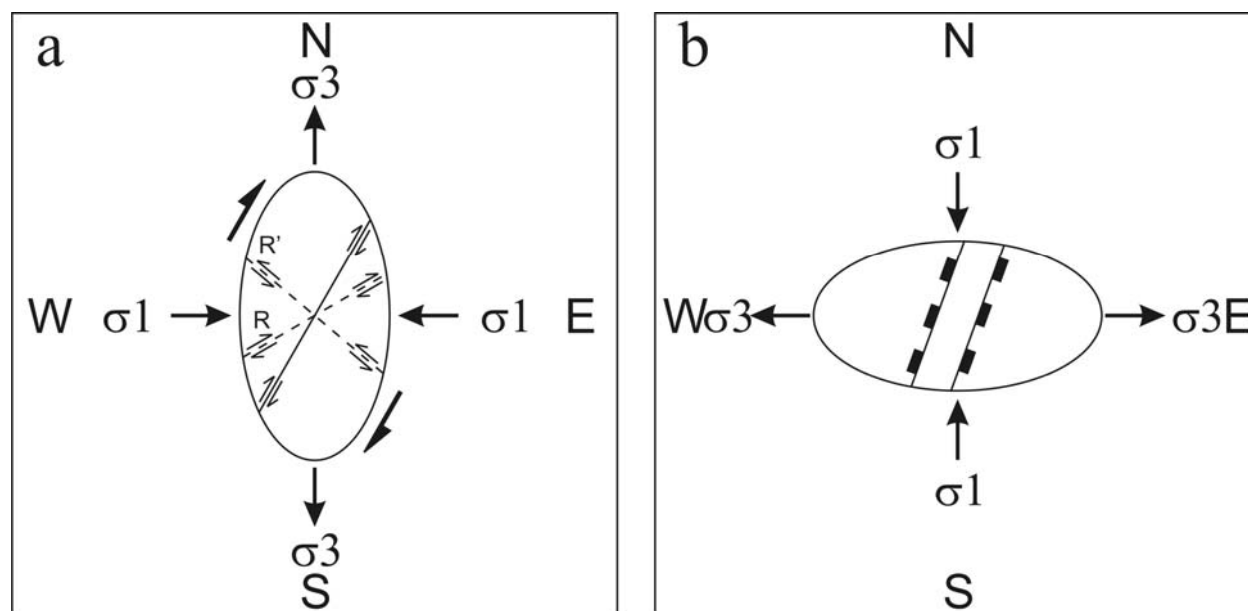


Figure 6.1 Integrated kinematic analyses indicated the E-W maximum principal stress axis (σ_1) with N-S tensional stress (σ_3) of D_{n-2} and D_{n-1} (a) before changing stress pattern to N-S maximum principal stress axis (σ_1) of D_n (b).

6.3 Tectonics Implication

This section discusses the tectonic significance of the structural results within the regional tectonic framework. The Khlong Marui Fault has been previously interpreted to form a conjugate system to the Ailao Shan-Red River Fault, Mae Ping Fault, and Three Pagodas Fault respectively (Lacassin et al., 1997; Tapponnier et al., 1986). A result of lateral extrusion accompanying the India-Asia collision had affected the dextral shear of the NNE-SSW fault system in the Eocene to Miocene followed by brittle sinistral shear in the late Miocene (Tapponnier et al., 1986).

However, many palaeogeographic reconstructions suggest a collision of the Western Burma with the Shan-Thai microcontinents in the Late Cretaceous to Early Tertiary resulting in dextral shear along NNE-SSW striking faults with associated conjugate shear fractures striking ENE-WSE and NW-SE (Bunopas, 1981; Charusiri, 1989; Charusiri et al., 2002; Hutchison, 1996; Mitchell, 1981). The Sn-W-REE rich S- and I-type Western Granite Belt is associated with this collision (Charusiri et al., 1993; Charusiri et al., 2002; Hutchison, 1996). The Western Granite intrusion and the northern Thailand orogenic event clearly coincide with the period of dextral shearing on the Khlong Marui Fault (Watkinson et al., 2008). The timing of this is consistent with the inherited core zircon ages of the mylonitic granite in the Khlong Marui shear zone. The mechanism of this collision produces an E-W shortening which fits with the palaeostress field reconstruction for the Khlong Marui dextral strike-slip system. Therefore, the two dextral ductile phases of the Khlong Marui Fault and the Western Granite magmatism were significantly influenced by the Western Burma and Shan-Thai collision in the Late Cretaceous.

Another model causing dextral shear is the subduction along the Sunda Trench (Watkinson et al., 2008). The model involves the northwards subduction of the Ceno-Tethys as India separated from Gondwana (Ramana et al., 1994; Metcalfe, 1996). The Ceno-Tethys was subducted in the Sunda Trench west of 95°E from Late Cretaceous time (Hall et al., 2008). The Khlong Marui Fault lies in the over-riding plate of this region. The dextral shear stresses of Ceno-Tethys and the Sunda Trench subduction could have been transferred upwards into the continental margin.

The continuation of dextral movement and E-W compression may have caused the exhumation of the fault core forming the positive flower structure. The major exhumation period was in the Eocene based on geochronology data. This period was tectonically influenced in the SE Asia region by the early time of India-Asia collision (Aitchison et al., 2007; Klootwijk et al., 1992; Molnar and Tapponnier, 1975; Searle et al., 1997). Therefore, the ductile core of the Khlong Marui Fault was exhumed at the same time as this collision starting. Palaeogeographic reconstructions in Eocene suggest the dextral shear of the NNE-SSW strike-slip systems (Fig. 6.2).

After Eocene, the exhumed faults related to the positive flower structure are pre-existing anisotropic in the rotated stress field producing NNE-SSW normal faults in the study area. The changing of the stress pattern involves a clockwise rotation of σ_1 from E-W to N-S caused by the India-Asia collision (Huchon et al., 1994). This collision had activated extrusion tectonics along the major strike-slip faults in Thailand including the Khlong Marui Fault (Charusiri et al., 2002; Morley, 2002). The E-W extension model, which is a result of an N-S directed maximum principle stress, fits quite well with the Cenozoic basin development in Thailand, both onshore and offshore (Briais et al., 1993; Charusiri et al., 2002; Morley, 2001, 2002; Packham, 1993; Pigott and Sattayarak, 1993; Polachan et al., 1991; Polachan and Sattayarak, 1989; Tapponnier et al., 1986). However, when the changing stress field affected the Khlong Marui Fault, the kinematics switched from dextral strike-slip to the normal faulting.

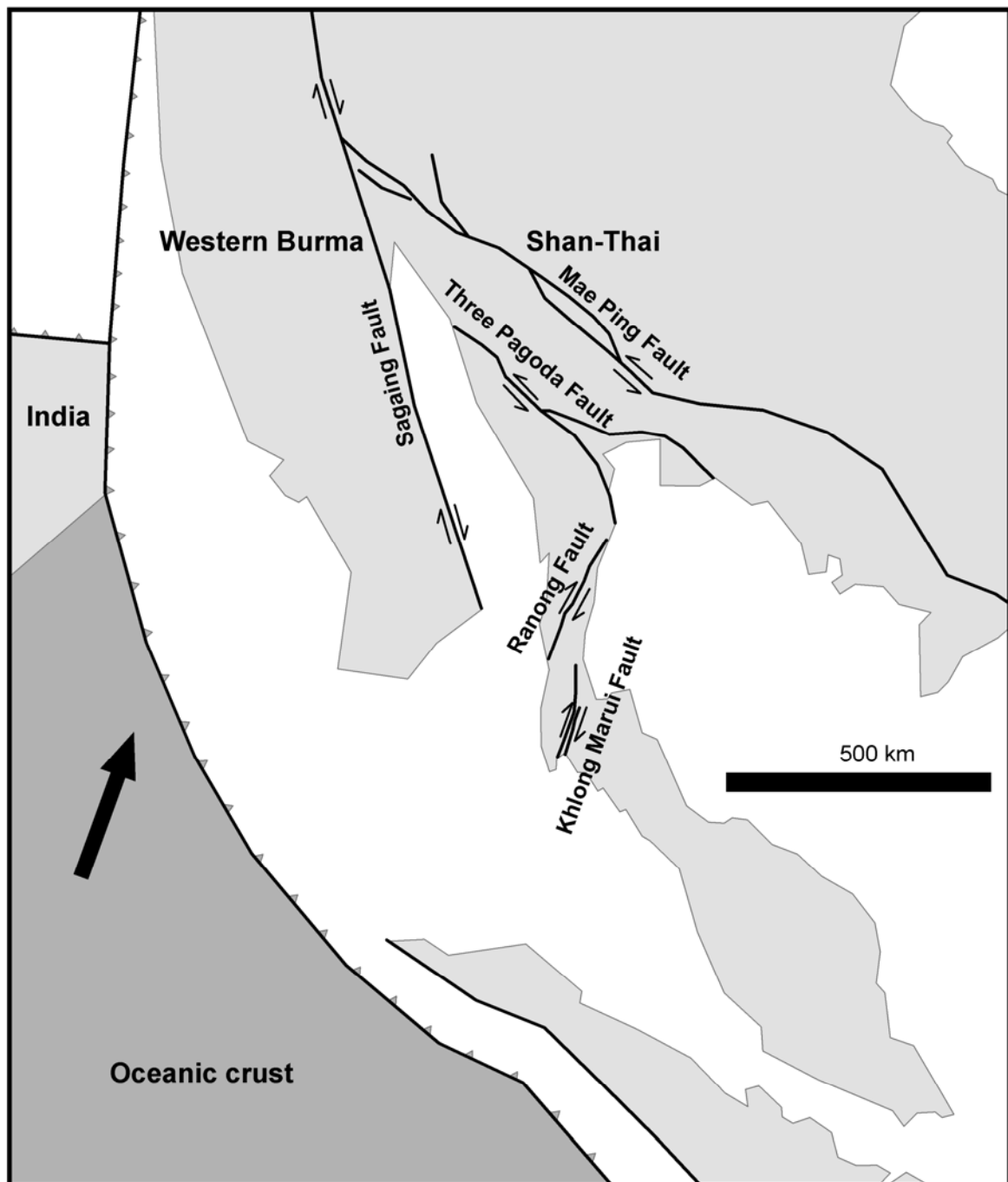


Figure 6.2 Tectonics reconstruction in Eocene based on Charusiri et al. (1993), Hall (2002), Mitchell (1993), Mitchell et al. (2007), Morley (2002), and Sarle et al. (2007). The collision between India and Asia had influenced the exhumation of the Khlong Marui ductile core.

Chapter 7

Conclusions

The results from structural analysis and geochronology suggest the kinematics of the Khlong Marui Fault. The following conclusions provide important constraints on its geology, structural style and evolution model.

- The core of the Khlong Marui Fault, the Khao Phanom area, mainly consists of mylonitic meta-sedimentary rocks associated with orthogneisses, mylonitic granites, and pegmatitic veins. The mylonite, which has been deformed and developed a mylonitic structure with varying grades of metamorphism, belongs to the Permo-Carboniferous Kaeng Krachan Group.
- Three deformation D_{n-2} , D_{n-1} , and D_n structures were recorded in the Khlong Marui shear zone. The early two phases of strike-slip deformation have similar orientation of strike 030° and dips to WNW and ESE. Both deformation phases are characterized by dextral ductile deformation but under different metamorphic grades. It is represented by the two stretching lineations recorded in the quartzite and quartz textures in the eastern Khao Phanom.
- D_{n-2} is preserved in isolated block of fibrolitic sillimanite mylonites which indicate that the rocks have experienced amphibolite metamorphic condition before overprinted by the D_{n-1} .
- D_{n-1} dominates the deformation in the Khlong Marui Faults. This deformation also forms the major lineament, foliation, and stretching lineation. Mylonitic foliation (C), secondary synthetic foliations (C'), and lineation indicate dextral sense of shear as well as σ -shaped clasts, domino-type boudinage, shear band-type foliation, asymmetric folds, asymmetric myrmekite, and "V"-pull-apart. Tension fracturing is represented by a major joint set towards 110° which is orientated perpendicular to the 030° stretching lineation.
- Synkinematic behavior of the pegmatite intrusion during the ductile stage is established by the parallel nature of tourmaline lineations in pegmatites and stretching lineations in the country rocks.
- Dynamically recrystallizing quartz records undulose extinction, basal gliding, bulging (BLG), subgrain rotation (SGR), and local grain boundary migration (GBM) under the dextral strike-slip deformation. Microstructures and mineral assemblages suggest that the rocks in the Khlong Marui shear zone have been metamorphosed at low to medium greenschist facies.

- Mean vorticity number (W_m) of quartz texture indicates simple shear flow with a small finite strain ellipsoid (R_f) in a transpression zone. Strain partitioning within the Khlong Marui shear zone is responsible for local transtension blocks.
- Mylonitic structures in this area are spectacularly overprinted by the Riedel shear fractures (R and R') and D_n . The synthetic Riedel shear fractures (R) are oriented in ENE-WSW and the associated antithetic Riedel shear fractures (R') trend to NW-SE. They are generally restricted to in between the major NNE-SSW striking faults.
- D_n involves the brittle normal faulting dominantly oriented striking between 000° and 030° . The faults in the area are geomorphically expressed by the fault scarp, triangular facets, and linear valley. The steeply dipping faults are associated with proto-cataclasites to cataclasites along both side of the ductile core. Normal fault component is suggested by the slickenside, striation, and associated shear sense indicators.
- The NNE striking dextral shearing, the major fracture, and two secondary fractures constrain the orientation of the maximum principal stress axis (σ_1) in the E-W direction of D_{n-2} and D_{n-1} . The data suggest that the tensional stress, represented by σ_3 , is oriented in the N-S direction.
- The two dextral ductile phases of the Khlong Marui Fault and the Western Granite magmatism were significantly influenced by the Western Burma and Shan-Thai collision and/or the subduction along the Sunda Trench in the Late Cretaceous.
- All zircons from the granitic materials samples share the same systematic ages although the mylonitic granite has the different intergrowth zoning from others. The same age of inherited core indicates that they have the same material from the Archean period with the different evolution. The similar zoning patterns and ages in zircon, from the pegmatites and the orthogneisses indicate that the pegmatites were derived from the orthogneiss material. The Upper Triassic to Upper Cretaceous outer core zircon ages is probably related to the granite intrusion period.
- The intense deformation conditions of rock in between un-deformed sedimentary host rock units suggests that the core of the Khlong Marui shear zone had been exhumed at mid-to-upper crustal levels to its present level. The continuation of dextral movement and E-W compression may have caused the exhumation of the fault core forming the positive flower structure.
- The major exhumation period of the ductile core in the Eocene is indicated by the steep linear in the plotting of geological age in Ma against the closure temperature of each

mineral from U-Pb, Rb-Sr, and Sm-Nd dating. Palaeogeographic reconstructions in Eocene suggest the dextral shear of the NNE-SSW strike-slip systems. This period was tectonically influenced in the SE Asia region by the early time of India-Asia collision.

- The exhumed faults related to the positive flower structure are pre-existing anisotropic in the rotated stress field producing NNE-SSW normal faults in the study area after Eocene. It is represented by the major lineament set lying along the fault scarp, linear valley, and parallel to the main stream.
- The palaeostress field of D_n , which is N-S direction of σ_1 and E-W direction of σ_3 , fits quite well with the E-W extension model. Therefore, the changing stress field in the Khlong Marui Fault, which has affected by switching from dextral strike-slip to the normal faulting, relates to the changing of the stress pattern caused by the India-Asia collision.

References

- Aitchison, J.C., Ali, J.R., Davis, A.M., 2007. When and where did India and Asia collide?. *J. Geophys. Res.* 112, B05423.
- Ampornmaha, A., 1995. Triassic carbonate rocks in the Phatthalung area, peninsular Thailand. *J. Southeast Asia Earth Sci.* 11, 225-236.
- Anczkiewicz, R., Thirlwall, M.F., 2003. Improving precision of Sm-Nd garnet dating by H₂SO₄ leaching – a simple solution to the phosphate inclusion problem. In: Vance, D., Müller, W., Villa, I.M. (Eds.), *Geochronology: linking the isotopic record with petrology and textures*. Geol. Soc. London, Spec. Publ., vol. 220, pp. 83-91.
- Armstrong, R.L., Jäger, E., Eberhardt, P., 1966. A comparison of K-Ar and Rb-Sr ages on Alpine biotites. *Earth Planet. Sci. Lett.* 1, 13-19.
- Beckinsale, R.D., Suensilpong, S., Nakapadungrat, S., Walsh, J.N., 1979. Geochronology and geochemistry of granite magmatism in Thailand in relation to a plate tectonic model. *J. Geol. Soc. (London)* 136, 529-540.
- Bignell, J.D., 1972. The geochronology of the Malayan Granites. Unpublished PhD Thesis, University of Oxford, 154 pp.
- Bobyarchick, A.R., 1986. The eigenvalues of steady flow in Mohr space. *Tectonophysics* 122, 35-51.
- Briais, A., Patraie, P., Tapponnier, P., 1993. Updated interpretation of magnetic anomalies and seafloor spreading stages in the South China Sea: implications to the Tertiary tectonics of Southeast Asia. *J. Geophys. Res.* 98 (B4), 6299-6328.
- Brown, G.F., Buravas, S., Javanaphet, J., Jalichandra, N., Johnston, W.D.Jr., Sethaput, V., Taylor, G.C.Jr., 1951. Geologic reconnaissance of the mineral deposits of Thailand. *U.S. Geol. Surv. Bull.* 984, 183.
- Bunge, H.-J., 1969. *Mathematische Methoden der Texturanalyse*. Akademie Verlag, Berlin.
- Bunopas, S., 1981. Paleogeographic history of western Thailand and adjacent parts of Southeast Asia: A plate tectonic interpretation. Unpublished PhD Thesis, Victoria University of Wellington, 810 pp.
- Cohen, A.S., O’Nions, R.K., Siegenthaler, R., Griffin, W.L., 1988. Chronology of the pressure-temperature history recorded by a granulite terrane. *Contrib. Mineral. Petrol.* 96, 303-311.
- Chaodumrong, P., Chaimanee, Y., 2002. Tertiary sedimentary basins in Thailand. *Proceedings of the symposium on geology of Thailand*. Department of Mineral Resources, Bangkok, pp. 156-169.
- Charusiri, P., 1989. Lithophile Metallogenic Epochs of Thailand: A Geological and Geochronological Investigation. Unpublished PhD Thesis, Queen’s university, Kingston, Ontario, Canada, 819 pp.
- Charusiri, P., Clark, A.H., Farrad, E., Archibald, D., Charusiri, B., 1993. Granite belts in Thailand: evidence from the ⁴⁰Ar/³⁹Ar geochronological and geological syntheses. *J. Southeast Asian Earth Sci.* 8, 127-136.

- Charusiri, P., Daorerk, V., Archibald, D., Hisada, K., Ampaiwan, T., 2002. Geotectonic evolution of Thailand: A new synthesis. *J. Geol. Soc. Thailand* 1, 1-20.
- Clark, C.D, Wilson, C., 1994. Spatial analysis of lineaments. *Comput. Geosci.* 20, 1237-1258.
- Curry, J.R., 2005. Tectonics and History of the Andaman Sea region. *J. Asian Earth Sci.* 25, 187-232.
- Dickin, A.P., 2005. *Radiogenic Isotope Geology*, 2nd edn. Cambridge University Press, Cambridge.
- England, P., Houseman, G., 1986. Finite strain calculations of continental deformation 2. Comparison with the India-Asia collision zone. *J. Geophys. Res.* 91, 3664-3676.
- Fontaine, H., Suteethorn, V., 1988. Late Paleozoic and Mesozoic fossils of West Thailand and their environments. *CCOP tech. Bull.* 20, 1-108.
- Fritz, H., Dallmeyer, R.D., Neubauer, F., 1996. Thick-skinned versus thin-skinned thrusting: Rheology controlled thrust propagation in the Variscan collisional belt (The southeastern Bohemian Massif, Czech Republic – Austria), *Tectonics* 15, 1389-1413.
- Ganguly, J., Tirone, M., Hervig, R.L., 1998. Diffusion kinetics of Samarium and Neodymium in garnet, and a method of determining cooling rates of rocks. *Science* 281, 805-807.
- Garson, M.S., Mitchell, A.H.G., 1970. Transform faulting in the Thai Peninsula. *Nature* 22, 45-47.
- Garson, M.S., Young, B., Mitchell, A.H.G., Tait, B.A.R., 1975. The geology of the tin belt in peninsular Thailand around Phuket, Phangnga and Takua Pa. *Overseas Mem. Inst. Geol. Sci. Lond.* 1, Department of Mineral Resources, Bangkok, 112 pp.
- Geological map of Thailand, scale 1:250,000, 1982. Changwat Phangnga NC47-14. Department of Mineral Resources, Bangkok.
- Geological map of Thailand, scale 1:1,000,000, 1999. Department of Mineral Resources, Bangkok.
- Gilley, L.D., Harrison, T.M., Leloup, P.H., Ryerson, F.J., Lovera, O.M., Wang, J.-H., 2003. Direct dating of left-lateral deformation along the Red River shear zone, China and Vietnam. *J. Geophys. Res.* 108, 2127-2148.
- Grant, E.R., 1976. Permian brachiopods from southern Thailand. *Paleont. Soc. Mem.* 9, 1-169.
- Grasemann, B., Fritz, H., Vannay, J., 1999. Quantitative kinematic flow analysis from the Main Central Thrust Zone (NW-Himalaya, India): implications for a decelerating strain path and the extrusion of orogenic wedges. *J. Struct. Geol.* 21, 837-853.
- Hall, R., 2002. Cenozoic geological and plate tectonic evolution of SE Asia and the SW Pacific: computer-based reconstructions, model and animations. *J. Asian Earth Sci.* 20, 353-431.
- Hall, R., van Hattum, M.W.A., Spakman, W., 2008. Impact of India-Asia collision on SE Asia: the record in Borneo. *Tectonophysics* 451, 366-389.
- Harrison, D, Chaodumrong, P., Charusribandhu, M., 1997. Assessment of Limestone Resources from Suratthani Province, Thailand. In: Dheeradilok, P. (Ed. in chief), *Proceedings of the International Conference on Southeast Asia and the South Pacific*. Bangkok, vol. 2, pp. 640-649.

- Herwegh, M., Handy, M.R., 1998. The origin of shape preferred orientations in mylonite: inferences from in-situ experiments on polycrystalline norcamphor. *J. Struct. Geol.* 20, 681-694.
- Herwegh, M., Handy, M.R., Heilbronner, R., 1997. Temperature- and strain rate-dependent microfabric evolution in monomineralic mylonite: evidence from in-situ deformation of norcamphor. *Tectonophysics* 280, 83-106.
- Hippertt, J.F.M., 1993. "V"-pull-apart microstructures: a new shear sense indicator. *J. Struct. Geol.* 15, 1393-1403.
- Huchon, P., Le Pichon, X., Rangin, C., 1994. Indochina peninsula and the collision of India and Eurasia. *Geology* 22, 27-30.
- Hutchison, C.S., 1996. Geological evolution of South-East Asia. *Geol. Soc. Malays.*, Kuala Lumpur, 368 pp.
- Ishihara, S., Sawata, H., Shibata, K., Terashima, S., Arrykul, S., Sato, K., 1980. Granites and Sn-W deposits of Peninsular Thailand. *Mining Geol., Spec. Issue* 8, 223-241.
- Jäger, E., Niggli, E., Wenk, E., 1967. Rb-Sr Altersbestimmungen an Glimmern der Zentralalpen. *Beitr. Geol. Karte Schweiz* 134, N.F., Bern.
- Javanaphet, J.C., 1969. Geological map of Thailand, scale 1:1,000,000. Department of Mineral Resources, Bangkok.
- Jung, S., Hellebrand, E., 2006. Trace element fractionation during high-grade metamorphism and crustal melting-constraints from ion microprobe data of metapelitic, migmatitic and igneous garnets and implications for Sm-Nd garnet chronology. *Lithos* 87, 193-213.
- Klootwijk, C.T., Gee, J.S., Peirce, J.W., Smith, G.M., McFadden, P.L., 1992. An early India-Asia contact; palaeomagnetic constraints from Ninetyeast Ridge, ODP Leg 121; with suppl. Data 92-15. *Geology* 20, 395-398.
- Kornsawan, A., Morley, C.K., 2002. The origin and evolution of complex transfer zones (graben shifts) in conjugate fault systems around the Funan Field, Pattani Basin, Gulf of Thailand. *J. Struct. Geol.* 24, 435-449.
- Lacassin, R., Maluski, H., Leloup, P.H., Tapponnier, P., Hinthong, C., Siribhakdi, K., Chauviroj, S., Charoenravat, A., 1997. Tertiary diachronic extrusion and deformation of western Indochina: Structure and $^{40}\text{Ar}/^{39}\text{Ar}$ evidence from NW Thailand. *J. Geophys. Res.* 102 (B5), 10013-10037.
- Law, R.D., Schmid, S.M., Wheeler, J., 1990. Simple-shear deformation and quartz crystallographic fabrics: a possible natural example from the Torridon area of NW Scotland. *J. Struct. Geol.* 12, 29-45.
- Leloup, P.H., Arnaud, N., Lacassin, R., Kienast, J.R., Harrison, T.M., Phan Trong, T.T., Replumaz, A., Tapponnier, P., 2001. New constraints on the structure, thermochronology, and timing of the Ailao Shan-Red River shear zone, SE Asia. *J. Geophys. Res.* 106, 6683-6732.

- Leloup, P.H., Lacassin, R., Tapponnier, P., Schärer, U., Dalai, Z., Xiaohan, L., Liangshang, Z., Shaocheng, J., Trinh, P.T., 1995. The Ailao Shan-Red River shear zone (Yunnan, China), Tertiary transform boundary of Indochina. *Tectonophysics* 251, 3-84.
- Lister, G.S., Hobbs, B.E., 1980. The simulation of fabric development during plastic deformation and its application to quartzite: the influence of deformation history. *J. Struct. Geol.* 2, 355-370.
- Mazin, J.M., Suteethorn, V., Buffetaut, E., Jaejer, J.J., Helmcke-Ingavat, R., 1991. Preliminary description of *Thaisaurus chonglakmai* n.g., n.sp., a new ichthyopterygian (Reptilia) from the Early triassic of Thailand. *Comptes Rendus de l'Académie des Sciences de Paris, series II*, 313, 1207-1212.
- Metcalf, I., 1991. Late Palaeozoic and Mesozoic palaeogeography of Southeast Asia. *Palaeogeogr., Palaeoclimatol., Palaeoecol.* 87, 211-221.
- Metcalf, I., 1996. Pre-Cretaceous evolution of SE Asian terranes. In: Hall, R., Blundell, D. (Eds.), *Tectonic Evolution of Southeast Asia*. Geol. Soc. London, Spec. Publ., vol. 106, pp. 97-122.
- Mitchell, A.H.G., 1981. Phanerozoic plate boundary in mainland SE Asia, the Himalayas, and Tibet. *J. Geol. Soc. (London)* 138, 109-122.
- Mitchell, A.H.G., 1993. Cretaceous-Cenozoic tectonic events in the western Myanmar (Burma)-Assam region. *J. Geol. Soc. (London)* 150, 1089-1102.
- Mitchell, A.H.G., Htay, M.T., Htun, K.M., Win, M.N., Oo, T., Hlaing, T., 2007. Rock relationships in the Mogoke metamorphic belt, Tatkon to Mandalay, central Myanmar. *J. Asian Earth Sci.* 29, 891-910.
- Molnar, P., Tapponnier, P., 1975. Cenozoic tectonics of Asia: effects of a continental collision. *Science* 189, 419-426.
- Morley, C.K., 2001. Combined escape tectonics and subduction rollback-back arc extension: a model for the evolution of Tertiary rift basins in Thailand, Malaysia, and Laos. *J. Geol. Soc. (London)* 158, 461-474.
- Morley, C.K., 2002. A tectonic model for the Tertiary evolution of strike-slip faults and rift basins in SE Asia. *Tectonophysics* 347, 189-215.
- Morley, C.K., 2007. Variations in Late Cenozoic-Recent strike-slip and oblique-extensional geometries, with in Indochina: The influence of pre-existing fabrics. *J. Struct. Geol.* 29, 36-58.
- Morley, C.K., Westaway, R., 2006. Subsidence in the super-deep Pattani and Malay basins of Southeast Asia: a coupled model incorporating lower-crustal flow in response to post-rift sediment loading. *Basin Res.* 18, 51-84.
- Nakapadungrat, S., Beckinsale, R.D., Suensilpong, S., 1984. Geochronology and geology of Thai granites. *Proceedings of the Conference on Applications of Geology and the National Development*. Chulalongkorn University, Bangkok, 75-93.

- Packham, G.H., 1993. Plate tectonics and the development of sedimentary basins of the dextral regime in western Southeast Asia. *J. Southeast Asian Earth Sci.* 8, 497-511.
- Passchier, C.W., 1986. Flow in natural shear zones-the consequences of spinning flow regimes. *Earth Planet. Sci. Lett.* 77, 70-80.
- Passchier, C.W., Trouw, R.A.J., 2006. *Microtectonics*, 2nd edn. Springer-Verlag, Heidelberg, Berlin.
- Pigott, J.D., Sattayarak, N., 1993. Aspects of sedimentary basin evolution assessed through tectonic subsidence analysis. Example: northern Gulf of Thailand. *J. Southeast Asian Earth Sci.* 8, 407-420.
- Pitakpaivan, K., 1969. Tin bearing granite and tin barren granite in Thailand. 2nd Tech. Conf. On Tin, Tin council, Bangkok, 283-297.
- Piyasin, S., 1975. Stratigraphy and sedimentology of the Kaeng Krachan Group (Carboniferous). In: Stokes, R.B., Tantisukrit, C., Campbell, K.V. (Eds.), *Proceedings of the Conference on the geology of Thailand*. Chiang Mai University, Chiang Mai, pp. 25-36.
- Platt, J.P., Behrmann, J.H., 1986. Structures and fabrics in a crustal-scale shear zone, Betic Cordillera, SE Spain. *J. Struc. Geol.* 8, 15-33.
- Polachan, S., Praditnan, S., Tongtaow, C., Janmaha, S., Intarawijitr, K., Sansuwan, C., 1991. Development of Cenozoic basins in Thailand. *Mar. Pet. Geol.* 8, 84-97.
- Polachan, S., Sattayarak, N., 1989. Strike-slip tectonics and the development of Tertiary basins in Thailand. In: Thanasuthipitak, T., Ounchanum, P. (Eds.), *Proceedings of the International symposium on intermontane basins: Geology and resources*. Chiang Mai University, Chiang Mai, pp. 243-253.
- Putthapiban, P., 1984. Geochemistry and geochronology of Phuket granite, Thailand. Unpublished PhD Thesis, La Trobe University, Melbourne, 414 pp.
- Rangin, C., Huchon, P., Le Pichon, X., Bellon, H., Lepvrier, C., Roques, D., Hoe, N.D., Quynh, P.V., 1995a. Cenozoic deformation of central and south Vietnam. *Tectonophysics* 251, 179-196.
- Rangin, C., Klein, M., Roques, D., Le Pichon, X., Van Trong, L., 1995b. The red River fault system in the Tonkin Gulf, Vietnam. *Tectonophysics* 243, 209-222.
- Raksaskulwong, L., Wongwanich, T., 1993. Stratigraphy of the Kaeng Krachan Group in peninsula and western Thailand. Department of Mineral Resources, Bangkok. (in Thai)
- Ramana, M.V., Nair, R.R., Sarma, K.V.L.N.S., Ramprasad, T., Krishna, K.S., Subrahmanyam, V., D'Cruz, M., Subrahmanyam, C., Paul, J., Subrahmanyam, A.S., Chandra Sekhar, D.V., 1994. Mesozoic anomalies in the Bay of Bengal. *Earth Planet. Sci. Lett.* 121, 469-475.
- Ree, J.H., 1991. An experimental steady-state foliation. *J. Struc. Geol.* 13, 1001-1011.
- Robin, P.-Y.F., Jowett, E.C., 1986. Computerized density contouring and statistical evaluation of orientation data using counting circles and continuous weighting functions. *Tectonophysics* 121, 207-233.

- Roe, R.J., 1965. Description of crystallite orientation of polycrystalline materials. II. General solution to pole figure inversion. *J. Appl. Phys.* 37, 2069-2072.
- Sabins, F.F., 1997. Remote sensing: principles and interpretation, 3rd edn. W.H. Freeman and Co., New York.
- Sakagami, S., 1970. Addition to the Permian Bryozoa from Ko Muk, Peninsular Thailand. *Geol. Palaeont. Southeast Asia* 8, 43-68.
- Schwartz, M.O., Rajah, S.S., Askury, A.K., Putthapiban, P., Djaswadi, S., 1995. The southeast Asian tin belt. *Earth Sci. Rev.* 23, 95-293.
- Searle, M.P., 2006. Role of the Red River Shear zone, Yunnan and Vietnam, in the continental extrusion of SE Asia. *J. Geol. Soc. (London)* 163, 1025–1036.
- Searle, M.P., Corfield, R.I., Stephenson, B., McCarron, J., 1997. Structure of the North Indian continental margin in the Ladakh-Zaskar Himalayas: implications for the timing of obduction of the Spontang ophiolite, India–Asia collision and deformation events in the Himalaya. *Geol. Mag.* 134, 297–316.
- Searle, M.P., Noble, S.R., Cottle, D.J., Waters, D.J., Mitchell, A.H.G., Hlaing, T., Horstwood, M.S.A., 2007. Tectonic evolution of the Mogoke metamorphic belt, Burma (Myanmar) constrained by U-Th-Pb dating of metamorphic and magmatic rocks. *Tectonics* 26, TC3014.
- Simpson, C., Wintsch, R.P., 1989. Evidence for deformation-induced K-feldspar replacement by myrmekite. *J. Met. Geol.* 7, 261-275.
- Sláma, J., Kosler, J., Condon, D.J., Crowley, J.L., Gerdes, A., Hancher, J.M., Horstwood, M.S.A., Morris, G.A., Nasdala, L., Norberg, N., Schaltegger, U., Schoene, B., Tubrett, M.N., Whitehouse, M.J., 2008. Plešovice zircon — A new natural reference material for U–Pb and Hf isotopic microanalysis, *Chem. Geol.* 249, 1-35.
- Schmid, S.M., Casey, M., 1986. Complete fabric analysis of some commonly observed quartz *c*-axis patterns. *Geophys. Monogr., Am. Geophys. Union* 36, 263-286.
- Stacey, J.S., Kramers, J.D., 1975. Approximation of terrestrial lead isotope evolution by a two-stage model. *Earth Planet. Sci. Lett.* 26, 207-221.
- Sylvester, P.J., Ghaderi, M., 1997. Trace element analysis of scheelite by excimer laser ablation-inductively coupled plasma-mass spectrometry (ELA-ICP-MS) using a synthetic silicate glass standard. *Chem. Geol.* 141, 49-65.
- Tantiwanit, W., Raksakulwong, L., Mantajit, N., 1983. The Upper Paleozoic Pebbly rocks in Southern Thailand. In: Natalaya, P. (Ed.), *Proceedings of the Workshop on Stratigraphic Correlation of Thailand and Malaysia*. Geol. Soc. Thailand, Bangkok, pp. 96-104.
- Tapponnier, P., Lacassin, R., Leloup, P.H., Schärer, U., Zhong, D., Wu, H., Liu, X., Ji, S., Zhang, L., Zhong, J., 1990. The Ailao Shan/Red River metamorphic belt: Tertiary left-lateral shear between Indochina and South China. *Nature* 343, 431-437.
- Tapponnier, P., Peltzer, G., Armijo, R., 1986. On the mechanism of collision between India and Asia. In: Coward, M.P., Ries, A.C. (Eds.), *Collision Tectonics*. Geol. Soc. London, Spec. Publ., vol.19, pp. 115-157.

- Tapponier, P., Peltzer, G., Le Dain, A.Y., Armijo, R., 1982. Propagating extrusion tectonics in Asia: new insights from simple experiments with plasticine. *Geology* 10, 611-616.
- Thöni, M., Miller, C., Zanetti, A., Habler, G., Goessler, W., 2008. Sm-Nd isotope systematics of high-REE accessory minerals and major phases: ID-TIMS, LA-ICP-MS and EPMA data constrain multiple Permian-Triassic pegmatite emplacement in the Koralpe, Eastern Alps. *Chem. Geol.* 254, 216-237.
- Tilton, G.R., Schreyer, W., Schertl, H.-P., 1991. Pb-Sr-Nd isotopic behavior of deeply subducted crustal rocks from the Dora Maira Massif, Western Alps, Italy-II: what is the age of the ultrahigh-pressure metamorphism?. *Contrib. Mineral. Petrol.* 108, 22-33.
- Van Orman, J.A., Grove, T.L., Shimizu, N., Layne, G.D., 2002. Rare earth element diffusion in a natural pyrope single crystal at 2.8 GPa. *Contrib. Mineral. Petrol.* 142, 416-424.
- Vissers, R.L.M., 1989. Asymmetric quartz *c*-axis fabric and flow vorticity: a study using rotated garnets. *J. Struct. Geol.* 11, 231-244.
- Wallis, S.R., 1992. Vorticity analysis in a metachert from the Sanbagawa Belt, SW Japan. *J. Struct. Geol.* 14, 271-280.
- Wallis, S.R., 1995. Vorticity analysis and recognition of ductile extension in the Sanbagawa belt, SW Japan. *J. Struct. Geol.* 17, 1077-1093.
- Wang, E., Burchfiel, B.C., Royden, L.H., Liangzhong, C., Jishen, C., Wenzin, L., Zhiliang, C., 1998. Late Cenozoic Xianshuihe-Xiaojiang, Red River and Dali fault systems of Southwestern Sichuan and Central Yunnan, China. *Geol. Soc. Am. Spec. Pap.* 327, 108 pp.
- Wang, P., Lo, C., Chung, S., Lee, T., Lan, C., Thang, T.V., 2000. Onset timing of left-lateral movement along the Ailao Shan-Red River Shear Zone: $^{40}\text{Ar}/^{39}\text{Ar}$ dating constraint from the Nam Dinh Area, northeastern Vietnam. *J. Asian Earth Sci.* 18, 281-292.
- Wang, Y., Fan, W., Zhang, Y., Peng, T., Chen, X., Xu, Y., 2006. Kinematics and $^{40}\text{Ar}/^{39}\text{Ar}$ geochronology of the Gaoligong and Chongshan shear systems, western Yunnan, China: Implication for early Oligocene tectonic extrusion of SE Asia. *Tectonophysics* 418, 235-254.
- Waterhouse, I.B., Pitakpaivan, K., Mantajit, N., 1981. The Permian Stratigraphy and paleontology of Southern Thailand. *Geol. Sur. Mem.* 4, Department of Mineral Resources, Bangkok, 213 pp.
- Watkinson, I., Elders, C., Hall, R., 2008. The kinematic history of the Khlong Marui and Ranong Faults, southern Thailand. *J. Struct. Geol.* 30, 1554-1571.
- Wenk, H. -R., 1985, Measurement of pole figures. In: Wenk, H.-R. (Ed.), *Preferred Orientation in Deformed Metals and Rocks*. Academic Press, Orlando, pp. 11-47.
- Wiedenbeck, M., Allé, P., Corfu, F., Griffin, W.L., Meier, M., Oberli, I., Quadt, A., Roddick, J.C., Spiegel, W., 1995. Three natural zircon standards for U-Th-Pb, Lu-Hf, trace element and REE analyses. *Geostand. Newslett.* 19, 1-23.
- Xypolias, P., 2009. Some new aspects of kinematics vorticity analysis in naturally deformed quartzites. *J. Struct. Geol.* 31, 3-10.

References

- Yanagida, I., 1970. Permian brachiopods from Khao Phrik, near Ratburi, Thailand. Geol. Palaeont. Southeast Asia 8, 69-96.

Appendix

A: Abbreviations

B: Sample Location

C: Data for LA-ICP-MS U-Pb Analysis of Zircon

Appendix A: Abbreviations

Abbreviation for minerals, after Kretz (1983), extended by Bucher & Frey (1994), and further abbreviations:

Bt	Biotite
Chl	Chlorite
Grt	Garnet
Hb	Hornblende
Kfs	K-feldspar
Pl	Plagioclase
Qtz	Quartz
Sil	Sillimanite
Tur	Tourmaline
Wm	White mica
Zrn	Zircon

BLG	Bulging
CPL	Cross polarized light
DEM	Digital elevation model
GBM	Grain boundary migration
GIS	Geographic information system
IR	Infrared
PPL	Plane polarized light
REE	Rare earth elements
SGR	Subgrain rotation
SRTM	Shuttle Radar Topography Mission
TM	Theamatic mapper
wr	Whole rock

D_x deformation event(s) where x indicates the number of specific deformation phase in their relative chronological order

S_x foliation planes of D_x

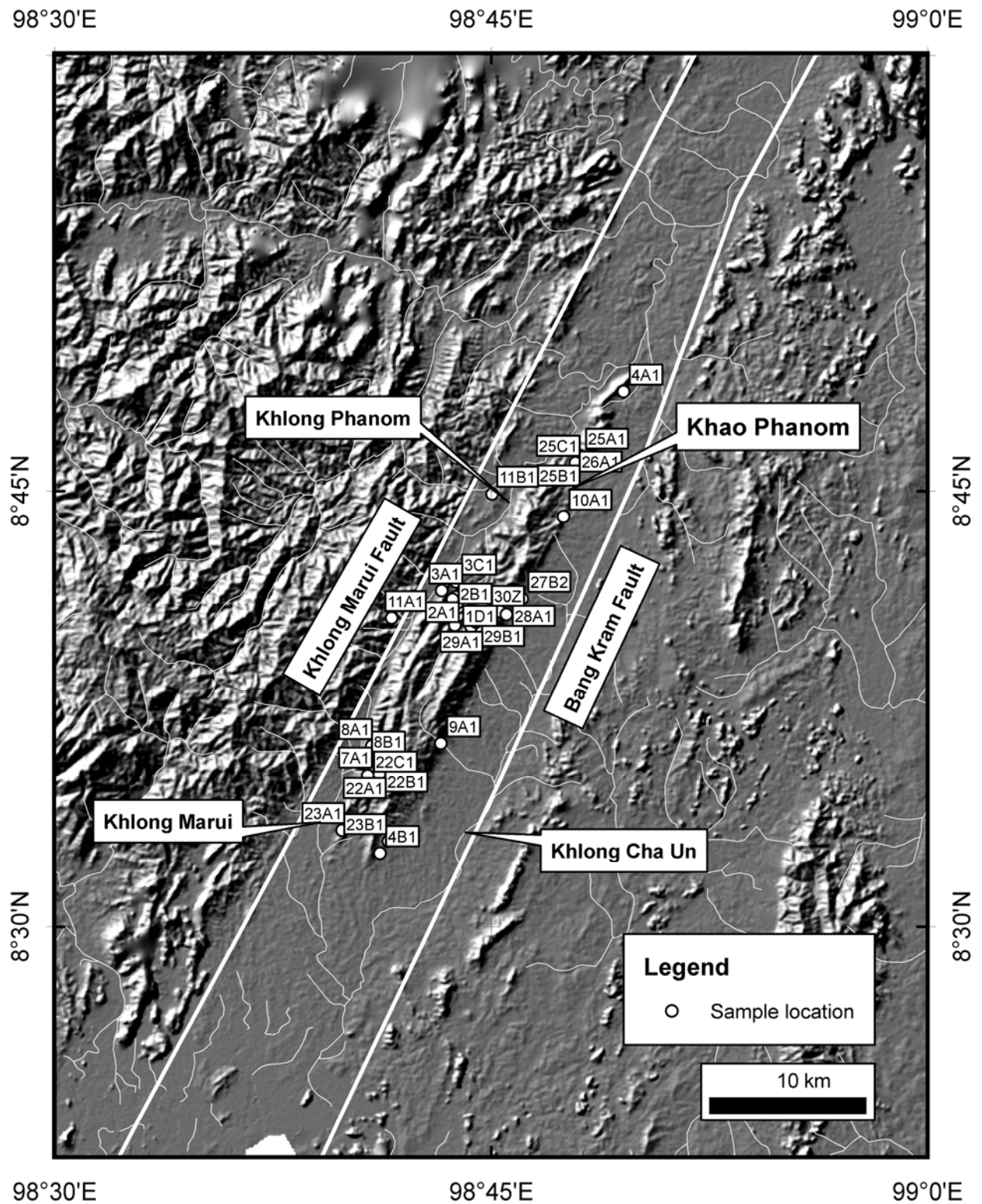
L_x mineral lineation on S_x planes

n number of data

f fault planes

s striations

Appendix B: Sample Location



Appendix C: Data for LA-ICP-MS U-Pb Analysis of Zircon

Sample PK29A1

Concordia age ~3000 Ma

Sample No.	$^{207}\text{Pb}/^{235}\text{U}$	2RSE(%)	$^{206}\text{Pb}/^{238}\text{U}$	2RSE(%)	Rho
pk29a1_pop1_15b	17.6404	16.589	0.6189	17.229	0.52
pk29a1_pop1_15a	18.3239	3.313	0.6472	3.379	0.51

Concordia age 2350±50 Ma

Sample No.	$^{207}\text{Pb}/^{235}\text{U}$	2RSE(%)	$^{206}\text{Pb}/^{238}\text{U}$	2RSE(%)	Rho
pk29a1_pop2_26b	8.4905	10.116	0.4067	9.800	0.48
pk29a1_pop2_29b	8.5253	7.539	0.3991	8.469	0.56
pk29a1_pop2_29a	8.7063	15.178	0.4159	15.205	0.50
pk29a1_pop2_26a	8.8851	9.341	0.4109	9.400	0.50
pk29a1_pop2_15a	9.6399	12.165	0.4548	12.723	0.52
pk29a1_pop2_15b	9.7656	5.014	0.4619	5.012	0.50

Concordia age 1150±20 Ma

Sample No.	$^{207}\text{Pb}/^{235}\text{U}$	2RSE(%)	$^{206}\text{Pb}/^{238}\text{U}$	2RSE(%)	Rho
pk29a1_pop1_14a	1.9078	14.970	0.1977	12.950	0.43
pk29a1_pop1_16a	1.9174	5.547	0.1793	6.098	0.55
pk29a1_pop1_12a	1.9936	6.429	0.1944	5.750	0.45
pk29a1_pop2_12b	2.0016	66.247	0.1695	104.932	0.79
pk29a1_pop1_12b	2.0225	6.227	0.1970	4.926	0.40
pk29a1_pop2_08c	2.1322	11.522	0.2000	11.896	0.52
pk29a1_pop2_10	2.1397	5.131	0.1994	6.864	0.67
pk29a1_pop2_08a	2.1879	4.309	0.2053	5.209	0.60
pk29a1_pop1_13b	2.2222	4.472	0.2056	4.471	0.50
pk29a1_pop2_12a	2.2297	11.859	0.1993	13.708	0.58
pk29a1_pop2_08b	2.2508	8.782	0.2140	6.899	0.39
pk29a1_pop1_13a	2.3647	19.789	0.2086	24.107	0.61
pk29a1_pop2_14b	2.6560	100.134	0.2114	63.191	0.32

Concordia age 1000±20 Ma

Sample No.	$^{207}\text{Pb}/^{235}\text{U}$	2RSE(%)	$^{206}\text{Pb}/^{238}\text{U}$	2RSE(%)	Rho
pk29a1_pop2_09a	1.6390	3.922	0.1679	2.906	0.37
pk29a1_pop1_04a	1.6522	11.854	0.1649	11.951	0.50
pk29a1_pop1_03b	1.6619	12.158	0.1668	6.752	0.28
pk29a1_pop1_04b	1.7480	15.784	0.1754	18.604	0.59
pk29a1_pop2_30	1.7729	14.160	0.1722	14.161	0.50
pk29a1_pop2_25	1.8306	23.609	0.1546	29.821	0.63

pk29a1_pop2_21b	1.8543	14.868	0.1786	15.238	0.51
-----------------	--------	--------	--------	--------	------

Concordia age 930±20 Ma

Sample No.	$^{207}\text{Pb}/^{235}\text{U}$	2RSE(%)	$^{206}\text{Pb}/^{238}\text{U}$	2RSE(%)	Rho
pk29a1_pop1_02b	1.4395	5.459	0.1556	5.537	0.51
pk29a1_pop1_02a	1.4925	4.136	0.1621	4.259	0.51
pk29a1_pop2_21a	1.4963	7.399	0.1428	11.930	0.81
pk29a1_pop1_20a	1.5365	10.395	0.1560	9.727	0.47
pk29a1_pop2_23	1.5755	8.213	0.1578	7.383	0.45

Concordia age 757±9 Ma

Sample No.	$^{207}\text{Pb}/^{235}\text{U}$	2RSE(%)	$^{206}\text{Pb}/^{238}\text{U}$	2RSE(%)	Rho
pk29a1_pop2_18b	0.9761	11.004	0.1168	8.888	0.40
pk29a1_pop2_13a	1.0489	9.925	0.1200	7.120	0.36
pk29a1_pop2_04a	1.1036	2.632	0.1237	1.820	0.35
pk29a1_pop2_04b	1.1051	41.686	0.1206	56.904	0.68
pk29a1_pop2_11a	1.1248	3.798	0.1243	3.906	0.51
pk29a1_pop2_11b	1.1791	4.996	0.1295	7.961	0.80
pk29a1_pop1_03a	1.1955	19.673	0.1272	13.156	0.33

Concordia age 534±5 Ma

Sample No.	$^{207}\text{Pb}/^{235}\text{U}$	2RSE(%)	$^{206}\text{Pb}/^{238}\text{U}$	2RSE(%)	Rho
pk29a1_pop2_16b	0.6500	8.034	0.0836	6.978	0.43
pk29a1_pop2_17b	0.6557	14.579	0.0840	11.173	0.38
pk29a1_pop2_14c	0.6610	9.555	0.0858	7.812	0.41
pk29a1_pop2_20a	0.6742	4.248	0.0879	4.046	0.48
pk29a1_pop2_14d	0.6750	13.153	0.0855	3.774	0.14
pk29a1_pop2_05a	0.6897	2.328	0.0860	2.227	0.48
pk29a1_pop1_11b	0.6918	11.894	0.0883	8.830	0.37
pk29a1_pop2_24b	0.6936	19.479	0.0858	24.358	0.63
pk29a1_pop2_07	0.6951	14.758	0.0889	14.598	0.49
pk29a1_pop2_16a	0.6955	9.188	0.0837	7.461	0.41
pk29a1_pop1_07a	0.7017	7.737	0.0809	7.177	0.46
pk29a1_pop2_03a	0.7157	3.828	0.0881	2.293	0.30
pk29a1_pop1_11a	0.7249	10.583	0.0891	10.477	0.49
pk29a1_pop1_06b	0.7426	12.067	0.0911	10.173	0.42

Appendix

Concordia age 340 ± 60 Ma

Sample No.	$^{207}\text{Pb}/^{235}\text{U}$	2RSE(%)	$^{206}\text{Pb}/^{238}\text{U}$	2RSE(%)	Rho
pk29a1_pop2_01b	0.3597	135.155	0.0379	123.635	0.46
pk29a1_pop2_16c	0.3889	25.223	0.0466	30.926	0.61
pk29a1_pop2_19b	0.3925	67.916	0.0516	71.773	0.53
pk29a1_pop2_09b	0.4688	109.261	0.0507	134.797	0.62
pk29a1_pop2_05b	0.5128	36.491	0.0663	43.542	0.60

Concordia age 45.6 ± 0.7 Ma

Sample No.	$^{207}\text{Pb}/^{235}\text{U}$	2RSE(%)	$^{206}\text{Pb}/^{238}\text{U}$	2RSE(%)	Rho
pk29a1_pop2_20b	0.0407	18.522	0.0069	8.750	0.24
pk29a1_pop1_17b	0.0446	7.074	0.0069	4.761	0.34
pk29a1_pop1_14c	0.0448	43.637	0.0071	15.741	0.18
pk29a1_pop1_07b	0.0449	5.045	0.0071	2.536	0.25
pk29a1_pop1_19b	0.0451	7.423	0.0070	7.239	0.49
pk29a1_pop2_17c	0.0464	18.152	0.0071	13.810	0.38
pk29a1_pop2_12c	0.0491	47.163	0.0074	20.066	0.21
pk29a1_pop1_18b	0.0491	14.799	0.0071	22.034	0.74
pk29a1_pop1_04c	0.0493	12.849	0.0072	2.361	0.09

Sample PK2A1

Concordia age ~ 2390 Ma

Sample No.	$^{207}\text{Pb}/^{235}\text{U}$	2RSE(%)	$^{206}\text{Pb}/^{238}\text{U}$	2RSE(%)	Rho
pk2a1_pop_1_06a	9.2906	3.499	0.4463	3.551	0.51
pk2a1_pop_1_06b	9.3748	1.710	0.4683	1.891	0.55

Concordia age 900 ± 100 Ma

Sample No.	$^{207}\text{Pb}/^{235}\text{U}$	2RSE(%)	$^{206}\text{Pb}/^{238}\text{U}$	2RSE(%)	Rho
pk2a1_pop2_01a	1.3953	13.397	0.1485	15.241	0.57
pk2a1_pop2_45a	1.5841	70.379	0.0946	47.328	0.34
pk2a1_pop2_21	1.6374	9.310	0.1691	9.202	0.49

Concordia age 440 ± 50 Ma

Sample No.	$^{207}\text{Pb}/^{235}\text{U}$	2RSE(%)	$^{206}\text{Pb}/^{238}\text{U}$	2RSE(%)	Rho
pk2a1_pop2_29	0.4663	25.037	0.0587	24.957	0.50
pk2a1_pop2_34b	0.6513	28.951	0.0841	25.955	0.45
pk2a1_pop1_11	0.6620	44.467	0.0910	26.574	0.30

Concordia age 220 ± 10 Ma

Sample No.	$^{207}\text{Pb}/^{235}\text{U}$	2RSE(%)	$^{206}\text{Pb}/^{238}\text{U}$	2RSE(%)	Rho
pk2a1_pop2_38	0.2390	20.388	0.0329	17.558	0.43
pk2a1_pop2_44	0.2436	6.988	0.0334	6.198	0.44

Concordia age 70 ± 2 Ma

Sample No.	$^{207}\text{Pb}/^{235}\text{U}$	2RSE(%)	$^{206}\text{Pb}/^{238}\text{U}$	2RSE(%)	Rho
pk2a1_pop1_07b	0.0635	15.093	0.0107	7.230	0.24
pk2a1_pop1_07d	0.0670	147.947	0.0099	100.833	0.34
pk2a1_pop1_07a	0.0782	34.096	0.0107	12.396	0.18
pk2a1_pop2_33	0.0715	4.515	0.0108	2.942	0.33
pk2a1_pop2_36	0.0754	9.412	0.0105	5.958	0.32

Concordia age 62 ± 1 Ma

Sample No.	$^{207}\text{Pb}/^{235}\text{U}$	2RSE(%)	$^{206}\text{Pb}/^{238}\text{U}$	2RSE(%)	Rho
pk2a1_pop1_09b	0.0594	7.488	0.0097	5.863	0.39
pk2a1_pop1_09a	0.0608	11.550	0.0097	2.509	0.11
pk2a1_pop1_01b	0.0698	85.603	0.0092	13.275	0.08
pk2a1_pop2_13	0.0699	32.645	0.0096	6.014	0.09
pk2a1_pop1_07b	0.0635	15.093	0.0107	7.230	0.24
pk2a1_pop1_07d	0.0670	147.947	0.0099	100.833	0.34
pk2a1_pop1_07a	0.0782	34.096	0.0107	12.396	0.18

Concordia age 55 ± 3 Ma

Sample No.	$^{207}\text{Pb}/^{235}\text{U}$	2RSE(%)	$^{206}\text{Pb}/^{238}\text{U}$	2RSE(%)	Rho
pk2a1_pop2_34c	0.0625	20.337	0.0087	16.266	0.40
pk2a1_pop2_45c	0.0627	29.301	0.0079	14.302	0.24
pk2a1_pop2_09c	0.0639	35.827	0.0089	19.991	0.28
pk2a1_pop2_01b	0.0649	27.470	0.0086	5.524	0.10

Concordia age 50.9 ± 0.6 Ma

Sample No.	$^{207}\text{Pb}/^{235}\text{U}$	2RSE(%)	$^{206}\text{Pb}/^{238}\text{U}$	2RSE(%)	Rho
pk2a1_pop1_06c	0.0427	10.214	0.0076	8.363	0.41
pk2a1_pop2_51d	0.0455	20.720	0.0076	15.349	0.37
pk2a1_pop2_42b	0.0485	30.988	0.0077	14.543	0.23
pk2a1_pop2_51e	0.0491	15.223	0.0076	10.481	0.34
pk2a1_pop2_46c	0.0496	90.060	0.0077	36.045	0.20
pk2a1_pop1_03b	0.0497	5.642	0.0078	3.951	0.35
pk2a1_pop2_46b	0.0508	136.421	0.0077	25.816	0.09

Appendix

pk2a1_pop2_37	0.0514	10.536	0.0080	7.154	0.34
pk2a1_pop2_05	0.0518	2.027	0.0080	1.560	0.38
pk2a1_pop2_14	0.0530	10.989	0.0080	2.781	0.13
pk2a1_pop2_35	0.0531	27.094	0.0079	7.798	0.14
pk2a1_pop2_51c	0.0554	15.690	0.0083	10.034	0.32
pk2a1_pop2_03b	0.0570	16.926	0.0081	12.740	0.38
pk2a1_pop1_06c	0.0427	10.214	0.0076	8.363	0.41

Sample PK30Z

Concordia age 2930±20 Ma

Sample No.	$^{207}\text{Pb}/^{235}\text{U}$	2RSE(%)	$^{206}\text{Pb}/^{238}\text{U}$	2RSE(%)	Rho
pk30z_pop4_05b	14.2218	19.531	0.4592	33.224	0.85
pk30z_pop2_03	16.5383	7.838	0.5500	15.194	0.97
pk30z_pop4_02a	16.9341	7.043	0.6049	5.608	0.40

Concordia age 2460±40 Ma

Sample No.	$^{207}\text{Pb}/^{235}\text{U}$	2RSE(%)	$^{206}\text{Pb}/^{238}\text{U}$	2RSE(%)	Rho
pk30z_pop2_02b	9.8495	6.832	0.4628	7.111	0.52
pk30z_pop4_05a	10.4069	6.587	0.4705	9.917	0.75
pk30z_pop2_02a	10.4473	18.515	0.4806	18.639	0.50
pk30z_pop4_02b	12.2215	17.766	0.5090	15.834	0.45

Concordia age 1440±50 Ma

Sample No.	$^{207}\text{Pb}/^{235}\text{U}$	2RSE(%)	$^{206}\text{Pb}/^{238}\text{U}$	2RSE(%)	Rho
pk30z_pop2_07b	2.2431	35.169	0.2066	21.977	0.31
pk30z_pop2_14b	3.0161	10.419	0.2357	8.976	0.43
pk30z_pop2_14a	3.1535	4.979	0.2457	4.213	0.42
pk30z_pop2_07a	3.2294	41.245	0.2662	39.550	0.48
pk30z_pop2_04	3.7791	12.742	0.2728	13.439	0.53

Concordia age 900±10 Ma

Sample No.	$^{207}\text{Pb}/^{235}\text{U}$	2RSE(%)	$^{206}\text{Pb}/^{238}\text{U}$	2RSE(%)	Rho
pk30z_pop2_17	1.0978	27.477	0.1249	29.128	0.53
pk30z_pop4_03c	1.2499	24.532	0.1295	20.485	0.42
pk30z_pop4_01b	1.3914	8.404	0.1441	11.216	0.67
pk30z_pop4_03a	1.4096	7.198	0.1548	3.159	0.22
pk30z_pop2_11a	1.4362	3.388	0.1479	3.452	0.51
pk30z_pop2_11b	1.4830	18.862	0.1526	18.862	0.50
pk30z_pop3_01a	1.6308	65.740	0.1810	56.843	0.43

Concordia age 525±10 Ma

Sample No.	$^{207}\text{Pb}/^{235}\text{U}$	2RSE(%)	$^{206}\text{Pb}/^{238}\text{U}$	2RSE(%)	Rho
pk30z_pop2_09	0.5971	242.030	0.0783	45.880	0.09
pk30z_pop2_12	0.6260	9.796	0.0757	9.001	0.46
pk30z_pop4_04b	0.6666	2.231	0.0858	1.780	0.40
pk30z_pop1_02a	0.7080	21.124	0.0872	19.777	0.47
pk30z_pop4_01a	0.7199	6.282	0.0876	6.705	0.53

Concordia age 49±1 Ma

Sample No.	$^{207}\text{Pb}/^{235}\text{U}$	2RSE(%)	$^{206}\text{Pb}/^{238}\text{U}$	2RSE(%)	Rho
pk30z_pop1_04a	0.0465	6.467	0.0074	7.079	0.55
pk30z_pop1_04b	0.0471	7.168	0.0074	7.588	0.53
pk30z_pop3_02	0.0492	11.093	0.0075	9.494	0.43
pk30z_pop1_05	0.0495	17.732	0.0078	17.959	0.51
pk30z_pop1_03	0.0501	24.726	0.0077	23.371	0.47
pk30z_pop3_04	0.0502	3.707	0.0078	3.491	0.47
pk30z_pop3_01b	0.0548	191.181	0.0078	36.977	0.10
pk30z_pop1_01b	0.0587	45.661	0.0085	45.608	0.50
pk30z_pop2_15b	0.0673	64.662	0.0078	58.195	0.45

Sample PK26

Concordia age 2450±100 Ma

Sample No.	$^{207}\text{Pb}/^{235}\text{U}$	2RSE(%)	$^{206}\text{Pb}/^{238}\text{U}$	2RSE(%)	Rho
pk26_11a	10.1973	7.378	0.4880	8.050	0.55
pk26_11b	10.3007	6.561	0.5068	6.680	0.51

Concordia age 1670±90 Ma

Sample No.	$^{207}\text{Pb}/^{235}\text{U}$	2RSE(%)	$^{206}\text{Pb}/^{238}\text{U}$	2RSE(%)	Rho
pk26_12b	3.8839	32.437	0.3006	32.969	0.51
pk26_12d	4.1862	15.965	0.3122	20.017	0.63
pk26_12a	4.3298	18.421	0.3423	17.733	0.48

Concordia age 70±20 Ma

Sample No.	$^{207}\text{Pb}/^{235}\text{U}$	2RSE(%)	$^{206}\text{Pb}/^{238}\text{U}$	2RSE(%)	Rho
pk26_12c	0.0842	42.850	0.0099	33.791	0.39
pk26_03b	0.5541	179.912	0.0594	94.373	0.26

Curriculum Vitae

Personal data

Name : Pitsanupong Kanjanapayont
Date of birth : 8 June 1978
Place of birth : Ratchaburi, Thailand
Nationality : Thai
Home address : 95/4 M.6 Nakhonpathom, Muang Nakhonpathom, Nakhonpathom 73000
Thailand
Affiliation : Department of Geology, Faculty of Science, Chulalongkorn University,
Bangkok 10330 Thailand
e-mail : pitsanupong@geo.sc.chula.ac.th, pitsanupong.k@hotmail.com

Education

1993-1995 : High school, Non-formal education center of Nakhonpathom, Nakhonpathom, Thailand
1995-1999 : B.Sc. (Geology), Chulalongkorn University, Bangkok, Thailand
Title “A structural geology study at Amphoe Wangwiset and Amphoe Sikao, Changwat Trang”
1999-2003 : M.Sc. (Geology), Chulalongkorn University, Bangkok, Thailand
Title “Geologic structural model illustrated by the Mesozoic stratigraphic units in the upper southern Thailand, with special reference to Changwat Krabi and Surat Thani”
2006-2009 : Dr.rer.nat. (Geology), University of Vienna, Vienna, Austria
Title “Structural analysis and geochronology of the Khlong Marui Fault, southern Thailand”

Research interests

Structural geology
Tectonics
Geochronology

Work experiences

January 2004 – June 2004 : Geologist, Technical Support and Development Division,
Bureau of Mineral Resources, Department of Mineral Resources,
Bangkok, Thailand
July 2004 – Present : Lecturer, Department of Geology, Faculty of Science,
Chulalongkorn University, Bangkok, Thailand

Abstracts and presentations in the international conferences

Kanjanapayont, P., Edwards, M.A., and Grasemann, B., 2007. Strain styles within the Klong Marui continental wrench fault, southern Thailand. EGU general assembly 2007, session TS 6.1, April 15-20, 2007, Vienna, Austria. (abstract and poster presentation)

Kanjanapayont, P., Edwards, M.A., and Grasemann, B., 2008. Lineament interpretation and deformation styles within the Klong Marui continental wrench fault, southern Thailand. EGU general assembly 2008, session TS 8, April 13-18, 2008, Vienna, Austria. (abstract and poster presentation)

Kanjanapayont, P., Edwards, M.A., and Grasemann, B., 2008. The dextral Klong Marui strike-slip fault, southern Thailand. International Meeting of Young Researchers in Structural Geology and Tectonics (YORSGET-08), July 1-3, 2008, Oviedo, Spain. (extended abstract and poster presentation)

Kanjanapayont, P., Edwards, M.A., and Grasemann, B., 2008. Kinematics of the Klong Marui continental wrench fault, southern Thailand. Fault Zones: Structure, Geomechanics and Fluid Flow, September 16-18, 2008, London, UK. (abstract and poster presentation)

Kanjanapayont, P., Grasemann, B., and Edwards, M.A., 2008. Deformation microstructures within the Klong Marui shear zone, southern Thailand. International Symposium on Geoscience Resources and Environments of Asian Terranes (GREAT 2008), 4th IGCP 516, 5th APSEG, November 24-26, 2008, Bangkok, Thailand. (extended abstract and oral presentation))

Kanjanapayont, P., Grasemann, B., and Edwards, M.A., 2009. Deformation ages within the Klong Marui continental wrench fault, southern Thailand. EGU general assembly 2009, session TS 2.2, April 19-24, 2009, Vienna, Austria. (abstract and poster presentation)